VOLUME 8 ISSUE 2 JUNE 2023

IJEG

International Journal of Engineering and Geosciences

e-ISSN 2548-0960

Assist. Prof. Dr. Yelda TURKAN
Oregon State University,
USA

Dr. G. Sanka N. PERERA
Sabaragamuwa University Faculty of Geomatics
Sri Lanka

Dr. Hsiu-Wen CHANG
National Cheng Kung University, Department of Geomatics
Taiwan

The International Journal of Engineering and Geosciences (IJEG)

The International Journal of Engineering and Geosciences (IJEG) is a tri-annually published journal. The journal includes a wide scope of information on scientific and technical advances in the geomatics sciences. The International Journal of Engineering and Geosciences aims to publish pure and applied research in geomatics engineering and technologies. IJEG is a double peer-reviewed (blind) OPEN ACCESS JOURNAL that publishes professional level research articles and subject reviews exclusively in English. It allows authors to submit articles online and track his or her progress via its web interface. All manuscripts will undergo a refereeing process; acceptance for publication is based on at least two positive reviews. The journal publishes research and review papers, professional communication, and technical notes. IJEG does not charge for any article submissions or for processing.

CORRESPONDENCE ADDRESS
Journal Contact: engineeringandgeoscience@gmail.com

CONTENTS

Volume 8 - Issue 2

RESEARCH ARTICLES

** **Assessment of latest global gravity field models by GNSS/Levelling Geoid**

Nazan Yılmaz 111

** **3D positioning accuracy and land cover classification performance of multispectral RTK UAVs**

Umut Gunes Sefercik, Taskin Kavzoglu, Ismail Colkesen, Mertcan Nazar, Muhammed Yusuf Ozturk, Samed Adali, Salih Dinc 119

** **Automatic detection of single street trees from airborne LiDAR data based on point segmentation methods**

Zehra Cetin, Naci Yastikli 129

** **Deep learning-based vehicle detection from orthophoto and spatial accuracy analysis**

Muhammed Yahya Biyik , Muhammed Enes Atik, Zaide Duran 138

** **A comprehensive analysis of different geometric correction methods for the Pleiades -1A and Spot-6 satellite images**

Buğrahan Özcihan, Levent Doğukan Özlü, Mümin İlker Karakap, Halime Sürmeli, Ugur Alganci, Elif Sertel 146

** **Genesis and spatio-temporal analysis of glacial lakes in the peri-glacial environment of Western Himalayas**

Fareeha Siddique, Atta-ur Rahman 154

** **The effect of DEM resolution on topographic wetness index calculation and visualization: An insight to the hidden danger unraveled in August, 2021 in Bozkurt**

Arif Oguz Altunel 165

** **Seasonal analysis and mapping of air pollution (PM10 and SO_2) during Covid-19 lockdown in Kocaeli (Türkiye)**

Burak Kotan, Arzu Erener 173

** **Assessment of the solar energy potential of rooftops using LiDAR datasets and GIS based approach**

Vancho Adjiski, Gordana Kaplan, Stojance Mijalkovski 188

** **Modeling of annual maximum flows with geographic data components and artificial neural networks**

Esra Aslı Çubukçu, Vahdettin Demir, Mehmet Faik Sevimli 200

International Journal of Engineering and Geosciences
https://dergipark.org.tr/en/pub/ijeg
e-ISSN 2548-0960

Assessment of latest global gravity field models by GNSS/Levelling Geoid

Nazan Yılmaz *[1]

[1]*Karadeniz Technical University, Department of Geomatics Engineering, Türkiye*

Keywords
GGMs
GNSS/Levelling
Geoid
Statistical values

Research Article
DOI: 10.26833/ijeg.1070042

Received: 08.02.2022
Accepted: 24.06.2022
Published: 19.10.2022

Abstract

This paper focuses on making a comparing of GNSS/Levelling data and data obtained from global geopotential models. For comparison, geoid undulations obtained by GNSS/Levelling method and geoid undulations obtained from global geopotential models have been used. As global geopotential models, SGG-UGM-2, XGM2019e_2159, GO_CONS_GCF_2_TIM_R6e, ITSG-Grace2018s, EIGEN-GRGS.RL04.MEAN-FIELD, GOCO06s, GO_CONS_GCF_2_TIM_R6, GO_CONS_GCF_2_DIR_R6 GGMs are used. The data sets used in the improvements of the models are altimetry, satellite, location data and topography. The disparities between the geoid undulations obtained from the GNSS/Levelling method and geoid undulations obtained from global geoid models have been taken. Some statistical criteria for these differences have been calculated. These criteria, such as smallest, biggest, average, standard deviation, Root Mean Square RMS statistical values of deviations between GNSS/Levelling geoid and global geopotential models, are taken into consideration when comparing the models. According to the comparison, the global gravity field model that best fits the GNSS/Levelling is selected.

1. Introduction

Spheric harmonic expansion is a widely performed presentment the earth gravity field. This presentment is meaned by potential coefficients in the spheric harmonic expansion of the field determined using the elements/parameters of the field measured at the earth's surface and/or in extraterrestrial space. The International Center for Earth Models of Gravity (ICGEM) publishes developed Global Gravity Field Models (GGMs) in time [1].

Because of the technological advances in working the earth's gravity field, latest GGMs's precision studies for diverse regions are of trend attention. Satellite gravimetric tasks bottomed on satellite-to-satellite observing and gradiometry make it potential to get big scale properties of the Earth's gravity field, defined with spheric harmonics [2].

Global geopotential models of spherical harmonic coefficients are used to determine the external gravitational field of the Earth. These coefficients are derived from satellite orbit perturbations, terrestrial gravity anomalies and altimeter data. Hundreds of thousands of coefficients and standard deviation values for these coefficients are estimated from millions of observations [3].

GGMs have been developed primarily as satellite-only models containing data from LAGEOS, CHAMP, GRACE, and GOCE, or qua composite models that combine satellite observations with terrestrial, aerial, ship-sourced gravity data, altitude data, and satellite altimetry measurements a comprehensive gravitational field by clarified spatial resolution [4].

Earth's gravity potential on a universal measure and in too great solution is an essential precondition for a variety of geodetic, geophysical and oceanographic research as well practices. Over the last 50 years, there have been developments and corrections in primary gravity modeling hypothesis as parallel the attendance of more precise and full data and developments in the computational facilities existing for digital modeling works [5].

ICGEM website (http://icgem.gfz-potsdam.de/tom_longtime) is published resolutions of gravity field models containing gravity information from special satellites [6].

Special gravity missions have reformed information of the Earth gravity field. CHAMP satellite was started on

* **Corresponding Author**
*(n_berber@ktu.edu.tr) ORCID ID 0000-0002-0615-8218

Cite this article
Yılmaz, N. (2023). Assessment of latest global gravity field models by GNSS/Levelling Geoid. International Journal of Engineering and Geosciences, 8(2), 111-118

July 15, 2000. It is composed the primary gravity field mission to carry a GPS receiver by permanent 3D following capacity as well a sensitive accelerometer to measure non-gravity beeves. The GOCE satellite was perfectly started on March 17, 2009 and began its operating stage in September 2009. The mission target, stated qua cumulative geoid precision, is a mistake of 1-2 cm at 200 harmonic degrees, corresponding to a half wavelength of about 100 [7].

GRACE satellite was started in March 2002 beneath the NASA Earth System Science Pathfinder Program. GRACE is jointly implemented by the NASA and German Aerospace Center. The primary instrument on the twin GRACE satellites is the K-Band Ranging system (KBR) that observes the intersatellite range to a precision of a few microns. This is the fundamental measurement for the GRACE gravity recovery [8].

GRACE has ensured advanced measurements of worldwide massif flow that have conduced major to mentality of big-scale varies in polar ice, groundwater preservation and ocean massif dispersion. Most of these results are obtained from the analysis of spheric gravity fields solved in terms of spheric harmonic fundamental functions. Nevertheless, free harmonic solutions from GRACE normally suffer from bad traceable gradients, outcoming from "stripes" which are traditionally extracted through experimental smoothing and/or "banding" algorithms [9].

GOCE, GRACE and GRACEFO satellites have been obtained wide developments in the grade of GGMs by solving satellite following, accelerometry, and gradiometry. Gravity field's particulars can be withdrawed handling a composition of satellite reproduced measurements and terrestrial gravity measurements with the inclusion of those measured on flitting platforms [10].

Global Navigation Satellite System (GNSS) has been commonly used in several scientific and engineering applications including positioning, navigation, and time transfer for several decades [11]. There are mainly two different orbital information, namely broadcast ephemerides and IGS final ephemerides used in the GPS positioning. The broadcast ephemerides used in practice and real time are obtained through assessments derived from the observations from the USA GPS reference stations. Broadcast ephemerides are formed (depending on GPS week) from satellite information and the accuracies they provide are adequate in many GPS applications [12].

Global positioning systems can be described as revolution today. These systems can be used in determining the approximate location of any object, navigating the means of transportation, in many measuring processes and in many areas that will make life easier [13]. When determining point positions with GNSS, it should be paid attention to both GNSS measurement errors and noise affecting GNSS frequencies. While GNSS measurement errors can be reduced with an appropriate measurement method, the noise affecting GNSS signals are resolved as a result of analyzes [14].

Global Navigation Satellite Systems (GNSS), scientific research, as well as commercial and non-commercial applications has gained great importance. GPS from America, GLONASS from Russia, BEIDOU from China and GALILEO from Europe provided convenience to the user on a global scale in the location determination issues thanks to Satellite systems's (GNSS) modernization and rapid development [15].

2. Global geopotential models

In this paper, SGG-UGM-2, XGM2019e_2159, GO_CONS_GCF_2_TIM_R6e, ITSG-Grace2018s, EIGEN-GRGS.RL04.MEAN-FIELD, GOCO06s, GO_CONS_GCF_2_TIM_R6, GO_CONS_GCF_2_DIR_R6 models have been used.

SGG-UGM-2 has 5′ × 5′ spatial resolution. It is up to degree 2190 and order 2159. It combines the GOCE SGG and SST-hl measurements, ITSG-Grace2018 NEQ system, satellite marine gravity anomalies as well continental gravity information reproduced from EGM2008 [5].

XGM2019e is a unified GGM symbolized by spheroidal harmonics up to 5399 degrees and orders suitable for 2′ (~4 km) spatial resolution. Combination of satellite data with gravity measurements is made usage complete normal equations up to 719 degrees and orders (15') [16].

GO_CONS_GCF_2_TIM_R6e is an expanded type of the satellite only GGM TIM_R6. TIM_R6 contains extra-terrestrial gravity field measurements over polar gap fields of the GOCE [17].

ITSG-Grace2018 is a GRACE's latest sets of gravity field resolutions. It is based on reprocessed GRACE measurement information (L1B RL03) and the recent atmosphere and ocean softening product (AOD1BRL06) [18].

EIGEN-GRGS.RL04.MEAN-FIELD which is based on CNES/GRGS RL04 is existing for the GRACE 2002 and 2016 time period. Extrapolated terms before August 2002 and after May 2016 are based on global fits of monthly coefficients of GRACE information [19].

GOCO06s is the last satellite specific GGM calculated by GOCO. Various observation methods is key in supplying nonstop high precision and the top probable spatial resolution of the Earth's gravity field. The full published dataset of GOCO06s occurs of a static gravity field solution of up to 300 degrees and orders [20].

GO_CONS_EGM_TIM_RL06 has reckoned qua a successor of the RL05 model issued in 2014. It tracks the philosophy of the former GOCE time models with the fundamental opinion that it is based on GOCE measurements only. It is ensured qua a spherical harmonic expansion, cutted at degree 300.

GO_CONS_EGM_TIM_RL06 was calculated qua the heir to the RL05 model issued in 2014. It is based on the reworked gravity gradients of the GOCE satellite and handling improved working touch. It is cutted at 300 degrees as a spheric harmonic expansion [21].

GO_CONS_GCF_2_DIR_R6 is the European Space Agency's Version 6 GOCE gravity field model. It is completed integration of GOCE-Satellite Gravity Gradiometry, GRACE and Satellite Laser Distance following information, ensuring both perfect orbits are compatible and Global Positioning System outcomes. It is a fixed universal only satellite GGM with d/o of 300 [22].

Table 1 shows global gravity models and their data, resolution and year. In this table, A represents altimetry, S represents satellite, G is for location data and T represents topography.

N is geoid height and it can be represented by spheric harmonic parameters using Eq. 1:

where (θ, λ) co-latitude and longitude of the calculation dot and R is the Earth's mean radius, $\bar{P}_{lm}$ is the associated Legendre polynomials, $\bar{C}_{lm}$ and $\bar{S}_{lm}$ are the spheric harmonic coefficients as l degree and m order.

$$N(\theta,\lambda) \approx R \sum_{l=2}^{i_{max}} \sum_{m=0}^{l} \bar{P}_{lm}(sin\theta)[\bar{C}_{lm}cosm\lambda + \bar{S}_{lm}sinm\lambda) \quad (1)$$

Table 1. Recent Global Geopotential Models

Model	Data	Max. Resolution (Degree)	Year
SGG-UGM-2	A, EGM2008, Grace), S(Goce)	2190	2020
XGM2019e_2159	A, G, S(GOCO06s), T	2190	2019
GO_CONS_GCF_2_TIM_R6e	G (Polar), S(Goce)	300	2019
ITSG-Grace2018s	S(Grace)	200	2019
EIGEN-GRGS.RL04.MEAN-FIELD	S	300	2019
GOCO06s	S	300	2019
GO_CONS_GCF_2_TIM_R6	S(Goce)	300	2019
GO_CONS_GCF_2_DIR_R6	S	300	2019

3. Study area and application

In the study, 30 points belonging to Turkey National Basic GNSS Network (TUTGA-99A) were used. The ellipsoidal heights of these points in the TUTGA-99 coordinate system are directly determined by GNSS measurements, and the orthometric heights are the points determined directly or indirectly in the Turkish National Vertical Control Network-1999 datum. You can see these points' distribution in Figure 1. In this paper, these points are named as test points.

Figure 1. Locations of test points

3.1. Application

The geoid undulations according to global geopotential models were interpolated by using user-defined points in ICGEM web page. The Kriging interpolation method as interpolation technique and WGS84 as reference system was used in these calculations.

Differences of geoid undulations obtained from global geopotential models and GNSS/Levelling have been shown in Table 2.

Differences of geoid height values and geoid undulations obtained from global geopotential models and GNSS/Levelling have been shown in Figure 2,3,4,5,6,7,8 and 9.

The differences between the Global Geopotential Models and GNSS/Levelling were calculated using Eq. 2.

$$\Delta N = N_{GNSS\,/\,Lev} - N_{GGM} \quad (2)$$

In this equation, ΔN is the geoid height differences, $N_{GNSS/Lev}$ is the geoid height calculated from GNSS/levelling and N_{GGM} is the geoid height calculated from GGMs. For the statistical examination of geoid height differences, minimum, maximum, mean and standard deviation values of ΔN are defined. In addition, the root mean square (RMS) values were calculated using Eq. 3.

$$RMS = \pm\left[\left(\sum_{i=1}^{k} \Delta N^2_{GPS\,/\,Niv-GM}\right) / k \right]^{1/2} \quad (3)$$

Where k is the number of the test points as 30.

The statistical information on the difference between geoid undulations obtained from GGMs and geoid undulations obtained from GNSS/levelling has been shown in Table 3.

Table 2. Differences of geoid undulations

N. N.	GNSS/Lev.-EIGEN-GRGS.RL04	GNSS/ Lev.-GO_CONS_GCF_2_DIR_R6	GNSS/ Lev.-GO_CONS_GCF_2_TIM_R6	GNSS/ Lev.-GO_CONS_GCF_2_TIM_R6e	GNSS/ Lev. -GOCO06s	GNSS/ Lev. -ITSG-Grace2018s	GNSS/ Lev. -SSG-UGM-2	GNSS/ Lev. -XGM2019e_2159
1	-0.173	-0.099	-0.090	-0.100	-0.088	-0.348	0.022	0.083
2	0.572	0.484	0.547	0.554	0.559	0.498	0.648	0.562
3	0.043	-0.057	-0.070	-0.071	-0.066	0.329	0.035	0.041
4	0.017	0.190	0.196	0.187	0.197	0.216	0.046	0.015
5	-0.460	-0.533	-0.544	-0.540	-0.541	-0.132	0.019	0.024
6	-0.461	-0.430	-0.376	-0.376	-0.383	0.205	0.066	0.091
7	0.835	0.832	0.796	0.798	0.784	1.035	0.336	0.372
8	0.309	0.191	0.248	0.249	0.260	-0.097	0.235	0.435
9	-0.182	-0.220	-0.183	-0.177	-0.184	0.193	0.210	0.096
10	0.068	0.033	0.055	0.052	0.076	-0.587	-0.061	-0.006
11	0.129	0.028	0.021	0.022	0.014	0.882	0.148	0.135
12	0.157	0.230	0.276	0.284	0.288	-0.464	-0.133	-0.028
13	0.788	0.793	0.832	0.842	0.839	0.848	-0.018	-0.024
14	0.101	0.131	0.146	0.143	0.140	0.195	0.047	0.028
15	0.555	0.483	0.473	0.476	0.466	0.582	0.137	0.214
16	-0.126	-0.123	-0.108	-0.115	-0.102	-0.674	0.077	0.186
17	-0.390	-0.364	-0.389	-0.393	-0.398	0.278	-0.035	-0.013
18	-0.131	-0.166	-0.182	-0.175	-0.182	-0.029	0.233	0.165
19	0.160	0.284	0.288	0.292	0.290	-0.129	0.153	0.133
20	-0.188	-0.066	-0.043	-0.046	-0.033	-0.480	-0.004	0.011
21	-0.135	-0.257	-0.205	-0.198	-0.190	0.027	0.062	0.031
22	-0.140	-0.127	-0.149	-0.155	-0.150	-0.131	0.165	0.135
23	0.110	0.198	0.217	0.216	0.230	0.006	0.132	0.168
24	-0.155	-0.153	-0.141	-0.135	-0.141	-0.145	0.095	0.082
25	0.353	0.301	0.291	0.287	0.298	0.298	0.123	0.145
26	0.367	0.346	0.329	0.329	0.329	-0.067	0.070	0.135
27	-0.302	-0.270	-0.253	-0.244	-0.231	-0.515	-0.059	0.000
28	0.195	0.138	0.129	0.133	0.134	0.065	-0.081	-0.041
29	-0.122	-0.238	-0.211	-0.204	-0.191	0.093	-0.001	-0.011
30	-0.495	-0.534	-0.560	-0.561	-0.562	-0.323	-0.069	-0.091

Table 3. Statistical Values of $N_{GNSS/Lev}$ - N_{GGM} (m)

Compared Models	**Min.**	**Max.**	**Mean**	**Std. Dev.**	**± RMS**
GNSS/Levelling-EIGEN-GRGS.RL04	0.495	0.835	0.043	0.348	0.345
GNSS/ Levelling-GO_CONS_GCF_2_DIR_R6	0.534	0.832	0.034	0.346	0.342
GNSS/ Levelling-GO_CONS_GCF_2_TIM_R6	0.560	0.832	0.045	0.348	0.345
GNSS/ Levelling-GO_CONS_GCF_2_TIM_R6e	0.561	0.842	0.046	0.349	0.346
GNSS/ Levelling -GOCO06s	0.562	0.839	0.049	0.348	0.346
GNSS/ Levelling -ITSG-Grace2018s	0.674	1.035	0.054	0.429	**0.425**
GNSS/ Levelling -SSG-UGM-2	0.133	0.648	0.087	0.151	**0.172**
GNSS/ Levelling -XGM2019e_2159	0.091	0.562	0.102	0.145	0.175

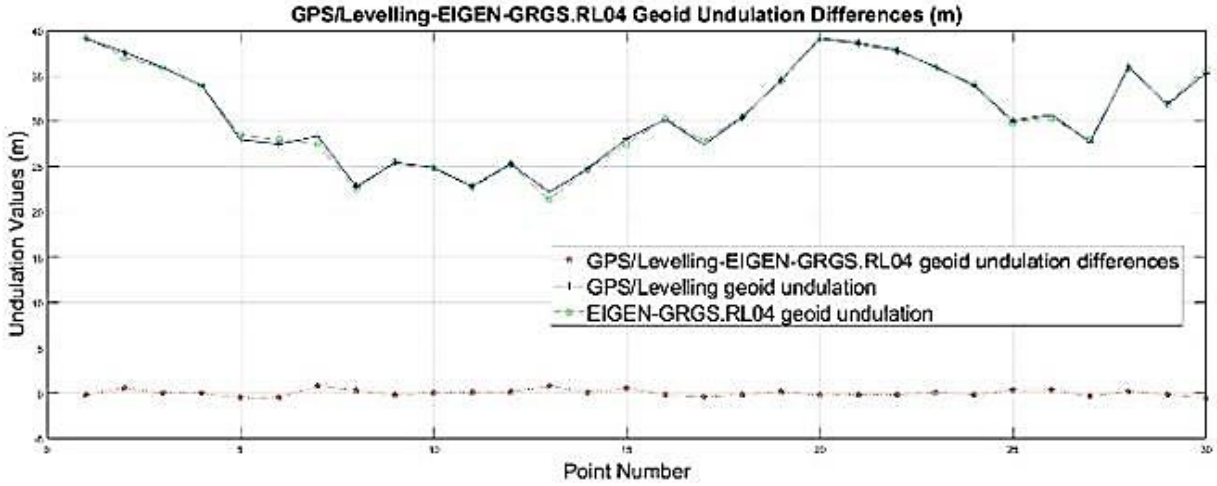

Figure 2. GNSS/Levelling-EIGEN-GRGS.RL04

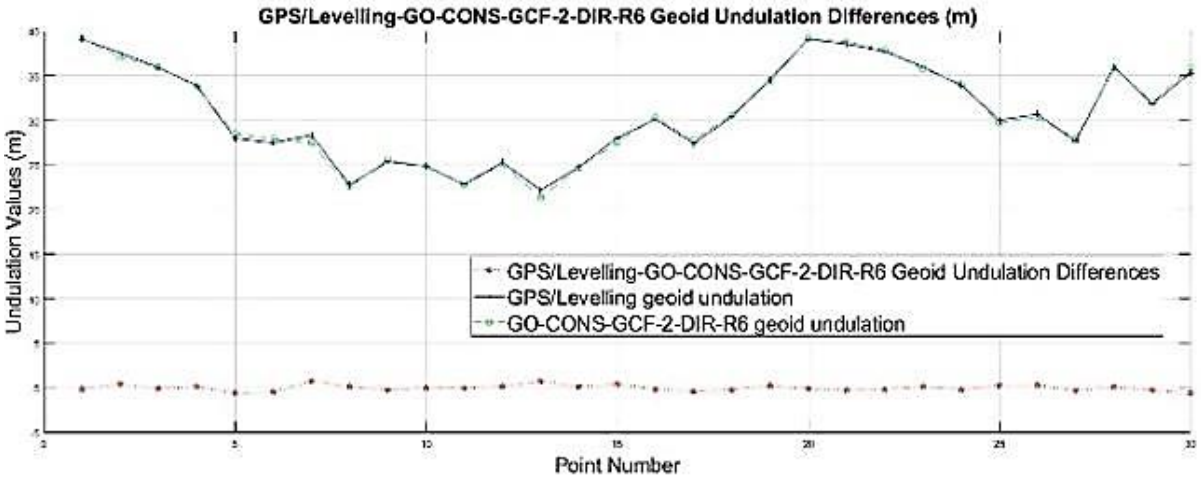

Figure 3. GNSS/ Levelling-GO_CONS_GCF_2_DIR_R6

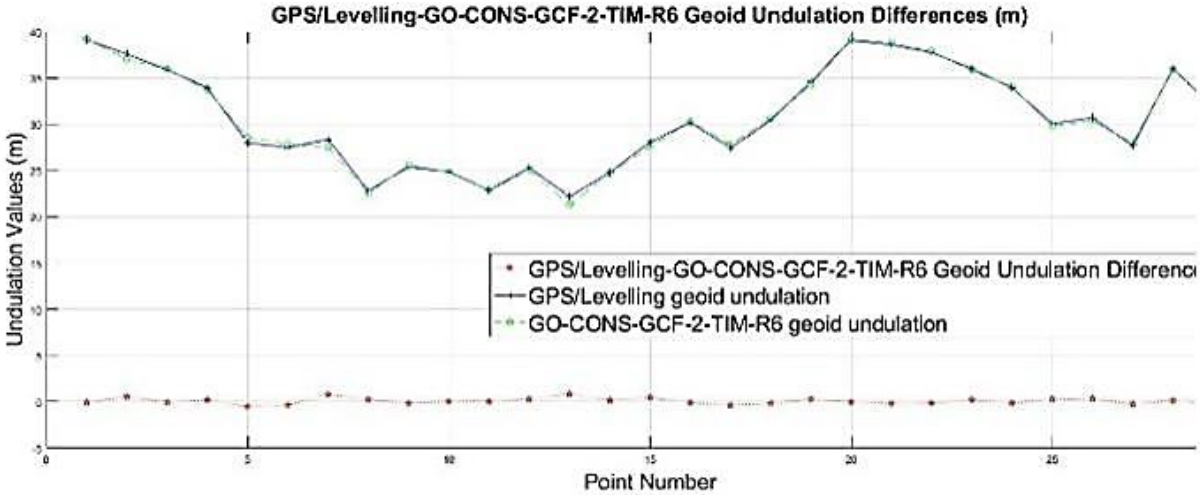

Figure 4. GNSS/ Levelling-GO_CONS_GCF_2_TIM_R6

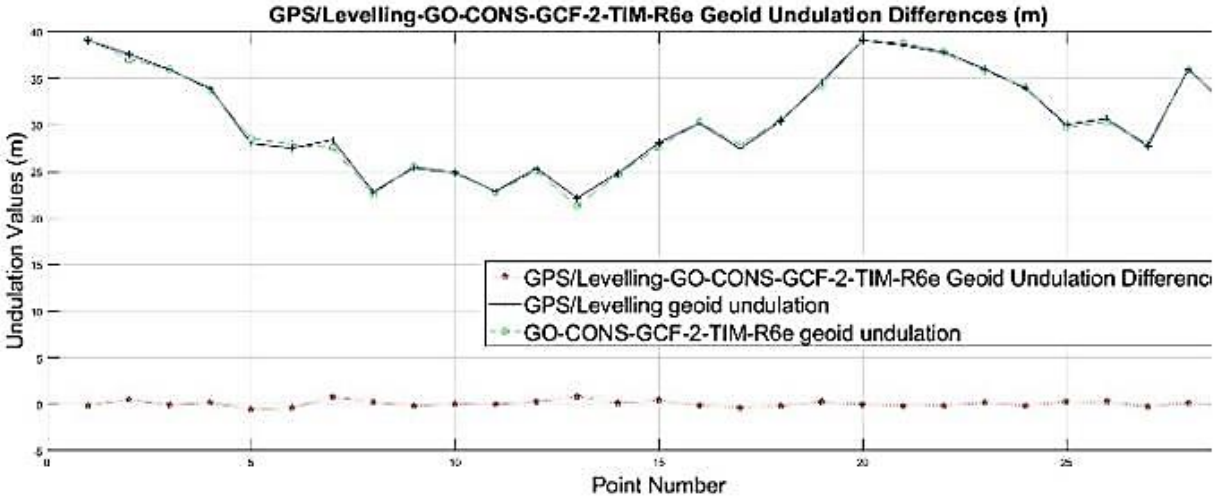

Figure 5. GNSS/ Levelling-GO_CONS_GCF_2_TIM_R6e

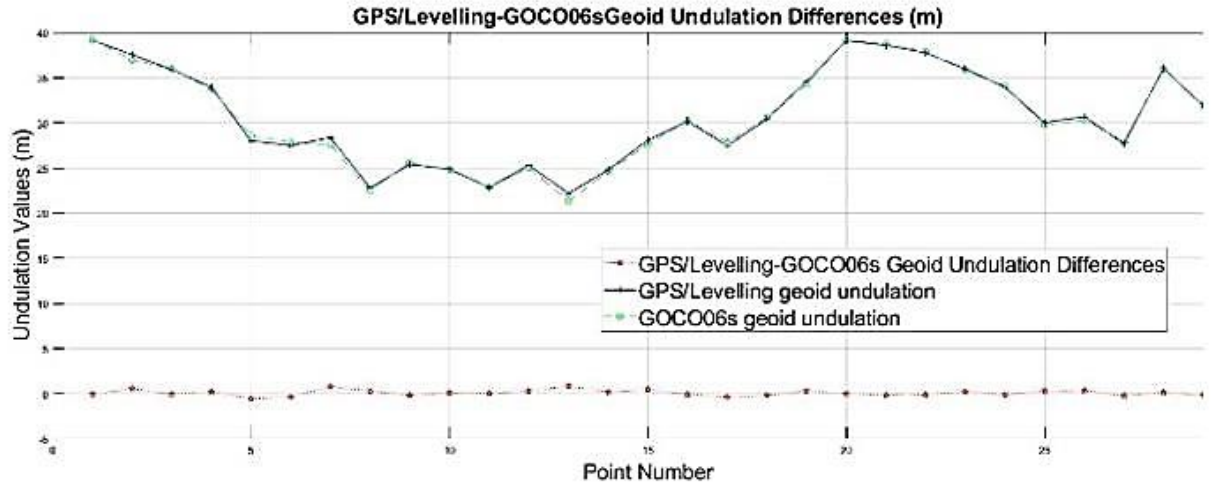

Figure 6. GNSS/ Levelling -GOCO06s

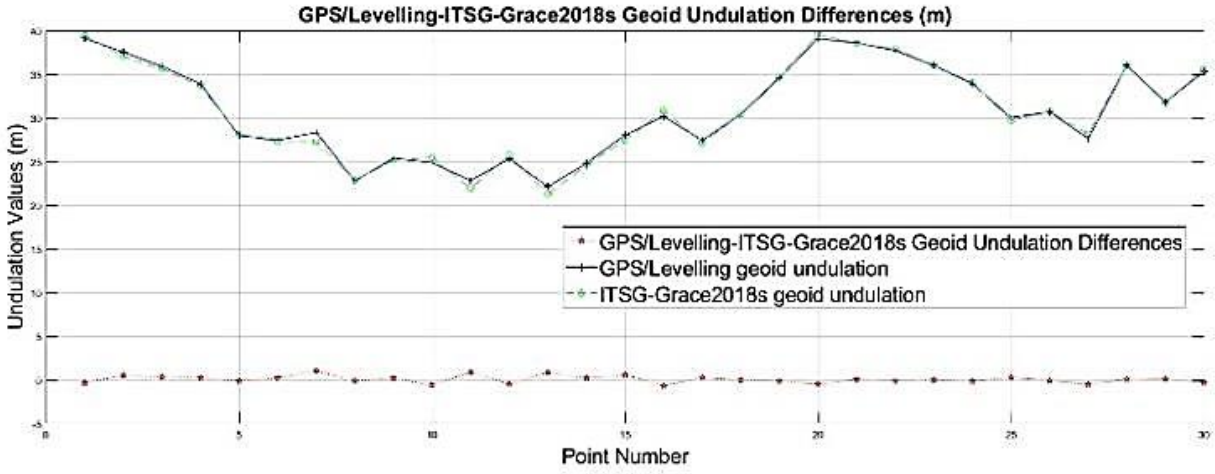

Figure 7. GNSS/ Levelling -ITSG-Grace2018s

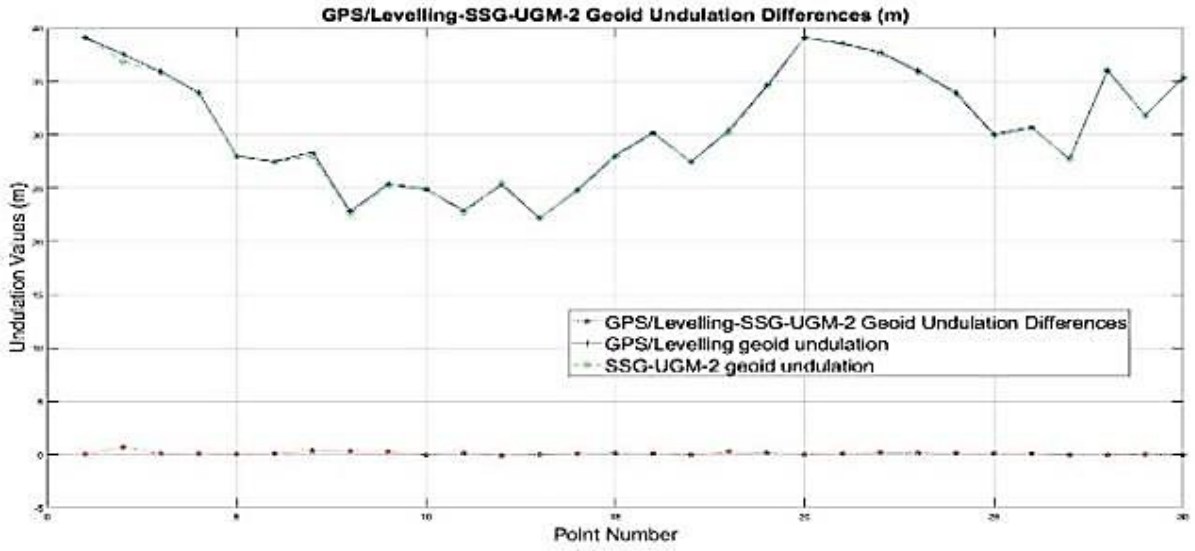

Figure 8. GNSS/ Levelling -SSG-UGM-2

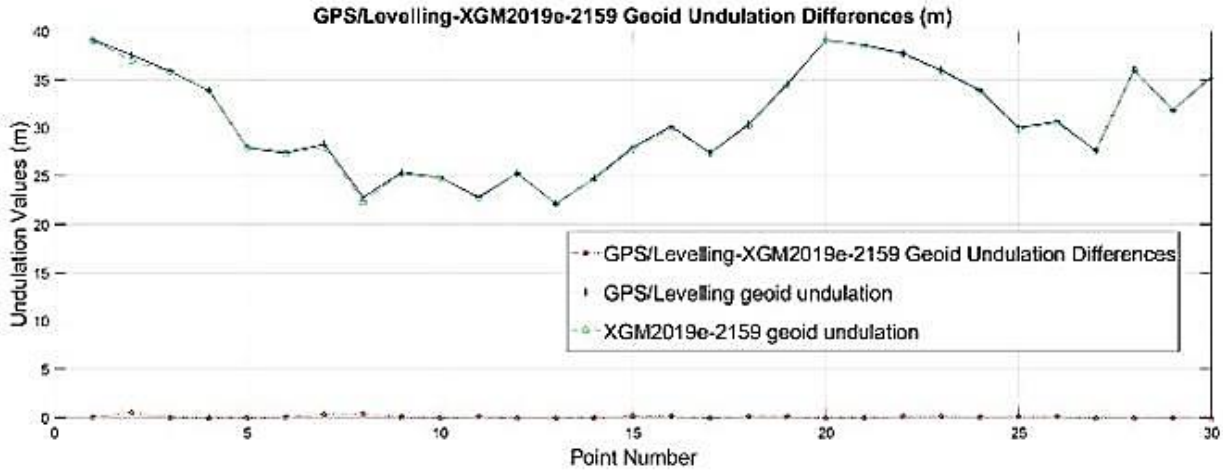

Figure 9. GNSS/ Levelling XGM2019e_2159

4. Conclusion

From the statistical values of the difference of geoid undulations calculated from global geoid models and the geoid undulations calculated from the local GNSS/Levelling geoid (Table 3) at the test points, it was seen that the global geopotential model that deviates the least from the GNSS/Levelling geoid is the SSG-UGM-2 global geoid. The deviation of the local GNSS/Levelling geoid and the SSG-UGM-2 geoid model from each other is approximately 17 cm. The smallest and largest values of the deviation of these two models from each other are approximately 13 cm and 65 cm, respectively. The calculated RMS value for the differences of local GNSS/Levelling geoid undulations and SSG-UGM-2 geoid undulations was found to be the smallest when compared with the calculated RMS values for the differences of other global models from the local GNSS/Levelling geoid. Looking at the criteria based on global geoid models from Table 1, it is seen that the resolutions of these models are different from each other. It is thought that the resolution of the SSG-UGM-2 geoid is much higher than the resolution of other global geoid models, causing this model to better match the local GNSS/Levelling geoid compared to other global geoid models.

From the statistical values of the differences in geoid undulations computed from the global geoid models and the geoid undulations calculated from the local GNSS/Levelling geoid (Table 3) at the test points, ITSG-Grace2018s geoid is the global geopotential that deviates the most from the GNSS/Levelling geoid. The RMS value of the local GNSS/Levelling geoid and ITSG-Grace2018s global geoid comparison is 43 cm. The smallest and largest values of the deviation of these two models from each other are approximately 67 cm and 104 cm, respectively. The calculated RMS value of the differences of local GNSS/Levelling geoid undulations and ITSG-Grace2018s geoid undulations was found to be the largest when checked with the calculated RMS values of the differences of other global models from the local GNSS/Levelling geoid.

It was observed that other global geoid models used in the study could not provide a better fit with Turkey's local GNSS/Levelling geoid than the SSG-UGM-2 global geoid model.

Looking at the compatibility of the GNSS/Levelling geoid and the global geoid models determined in recent

years, respectively, are SSG-UGM-2, XGM2019e_2159, GO_CONS_GCF_2_DIR_R6, EIGEN-GRGS.RL04, GO_CONS_GCF_2_TIM_R6, GOCO06s, GO_CONS_GCF_6.

Conflicts of interest

The authors declare no conflicts of interest.

References

1. Apeh, O. I., Moka, E. C., & Uzodinma, V. N. (2018). Evaluation of gravity data derived from global gravity field models using terrestrial gravity data in Enugu State, Nigeria. *Journal of Geodetic Science*, *8*(1), 145-153.
2. Heiskanen, W. A. (1967). Physical geodesy. *Determination of the Geoid from Ground Anomalies*, *8*, 325-330.
3. Yilmaz, M., Turgut, B., Gullu, M., & Yilmaz, I. (2016). Evaluation of recent global geopotential models by GNSS/Levelling data: internal Aegean region. *International Journal of Engineering and Geosciences*, *1*(1), 15-19.
4. El-Ashquer, M., Al-Ajami, H., Zaki, A., & Rabah, M. (2020). Study on the selection of optimal global geopotential models for geoid determination in Kuwait. *Survey review*, *52*(373), 373-382. https://doi.org/10.1080/00396265.2019.1611256.
5. Pavlis, N. K., Holmes, S. A., Kenyon, S. C., & Factor, J. K. (2012). The development and evaluation of the Earth Gravitational Model 2008 (EGM2008). *Journal of geophysical research: solid earth*, *117*(B4). https://doi.org/10.1029/2011jb008916.
6. Liang, W., Li, J., Xu, X., Zhang, S., & Zhao, Y. (2020). A high-resolution Earth's gravity field model SGG-UGM-2 from GOCE, GRACE, satellite altimetry, and EGM2008. *Engineering*, *6*(8), 860-878.
7. Pail, R., Bruinsma, S., Migliaccio, F., Förste, C., Goiginger, H., Schuh, W. D., ... & Tscherning, C. C. (2011). First GOCE gravity field models derived by three different approaches. *Journal of Geodesy*, *85*(11), 819-843. https://doi.org/ 10.1007/s00190-011-0467-x.
8. Save, H., Bettadpur, S., & Tapley, B. D. (2016). High-resolution CSR GRACE RL05 mascons. *Journal of Geophysical Research: Solid Earth*, *121*(10), 7547-7569. https://doi.org/10.1002/2016JB013007.
9. Watkins, M. M., Wiese, D. N., Yuan, D. N., Boening, C., & Landerer, F. W. (2015). Improved methods for observing Earth's time variable mass distribution with GRACE using spherical cap mascons. *Journal of Geophysical Research: Solid Earth*, *120*(4), 2648-2671. https://doi.org/10.1002/2014JB011547.
10. Ince, E. S., Abrykosov, O., Förste, C., & Flechtner, F. (2020). Forward gravity modelling to augment high-resolution combined gravity field models. *Surveys in Geophysics*, *41*(4), 767-804. https://doi.org/10.1007/s10712-020-09590-9.
11. Ogutcu, S. (2020). Performance assessment of IGS combined/JPL individual rapid and ultra-rapid products: Consideration of Precise Point Positioning technique. *International Journal of Engineering and Geosciences*, *5*(1), 1-14.
12. Tusat, E., & Ozyuksel, F. (2018). Comparison of GPS satellite coordinates computed from broadcast and IGS final ephemerides. *International Journal of Engineering and Geosciences*, *3*(1), 12-19.
13. Pırtı, A., Hoşbaş, R. G., Şenel, B., Köroğlu, M., & Bilim, S. (2021). Galileo uydu sistemi ve sinyal yapısı. *Geomatik*, *6*(3), 207-216.
14. Başçiftçi, F. (2021). TUSAGA-AKTİF Noktalarında Gürültü Analizi, Türkiye'nin Güneydoğusu Örneği. *Geomatik*, *6*(2), 135-147.
15. Özdemir, E. G. (2022). Bağıl ve mutlak (PPP) konum çözüm yaklaşımı sunan Web-Tabanlı çevrimiçi veri değerlendirme servislerinin farklı gözlem periyotlarındaki performanslarının araştırılması. *Geomatik*, *7*(1), 41-51.
16. Zingerle, P., Pail, R., Gruber, T., & Oikonomidou, X. (2020). The combined global gravity field model XGM2019e. *Journal of Geodesy*, *94*(7), 1-12. https://doi.org/10.1007/s00190-020-01398-0.
17. Zingerle, P., Brockmann, J. M., Pail, R., Gruber, T., & Willberg, M. (2019). The polar extended gravity field model TIM_R6e. https://doi.org/10.5880/ICGEM.2019.005.
18. Kvas, A., Behzadpour, S., Ellmer, M., Klinger, B., Strasser, S., Zehentner, N., & Mayer-Gürr, T. (2019). ITSG-Grace2018: Overview and evaluation of a new GRACE-only gravity field time series. *Journal of Geophysical Research: Solid Earth*, *124*(8), 9332-9344. https://doi.org/10.1029/2019JB017415.
19. Lemoine, J. M., Bourgogne, S., Biancale, R., Reinquin F., & Bruinsma, S. (2019). EIGEN-GRGS.RL04.MEAN-FIELD – Mean Earth gravity field model with a time-variable part from CNES/GRGS RL04. 25 Years of Progress in Radar Altimetry Symposium, 24-29 September, Portugal.
20. Kvas, A., Brockmann, J. M., Krauss, S., Schubert, T., Gruber, T., Meyer, U., ... & Pail, R. (2021). GOCO06s–a satellite-only global gravity field model. *Earth System Science Data*, *13*(1), 99-118. https://doi.org/10.5194/essd-13-99-2021.
21. Brockmann, J. M., Schubert, T., & Schuh, W. D. (2021). An improved model of the Earth's static gravity field solely derived from reprocessed GOCE data. *Surveys in Geophysics*, *42*(2), 277-316. https://doi.org/10.1007/s10712-020-09626-0.
22. Alemu, E. (2021). Evaluation of GGMs based on the terrestrial gravity disturbance and Moho depth in Afar, Ethiopia. *Artificial Satellites: Journal of Planetary Geodesy*, *56*. https://doi.org/10.2478/arsa-2021-0007.

International Journal of Engineering and Geosciences
https://dergipark.org.tr/en/pub/ijeg
e-ISSN 2548-0960

3D positioning accuracy and land cover classification performance of multispectral RTK UAVs

Umut Gunes Sefercik [*1], Taskin Kavzoglu[1], Ismail Colkesen[1], Mertcan Nazar[1], Muhammed Yusuf Ozturk[1], Samed Adali [1], Salih Dinc [1]

[1]*Gebze Technical University, Faculty of Engineering, Department of Geomatics Engineering, Kocaeli, Türkiye*

Keywords
UAV
Multispectral
RTK
Machine Learning
Land Cover Classification

Research Article
DOI: 10.26833/ijeg.1074791

Received: 16.02.2022
Accepted: 19.04.2022
Published: 19.10.2022

Abstract

Lately, unmanned aerial vehicle (UAV) become a prominent technology in remote sensing studies with the advantage of high-resolution, low-cost, rapidly and periodically achievable three-dimensional (3D) data. UAV enables data capturing in different flight altitudes, imaging geometries, and viewing angles which make detailed monitoring and modelling of target objects possible. Against earlier times, UAVs have been improved by integrating real-time kinematic (RTK) positioning and multispectral (MS) imaging equipment. In this study, positioning accuracy and land cover classification potential of RTK equipped MS UAVs were evaluated by point-based geolocation accuracy analysis and pixel-based ensemble learning algorithms. In positioning accuracy evaluation, ground control points (GCPs), pre-defined by terrestrial global navigation satellite system (GNSS) measurements, were used as the reference data while Random Forest (RF) and Extreme Gradient Boosting (XGBoost) algorithms were applied for land cover classification. In addition, the spectral signatures of some major land classes, achieved by UAV MS bands, were compared with reference terrestrial spectro-radiometer measurements. The results demonstrated that the positioning accuracy of MS RTK UAV is ±1.1 cm in X, ±2.7 cm in Y, and ±5.7 cm in Z as root mean square error (RMSE). In RF and XGBoost pixel-based land cover classification, 13 independent land cover classes were detected with overall accuracies and kappa statistics of 93.14% and 93.37%, 0.92 and 0.93, respectively.

1. Introduction

In the last decades, the unmanned aerial vehicle (UAV) has become one of the most demanded remote sensing techniques due to high resolution and accurate data derived from different flight altitudes. Due to the increasing demand for high-tech equipment in various applications, the technological level of UAVs is developing day by day. For accurate orientation of the collected aerial photos without using ground control points (GCPs), UAVs have been equipped with real-time kinematic (RTK) global navigation satellite system (GNSS) receivers [1,2]. For measuring the detailed physical and chemical properties of biological materials such as agricultural products and water bodies, the multispectral and hyperspectral cameras have been integrated [3]. Besides the advantages of new technologies, some limitations still exist for the UAV technology [4,5]. No doubt, the most significant limitation is the area coverage due to low altitude legal flights. Because of that reason, a great number of flights are required for large study areas and thousands of aerial photos complicate the photogrammetric processing. In addition, the contribution levels of new technologies to the qualities of former UAV data and products are not clear in the literature.

Earth's surface and objects reflect sunlight according to their spectral reflectance characteristics.

* **Corresponding Author**

*(sefercik@gtu.edu.tr) ORCID ID 0000 – 0003 – 2403 – 5956
(kavzoglu@gtu.edu.tr) ORCID ID 0000 – 0002 – 9779 – 3443
(icolkesen@gtu.edu.tr) ORCID ID 0000 – 0001 – 9670 – 3023
(mnazar@gtu.edu.tr) ORCID ID 0000 – 0002 – 3280 – 5685
(m.ozturk2020@gtu.edu.tr) ORCID ID 0000 – 0001 – 6459 – 9356
(samed.adali2017@gtu.edu.tr) ORCID 0000 – 0002 – 6464 – 0619
(salih.dinc2017@gtu.edu.tr) ORCID 0000 – 0002 – 7641 – 8548

Cite this article

Sefercik, U. G., Kavzoglu, T., Colkesen, İ., Nazar, M., Ozturk, M. Y., Adalı, S., & Din., S. (2023). 3D positioning accuracy and land cover classification performance of multispectral RTK UAVs. International Journal of Engineering and Geosciences, 8(2), 119-128

Different technologies and methods are utilized to distinguish objects from each other by capturing and analyzing spectral reflectance. Remote sensing is a prominent technology for visualizing, processing, and interpreting spectral reflectance values. Using an image classification method on remotely sensed data, land use and land cover (LULC) of various areas can be determined. Also, thematic maps can be generated for various purposes as detection of forest areas [6], forest biomass mapping [7], farmland extraction [8], soil type detection [9], disaster monitoring and management [10-11], detection of land surface temperature [12], and monitoring of LULC change [13].

Image classification is one of the highly familiar topics in remote sensing science with decades of work on scientific literature. Moreover, establishing advanced classification techniques and improving classification accuracy is a hot topic [14-17]. Still, image classification is considered a challenging task because the classification performance can be affected by parameters such as complexity of the utilized dataset, applied image-processing method, and preferred classification technique [18]. One of the most powerful image classification approaches is machine learning which enables utilization of non-parametric and abnormal complex datasets. Also, machine learning offers higher classification accuracy against conventional algorithms in most cases [19-21]. As a concept of machine learning ensemble learning method incorporates various classifiers to generate a combined classification algorithm for increasing the robustness of the classification [22]. Furthermore, ensemble learning algorithms such as Adaptive Boosting (AdaBoost), Random Forest (RF), and Extreme Gradient Boosting (XGBoost) are commonly utilized in LULC classification studies because of their high reliability and accuracy [23,24]. In addition, apart from frequently utilized RGB imagery, multispectral, thermal and even hyperspectral sensors are used in the literature for LULC studies and research [25-29].

In this study, it is aimed to investigate the potential of RTK GNSS positioning and multispectral imaging of the UAVs. Accordingly, the data derived from DJI Phantom IV Multispectral RTK, one of the most preferred UAVs for particularly agricultural purposes, was comprehensively investigated. The geolocation accuracy of the UAV was analyzed by comparing the results of image orientation with and without GCPs. The performances of the UAV's spectral bands were analyzed by comparing spectral reflectance values derived from reference spectro-radiometer measurements on the ground [30]. Moreover, the land cover classification potential of the multispectral UAV was analyzed with RF and XGBoost pixel-based classification algorithms using 13 independent land cover classes [31-33].

2. Study Area and Materials

2.1. Study Area

The study area is a part of Gebze Technical University (GTU) Campus located in Kocaeli Metropolitan, Turkey. The size of the area is 500 m×225 m covering several land classes such as cultivated areas, different species of trees, meadow, soil and buildings. The topography is mostly flat and orthometric heights are between 4 m and 20 m. Figure 1 shows the location and orthomosaic of the study area and an instance aerial photo in NIR (near-infrared) imaging band. Figure coordinates are geographical, and the datum is WGS84 (World Geodetic System 1984).

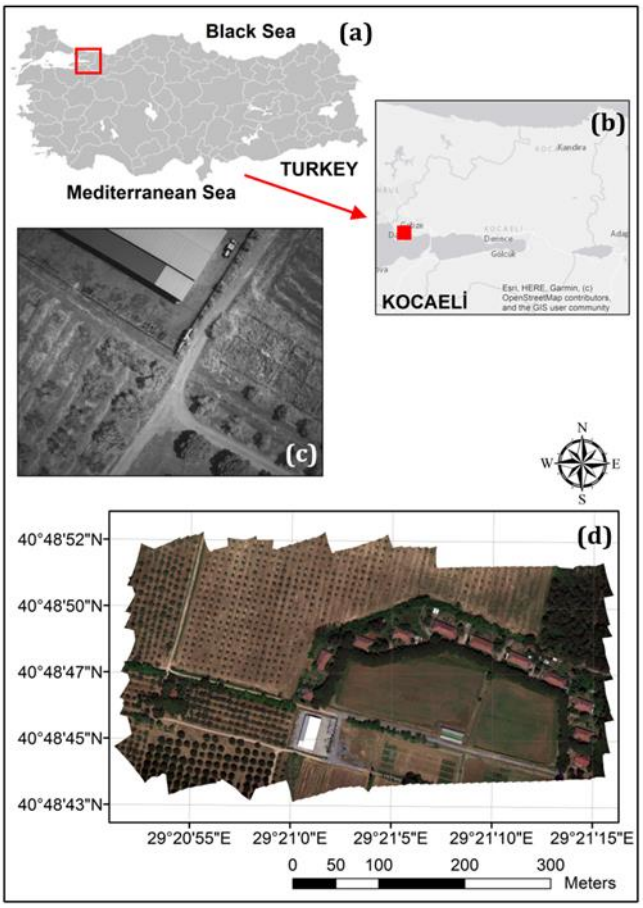

Figure 1. Location of the Kocaeli Metropolitan in Turkey (a), location of the GTU Campus in Kocaeli (b), an instance of NIR band aerial photo (c) and UAV orthomosaic of the study area (d)

2.2. Materials

In the study, UAV flights were completed with DJI Phantom IV Multispectral RTK UAV with six imaging bands as RGB, red, green, blue, red edge (RE) and NIR. For the spectral reflectance calibration, MAPIR Camera Reflectance Calibration Ground Target Package V2 which has four different targets in different colors as black, dark gray, light gray and white was utilized. Reference GCP surveys and spectral measurements in the field were completed by using CHC i80 GNSS receiver and ASD Fieldspec3 spectro-radiometer, respectively. Figure 2 illustrates the utilized UAV and reflectance calibration target. The properties of the utilized UAV are presented in Table 1. The diffuse reflectance values used in spectral reflectance calibration of aerial photos and reflectance curves are displayed in Table 2 and Figure 3. The total of used materials is available at GTU Geomatics Engineering Department's Advanced Remote Sensing Technology Laboratory (ARTLAB).

Table 1. Properties of DJI Phantom IV Multispectral UAV

Property	Value
Camera	Six 1/2.9" CMOS sensors including one RGB and five monochromes with effective pixel resolution of 2.08 megapixel
Sensor wavelengths	Blue (B): 450 nm ± 16 nm; Green (G): 560 nm ± 16 nm; Red (R): 650 nm ± 16 nm; Red edge (RE): 730 nm ± 16 nm; Near-infrared (NIR): 840 nm ± 26 nm
Gimbal	3-axis as pitch, roll, yaw
Flight duration	Approx. 27 minutes
Weight	1487 g
Speed	14 m/s in P-mod; 16 m/s in A-mod
Wind speed resistance	Max. 10 m/s
Operating temperature	0° to 40°C
Outdoor positioning module	GPS, GLONASS, Galileo, Beidou
Hover accuracy range	RTK enabled: ± 0.1 m V, ± 0.1 m H; RTK disabled: ± 0.1 m V, ± 0.3 m H (Vision); ± 0.5 m V, ± 1.5 m H (GPS)
Positioning accuracy RTK	1 cm + 1 ppm Horizontal; 1.5 cm + 1 ppm Vertical

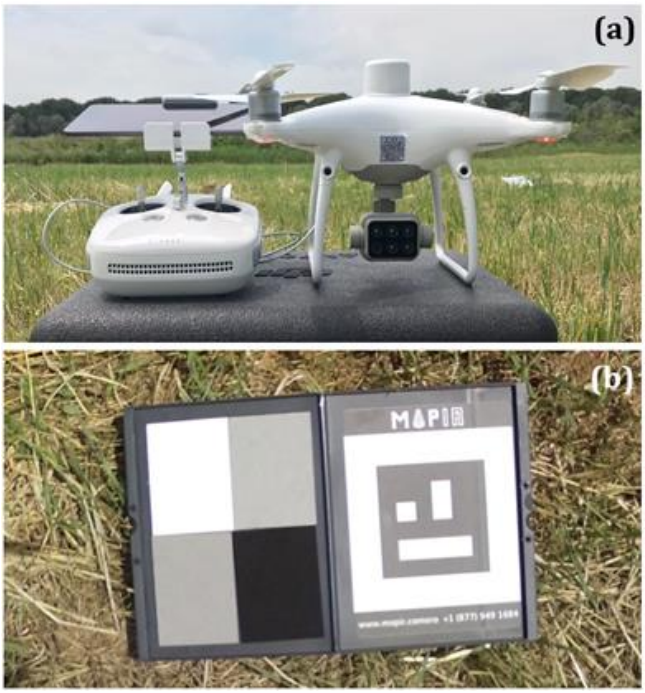

Figure 2. Utilized DJI Phantom IV Multispectral UAV (a) and MAPIR Camera Reflectance Calibration Ground Target Package V2 (b)

Table 2. Reference diffuse reflectance values for MAPIR camera calibration ground target

	Camera Calibration Ground Targets			
Bands	Black	Dark Gray	Light Gray	White
Blue	0.020136	0.182556	0.247980	0.791917
Green	0.019630	0.193762	0.263037	0.866432
Red	0.019371	0.198543	0.262901	0.871958
RE	0.019563	0.212881	0.262741	0.869990
NIR	0.021459	0.228368	0.275486	0.862524

3. Methodology

The used methodology has five different stages as UAV data acquisition and reference terrestrial surveys, image alignment and dense cloud generation, reflectance calibration and orthomosaic generation, pixel-based land cover classification, and accuracy validations. UAV data processing steps were accomplished utilizing Agisoft Metashape Professional, a structure from motion (SfM) based image matching software. Land cover classification using RF and XGBoost pixel-based classification algorithms were achieved in the RStudio which operates based on the R programming language. In Figure 4, conducted methods are shown with utilized software packages.

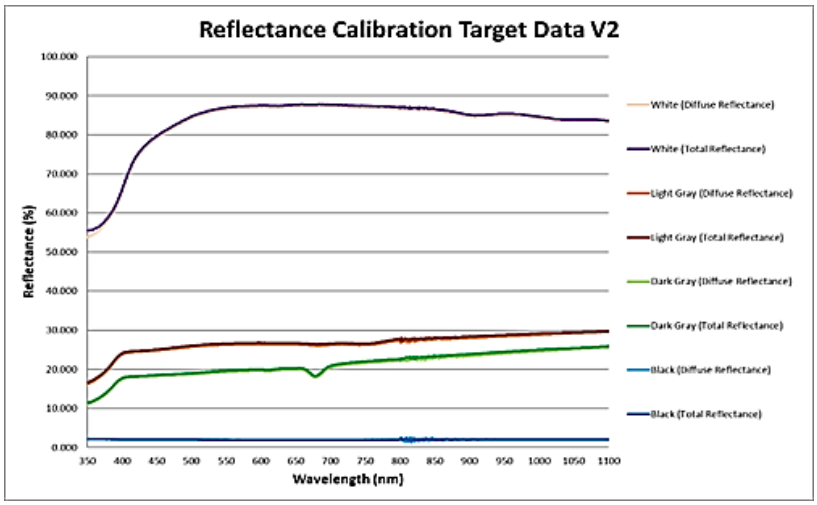

Figure 3. Reflectance curve graph of the MAPIR reflectance calibration targets

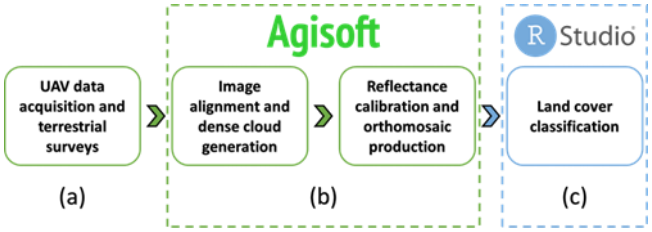

Figure 4. Methods of the study including UAV data acquisition and terrestrial surveys (a), UAV data processing in Agisoft Metashape (b) and land cover classification using RStudio (c)

3.1. UAV data acquisition and terrestrial surveys

UAV data acquisition was carried out by preparing UAV flight plans using DJI GS (Ground Station) PRO UAV flight planning software. In the utilized software two UAV flights were designed considering coarse strip angles in polygonal mode to cover whole study area with the minimum number of photos (Figure 5).

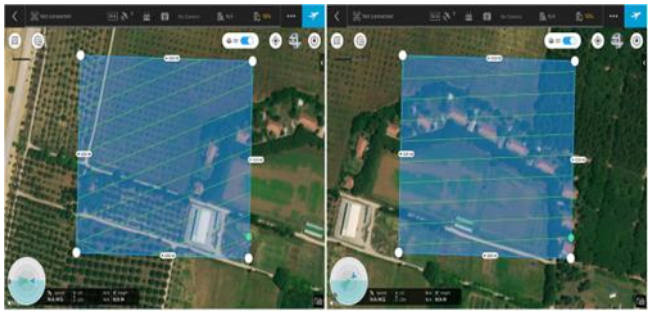

Figure 5. UAV flight plans showing the first (left) and second (right) polygonal flights

For more realistic surface determination of terrain and non-terrain objects, ground sampling distance (GSD), definition of spatial resolution, is one of the most significant parameters. In UAV flights, GSD is directly proportional with flight altitude and minimum GSD can be obtained with minimum flight altitude according to the following equation (1). Here, an important note: lower altitude means more aerial photos to stereo coverage of the study area. That's why, number of required photos should be considered when adjusting the flight altitude and GSD.

$$\frac{f}{h} = \frac{p}{GSD} \quad (1)$$

Where, f is the focal length of used digital camera, p is the pixel size of camera sensor and h is the flight altitude. During the polygonal UAV flights, the flying altitude was selected as 70 m considering the highest objects in flight plans, number of aerial photos for fully stereo coverage and high spatial resolution (3.66 cm GSD). In addition, the minimum overlap ratios for front and side were preferred as 80% and %60, respectively to increase the quality of stereo matching, depth extraction and generated digital surface model (DSM) used for true orthomosaic production. Image capture time interval and UAV flight speed were set to two seconds and 5 m/s, respectively. With UAV flights, 530 aerial photos were obtained. Before the flights, IMU (Inertial Measurement Unit), compass, gimbal and vision sensors of the UAV were calibrated and the photos of the MAPIR reflectance panel were taken. Moreover, in-situ spectro-radiometer surveys were conducted simultaneously with UAV flights to measure reflectance values in the same lighting conditions with captured aerial photos. Reflectance values obtained from the in-situ spectro-radiometer measurements for blue, green, red, RE and NIR bands were used to validate pixel-based land cover classification results.

In normal conditions, RTK GNSS equipped DJI Phantom IV Multispectral does not require GCPs for image orientation. However, for point-based geolocation accuracy analysis, nine independent GCPs were established in the area and measured by utilizing Continuously Operating Reference Stations (CORS) RTK GNSS method. Figure 6 shows the distribution of established GCPs over the study area, an instance terrestrial GCP measurement and a photo captured by the UAV on the ground for reflectance calibration.

When capturing a proper photo by UAV camera for reflectance calibration, some requirements should be considered. First, the calibration panel should be placed in a flat terrain, fully and centrally displayed on the UAV image and not be obstructed by any shadow or material. Second, the image of the calibration panel should be captured from a maximum height depending on the manufacturer recommendation. For MAPIR reflectance calibration panel, utilized in this study, the maximum height for image capturing was declared as 15 feet (~4.5 m) [34]. For better determination of the MAPIR calibration panel with higher spatial resolution and more accurate masking process, we recommend ~1.5 m distance between UAV camera and the calibration panel for best calibration performance.

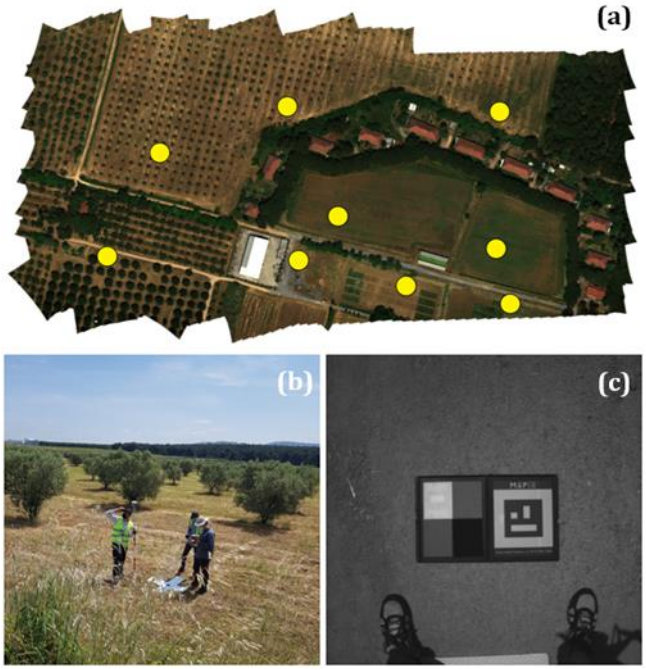

Figure 6. GCP distribution over the study area (a), an instance terrestrial GCP measurement (b) and an instance photo taken for reflectance calibration (c)

3.2. Image alignment and dense cloud generation

Image alignment procedure was done in Agisoft Metashape, a SfM based photogrammetric image matching software. The SfM algorithm operates based on the stereoscopic viewing principle to extract and build 3D geometry utilizing a set of overlapping photos with an offset (base) value [36-41]. In other words, using the SfM technique, photos of an object from multiple viewpoints are taken to realize camera positions and orientations for establishing a spatial connection between common points. Image alignment was performed using aerial photos, yielding a sparse point cloud containing approx. 3 million points. Because of the precise coordinates of the UAV data, the geometric correction was carried out without the GCPs, resulting in a shorter and more efficient alignment process. After the alignment process, a dense point cloud of approx. 38 million points was obtained by extracting depth maps from aerial photos. To eliminate the noise effects especially in the areas with dense trees, dense point clouds were filtered by fencing and classifying noisy points (Figure 7). Generated sparse and dense point clouds are represented in Figure 8.

3.3. Reflectance calibration and orthomosaic production

Obtaining the appropriate spectral data from the imagery is an essential task in land cover classification. Therefore, it is of utmost importance to capture the reflectance values of objects to make accurate analyses. It is required to calibrate the imagery, obtained using different imaging bands, using a sensor calibration method such as a ground reflectance target. Ground reflectance targets are measured in an ideally illuminated environment to acquire reference spectral values. Utilizing reference spectral reflectance data, aerial photos can be calibrated. Therefore, using calibration photos with reference diffuse reflectance values and sun sensor data from the UAV, the camera reflectance calibration process was realized. During the calibration process, all of the calibration targets were masked individually to isolate the target from the rest for an accurate operation (Figure 9) [42].

Using the dense point cloud data, a 7 cm gridded DSM was generated for utilizing in true-orthomosaic production. Finally, a 16-bit orthomosaic with a pixel resolution of 3.66 cm (same as the GSD) was produced using both calibrated aerial photos and the DSM.

3.4. Land cover classification

Before the land cover classification, 13 land cover classes were determined as concrete, coniferous, cultivated, deciduous, meadow, non-cultivated, olive trees, pasture, shadow, soil, tile-roof, water, white roof in the study area. Utilizing the RStudio, an open-source software for data science, pixel-based ensemble learning classification approaches RF and XGBoost were used to classify the calibrated UAV orthomosaic. To test the performance of multispectral UAV data in land cover classification, RE and NIR bands were utilized to calculate some vegetation indices (VIs) as Normalized Difference Vegetation Index (NDVI) and the Normalized Difference Red Edge Index (NDRE). Moreover, NDVI and NDRE data were appended to calibrated orthomosaic with 5-bands (red, green, blue, RE, NIR) as the 6th and 7th bands, respectively, by layer stacking process. A sufficient number of test and training data were collected for each land cover class during the sample gathering process. Table 3 shows the total training and test pixel counts.

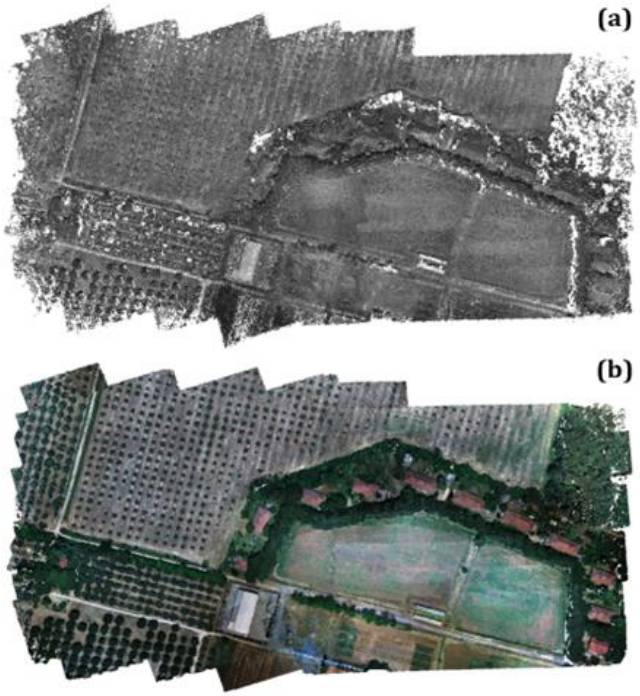

Figure 7. Generated sparse (a) and dense point clouds (b)

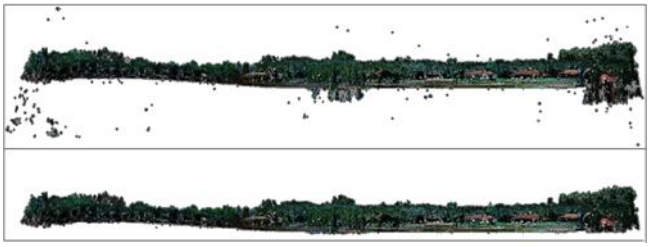

Figure 8. Noisy (upper) and filtered (lower) dense point clouds

Table 3. Total training and test pixel counts in each class

Land Cover Class	Total Training Pixel	Total Test Pixel
Concrete	5547	15139
Coniferous	5102	15524
Cultivated	5128	15417
Deciduous	5176	15325
Meadow	5270	15173
Non-cultivated	5230	15280
Olive trees	5088	15229
Pasture	5390	15649
Shadow	5034	15088
Soil	5098	15169
Tile-roof	5135	15003
Water	5298	15724
White-roof	5259	15304

4. Results and Discussion

Figure 10 shows the spectral signatures of independent land cover classes detected by in-situ spectro-radiometer measurements.

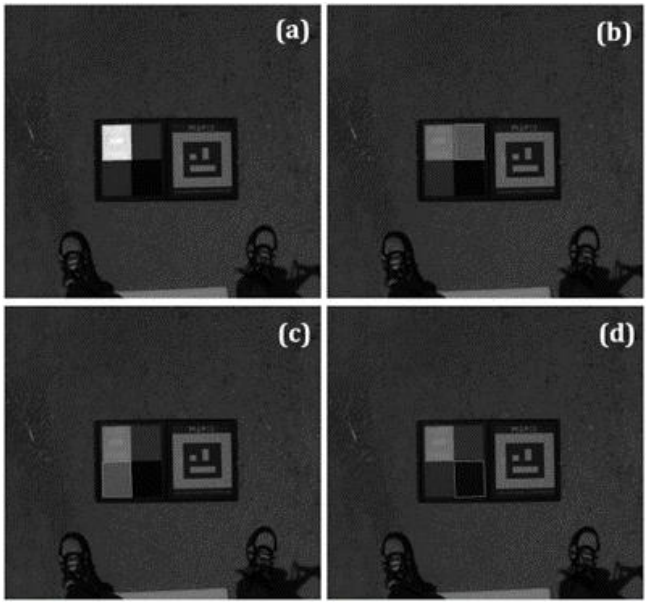

Figure 9. Masked reflectance targets: (a) white, (b) light gray, (c) dark gray and (d) black

Table 4 presents the GCP-based positioning accuracy results of multispectral RTK UAV. In accuracy validation, the reference GCPs, measured by terrestrial GNSS measurements, were found on the generated UAV orthomosaic and the X, Y, Z values were compared. The results demonstrated that RTK UAV positioning accuracy is ±1.1 cm in X, ±2.7 cm in Y, and ±5.7 cm in Z as RMSE. With the highest RMSE value (± 5.7 cm) in Z-direction, it is observed that the performance of UAV RTK GNSS is lower in vertical positioning in comparison with horizontal.

Figure 11 displays the generated orthomosaic before and after spectral reflectance calibration process. The great importance of spectral calibration is clear in the Figure. Without spectral reflectance calibration the land cover classification results will be misleading.

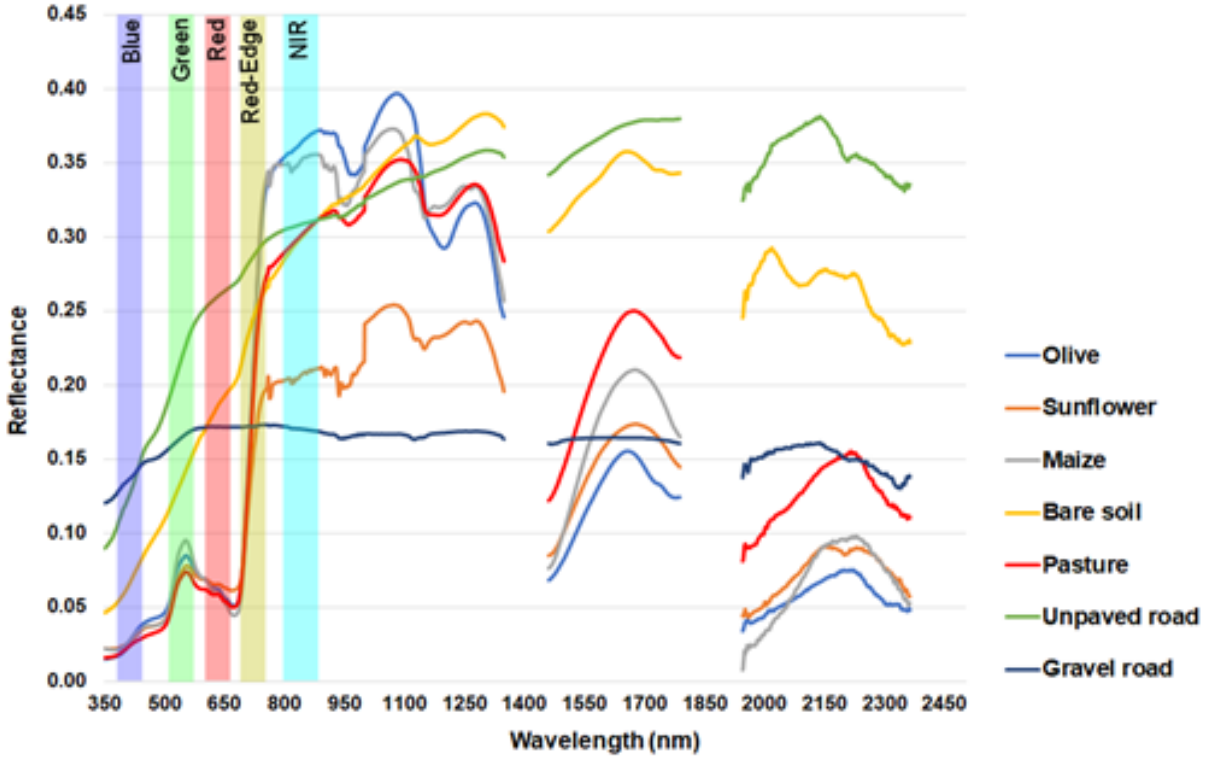

Figure 10. Spectral signatures of land cover classes determined by in-situ spectro-radiometer measurements

Table 4. 3D geolocation accuracy point-based evaluation results obtained by comparing terrestrial GNSS measurements with GCP coordinates acquired from orthomosaic

GCP	Terrestrial Measurements			UAV RTK GNSS			Errors (±)		
	X (m)	Y (m)	Z (m)	X (m)	Y (m)	Z (m)	ΔX (m)	ΔY (m)	ΔZ (m)
1	445408.933	4520098.918	51.970	445408.944	4520098.875	51.903	0.011	0.043	0.067
2	445322.326	4519934.340	46.441	445322.331	4519934.339	46.447	0.005	0.001	0.006
3	445419.067	4519917.866	45.603	445419.074	4519917.866	45.646	0.007	0.000	0.043
4	445044.946	4519962.328	53.575	445044.934	4519962.314	53.550	0.012	0.014	0.025
5	445212.315	4520103.774	52.226	445212.326	4520103.725	52.179	0.011	0.049	0.047
6	445259.375	4520000.639	48.369	445259.385	4520000.629	48.439	0.010	0.010	0.070
7	445406.205	4519969.530	47.736	445406.228	4519969.528	47.800	0.023	0.002	0.064
8	445094.118	4520060.561	54.458	445094.124	4520060.516	54.356	0.006	0.045	0.102
9	445222.708	4519959.093	47.992	445222.710	4519959.089	48.013	0.002	0.004	0.021

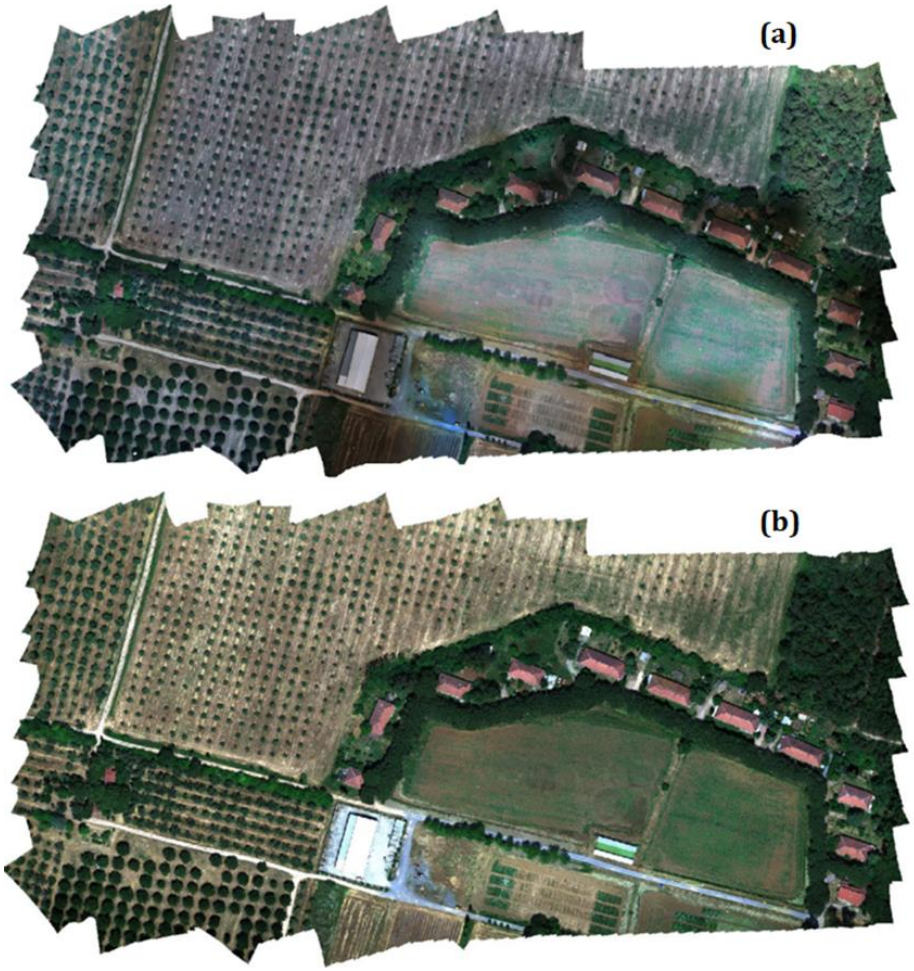

Figure 11. Non-calibrated orthomosaic (a) and calibrated orthomosaic (b) of the study area

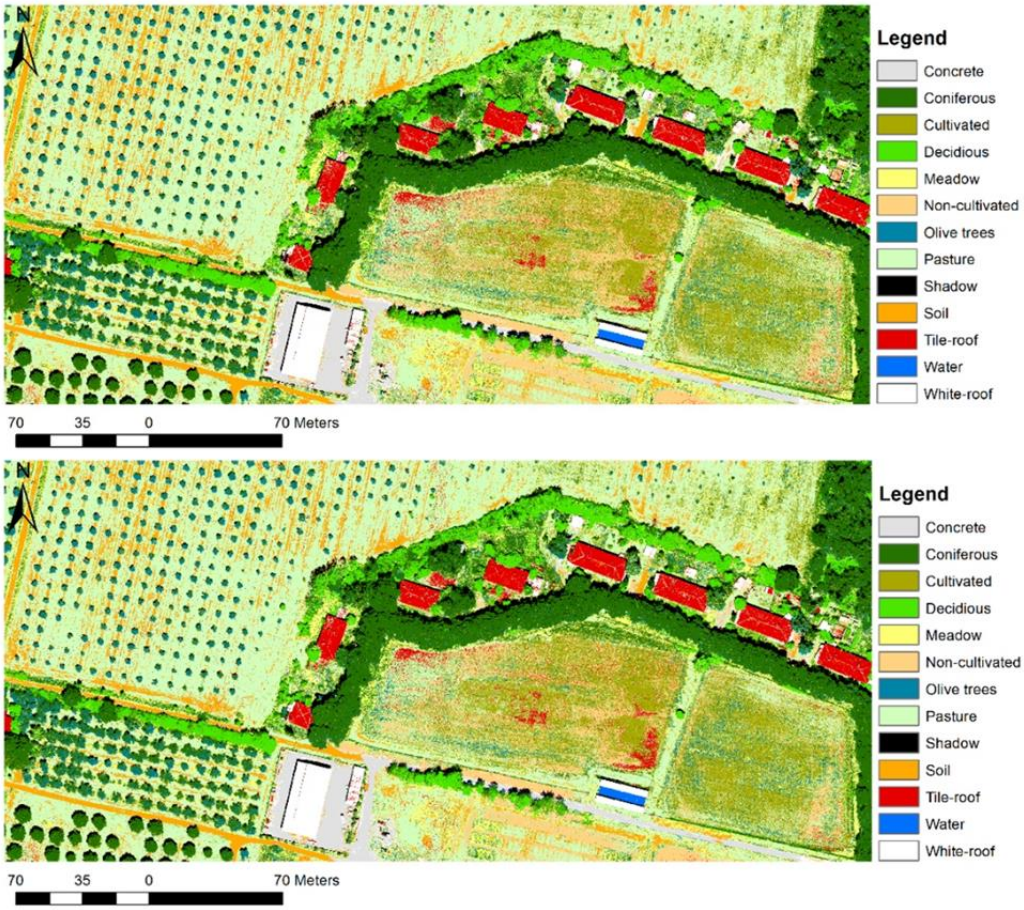

Figure 12. RF (upper) and XGBoost (lower) pixel-based classification results, orthomosaic cropped for the convenience

Classification maps of the RF and XGboost ensemble learning pixel-based classifiers are given in Figure 12. Classification results were checked by overall accuracy, kappa and F-score statistics for the purpose of evaluating the land cover classification performance of the utilized MS UAV (Table 5). Also, a confusion matrix was prepared to interpret the classification results in detail providing further insight about the land cover classes (Table 6).

The results demonstrated that both classifiers have high performance and have very similar results for each land cover class. While the XGBoost algorithm slightly outperformed the RF by overall accuracy, the difference is relatively small. Both classifiers have overall accuracies of more than 93% and kappa statics of greater than 0.9. Also, for RF and XGBoost classification methods minimum and maximum F-scores are relatively close, 82.89% and 84.19%, 99.97% and 99.92%, respectively. The lowest accuracies exist in meadow, cultivated and deciduous land cover classes. The complex and dynamic structure of the densely forested or vegetated areas can have an influence on classification results. In addition, due to being very sensitive to changes in the environment as the season of the year, wind and lighting conditions, regions with trees or different vegetation covers can have differentiating spectral signatures.

Table 5. RF and XGBoost pixel-based classification results showing F-scores of each land cover class, overall accuracy, and kappa statistic

Measurement	Land Cover Class	RF	XGBoost
	Concrete	98.21	98.28
	Coniferous	85.03	85.37
	Cultivated	88.72	88.90
	Deciduous	89.03	88.89
	Meadow	82.89	84.19
	Non-cultivated	93.99	94.63
F-score	Olive trees	91.66	92.52
	Pasture	94.36	94.65
	Shadow	97.58	97.48
	Soil	98.52	98.27
	Tile-roof	97.12	96.86
	Water	99.97	99.92
	White-roof	93.66	93.96
Overall accuracy	Whole area	93.14	93.37
Kappa	Whole area	0.92	0.93

Table 6. Confusion matrix results of the RF and XGBoost classification algorithms

RF Classification

	A	B	C	D	E	F	G	H	I	J	K	L	M	UA
A	14799	0	0	0	0	5	0	0	0	9	0	0	151	98.95
B	0	13723	232	710	572	0	667	4	703	0	14	0	0	82.00
C	0	1132	14444	716	320	1	423	75	0	0	0	0	3	84.50
D	0	109	29	13366	1306	0	1	0	0	0	0	0	0	89.64
E	0	405	91	396	12049	0	481	28	0	0	0	0	0	89.02
F	0	0	8	0	0	14209	0	120	0	0	120	0	295	95.80
G	0	118	122	73	320	0	13647	1	0	0	0	0	2	94.97
H	1	2	400	0	569	229	0	15277	0	95	41	0	11	91.70
I	0	37	0	2	0	0	0	0	14383	0	0	0	0	99.63
J	11	0	0	0	28	4	0	52	0	15006	257	0	0	98.08
K	0	0	54	0	9	28	0	99	2	71	14522	0	199	97.18
L	0	0	0	0	0	0	0	0	0	0	0	15698	0	100.00
M	340	0	2	0	0	804	0	0	0	0	49	26	14643	91.53
PA	97.49	88.29	93.39	88.44	77.55	92.24	88.58	97.18	95.61	98.97	97.05	99.94	95.88	

XGBoost Classification

	A	B	C	D	E	F	G	H	I	J	K	L	M	UA
A	14771	0	0	0	0	3	0	0	0	3	0	0	151	98.90
B	0	13708	256	695	684	0	712	4	658	0	1	0	0	82.54
C	0	1118	14365	617	363	1	462	73	0	0	0	0	1	84.40
D	0	146	38	13498	1374	0	2	0	0	0	0	0	0	90.24
E	0	382	109	356	11767	0	561	35	0	8	0	0	0	89.58
F	2	0	39	0	0	14095	0	141	0	0	131	0	305	96.32
G	0	128	159	86	340	0	13481	1	0	0	0	0	0	95.55
H	0	2	381	0	624	235	1	15215	0	69	58	0	8	91.89
I	0	42	0	11	0	0	0	0	14426	0	0	0	0	99.73
J	15	0	0	0	21	6	0	54	0	15025	198	0	0	97.71
K	0	0	28	0	0	16	0	133	4	76	14561	0	166	96.92
L	0	0	0	0	0	0	0	0	0	0	0	15715	0	100.00
M	363	0	7	0	0	924	0	0	0	0	54	9	14673	92.30
PA	97.68	88.39	93.90	87.57	79.41	92.99	89.67	97.58	95.33	98.85	96.79	99.83	95.68	

Note: Class keys are A: Concrete; B: Coniferous; C: Cultivated; D: Deciduous; E: Meadow; F: Non-cultivated; G: Olive trees; H: Pasture; I: Shadow; J: Soil; K: Tile-roof; L: Water; M: White-roof. UA: User's accuracy; PA: Producer's accuracy.

5. Conclusion

In the study, the 3D positioning accuracy and land cover classification performance of one of the most common MS RTK equipped UAVs DJI Phantom IV MS was investigated. The results demonstrated that the positioning accuracy of the device is ±1.1 cm in X, ±2.7 cm in Y and ±5.7 cm in height as RMSE. The positioning accuracy is higher in planimetric directions in comparison with vertical direction. In land cover classification side, the overall accuracies are more than 93% both for RF and XGBoost pixel-based ensemble learning classifiers. The kappa statistics are 0.92 and 0.93 and F-scores of independent land cover classes fluctuate

between 82.89% - 99.97% and 84.19% - 99.92% for RF and XGBoost, respectively. While looking at F-scores of each land cover class, the lowest accuracies were obtained in forest and vegetated areas.

Acknowledgement

We would like to thank TÜBİTAK for supporting this study within the scope of 2209-A University Students Research Projects Support Program.

Author contributions

Umut Gunes Sefercik: Planning, aerial data acquisition and processing, terrestrial measurements, analysis, validation, paper preparation. **Taskin Kavzoglu:** Planning, validation, paper preparation. **Ismail Colkesen**: Planning, terrestrial measurements, analysis, validation, paper preparation. **Mertcan Nazar:** Aerial data acquisition and processing, terrestrial measurements, analysis, validation, paper preparation. **Muhammed Yusuf Ozturk:** Terrestrial measurements, analysis. **Samed Adali:** Aerial data acquisition and processing, terrestrial measurements, analysis. **Salih Dinc:** Aerial data acquisition and processing, terrestrial measurements, analysis.

Conflicts of interest

The authors declare no conflicts of interest.

References

1. Rabah, M., Basiouny, M., Ghanem, E., & Elhadary, A. (2018). Using RTK and VRS in direct geo-referencing of the UAV imagery. NRIAG Journal of Astronomy and Geophysics. 7(2), 1-7.
2. Ekaso, D., Nex, F., & Kerle, N. (2020). Accuracy assessment of real-time kinematics (RTK) measurements on unmanned aerial vehicles (UAV) for direct geo-referencing, Geo-spatial Information Science, 23(2), 165-181.
3. Bae, J., Bae, H., Kim, G., Park, E., & Cho, B. (2020). Development of unmanned aerial vehicle remote sensing technology for abiotic stress monitoring of citrus 'Unshiu' using multispectral imaging. Journal of the Korean Society for Nondestructive Testing, 40, 274-284.
4. Fields, N. R. (2012). Advantages and challenges of unmanned aerial vehicle autonomy in the Postheroic age. Master's Thesis, James Madison University, 205.
5. Forsman, J., & Westergren, M. (2019). Potential and limitations with UAV deliveries to ships at sea, Bachelor's Thesis in Marine Engineering, Department of Mechanics and Maritime Sciences, Chalmers University of Technology, 1-38.
6. Fraser, B. T., & Congalton, R. G. (2019). Evaluating the effectiveness of Unmanned Aerial Systems (UAS) for collecting thematic map accuracy assessment reference data in New England forests. Forests, 10(1), 24.
7. Du, L., Zhou, T., Zou, Z., Zhao, X., Huang, K., & Wu, H. (2014). Mapping forest biomass using remote sensing and national forest inventory in China. Forests, 5(6), 1267-1283.
8. Sun, Z., Wang, D., & Zhong, G. (2018). Extraction of farmland geographic information using OpenStreetMap data. In 2018 7th International Conference on Agro-geoinformatics, 1-4.
9. Kempen, B., Brus, D. J., & Heuvelink, G. B. (2012). Soil type mapping using the generalised linear geostatistical model: A case study in a Dutch cultivated peatland. Geoderma, 189, 540-553.
10. Kavzoglu, T., Teke, A., & Yilmaz, E. O. (2021). Shared blocks-based ensemble deep learning for shallow landslide susceptibility mapping. Remote Sensing, 13(23), 4776.
11. Rahaman, S. M., Khatun, M., Garai, S., Das, P., & Tiwari, S. (2022). Forest Fire Risk Zone Mapping in Tropical Forests of Saranda, Jharkhand, Using FAHP Technique. In Geospatial Technology for Environmental Hazards, 177-195, Springer, Cham.
12. Şekertekin, A., & Marangoz, A. M. (2019). Zonguldak metropolitan alanındaki arazi kullanımı arazi örtüsünün yer yüzey sıcaklığına etkisi. Geomatik, 4(2), 101-111.
13. Yılmaz, O. S., Gülgen, F., Güngör, R., & Kadı, F. (2018). Uzaktan algılama teknikleri ile arazi kullanım değişiminin incelenmesi: Köprübaşı İlçesi örneği. Geomatik, 10, 233-241.
14. Harsanyi, J. C., & Chang, C. I. (1994). Hyperspectral image classification and dimensionality reduction: An orthogonal subspace projection approach. IEEE Transactions on Geoscience and Remote Sensing, 32(4), 779-785.
15. Chapelle, O., Haffner, P., & Vapnik, V. N. (1999). Support vector machines for histogram-based image classification. IEEE Transactions on Neural Networks, 10(5), 1055-1064.
16. Ciregan, D., Meier, U., & Schmidhuber, J. (2012). Multi-column deep neural networks for image classification. IEEE Conference on Computer Vision and Pattern Recognition, 3642-3649.
17. Lavreniuk, M., Kussul, N., & Novikov, A. (2018). Deep learning crop classification approach based on sparse coding of time series of satellite data. In IEEE International Geoscience and Remote Sensing Symposium, 4812-4815.
18. Lu, D., & Weng, Q. (2007). A survey of image classification methods and techniques for improving classification performance. International Journal of Remote Sensing, 28(5), 823-870.
19. Hansen, M., Dubayah, R., & DeFries, R. (1996). Classification trees: an alternative to traditional land cover classifiers. International Journal of Remote Sensing, 17(5), 1075-1081.
20. Rogan, J., Miller, J., Stow, D., Franklin, J., Levien, L., & Fischer, C. (2003). Land-cover change monitoring with classification trees using Landsat TM and ancillary data. Photogrammetric Engineering & Remote Sensing, 69(7), 793-804.
21. Mondal, A., Kundu, S., Chandniha, S. K., Shukla, R., & Mishra, P. K. (2012). Comparison of support vector machine and maximum likelihood classification technique using satellite imagery. International Journal of Remote Sensing and GIS, 1(2), 116-123.

22. Pal, M. (2008). Ensemble of support vector machines for land cover classification. International Journal of Remote Sensing, 29(10), 3043-3049.
23. Chan, J. C. W., & Paelinckx, D. (2008). Evaluation of Random Forest and Adaboost tree-based ensemble classification and spectral band selection for ecotope mapping using airborne hyperspectral imagery. Remote Sensing of Environment, 112(6), 2999-3011.
24. Georganos, S., Grippa, T., Vanhuysse, S., Lennert, M., Shimoni, M., & Wolff, E. (2018). Very high resolution object-based land use–land cover urban classification using extreme gradient boosting. IEEE Geoscience and Remote Sensing Letters, 15(4), 607-611.
25. Sun, L., & Schulz, K. (2015). The improvement of land cover classification by thermal remote sensing. Remote sensing, 7(7), 8368-8390.
26. Sefercik, U. G., Kavzoglu, T., Colkesen, I., Adali, S., Dinc, S., Nazar, M., & Ozturk, M. Y. (2021). Land cover classification performance of multispectral RTK UAVs. The International Archives of Photogrammetry, Remote Sensing and Spatial Information Sciences, XLVI-4-W5-2021, 489-492.
27. Bhosle, K., & Musande, V. (2019). Evaluation of deep learning CNN model for land use land cover classification and crop identification using hyperspectral remote sensing images. Journal of the Indian Society of Remote Sensing, 47(11), 1949-1958.
28. Avcı, C., Budak, M., Yağmur, N. & Balçık, F. (2023). Comparison between random forest and support vector machine algorithms for LULC classification. International Journal of Engineering and Geosciences, 8 (1), 1-10. https://doi.org/10.26833/ijeg.987605
29. Khorrami, B., Gunduz, O., Patel, N., Ghouzlane, S., & Najjar, M. (2019). Land surface temperature anomalies in response to changes in forest cover. International Journal of Engineering and Geosciences, 4(3), 149-156.
30. Jenal, A., Lussem, U., Bolten, A., Gnyp, M., Schellberg, J., Jasper, J., Bongartz, J., & Bareth, G. (2020). Investigating the potential of a newly developed UAV-based VNIR/SWIR imaging system for forage mass monitoring. PFG – Journal of Photogrammetry Remote Sensing and Geoinformation Science, 88, 493-507.
31. Chen, T., & Guestrin, C. (2016). XGBoost: A scalable tree boosting system. In Proceedings of the 22nd ACM SIGKDD International Conference on Knowledge Discovery and Data Mining; Association for Computing Machinery, San Francisco, CA, USA, 785-794.
32. Ma., L., Zhou, M., & Li, C. (2017). Land covers classification based on Random Forest method using features from full-waveform lidar data, International Archives of the Photogrammetry, Remote Sensing and Spatial Information Sciences, 42(2/W7), 263-268.
33. Zhang, W., Li, W., Zhang, C., Hanink, D. M., Li, X., & Wang, W. (2017). Parcel-based urban land use classification in megacity using airborne LiDAR, high resolution orthoimagery, and Google Street View. Computer Environment Urban Systems, 64, 215-228.
34. MAPIR calibration target capture procedure, https://www.mapir.camera/pages/calibration-target-capture-procedure-v2
35. Westoby, M. J., Brasington, J., Glasser, N. F., Hambrey, M. J., & Reynolds, J. M. (2012). 'Structure-from-Motion'photogrammetry: A low-cost, effective tool for geoscience applications. Geomorphology, 179, 300-314.
36. Sefercik, U. G., Tanrikulu, F., & Atalay, C. (2019). Photogrammetric 3D modelling potential comparison of SFM-based new generation image matching software. In The 40th Asian Conference on Remote Sensing, Korea.
37. Yakar, M., & Dogan, Y. (2018, November). 3D Reconstruction of Residential Areas with SfM Photogrammetry. In Conference of the Arabian Journal of Geosciences (pp. 73-75). Springer, Cham.
38. Şasi, A. & Yakar, M. (2018). Photogrammetric modelling of Hasbey Dar'ülhuffaz (Masjid) using an unmanned aerial vehicle. International Journal of Engineering and Geosciences, 3 (1), 6-11.
39. Yakar, M., & Doğan, Y. (2018). GIS and three-dimensional modeling for cultural heritages. *International Journal of Engineering and Geosciences*, *3*(2), 50-55.
40. Ulvi, A., Yakar, M., Yiğit, A. Y. & Kaya, Y. (2020). İha Ve Yersel Fotogrametrik Teknikler Kullanarak Aksaray Kızıl Kilisenin 3b Modelinin Ve Nokta Bulutunun Elde Edilmesi. Geomatik, 5 (1), 19-26.
41. Mırdan, O. & Yakar, M. (2017). Tarihi Eserlerin İnsansız Hava Aracı İle Modellenmesinde Karşılaşılan Sorunlar. Geomatik, 2 (3), 118-125.
42. Teixeira, A. A., Mendes Júnior, C. W., Bredemeier, C., Negreiros, M., Aquino, R. D. S. (2020). Evaluation of the radiometric accuracy of images obtained by a Sequoia multispectral camera. Engenharia Agrícola, 40, 759-768.

International Journal of Engineering and Geosciences
https://dergipark.org.tr/en/pub/ijeg
e-ISSN 2548-0960

Automatic detection of single street trees from airborne LiDAR data based on point segmentation methods

Zehra Cetin [*1], **Naci Yastikli** [1]

[1]*Yıldız Technical University, Faculty of Civil Engineering, Department of Geomatics, Istanbul, Türkiye*

Keywords
Classification
Segmentation
Mean shift
DBSCAN
Urban street trees

Research Article
DOI: 10.26833/ijeg.1079210

Received: 25.02.2022
Accepted: 09.08.2022
Published: 19.10.2022

Abstract

As a primary element of urban ecosystem, street trees are very essential for environmental quality and aesthetic beauty of urban landscape. Street trees play a crucial role in everyday life of city inhabitants and therefore, comprehensive and accurate inventory information for street trees is required. In this research, an automatic method is proposed to detect single street trees from airborne Light Detection and Ranging (LiDAR) point cloud instead of traditional field work or photo interpretation. Firstly, raw LiDAR point cloud data have been classified to obtain high vegetation class with a hierarchical rule-based classification method. Then, the LiDAR points in high vegetation class were segmented with mean shift and Density Based Spatial Clustering of Applications with Noise (DBSCAN) algorithms to acquire single urban street trees in the Davutpasa Campus of Yildiz Technical University, Istanbul, Turkey. The accuracy assessment of the acquired street trees was also conducted using completeness and correctness analyses. The acquired results from urban study area approved the success of the proposed point-based approach for automatic detection of single street trees using LiDAR point cloud.

1. Introduction

The trees on the streets are important component of urban vegetation as creating shades, decorating roads, alleviating urban environmental pollution, reducing street noise, decreasing CO_2 emissions and building energy consumption, moderating heat accumulation in urban street canyons [1-4]. However, growth conditions of street trees can be very harsh as they have little space on the roadsides, and they can be affected by spread of diseases besides many natural and abiotic factors in single-species plantations [2, 5]. Also, street trees should be carefully positioned not to block utility lines below or above the ground and street luminaries [6]. Therefore, detection of the single street trees in urban areas is necessary for local governments to plan urban horticulture, manage and maintenance land use and land covers.

The inventory studies of urban street trees have been usually carried out by field investigation or manual visual interpretation of aerial images [4, 6]. The recent advent of the LiDAR systems provides rapid and cost-effective three-dimensional (3D) data acquisition of street trees [1]. Several segmentation approaches have been recommended to detect single trees using airborne laser scanning data [3, 7]. The initial techniques for identification of individual trees from LiDAR point cloud have been based on the methods which were developed to process optical imagery [8-10]. Region growing and watershed segmentation are the most popular and often used raster-based segmentation methods for airborne LiDAR data to obtain single street trees [2, 11-12]. Solberg et al. [13] employed a region-growing algorithm for single tree segmentation and their approach produced results equally good with other studies. Kwak et al. [14] used the watershed segmentation for delineation of individual trees and they concluded that

* **Corresponding Author**

*(zerisir@yildiz.edu.tr) ORCID ID 0000-0003-0518-5780
(ynaci@yildiz.edu.tr) ORCID ID 0000-0001-9045-9672

Cite this article

Çetin, Z., &Yastıklı, N. (2023). Automatic detection of single street trees from airborne LiDAR data based on point segmentation methods. International Journal of Engineering and Geosciences– 2023, 8(2), 129-137

LiDAR data can be successfully utilized for detecting single trees and estimating their heights. The template-matching [15], wavelet analysis [16], multi-stage filtering [17] and fitting functions [18] are one of the other methods for segmentation of the individual tree crowns. The loss of information owing to the interpolation of initial 3D point cloud to the grid structure is the major drawback of these segmentation methods [10, 19].

In this paper, we aimed to detect single street trees in the urban study area using raw LiDAR data with the suggested 2D point-based segmentation methods. An automatic hierarchical rule-based classification approach was firstly proposed to acquire high vegetation class. The mean shift and DBSCAN clustering methods had been utilized for automatic point-based segmentation of the high vegetation points to obtain single street trees in the Davutpasa Campus of Yildiz Technical University, Istanbul, Turkey as study area. The accuracy assessment of the acquired single street trees was also conducted using completeness and correctness analyses.

The study consists of five main sections. Study area and dataset is given in section 2. Section 3 contains the methods, including high vegetation classification, point-based segmentation, accuracy assessment subsections. The results and discussion section (section 4) presents the analysis and an experimental evaluation of 2D point-based urban street tree segmentation process. The study concludes with Section 5.

2. Study area and dataset

The Davutpasa Campus of Yildiz Technical University, which is located in Istanbul, Turkey was selected as the urban study area for this research (Fig. 1). There are different types of buildings, a wide variety of plant species and trees, driveways, walking paths, parking lots, recreation areas, as well as many street trees in the urban study area. Two different test areas, test area A and B, were used to automatic detection of single street trees from airborne raw LiDAR point cloud in the urban study area (Fig. 2 and Fig. 3).

The LiDAR data with the density of 16 points/m^2 was collected by Metropolitan Municipality of Istanbul in September, 2013 in the study area with "Riegl LSM-Q680i" laser scanner mounted on "Eurocopter AS350". The flying height and speed of the helicopter were approximately 600 m and 148 km/h, respectively during the data acquisition with integrated "IGI DigiCam" camera, "IGI Aerocontrol" georeference system, and the LiDAR system. The ground truth data has been obtained by field investigation for accuracy assessment process of the proposed point segmentation methods.

Figure 1. The Davutpasa Campus of Yildiz Technical University (yellow line) (Google Earth, 2013)

(a) (b) (c)

Figure 2. Test area A: City map image (2013) (a), street trees (b), and the raw LiDAR point clouds colored by intensity (c)

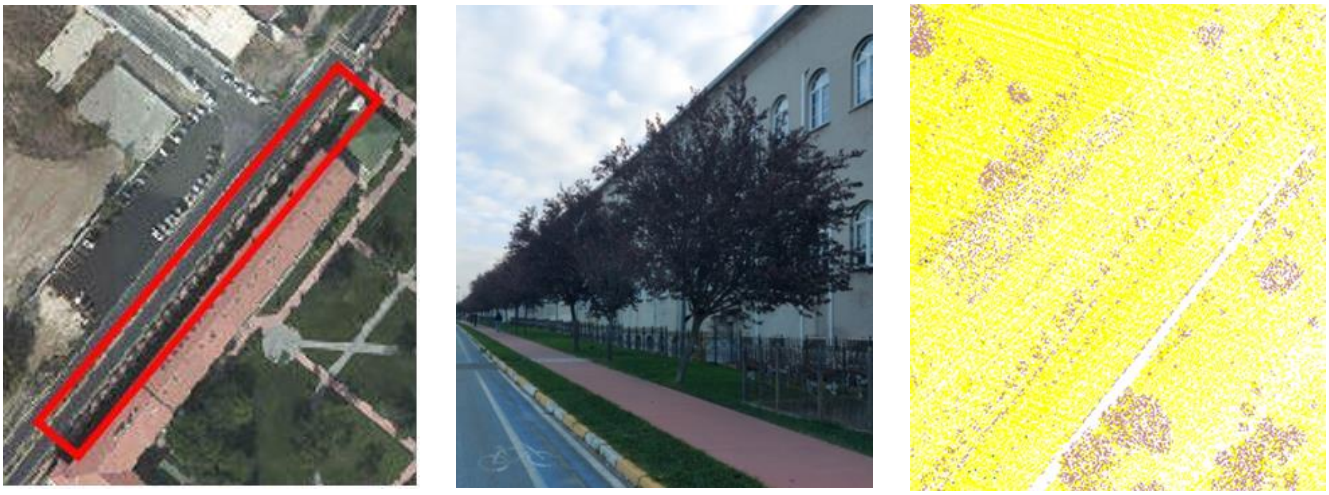

(a) (b) (c)

Figure 3. Test area B: City map image (2013) (a), street trees (b), and the raw LiDAR point clouds colored by intensity (c)

3. Methods

In the present study, the point-based workflow to detect single street trees can be split in two parts as classification and segmentation. The flowchart of the proposed approach can be seen in Fig. 4.

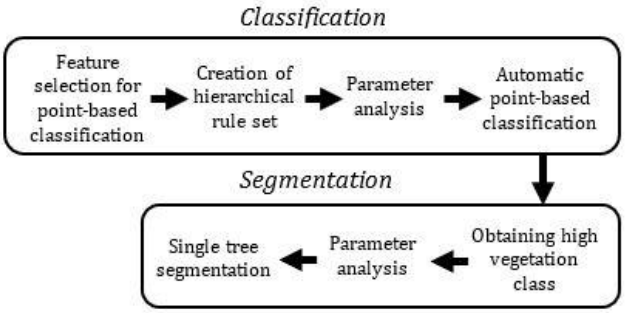

Figure 4. Flowchart of the proposed method for automatic detection of single street trees

3.1. Point-based classification of high vegetation

The point-based classification approaches of LiDAR points aim to determine an object class for every single laser point [20-23]. Different point-based classification methods including machine learning-based and rule-based classifications are available for the classification of LiDAR dataset. The 3D LiDAR point clouds are classified with the point-based classification methods using different classification features such as height features, eigenvalues, surface-based features, local plane features, multiple returns features, echo amplitude, echo width, etc. which are calculated for all individual LiDAR points [24-27].

In this paper, classification of LiDAR data of the test areas (test area A and B) was executed with proposed an automatic hierarchical rule-based classification method. The hierarchical rule set was constituted using the selected geometric features for point-based classification and after parameter analyses, the ground, low, medium and high vegetation, building, low point, air point, and default classes were acquired with the determined parameters (Table 1). The all-high vegetation points acquired as a result of the point-based classification were separated from the points of other terrain classes. The classification process of LiDAR point cloud has been achieved using TerraScan module of Terrasolid. The details of the used point-based classification method to acquire high vegetation class can be found in Yastikli and Cetin [12].

Table 1. The hierarchical rule set and obtained classes

Point-based classification	
Rules	Classes
By class	Default
Low points	Low point
Ground	Ground
Below surface	Low point
Air points	Air point
By height from ground 1	Low vegetation
By height from ground 2	Medium vegetation
By height from ground 3	High vegetation
Building	Building

3.2. Point-based segmentation of single trees

All individual laser points are grouped into subsets according to their similar characteristics with the point-based segmentation methods. Point-based methods mainly segment the data using geometric features [28]. The commonly adopted three important strategies for point-based segmentation of LiDAR data are geometric fitting, region growing, and clustering [28-29]. The high vegetation points, obtained from the automatic point-based classification of LiDAR data, were segmented using popular mean shift and DBSCAN clustering algorithms after detailed parameter analysis for best segmentation results in this research. 2D tree segmentation process for the detection of single street trees was carried out using Python programming language (Python 3.6.4) in Jupyter Notebook.

3.2.1. Mean shift clustering

Mean shift [30] is a nonparametric, recursive, and kernel-based clustering approach which shifts each data to local maximum of density function [31]. Mean shift does not require a pre-determined number of clusters and nor restrict the shape of clusters [32]. Mean shift is a center-based algorithm, and firstly, the algorithm chooses a random point from the data set as cluster center. Typically, it examines the center of mass of its local neighborhood and then shifts the point in the general direction of that center of mass [33].

In the mean shift clustering algorithm, the bandwidth of a kernel function is the most significant parameter [34]. Bandwidth, which determines the size of the region to be searched, can be adjusted manually or estimated using the bandwidth function. A specific bandwidth selection considerably decreases the bias while the variance value remains theoretically unchanged [34].

3.2.2. DBSCAN clustering

Density Based Spatial Clustering of Applications with Noise (DBSCAN) [35] is based on the concept of dense regions and performs well in determining arbitrarily-shaped clusters [36]. The three important elements for DBSCAN algorithms are the seeds members of the group, borders of the group, and noise which does not have any effect in the group [37-38]. The main idea of the DBSCAN is based on the requirement of a certain number of neighbor points at a certain radius for each core point [39]. The algorithm starts with an arbitrary core point, and controls if the neighboring points create a dense region [40]. A cluster is started if there are enough points in the neighborhood of the core point; otherwise, the point is labeled as noise [39]. The iterative process ends when no new points are added to any cluster [41]. DBSCAN algorithm requires two input parameters; the radius (the maximum distance of one core point to its neighbors) and minimum samples (density threshold of points in a neighborhood for a point to be regarded as a core point) [36, 42].

3.3. Accuracy assessment

Accuracy assessment is a necessary process to determine the performance of the segmentation methods. In this study, accuracy assessment process for the proposed segmentation methods was carried out according to completeness (Eq. (1)) and correctness (Eq. (2)) analyses [43-45].

$$\text{Completeness} = (TP)/(TP+FN) \quad (1)$$

$$\text{Correctness} = (TP)/(TP+FP) \quad (2)$$

TP, FP, and FN define perfect segmentation, over-segmentation, and under-segmentation, respectively [46]. TP refers to the true positive entities segmented correctly, FP is the false positive entities that were obtained in the segmentation but do not correspond to an entity in the ground truth data, and FN refers to the negative entities available in the ground truth data which were not acquired in the segmentation [47].

4. Results and Discussion

The automatic 3D point-based classification results of LiDAR point cloud in the test areas (test area A and test area B) using geometric features were given in Fig. 5, and only high vegetation points separated from the other terrain classes were shown in Fig. 6. According to the point-based classification results (see Fig. 5 and Fig. 6), it can be realized that the points of high vegetation class is obtained precisely for the tree crown segmentation of single street trees in the study area.

The 2D single tree segmentation results in test area A and B with mean shift clustering and DBSCAN clustering are given in Fig. 7 and Fig. 8, respectively, including the raw LiDAR point clouds, the segmented street trees, and the segmented street trees overlaid on the grey coded Digital Surface Model (DSM). When the segmentation results are analyzed, it is seen that the single street trees were successfully determined with the point-based segmentation using both mean shift and DBSCAN clustering algorithms. The segmentation results performed by mean shift and DBSCAN are close to each other in test area A and exactly the same in the test area B.

In Fig. 9, the reference urban single street trees, TP, FP, FN acquired with mean shift and DBSCAN clustering algorithms are given as a result of accuracy assessment of detected trees in the test area A. In the test area A, 17 clusters were determined as single street trees correctly (TP) using both mean shift and DBSCAN clustering algorithms. While there is no incorrectly clustered mean shift and DBSCAN clustering were obtained as 100% in the test area B (Table 2). The completeness and correctness results for both two segmentation methods are very satisfying as expected because of the accurate point-based classification of high vegetation class, and detailed parameter analyses for point-based segmentations. Mean shift clustering method single street tree with mean shift clustering, only 1 cluster were determined as single street tree wrongly (FP) with DBSCAN clustering. The points of 2 street trees couldn't also be segmented as tree clusters (FN) using both mean shift and DBSCAN clustering. The results of the segmentation were 89.47% completeness and 100% correctness for mean shift clustering method, and 89.47% completeness and 94.44% correctness for DBSCAN clustering method (Table 2) in the test area A. In Fig. 10, reference urban single street trees, TP trees acquired with mean shift and DBSCAN clustering algorithms are given as a result of accuracy assessment of detected trees in the test area B. In the test area B, all 31 clusters were also detected as single street trees correctly (TP) using both mean shift and DBSCAN clustering algorithms. Since there were no single street trees identified wrongly (FP), and there were any single street trees couldn't be segmented (FN) in the test area B, the completeness and correctness values for both mean shift and DBSCAN clustering were obtained as 100% in the test area B (Table 2). The completeness and correctness results for both two segmentation methods

are very satisfying as expected because of the accurate point-based classification of high vegetation class, and detailed parameter analyses for point-based segmentations. Mean shift clustering method outperformed slightly to DBSCAN clustering according to the correctness value only in the test area A.

Table 2. Completeness and correctness values

	Mean shift clustering		DBSCAN clustering	
	Complet.	Correct.	Complet.	Correct.
Test area A	89.47%	100%	89.47%	94.44%
Test area B	100%	100%	100%	100%

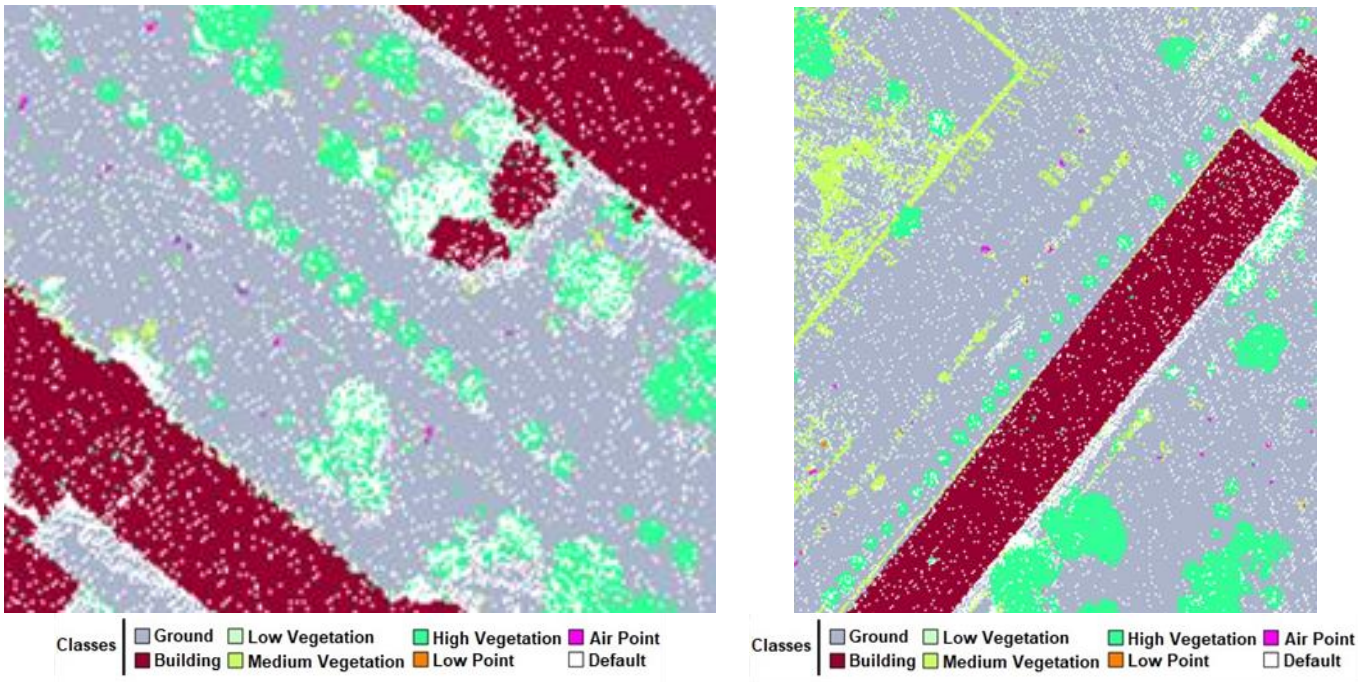

(a) (b)

Figure 5. The automatic point-based classification results of test area A (a) and test area B (b)

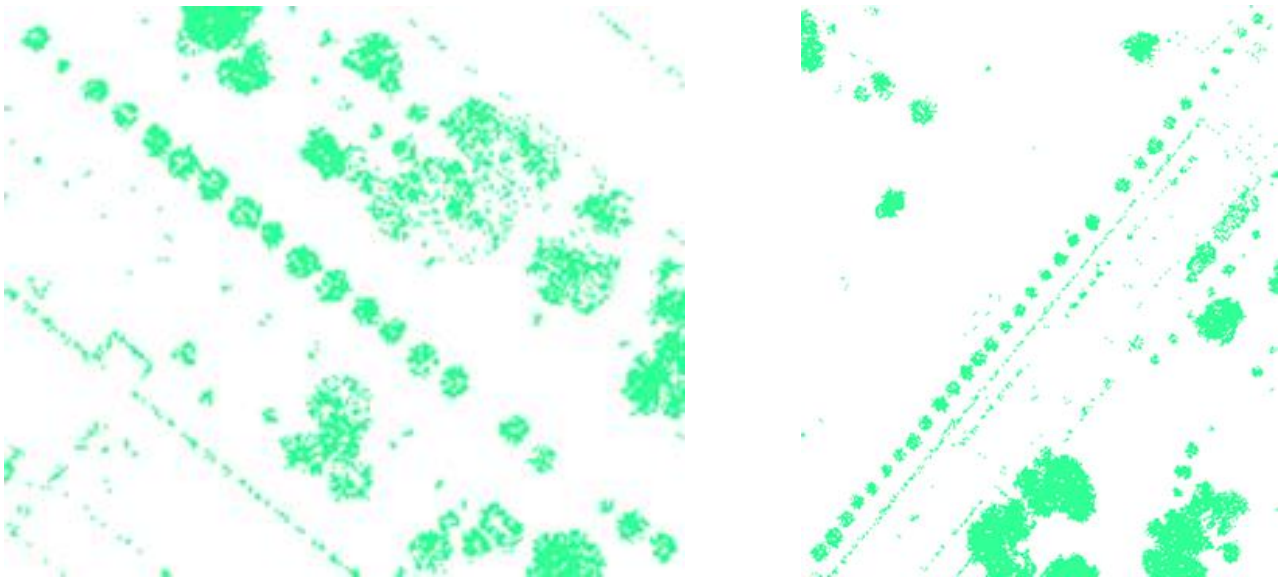

(a) (b)

Figure 6. The high vegetation points in test area A (a) and in test area B (b)

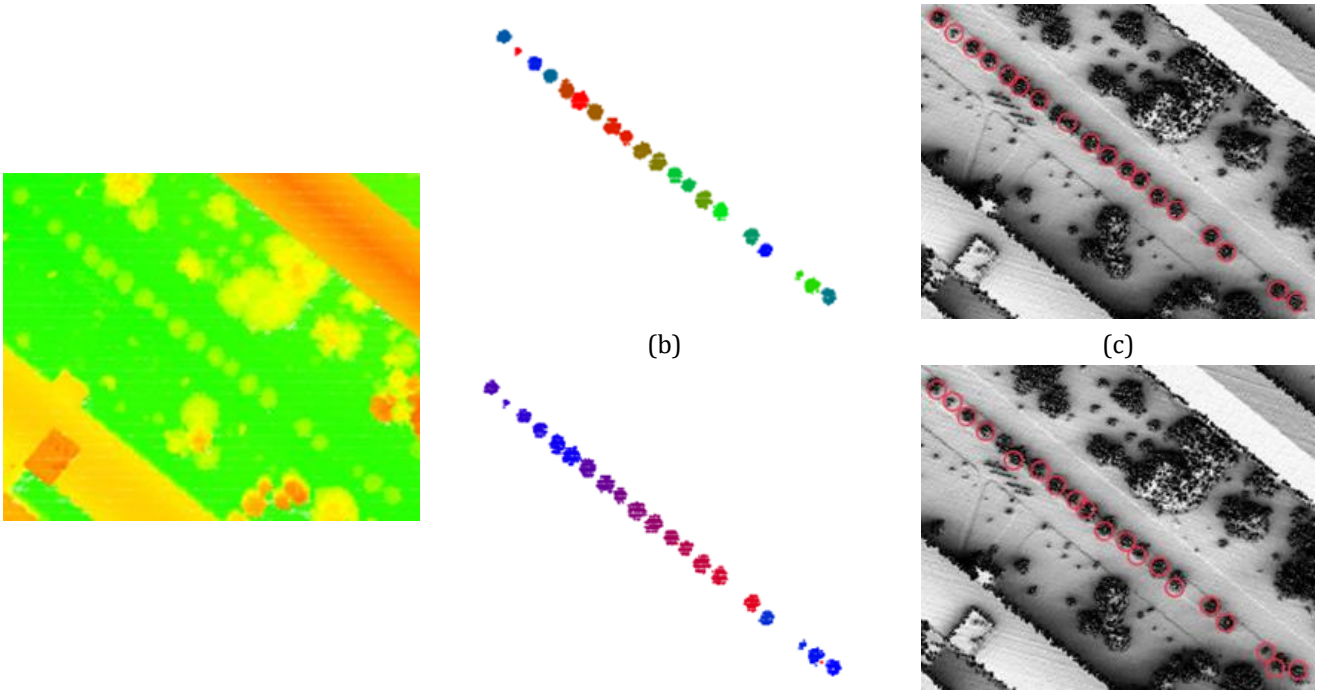

(a) (b) (c) (d) (e)

Figure 7. The test area A: raw LiDAR clouds colored by height (a), the segmented street trees using mean shift clustering (b) and the segmented street trees (red circles) overlaid on the grey coded DSM (c), the segmented street trees using DBSCAN clustering (d) and the segmented street trees (red circles) overlaid on the grey coded DSM (e)

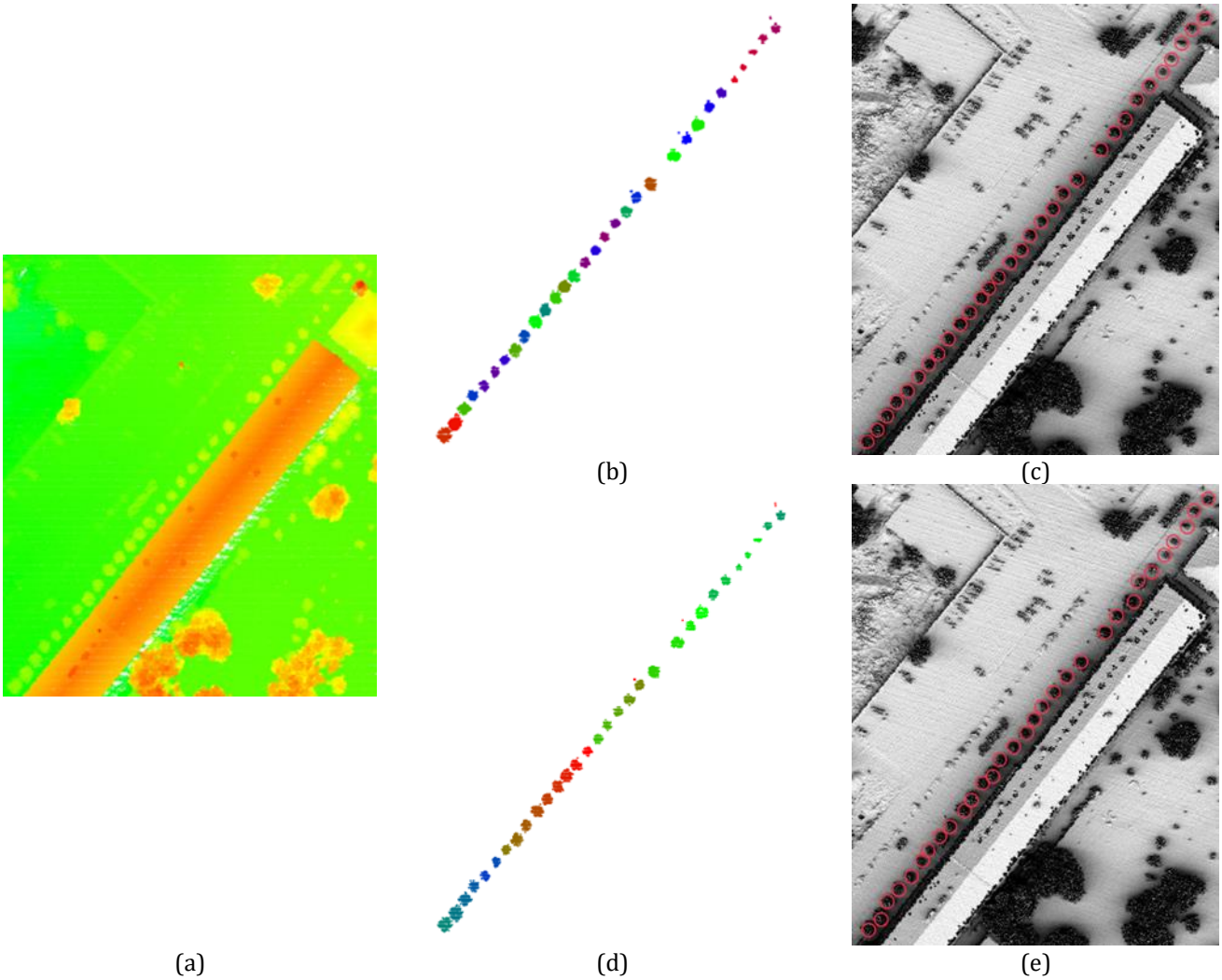

(a) (b) (c) (d) (e)

Figure 8. The test area B: raw LiDAR clouds colored by height (a), the segmented street trees using mean shift clustering (b) and the segmented street trees (red circles) overlaid on the grey coded DSM (c), the segmented street trees using DBSCAN clustering (d) and the segmented street trees (red circles) overlaid on the grey coded DSM (e)

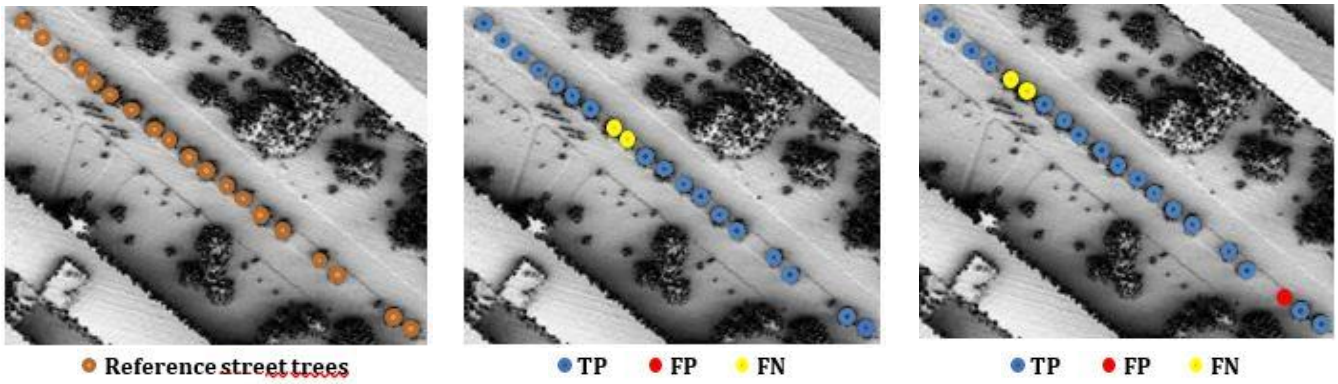

(a) (b) (c)

Figure 9. The test area A: the reference trees (a), TP, FP, FN trees acquired with mean shift clustering (b), and TP, FP, FN trees acquired with DBSCAN clustering (c)

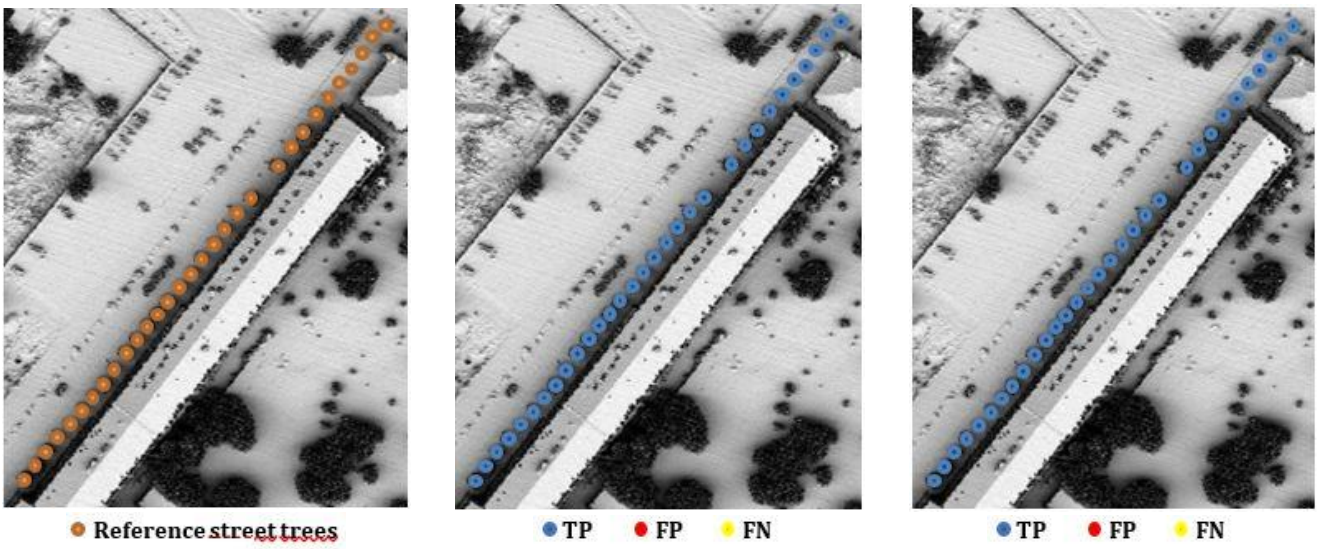

(a) (b) (c)

Figure 10. The test area B: the reference trees (a), TP trees acquired with mean shift clustering (b), and TP trees acquired with DBSCAN clustering (c)

5. Conclusion

In this study, an automatic point-based segmentation approach is proposed to detect single street trees using raw airborne LiDAR point cloud. The LiDAR data were classified with hierarchical rule-based classification method, and acquired high vegetation class' points were segmented with mean shift and DBSCAN algorithms to detect single street trees automatically in the test area A and test area B which were located in Davutpasa Campus of Yildiz Technical University, Istanbul, Turkey. The accuracy assessment had been performed with respect to the detection rate of the single street trees in the test areas. The results of completeness and correctness were acquired 89.47% and 100%, respectively for mean shift clustering algorithm and 89.47% and 94.44%, respectively for DBSCAN clustering algorithm in the test area A. In the test area B, all completeness and correctness results are obtained 100% for both mean shift and DBSCAN clustering algorithms. Obtained results verified the success of proposed methods for automatic detection of single street trees using airborne raw LiDAR data without any information loss. The automatic segmentation results are quite satisfactory for both mean shift and DBSCAN clustering algorithms. The proposed approach for automatic detection of single street trees using airborne LiDAR data can be used effectively by local governments and city planners to plan urban horticulture, manage and maintenance land use and land covers studies.

Acknowledgement

We would like to thank the Metropolitan Municipality of Istanbul for supplying the LiDAR dataset covering the Davutpasa campus of Yildiz Technical University, Istanbul, Türkiye.

Author contributions

Zehra Cetin: Conceptualization, Methodology, Software, Data curation, Writing-Original draft preparation, Software, Validation, Visualization, Investigation, Writing-Reviewing and Editing. **Naci Yastikli:** Conceptualization, Methodology, Software, Data curation, Writing-Original draft preparation, Software, Validation, Visualization, Investigation, Writing-Reviewing and Editing.

Conflicts of interest

The authors declare no conflicts of interest.

References

1. Wu, B., Yu, B., Yue, W., Shu, S., Tan, W., Hu, C., Huang, Y., Wu, J., & Liu, H. (2013). A Voxel-Based Method for Automated Identification and Morphological Parameters Estimation of Individual Street Trees from Mobile Laser Scanning Data. Remote Sensing, 2013 (5), 584-611.
2. Aval, J., Demuynck, J., Zenou, E., Fabre, S., Sheeren, D., Fauvel, M., Adeline, K., & Briottet, X. (2018). Detection of individual trees in urban alignment from airborne data and contextual information: A marked point process approach, ISPRS Journal of Photogrammetry and Remote Sensing, 146, 197-210.
3. Husain, A. & Vaishya, R. C. (2019). Detection and thinning of street trees for calculation of morphological parameters using mobile laser scanner data, Remote Sensing Applications: Society and Environment, 13, 2019, 375-388.
4. Wang, Y., Wang, J., Chang, S., Sun, L., An, L., Chen, Y., & Xu, J. (2021). Classification of Street Tree Species Using UAV Tilt Photogrammetry, Remote Sensing, 2021, 13, 216.
5. Jutras, P., Prasher, S., & Mehuys, G. (2009). Prediction of street tree morphological parameters using artificial neural networks. Computers and Electronics in Agriculture, 67, 9-17.
6. Huang, P., Chen, Y., Li, J., Yu, Y., Wang, C., & Nie, H. (2015). Extraction of street trees from mobile laser scanning point clouds based on subdivided dimensional features. 2015 IEEE International Geoscience and Remote Sensing Symposium (IGARSS), 557-560, Milan, Italy.
7. Zhang, J., Sohn, G., & Brédif, M. (2013). Single Tree Detection from Airborne Laser Scanning Data Using A Marked Point Process Based Method, ISPRS Annals of the Photogrammetry, Remote Sensing Spatial Information Sciences, II-3/W1, 41–46.
8. Ke, Y. & Quackenbush, L.J., (2011). A review of methods for automatic individual tree-crown detection and delineation from passive remote sensing. International Journal of Remote Sensing. 32 (17), 4725–4747.
9. Leckie, D.G., Gougeon, F.A., Tinis, S., Nelson, T., Burnett, C.N., & Paradine, D., (2005). Automated tree recognition in old growth conifer stands with high resolutiondigital imagery. Remote Sensing Environment, 94, 311–326.
10. Vega, C., Hamrouni, A., El Mokhtari, S., Morel, J., Bock, J., Renaud, J. P., Bouvier, M., & Durrieu, S. (2014). Ptrees: A Point-Based Approach to Forest Tree Extraction from Lidar Data. International Journal of Applied Earth Observation and Geoinformation, 33: 98–108.
11. Mongus, D., & Žalik, B. (2015). An Efficient Approach to 3D Single Tree-Crown Delineation in Lidar Data. ISPRS Journal of Photogrammetry and Remote Sensing, 108: 219–233.
12. Li, W., Guo, Q., Jakubowski, M. K., & Kelly, M. (2012). A New Method for Segmenting Individual Trees from the Lidar Point Cloud. Photogrammetric Engineering and Remote Sensing, 78 (1): 75–84.
13. Solberg, S., Naesset, E., & Bollandsas, O.M. (2006). Single tree segmentation usingairborne laser scanner data in a structurally heterogeneous spruce forest. Photogrammetric Engineering and Remote Sensing, 72 (12), 1369–1378.
14. Kwak, D.-H., Lee, W.-K., Lee, J.H., Biging, G.S., & Gong, P. (2007). Detection of individualtrees and estimation of tree height using LiDAR data. Journal of Forestry Research, 12, 425–434.
15. Korpela, I., Tuomola, T., & Välimäki, E. (2007). Mapping forest plots: an efficientmethod combining photogrammetry and field triangulation. Silva Fennica, 41 (3),457–469.
16. Falkowski, M.J., Smith, A.M.S., Hudak, A.T., Gessler, P.E., Vierling, L.A., & Crookston, N. L. (2006). Automated estimation of individual conifer tree height and crown diam-eter via two-dimensional spatial wavelet analysis of lidar data. Canadian Journal of Remote Sensing, 32 (2), 153.
17. Jing, L., Hu, B., Li, J., & Noland, T. (2012). Automated delineation of individual tree crowns from LiDAR data by multi-scale analysis and segmentation. Photogrammetric engineering and remote sensing 78, 1275-1284.
18. Popescu, S.C., Wynne, R.H., & Nelson, R.F. (2002). Estimating plot-level tree heights withlidar: local filtering with a canopy-height based variable window size. Computers and Electronics in Agriculture, 37, 71–95.
19. Yastikli, N. & Cetin, Z. (2021). Classification of raw LiDAR point cloud using point-based methods with spatial features for 3D building reconstruction. Arabian Journal of Geosciences, 14, 146.
20. Yastikli, N. & Cetin, Z. (2016). Classification of LiDAR data with point based classification methods. The International Archives of the Photogrammetry, Remote Sensing and Spatial Information Sciences, 41(B3):441–445.
21. Doğruluk, M., Aydın, C.C. & Yanalak, M. (2018). Kırsal Alanlarda SYM Üretiminde Filtreleme Yöntemlerinin Performans Analizi: Hava LiDAR Uygulaması; İstanbul Örneği. Geomatik, 3 (3), 242-253.
22. Kuçak, R. A., Erol, S. & Alkan, R. M. (2023). iPad Pro LiDAR sensörünün profesyonel bir yersel lazer tarayıcı ile karşılaştırmalı performans analizi. Geomatik, 8 (1), 35-41.
23. Karasaka, L. & Beg, A. A. R. (2021). Yersel Lazer Tarama Yöntemi ile Farklı Geometrik Yapıdaki Özelliklerin Modellenmesi. Geomatik, 6 (1), 54-60.
24. Chehata, N. & Bretar, F. (2008). Terrain modeling from lidar data: hierarchical K-means filtering and Markovian regularization. 15th IEEE International Conference on Image Processing, 1900-1903, San Diego, CA.
25. Mallet, C., Bretar, F., Roux, M., Soergel, U., & Heipke C (2011). Relevance assessment of full-waveform Lidar data for urban area classification. ISPRS

Journal of Photogrammetry and Remote Sensing, 66(6), 71–84.
26. Kim, H. B. & Sohn, G. (2013). Point-based classification of power line corridor scene using random forests. Photogrammetric Engineering and Remote Sensing, 79: 821–833.
27. Canaz Sevgen, S. (2019). Airborne lidar data classification in complex urban area using random forest: a case study of Bergama, Turkey. International Journal of Engineering and Geosciences, 4 (1), 45-51.
28. Che, E., Olsen, M. J., Parrish, C. E., & Jung, J., 2019. Pavement marking retro-reflectivity estimation and evaluation using mobile lidar data. Photogrammetric Engineering and Remote Sensing (submitted for publication), 85(8):573-583.
29. Zolanvari, S. M. I., Laefer, D. F., & Natanzi, A. S. (2018). Three-dimensional building façade segmentation and opening area detection from point clouds. ISPRS Journal of Photogrammetry and Remote Sensing, 143.
30. Fukunaga, K. & Hostetler, L. D. (1975). The estimation of the gradient of a density function, with applications in pattern recognition, IEEE Transactions on Information Theory, 21, pp.32-40.
31. Wen, Z. Q. & Cai, Z. X. (2006). Mean shift algorithm and its application in tracking of objects. In: Proceedings of 5th International Conference on Machine Learning and Cybernetics, Dalian 2006, 4024- 4028.
32. Anand, S., Mittal, S., Tuzel, O., & Meer, P., (2014). Semi-supervised kernel mean shift clustering. IEEE Transactions on Pattern Analysis and Machine Intelligence 36, 1201–1215 (2014).
33. Friedman, L., Netanyahu, N.S., & Shoshany, M. (2013) Mean shift based clustering of remotely sensed data with agricultural and land-cover applications. International Journal of Remote Sensing, 34:17, 6037-6053.
34. Meng, F., Liu, H., Liang, Y., Liu, W., & Pei, J. (2017). A Bidirectional Adaptive Bandwidth Mean Shift Strategy for Clustering. ICIP, 2017.
35. Ester, M., Kriegel, H. H. P., Sander, J. J., & Xu, X. (1996). A Density-Based Algorithm for Discovering Clusters in Large Spatial Databases with Noise. Second International Conference on Knowledge Discovery and Data Mining, 2, 226–231.
36. Boonchoo, T., Ao, X., Liu, Y., Zhao, W., Zhuang, F., & He, Q. (2019). Grid-based DBSCAN: Indexing and inference. Pattern Recognition, 90.
37. Elbarawy, Y. M., Mohamed, R. F., & Ghali, N. I. (2014) Improving social network community detection using DBSCAN algorithm. IEEE World Symposium on Computer Applications & Research (WSCAR), 1-6, Sousse, Tunisia.
38. Khatoon, M., Banu, W. A., (2019). An efficient method to detect communities in social networks using DBSCAN algorithm, Social Network Analysis and Mining, (2019) 9: 9.
39. Nasiboglu, R., Tezel, B. T., & Nasibov, E. (2019). Learning the stress function pattern of ordered weighted average aggregation using DBSCAN clustering. International Journal of Intelligent Systems, 2019, 34(3):477-492.
40. Gallego, C. E. V., Gómez Comendador, V. F., Saez Nieto, F. J., & Martinez, M. G. (2018). Discussion On Density-Based Clustering Methods Applied for Automated Identification of Airspace Flows. IEEE/AIAA 37th Digital Avionics Systems Conference (DASC), 2018, 1-10, London, UK.
41. Ferrara, R., Virdis, S., Ventura, A., Ghisu, T., Duce, P., & Pellizzaro, G. (2018). An automated approach for wood-leaf separation from terrestrial LIDAR point clouds using the density based clustering algorithm DBSCAN. Agricultural and Forest Meteorology. 262.
42. Ozdemir, S., Akbulut, Z., Karslı, F. & Acar, H. (2021). Automatic extraction of trees by using multiple return properties of the lidar point cloud. International Journal of Engineering and Geosciences, 6 (1), 20-26.
43. Rottensteiner, F., Trinder, J., Clode, S., & Kubik, K. (2007). Building detection by fusion of airborne laser scanner data and multi spectral images: performance evaluation and sensitivity analysis. ISPRS Journal of Photogrammetry and Remote Sensing, 135-149, 2007.
44. Uzar, M. & Yastikli, N. (2013). Automatic building extraction using LiDAR and aerial photographs, Boletim de Ciências Geodésicas ,19, 153–171.
45. Akbulut, Z., Ozdemir, S., Acar, H., Dihkan, M. & Karslı, F. (2018). Automatic extraction of building boundaries from high resolution images with active contour segmentation. International Journal of Engineering and Geosciences, 3 (1), 36-42.
46. Li, W., Guo, Q., Jakubowski, M., & Kelly, M. (2012). A New Method for Segmenting Individual Trees from the Lidar Point Cloud. Photogrammetric Engineering and Remote Sensing. 78. 75-84.
47. Yastikli, N. & Cetin, Z. (2020). Detection of Individual Trees in Urban Areas Using the Point Cloud Produced by Dense Image Matching Algorithms, FIG Working Week 2020, Amsterdam, Holland.

International Journal of Engineering and Geosciences
https://dergipark.org.tr/en/pub/ijeg
e-ISSN 2548-0960

Deep learning-based vehicle detection from orthophoto and spatial accuracy analysis

Muhammed Yahya Biyik [1], Muhammed Enes Atik [*1], Zaide Duran [1]

[1]*Istanbul Technical University, Geomatics Engineering Department, Türkiye*

Keywords
UAV
Photogrammetry
Deep Learning
Orthophoto
Object Detection

Research Article
DOI: 10.26833/ijeg.1080624

Received: 28.02.2022
Accepted: 24.06.2022
Published: 19.10.2022

Abstract

Deep Learning algorithms are used by many different disciplines for various purposes, thanks to their ever-developing data processing skills. Convolutional neural network (CNN) are generally developed and used for this integration purpose. On the other hand, the widespread usage of Unmanned Aerial Vehicles (UAV) enables the collection of aerial photographs for Photogrammetric studies. In this study, these two fields were brought together and it was aimed to find the equivalents of the objects detected from the UAV images using deep learning in the global coordinate system and to evaluate their accuracy over these values. For these reasons, v3 and v4 versions of the YOLO algorithm, which prioritizes detecting the midpoint of the detected object, were trained in Google Colab's virtual machine environment using the prepared data set. The coordinate values read from the orthophoto and the coordinate values of the midpoints of the objects, which were derived according to the estimations made by the YOLO-v3 and YOLOV4-CSP models, were compared and their spatial accuracy was calculated. Accuracy of 16.8 cm was obtained with the YOLO-v3 and 15.5 cm with the YOLOv4-CSP. In addition, the mAP value was obtained as 80% for YOLOv3 and 87% for YOLOv4-CSP. F1-score is 80% for YOLOv3 and 85% for YOLOv4-CSP.

1. Introduction

Vehicle tracking and traffic situation analysis play an essential role in safe autonomous driving. Vehicle detection from unmanned aerial vehicle (UAV) imagery is a crucial task for many computers vision-based applications [1]. However, various factors associated with aerial photos, such as different vehicle sizes, orientations, types, density, limited datasets, and inference speed, make it a difficult process [2]. Many deep learning-based strategies have been developed in the literature in recent years to solve these issues [3].

When image processing techniques are combined with deep learning, successful techniques have begun to emerge in this regard [4]. Unmanned aerial vehicle (UAV) images are also widely used for object detection and tracking. UAVs have another concept increasing due to their customizability for different purposes and conditions. Considering these two solutions together is an inevitable unity, but it is possible to see their examples in many fields such as cultural heritage [5-7], building extraction [8, 9], mapping [10], geology [11], mining [12], shoreline extraction [13]. Images obtained with high sensitivity in very low flight using UAVs can be produced at a lower cost than images obtained from conventional aerial photogrammetry [10].

For computer vision and image processing, artificial intelligence (AI) offers new methodologies and benefits. Deep learning (DL) algorithms are becoming increasingly popular since they are resilient and require fewer human operations [14]. Deep learning has an essential role in many typical applications and it is gradually developing [15]. Deep Learning is essentially one of the sub-branches of artificial intelligence technology. Although Artificial Intelligence has been on the agenda since the 1950s, Deep Learning has been more effective since the 2010s [16]. The main reasons for this are the developing hardware features and the new algorithms and methods developed depending on the increasing amount of data. In simple terms, deep learning is the process of mathematically modeling the learning process of human beings.

* **Corresponding Author**

(biyik16@itu.edu.tr) ORCID ID 0000-0001-9848-9673
*(atikm@itu.edu.tr) ORCID ID 0000-0003-2273-7751
(duranza@itu.edu.tr) ORCID ID 0000-0002-1608-0119

Cite this article

Bıyık, M. Y., Atik, M. E., & Duran, Z. (2023). Deep learning-based vehicle detection from orthophoto and spatial accuracy analysis. International Journal of Engineering and Geosciences, 8(2), 138-145

Convolutional Neural Network (CNN) has been developed based on imitating the working principles of the neural networks and learning mechanism in the human brain [16]. Neural networks are capable of solving complicated problems with accuracy [17]. Object detection is a challenging topic in photogrammetry and computer vision. One of the primary issues is the need for human interaction in object detection [18]. CNN models are one of the important tools to reduce human intervention. CNN processes images used as input in layers for object detection. As a result of various filtering processes, the image becomes a flat matrix. As a result of the mathematical equations that are solved based on the parameters determined for the model using the resulting matrix, a weight and a bias value are determined for each node. Objects in the new images evaluated as a result of these weights are detected.

CNN-based object approaches are examined under two title: two-stage and single-stage detection methods [19]. Regions with convolutional neural networks (R-CNN), Fast R-CNN and Faster RCNN can be counted as two-stage detectors. R-CNN divides images into region proposals and applies CNN for each region respectively. CNN decides the appropriate region and object size. However, two-stage approaches stand out with their slowness. The speed problem is solved with single-stage approaches. You Only Look Once (YOLO) is a single-stage object detection approach. YOLO thinks that object detection is a regression problem and obtain the position of the object, category and corresponding confidence score. It increases the detection speed and detects the object in the real-time target [20].

The aim of this study is to consider the DL algorithms developed for detection from a photogrammetric perspective and to compare the midpoints of the detected objects using the produced position accuracies. Vehicle detection was performed over orthophoto using YOLOv3 and YOLOv4-CSP algorithms. The midpoint coordinates of the detected vehicles are obtained in the EPSG:5254 TUREF / TM30 coordinate system. Accuracy analysis was performed by comparing the detected coordinates and reference coordinates.

2. Literature Review

There are different neural network algorithms for object detection. For example, deep learning algorithms were used in these studies [19, 21, 22, 23].

In the study by Cepni et al. (2020) [19], vehicles were selected as the object to be detected and their data were analyzed according to the YOLOv3- YOLOv3-spp and YOLOv3-tiny algorithms, with the models they trained on Google Colab using the COCO data set and UAV images. Average IoU is obtained as 84,88% with YOLOv3-spp. Zhao et al. [21] presented a compact solution for vehicle detection, tracking and ground coordinate using a microcomputer integrated UAV system. They preferred YOLOv3 as a deep learning algorithm in the model they established in real-time. However, the model used was chosen as a pre-trained model due to the physical conditions of the UAV platform. They stated that they preferred a passive system to calculate the coordinates of the target object, so the positioning process was carried out according to the data obtained from the GPS and IMU sensors on the UAV. In the study, mAP value of 90.61% was reached with YOLOv3. Božić-Štulić et al. [24] aim to perform automatic object detection and positioning from aerial photographs using convolutional neural networks (CNN) without the need for Ground Control Points (GCP), in a three-stage proposed method as a new approach. The vehicle detection accuracy is 82.5% by using R-CNN. Liu et al. [25] have presented a solution called UAV-YOLO to solve the difficulties experienced in detecting small objects from UAV-based images in their study based on deep learning algorithms. They stated the study's aims as creating an image data set obtained from the UAV platform to improve the human detection performance and improve the neural network structure of the YOLO algorithm. In the study, the YOLOv3 algorithm was chosen and an improvement was made for the purpose of the study by using the Darknet software framework. In this way, model training and backbone structure optimization were provided. As a result of the study, a 90.86% mAP value was obtained in object detection made on UAV images. Zhang et al. [26] explains the stages of the approach they developed based on the problems experienced by object detection algorithms and integrated with the TrackleNet Tracker (TNT) method in their photograph and video series. In this approach, the RetinaNet method was preferred for object detection, as it was more convenient in the subsequent monitoring phase. In the multi-object detection phase, the TNT method is included to eliminate incomplete or unreliable detections that may arise. Subsequently, Visual Odometry and Ground Plane Estimation were made using the multi-image stereo (MWS) method. Finally, 3D object positioning was done from 2D image coordinates, thanks to the camera parameters and the data obtained in the previous processes. The detection performance of the study is 97.8% Map for cars. Radovic, et al. [27] determined their motivation as testing CNN object detection algorithms that can be used for autonomous UAV applications in civil engineering. They preferred the YOLO algorithm in training the artificial network. Images obtained using Google Maps platform were used to test the trained model. They obtained 97.5% accuracy using satellite images. In the study conducted by Atik et al. [15], it was aimed to detect different objects over DOTA data with YOLO-v2 and YOLO-v3 algorithms. The vehicles are detected with 59% F1-score using YOLOv3.

3. Material and Method

3.1. Dataset

In the study, two separate data sets were used for training and testing. The dataset used for the training consists of aerial images obtained with UAV on the Prince Sultan University campus. This dataset, published as open-source on GitHub, was prepared for vehicle detection from UAV-based images [28]. The platform height was specified as 55 m and 80 m while the images were collected (Fig. 1). The training set contains 218 images and 3,365 instances of labeled cars.

Figure 1. A sample image from training dataset

For the performance tests of the algorithms, aerial images obtained from the UAV flight over Istanbul Technic University Ayazaga Campus were used (Fig. 2). Forward overlap 80% and side overlaps of 70% and flown at a height of 80 m above were selected as flight parameters. Ground Sampling Distance (GSD) is around 3 cm/pixel. Vehicle detection was performed on the scaled and coordinated orthophotos created with these images. For accuracy analysis, vehicles were manually labeled and ground truth was produced.

Figure 2. A sample image from test dataset

3.2. You Only Look Once (YOLO)

You Only Look Once (YOLO) [20] is among the most well-known deep learning algorithms, and it stands out with its speed thanks to its single-stage detection architecture. In addition, if necessary, optimizations are made, it can work as CPU-based and is open source. Also, some pixels will have object conflict. Thanks to the "Anchor Box" approach in the YOLO algorithm, this problem can be solved.

There are some points to consider when using the YOLO algorithm. Because it processes images in one step, large images can exceed hardware capacities, and the detection accuracy of small objects in large images may be low. For this reason, the data to be used should be well examined. If necessary, large-size images should be divided into parts. Label files created as a result of the labeling process should be prepared in the format required by the YOLO algorithm. This format is shown in Table 1. The x and y coordinates, representing the centroid of the boxes drawn during labeling, take a value between 0 and 1. Width and height are values for the dimensions of the rectangle drawn for the label or bounding box (Fig. 3).

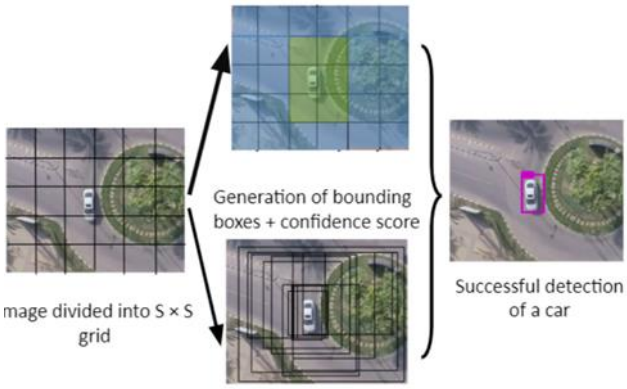

Figure 3. YOLO Algorithm work schema [28]

YOLO-v3 has residual skip connections and an up-sampling layer. Also, it makes detections at three different scales at layer 61, 94 and 106 [29]. It has darknet53 backbone [30]. Moreover, Rectified Linear Unit (ReLU) function was preferred as an activation function in YOLO-v3. In this study, YOLOv4-CSP (Cross-Spatial-Partial) is used. It has similar architect, but it uses the CSPdarknet53 backbone. YOLOv4-CSP [31] has cut-mix and mosaic data augmentation layers as default and without increasing training or detection time. YOLOv4-CSP uses a mish activation function and it has a Spatial Pyramid Pooling (SPP) module. The main difference between YOLO-v3 and YOLOv4-CSP algorithms is the backbone structure they use. Darknet53 is used for YOLO-v3, while CSPDarknet53 is used for YOLOv4-CSP. Accordingly, YOLO-v3 consists of a total of 106 layers, while YOLOv4-CSP contains a total of 161 layers.

The mathematical expression of the confidence score for the predictions made by the YOLO algorithm is specified in equation 2.1, as expressed in the article explaining the YOLO-v3 algorithm [30].

$$\Pr(Class_i|Object) * \Pr(Object) * IoU_{pred}^{truth} = \Pr(Class_i) * IoU_{pred}^{truth} \quad (1)$$

According to the equation, the confidence score of a prediction box is the product of the confidence score of the object that can be detected in it and the IOU value obtained for the box. It takes a value between 0 and 1. A high IOU value is an indicator of how accurately the dimensions of the detected object and the region it is located are detected.

3.3. Evaluation Metrics

As evaluation metrics, F1-score and mean average precision (mAP) are utilized. Precision is used to calculate the percentage of points that are classified as positive. The recall of a collection of positives is the percentage of true positives. The mean Average Precision, or mAP score, is the mean precision over all classes and/or overall IoU thresholds, depending on the numerous detection challenges that occur.

$$Precision = \frac{TP}{TP + FP} \quad (2)$$

$$Recall = \frac{TP}{TP + FN} \quad (3)$$

$$F1\ score = 2\frac{Precision\ .\ Recall}{Precision +\ Recall} \quad (4)$$

$$AP = \sum_{k=0}^{k=n-1} [\text{Recalls(k)} - \text{Recalls(k} + 1)] * \text{Precisions(k)} \quad (5)$$

$$mAP = \frac{1}{n}\sum_{k=1}^{k=n} AP_k \quad (6)$$

True positive (TP) is the number of points that are prediction is positive and the actual label is positive. False positive (FP) is the number of points that are prediction is positive and the actual label is negative. False negative (FN) is the number of points that are prediction is negative and the actual label is positive [32].

4. Experiment

The algorithms compared within the scope of the study were YOLO-v3 and YOLOv4-CSP algorithms. Both algorithms are prepared in accordance with the Darknet software framework. In order to compare the models, all parameters were kept constant during the training of the models. During the training of both models, parameter values published as open source by the publishers of Darknet Software Architecture were used. The workflow is presented in Fig. 4.

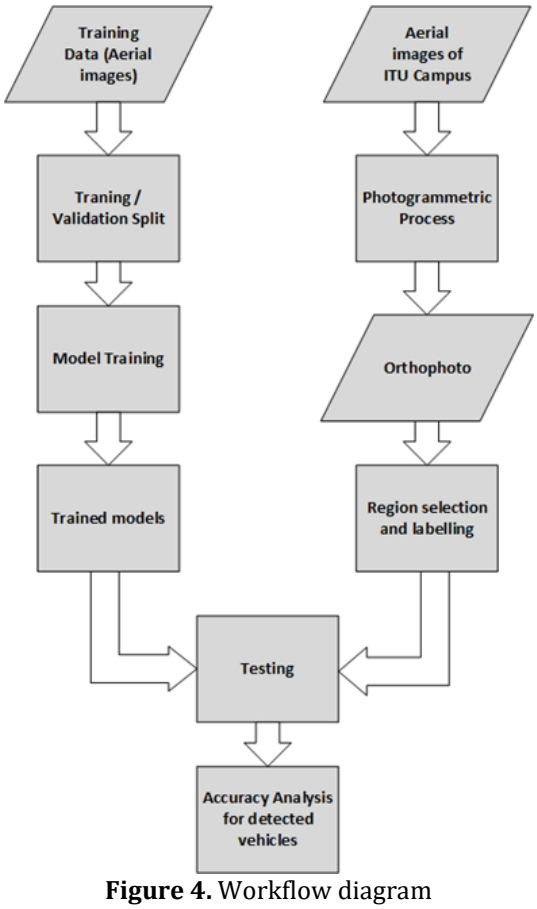

Figure 4. Workflow diagram

4.1. Producing Orthophoto

Photogrammetry is a scientific technique to calculate an object's three-dimensional coordinates by measuring the correspondence points in overlapping images and to provide reliable sensor calibrate for 3D object modelling from digital images [33]. As computer vision algorithms and photogrammetric technologies are combined, procedures that automate the image-based 3D modeling process become more common [34]. Agisoft Photoscan was used to model the point cloud. The software is based on the Structure-from-Motion (SfM) algorithm, which works on the basis of photogrammetry principles, in which the 3D coordinates of an object are determined by measuring the matching points between two overlapping photos.

Removing the errors due to topography in photographs and making them vertical is called orthorectification. The final product with coordinate information is called orthophoto. Coordinates of certain points are marked on the Orthophoto by using the GCP whose coordinates are known. As a result of balancing and interpolation processes, the coordinate values of any location on the orthophoto can be obtained. Although there are open source and paid software solutions for these operations, while producing the orthophoto, 372 images of 4000x3000 pixels were used (Fig. 5). The orthophoto has 3 cm/pixel spatial resolution. One of the factors affecting the accuracy of the orthophoto is the distribution of ground control points on the area. In the study, attention was paid to the homogeneous distribution of ground control points. In addition, care was taken to produce the generated point cloud at high density (83 pts/m^2). Thus, the digital elevation model (DEM) produced has high accuracy as a result of interpolation. DEM quality is one of the main factors affecting orthophoto accuracy.

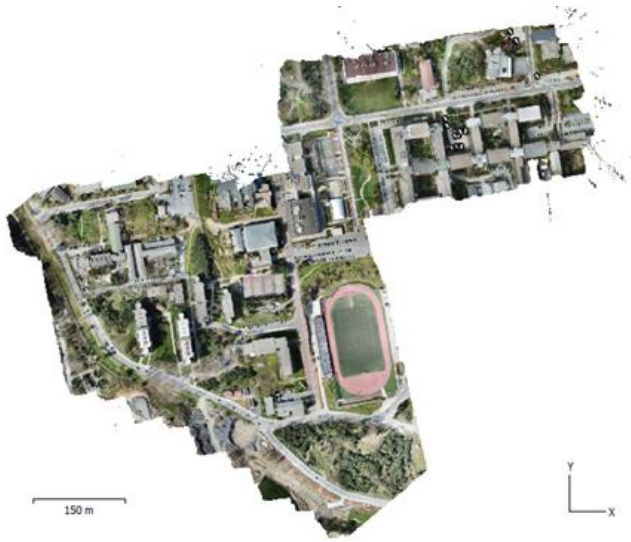

Figure 5. Orthophoto of Istanbul Technical University Ayazaga Campus.

The produced Orthophoto contains 10 ground control points (GCP). 3D coordinates of GCPs were measured by terrestrial measurements (using Global Navigation Satellite System (GNSS)). In addition, in order to calculate the accuracy of the model, 5 control points were

selected from the images in conditions that can be distinguished and intersect. The technical report of the model was prepared using Agisoft Professional software. The accuracy values obtained based on this report are shown in Table 1.

Table 1. Accuracy assessment result of check points.

Point	X Error (cm)	Y Error (cm)	Z Error (cm)	Total (cm)
3	0,2	0,5	0,1	0,5
6	-3,7	-1,0	5,6	6,8
7	2,4	0,0	-5,7	6,2
8	2,0	-0,2	-5,7	6,1
9	-0,4	-0,4	1,7	1,8
∑	2,2	0,5	4,4	5,0

4.2. Training

Within the scope of the study, YOLO-v3 and YOLOv4-CSP models were trained. Model training was done in cloud environment using Google Colab. The training period varies depending on the hardware power. The training dataset divided into 90% training and 10% validation. Training parameters are given in Table 2.

Table 2. Training parameters.

Parameter	YOLOv3	YOLOv4-CSP
Batch Size	16	16
Subdivision	4	4
Width x height	608x608	608x608
Max. batch	6000	6000
Learning rate	0.001	0.001
Momentum	0.9	0.9

During the training phase, the parameter files of the models were accepted as standard and no changes were made. The data used during model training are data shared as open source. The images are separated as training and validation data, the same distribution is used for each model. Although 2000 iterations are recommended for each number of classes, since there is only one class in our study, the models are trained with 6000 iterations, which is the minimum number of iterations recommended by the developers. The weights with the highest sensitivity value among the obtained weights were selected for the test. Trained models were tested on images selected over orthophoto.

Table 3. Analysis of position accuracy of vehicles detected on Figure 7, test area 2 using Model YOLO-v3

	Orthophotos Coordinates (m)		Detected Coordinates (m)		Variation (m)			
Object	RIGHT	UP	RIGHT	UP	RIGHT	UP	Vx^2	Vy^2
1	418093,865	4552668,461	-	-	-	-	-	-
2	418096,459	4552657,237	418096,443	4552657,497	0,016	-0,260	0,000	0,068
3	418104,607	4552621,107	-	-	-	-	-	-
4	418109,700	4552640,200	-	-	-	-	-	-
5	418110,083	4552622,712	418110,131	4552622,884	-0,048	-0,172	0,002	0,029
6	418112,624	4552623,083	-	-	-	-	-	-
7	418115,305	4552641,617	-	-	-	-	-	-
8	418117,522	4552623,495	-	-	-		-	-
9	418117,788	4552647,484	418118,028	4552647,399	-0,240	0,085	0,058	0,007
10	418119,946	4552623,651	-	-	-	-	-	-
11	418126,056	4552648,435	418125,993	4552648,197	0,063	0,238	0,004	0,057
							RMSE=	0,168 m

Table 4. Analysis of position accuracy of vehicles detected on Figure 7, test area 2 using Model YOLOv4-CSP

	Orthophotos Coordinates (m)		Detected Coordinates (m)		Variation (m)			
Object	RIGHT	UP	RIGHT	UP	RIGHT	UP	Vx^2	Vy^2
1	418093,865	4552668,461	418093,829	4552668,681	0,036	-0,220	0,001	0,048
2	418096,459	4552657,237	418096,388	4552657,290	0,071	-0,054	0,005	0,003
3	418104,607	4552621,107	418104,518	4552621,481	0,088	-0,374	0,008	0,140
4	418109,700	4552640,200	418109,650	4552640,245	0,050	-0,045	0,003	0,002
5	418110,083	4552622,712	418109,980	4552622,856	0,103	-0,144	0,011	0,021
6	418112,624	4552623,083	418112,662	4552623,159	-0,039	-0,077	0,002	0,006
7	418115,305	4552641,617	418115,276	4552641,704	0,028	-0,087	0,001	0,008
8	418117,522	4552623,495	418117,519	4552623,833	0,003	-0,338	0,000	0,114
9	418117,788	4552647,484	418117,780	4552647,550	0,007	-0,066	0,000	0,004
10	418119,946	4552623,651	418119,899	4552623,902	0,047	-0,251	0,002	0,063
11	418126,056	4552648,435	418125,800	4552648,582	0,256	-0,147	0,066	0,022
							RMSE=	0,155 m

Table 5. Comparison of models using common detected vehicles on test area 2

	Orthophotos Coordinates (m)		Detected Coordinates (m)		Variation (m)			
Object	RIGHT	UP	RIGHT	UP	RIGHT	UP	Vx^2	Vy^2
2	418096,459	4552657,237	418096,388	4552657,290	0,071	-0,054	0,005	0,003
5	418110,083	4552622,712	418109,980	4552622,856	0,103	-0,144	0,011	0,021
9	418117,788	4552647,484	418117,780	4552647,550	0,007	-0,066	0,000	0,004
11	418126,056	4552648,435	418125,800	4552648,582	0,256	-0,147	0,066	0,022
							RMSE=	0,128 m

5. Results

In the study, accuracy analysis was analyzed in two stages, the accuracy of the algorithm applied and the spatial accuracy of the detected vehicles.

Two regions were selected over orthophoto for evaluation. The detection performances of the algorithms were compared. In addition to the confidence values of the vehicles found by the algorithms, the number of vehicles they could detect was also evaluated. 0.80 mAP was achieved with Yolo-v3, while 0.87 mAP was achieved with YOLOv4-CSP. The YOLOv4-CSP has an F1 score of 0.85, while the YOLO-V3 has an F1 score of 0.80 (Fig. 6 and Fig. 7). The accuracy of the trained models is presented in Table 6. The confusion matrix is presented in Table 7 and Table 8.

Table 6. Statistical outputs of models

Model	mAP	mIOU	F1 Score
YOLO-v3	0.80	0.55	0.80
YOLOv4-CSP	0.87	0.60	0.85

Table 7. The detection performance of the algorithms for sample images.

Figure	Model	Detection Ratio	Confidence Score Mean
Test Area 1	YOLO-v3	0,64	79.0
Test Area 1	YOLOv4-CSP	1.0	99,18
Test Area 2	YOLO-v3	0,78	91.0
Test Area 2	YOLOv4-CSP	1.0	98,78

Table 8. Confusion matrix of YOLOv4-CSP and YOLOv3

	YOLOv4-CSP		YOLOv3	
	Predicted Positive	Predicted Negative	Predicted Positive	Predicted Negative
Actual Positive	TP=26	FN=2	TP=26	FN=2
Actual Negative	FP=1	TN=0	FP=1	TN=0

Figure 6. Evaluation result on test area 1 (YOLO-v3 on the left; YOLOv4-CSP on the right)

Figure 7. Evaluation result on test area 2 (YOLO-v3 on the left; YOLOv4-CSP on the right).

The operator marked the midpoints of the detected vehicles to obtain reference values (Fig. 8). Then, the coordinates of the midpoints of the bounding boxes created by the algorithms are calculated. Thus, a spatial accuracy analysis was performed. Spatial accuracy analysis was applied separately for both all vehicles and common vehicles detected by both algorithms. Since all vehicles detected by YOLO-v3 were also detected by YOLOv4-CSP, only the accuracy of YOLOv4-CSP in common vehicles was analyzed. The purpose of preparing Table 4 is to show the position accuracy of the detected vehicles only for both models. Spatial accuracy for all tools is 16.8 cm for YOLOv3 and 15.6 cm for YOLOv4-CSP (Table 3 and Table 4). In common detected vehicles, the accuracy of YOLOv4 is 12.8 cm.

Figure 8. Obtaining the midpoints of the vehicles via Agisoft Metashape software

6. Discussion

As a result of the comparison between YOLO-v3 and YOLOv4-CSP, it was seen that the detection accuracy of the YOLOv4-CSP algorithm was higher in terms of both detection rate and spatial accuracy. YOLOv4-CSP can detect almost all vehicles in images. YOLO-v3 is unable to detect most vehicles close to image boundaries. The confidence value of the vehicles found is also higher in YOLOv4-CSP. The CSPDarknet architecture and the many layers make YOLOv4-CSP superior to YOLO-v3.

According to the accuracy analysis, the YOLOv4-CSP model detected the midpoints with higher accuracy than the YOLO-v3 model. Considering the common vehicles, vehicle positions can be detected with high accuracy with the YOLOv4-CSP. Bounding boxes are found by YOLOv4-CSP with higher accuracy. As seen in Table 6, the mIoU value is higher than that of YOLOv4-CSP. High mIoU in this case means high location accuracy. Appropriate data set and parameter selection in deep learning networks is important not only for detecting vehicles but also for obtaining accurate spatial information.

The reason for choosing YOLOv4-CSP among YOLOv4-CSP versions is to provide a healthier comparison with YOLO-v3. Thus, the effect of CSP optimization used in the backbone will be better understood. In addition, YOLOv4-CSP also requires less hardware resources and training time during training as it contains fewer layers than other YOLOv4-CSP versions. Finally, new YOLO versions are releasing with different approaches. According to their developers' claim some of them shows better mAP performance than the YOLOv4-CSP.

Consequently, However, as a point to be noted, the coordinate values reached do not express an absolute accuracy, it should be noted that the coordinate values taken from the orthophoto and accepted as correct have at least as much error as the orthophoto. However, since the same orthophoto was used during the study, this error amount was ignored assuming that it was equally distributed to each determination.

Area-based matching methods are also used for vehicle detection [35]. However, in area-based approaches, changes in the resolution or point of view of the image adversely affect the detection performance. It is more appropriate to use deep learning approaches instead of domain-based approaches, which are useful in cases where the search and target image are very similar. Especially in complex city structures, deep learning-based approaches are more suitable for vehicle detection. The YOLOv4-CSP algorithm correctly detected almost all vehicles in the images (Table 7).

In addition, training and test data were obtained from different sources in the study. This problem is called domain-shift in the literature. Models trained on aerial photographs obtained from a different region with a different UAV were tested on a completely different orthophoto with training data. It has been concluded that YOLOv4-CSP is less affected by the domain-shift problem and can be used in such cases.

7. Conclusion

In this study, we detect the vehicles from the orthophoto using different deep learning algorithms and analyze the spatial accuracy of the midpoints of the vehicles detected. It is possible that this work, which currently requires manual interventions and is carried out with non-instantaneous data, will become a fully autonomous and instantaneous solution in the future. In order to achieve this, it is a preferable solution to derive the positions of the detected objects depending on the UAV location, with the increase in the capabilities of the GNSS and IMU sensors on the UAVs.

In addition, the servicing of GNSS coordinates instead of limiting the results to image coordinates, especially in object detection studies with air platforms, will speed up and facilitate the production of location information, which many disciplines need.

Finally, new YOLO versions are releasing with different approaches. According to their developers' claim some of them shows better mAP performance than the YOLOv4-CSP. So, this study can be expanse with YOLO-v5 and YOLO-X.

Author contributions

Muhammed Yahya Biyik: Data curation, Software, Field study, Writing-Original draft preparation, Visualization **Muhammed Enes Atik:** Methodology, Writing-Original draft preparation, Software, Validation, Conceptualization **Zaide Duran:** Conceptualization, Investigation, Writing-Reviewing and Editing, Supervision.

Conflicts of interest

The authors declare no conflicts of interest.

References

1. Luo, X., Tian, X., Zhang, H., Hou, W., Leng, G., Xu, W., ... & Zhang, J. (2020). Fast automatic vehicle detection in uav images using convolutional neural networks. *Remote Sensing*, 12(12), 1994.
2. Lu, J., Ma, C., Li, L., Xing, X., Zhang, Y., Wang, Z., & Xu, J. (2018). A vehicle detection method for aerial image based on YOLO. *Journal of Computer and Communications*, 6(11), 98-107.
3. Sang, J., Wu, Z., Guo, P., Hu, H., Xiang, H., Zhang, Q., & Cai, B. (2018). An improved YOLOv2 for vehicle detection. Sensors, 18(12), 4272.
4. Jazayeri, A., Cai, H., Zheng, J. Y., & Tuceryan, M. (2011). Vehicle detection and tracking in car video based on motion model. *IEEE Transactions on Intelligent Transportation Systems*, *12*(2), 583-595.
5. Senkal, E., Kaplan, G., & Avdan, U. (2021). Accuracy assessment of digital surface models from unmanned aerial vehicles' imagery on archaeological sites. *International Journal of Engineering and Geosciences*, *6*(2), 81-89.
6. Şasi A., & Yakar, M. (2018). Photogrammetric modelling of hasbey dar'ülhuffaz (masjid) using an unmanned aerial vehicle. *International Journal of Engineering and Geosciences*, *3*(1), 6-11.
7. Ulvi, A., Yakar, M., Yigit, A. Y., & Kaya, Y. (2020). İha ve Yersel Fotogrametrik Teknikler Kullanarak Aksaray

Kızıl Kilisenin 3b Modelinin ve Nokta Bulutunun Elde Edilmesi. *Geomatik*, *5*(1), 19-26.

8. Gönültaş, F., Atik, M. E. & Duran, Z. (2020). Extraction of Roof Planes from Different Point Clouds Using RANSAC Algorithm. *International Journal of Environment and Geoinformatics*, 7 (2), 165-171. https://doi.org/10.30897/ijegeo.715510
9. Atik, M. E., Donmez, S. O., Duran, Z., & İpbuker, C. (2018). Comparison Of Automatic Feature Extraction Methods for Building Roof Planes by Using Airborne Lidar Data and High-Resolution Satellite Image. *In Proceedings, 7th International Conference on Cartography and GIS (*pp. 857-863), 18-23 June 2018, Sozopol, Bulgaria.
10. Ulvi, A., Yakar, M., Yiğit, A. Y. & Kaya, Y. (2020). İha ve Yersel Fotogrametrik Teknikler Kullanarak Aksaray Kızıl Kilisenin 3b Modelinin ve Nokta Bulutunun Elde Edilmesi. Geomatik, 5 (1), 19-26. https://doi.org/10.29128/geomatik.560179
11. Agca. M., Gültekin, N., & Kaya, E. (2020). İnsansız hava aracından elde edilen veriler ile kaya düşme potansiyelinin değerlendirilmesi: Adam Kayalar örneği, Mersin. *Geomatik*, *5*(2), 134-145.
12. Alptekin, A. & Yakar, M. (2020). Determination of pond volume with using an unmanned aerial vehicle. Mersin Photogrammetry Journal, 2 (2), 59-63.
13. Aykut, N. O. (2019). İnsansız Hava Araçlarının Kıyı Çizgisinin Belirlenmesinde Kullanılabilirliğinin Araştırılması. *Geomatik*, *4*(2), 141-146.
14. Atik, S. O., & Ipbuker, C. (2021). Integrating Convolutional Neural Network and Multiresolution Segmentation for Land Cover and Land Use Mapping Using Satellite Imagery. *Applied Sciences*, *11*(12), 5551.
15. Atik, M. E., Duran, Z., & Özgünlük, R. (2022). Comparison of YOLO Versions for Object Detection from Aerial Images. *International Journal of Environment and Geoinformatics*, *9*(2), 87-93.
16. Bengio, Y., Goodfellow, I., & Courville, A. (2017). *Deep learning* (Vol. 1). Cambridge, MA, USA: MIT press.
17. Tasdemir, S., & Ozkan, I. A. (2019). ANN approach for estimation of cow weight depending on photogrammetric body dimensions. *International Journal of Engineering and Geosciences*, *4*(1), 36-44.
18. Sariturk, B., Bayram, B., Duran, Z., & Seker, D. Z. (2020). Feature extraction from satellite images using segnet and fully convolutional networks (FCN). *International Journal of Engineering and Geosciences*, *5*(3), 138-143.
19. Cepni, S., Atik, M. E., & Duran, Z. (2020). Vehicle detection using different deep learning algorithms from image sequence. *Baltic Journal of Modern Computing*, *8*(2), 347-358.
20. Redmon, J., Divvala, S., Girshick, R., & Farhadi, A. (2016). You only look once: Unified, real-time object detection. In *Proceedings of the IEEE conference on computer vision and pattern recognition* (pp. 779-788).
21. Zhao, X., Pu, F., Wang, Z., Chen, H., & Xu, Z. (2019). Detection, tracking, and geolocation of moving vehicle from uav using monocular camera. *IEEE Access*, *7*, 101160-101170.
22. Atik, S. O., & Ipbuker, C. (2020). Instance Segmentation of Crowd Detection in The Camera Images. In *Proceeding of 41st Asian Conference on Remote Sensing 2020 (ACRS2020)*, Deqing City, Virtual, 9-11 November 2020.
23. Cazzato, D., Cimarelli, C., Sanchez-Lopez, J. L., Voos, H., & Leo, M. (2020). A survey of computer vision methods for 2d object detection from unmanned aerial vehicles. *Journal of Imaging*, *6*(8), 78.
24. Božić-Štulić, D., Kružić, S., Gotovac, S., & Papić, V. (2018). Complete model for automatic object detection and localisation on aerial images using convolutional neural networks. *Journal of Communications Software and Systems*, *14*(1), 82-90.
25. Liu, M., Wang, X., Zhou, A., Fu, X., Ma, Y., & Piao, C. (2020). Uav-yolo: Small object detection on unmanned aerial vehicle perspective. *Sensors*, *20*(8), 2238.
26. Zhang, H., Wang, G., Lei, Z., & Hwang, J. N. (2019, October). Eye in the sky: Drone-based object tracking and 3d localization. In *Proceedings of the 27th ACM International Conference on Multimedia* (pp. 899-907).
27. Radovic, M., Adarkwa, O., & Wang, Q. (2017). Object recognition in aerial images using convolutional neural networks. *Journal of Imaging*, *3*(2), 21.
28. Benjdira, B., Khursheed, T., Koubaa, A., Ammar, A., & Ouni, K. (2019, February). Car detection using unmanned aerial vehicles: Comparison between faster r-cnn and yolov3. In *2019 1st International Conference on Unmanned Vehicle Systems-Oman (UVS)* (pp. 1-6). IEEE.
29. Kim, S., & Kim, H. (2021). Zero-centered fixed-point quantization with iterative retraining for deep convolutional neural network-based object detectors. *IEEE Access*, *9*, 20828-20839.
30. Redmon, J., & Farhadi, A. (2018). Yolov3: An incremental improvement. *arXiv preprint arXiv:1804.02767*.
31. Bochkovskiy, A., Wang, C. Y., & Liao, H. Y. M. (2020). Yolov4: Optimal speed and accuracy of object detection. *arXiv preprint arXiv:2004.10934*.
32. Atik, M. E., Duran, Z., & Seker, D. Z. (2021). Machine learning-based supervised classification of point clouds using multiscale geometric features. ISPRS *International Journal of Geo-Information*, 10(3), 187.
33. Duran, Z., & Aydar, U. (2012). Digital modeling of world's first known length reference unit: The Nippur cubit rod. Journal of cultural heritage, 13(3), 352-356.
34. Duran, Z., & Atik, M. E. (2021). Accuracy comparison of interior orientation parameters from different photogrammetric software and direct linear transformation method. *International Journal of Engineering and Geosciences*, 6(2), 74-80.
35. Zhu, H., & Yu, F. (2016). A cross-correlation technique for vehicle detections in wireless magnetic sensor network. *IEEE Sensors Journal*, 16(11), 4484-4494.

International Journal of Engineering and Geosciences
https://dergipark.org.tr/en/pub/ijeg
e-ISSN 2548-0960

A comprehensive analysis of different geometric correction methods for the Pleiades -1A and Spot-6 satellite images

Buğrahan Özcihan [1], Levent Doğukan Özlü [1,2], Mümin İlker Karakap [1], Halime Sürmeli [2], Ugur Alganci [1], Elif Sertel [*1]

[1]*Istanbul Technical University, Civil Engineering Faculty, Geomatics Engineering Department, Istanbul, Türkiye*
[2]*Turkish Aerospace Industries, Inc. (TAI), Ankara, Türkiye*

Keywords
Remote Sensing
Geometric Correction
Accuracy Analysis
Empirical Models
Physical Models

Research Article
DOI: 10.26833/ijeg.1086861

Received: 13.03.2022
Accepted: 14.05.2022
Published: 19.10.2022

Abstract

Satellite images have been widely used in the production of geospatial information such as land use and land cover mapping and the generation of several thematic layers via image processing techniques. The systematic sensor and platform-induced geometry errors influence images acquired by sensors onboard various satellite platforms. Thus, geometric correction of satellite images is essential for image pre-processing to extract accurate and reliable locational information. Geometric correction of satellite images obtained from two different satellites, Pleiades 1A (PHR) and SPOT-6, was performed within the scope of this study using empirical models and a physical model. The 2D polynomial model, 3D rational function model with calculated RPCs from GCPs, 3D rational function model with RPCs from satellite, RPC refinement model using GCPs, and Toutin's physical model were used. Several experiments were carried out to investigate the effects of various parameters on the performance of the geometric correction procedure, such as GCP reference data source, GCP number and distribution, DEM source, spatial resolution, and model. Our results showed that lower RMSE values could be achieved with the model that uses RPC from data providers for PHR and SPOT, followed by the RPC refinement method for PHR and Toutin method for SPOT. In general, GCPs from the HGM data source and ALOS DEM combination provided better results. Lastly, lower RMSE values, thus better locational accuracy values, were observed with the PHR image except for a single test.

1. Introduction

Geospatial data is widely used in many disciplines for various purposes, including combating global warming, developing location-based services and navigation maps, producing thematic maps for city and regional planning, and estimating crop yield [1-8].

Remote sensing platforms provide a wide range of spatial data with different technical characteristics. However, a remote sensing image, which allows us to access up-to-date geographical information quickly, may contain geometric distortions caused by Earth's curvature, topographical conditions, and sensor data acquisition geometry. Before any further analysis of a remotely sensed image, pre-processing is required to obtain accurate and reliable geo-information [9-10]. Preprocessing is divided into two-fold: radiometric correction and geometric correction. Detector-based radiometric problems in images causing unexpected reflections are removed during the radiometric correction. Geometric correction is the process of minimizing the geometric distortions and defining the image in a specific coordinate system and datum [10-11]. According to Toutin [12], geometric distortions are commonly present in remotely sensed images. Therefore, it is necessary to geometrically correct images to reliably use them as a base map in a geographic information system (GIS), conduct accurate angle and distance measurements from these images or generate a precise spatial database of different features [13].

* **Corresponding Author**

(ozcihan17@itu.edu.tr) ORCID ID 0000-0002-4540-3140
(ozlul17@itu.edu.tr) ORCID ID 0000-0001-7121-8101
(karakap16@itu.edu.tr) ORCID ID 0000-0002-7128-2100
(halimerek@gmail.com) ORCID ID 0000-0002-7430-183X
(alganci@itu.edu.tr) ORCID ID 0000-0002-5693-3614
*(sertele@itu.edu.tr) ORCID ID 0000-0003-4854-494X

Cite this article

Özcihan, B., Özlü, L. D., Karakap, M. İ., Sürmeli, H., Algancı, U., & Sertel, E. (2023). A comprehensive analysis of different geometric correction methods for the Pleiades -1A and Spot-6 satellite images. International Journal of Engineering and Geosciences, 8(2), 146-153

Since the geometric correction of satellite images is a vital step for many remote sensing-based applications, several researches have been conducted on the analysis of different models' performance and accuracy by considering the effects of used digital elevation models (DEM), and ground control points (GCP).

Alganci et al. [14] emphasized the importance of appropriate DEM selection considering the purpose and scale of the study because DEM accuracy directly affects individual calculations and process chains. DEM's accuracy is very effective and important for geometric correction operations. In addition to the DEM's accuracy, the topographic characteristics of the study area are also impacting the performance of geometric correction processes. According to results in the same study, elevation values obtained from SPOT and PHR DSM's were better than SRTM, ALOS, and ASTER data. ALOS DSM provided significantly better results than other freely available DEMs. ASTER GDEM, which has a 30-m spatial resolution and is freely available, is also used in many studies of geometric correction.

Ground Control Points (GCP) also play an important role in geometric correction accuracy [9,15]. According to Samadzadegan et al., [16], the number and distribution of the ground control points highly affect the accuracy of geometric correction model results. The necessity of the homogeneous distribution of GCPs is clearly stated in previous research. Furthermore, the number of GCPs required varies depending on the mathematical model used. According to Toutin [12], the 2D/3D non-parametric models are sensitive to GCP's distribution and need many GCPs (>20-60), while 3D parametric models are not that sensitive to distribution and need few GCPs (3-8).

Besides DEM and GCPs, mathematical models are one of the main important components of the geometric correction process. In the study of Samadzadegan et al. [16], the DLT model, RFM, and Affine models were applied to SPOT, IRS, and IKONOS satellite images and according to the results, RFM provided better results than the other models. In another study by Kartal et al. [11], empirical models, which are the rational function model (RFM), RPC Refinement model and physical Toutin model, were applied to Pleiades images. ASTER GDEM was used for the ortho-rectification process. The physical Toutin model provided the highest accuracy in both study areas, followed by the first-order Rational Polynomial Coefficient (RPC) refinement model. They concluded that it is important to have sensor parameters to perform successful correction to imagery and non-parametric models are not as accurate as parametric models. Toutin [12], stated that 2D/3D polynomial nonparametric functions do not reflect the source of distortions thus they can be used only for images with small distortions, and they are also very sensitive to input errors like unsuitably distributed GCPs. According to the same study, the 3D rational function, which is also a non-parametric function, provides better accuracy than polynomial functions but is lower than parametric functions.

In another study on geometric correction, Ye et al. [17] performed geometric corrections on very high-resolution WorldView-2 satellite images (0.5m) with different models and compared the results. They used a physical model and RFM models, RPCs provided by the data provider, RPCs calculated by Least Square iterative method, and RPCs calculated by Correcting Characteristic Value method. Their results provided that both methods used in RPC calculation yielded more successful results than the coefficients provided by the metadata, and the CCVM method gave slightly more accurate results than the LS method. It was observed that the physical model gave better results than the model using the RPC coefficients provided by the provider, but fell behind the two methods performed by RPC calculations.

Son et al. [18] proposed an iterative precision geometry correction approach by implementing an image pyramid including GCP chip matching, outlier detection, and precise sensor modeling for the automatic detection of GCPs. They utilized their proposed approach to KOMPSAT-3 images and obtained average geometric accuracy of 1.5 pixels and a maximum of 2 pixels.

Zhang et al. [15] evaluated the geolocation accuracy of the Chinese First Polar Microsatellite (Ice Pathfinder, BNU-1) Imagery. The geometric calibration model of BNU-1 did not achieve good accuracy metrics due to the inaccuracy of satellite attitude and orbit parameters, which have to be precisely determined for a sensor-based calibration model. They used MODIS images to extract accurate GCPs and used them to correct the geolocation errors of BNU-1 images. They applied their methodology to Twenty-eight images of Antarctica and fifteen images of Arctic regions and improved the geometric correction accuracy from 10 km to 300m.

Mezouar et al. [19] performed a particle swarm optimization method-based approach to optimize the FRM over Alsat -2 images and reported an accuracy improvement between 21% and 38% over state-of-the-art approaches.

To obtain sub-pixel geometric accuracy, Misra et al. [20] proposed a feature detection approach based on mode-guided tiled scale-invariant feature transform (MT-SIFT) in hierarchical stages. They evaluated their automatic approach for Resourcesat multispectral camera images of different landscapes. They achieved the root mean square error (RMSE) of 0.12 pixels at a spatial resolution of 5 m.

A very current study by Wang et al. [21] proposes orthorectification of GF-3 SAR images using RPC files and TPs generated by SIFT algorithm. Their GCP-free experiment resulted in a mean RMSE of 0.724 pixels among 1,468 images.

By contemplating the important and dominant factors of geometric correction from the above literature, this study aims to comprehensively evaluate empirical and physical geometric correction models on high (HR) and very high-resolution (VHR) satellite images of Istanbul, Turkey. The effects of the freely available DEM sources, quantity and quality of GCPs, and spatial resolution of the satellite images on geometric correction models are investigated within this scope. The remainder of the paper is organized as follows. Section 2 provides detailed information about the study region and used datasets; Section 3 gives a detailed explanation of methods and analysis workflow, Section 4 presents

quantitative results, and Section 5 provides concluding remarks.

2. Study Area and Data

Within the scope of this study, satellite images of Istanbul were obtained from two different satellite platforms to be geometrically corrected using DEM and GCP data obtained from different sources. In this sense, the data used is presented under three subheadings: satellite imagery, ground control points and digital elevation models.

2.1. Satellite Imagery

This study investigates the performance of empirical and physical geometric correction methods on HR and VHR satellite images, obtained from SPOT-6 and Pleiades (PHR) satellites (Figure 1).

Pleiades 1A and 1B are VHR twin satellites, with a native spatial resolution of 0.7 meters for panchromatic and 2.8 meters for multispectral sensors. The products delivered by the provider are processed and resampled to 0.5m for panchromatic and 2.0m for multispectral images. A PHR image covers an area of approximately 20 km^2 on the ground. In this study, we used a Pleiades image covering the south-eastern part of the European side of Istanbul and captured on 15.05.2020.

SPOT-6 and SPOT-7 are twin satellites, with a spatial resolution of 1.5 meters for panchromatic and 6 meters for multispectral sensors. We used a SPOT-6 image of the European side of Istanbul, which was captured on 07.06.2020.

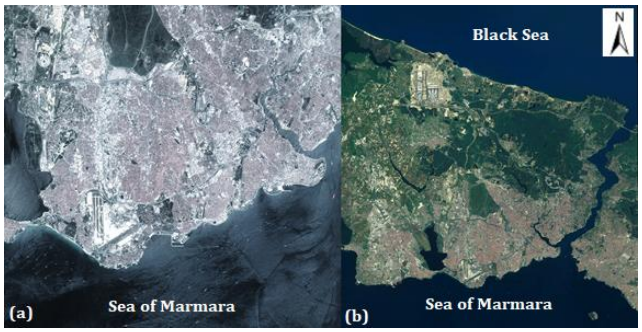

Figure 1. Preview of used satellite images a) PHR, b) SPOT

2.2. Ground Control Points

Ground Control Point (GCP) is very important to improve the accuracy of a satellite image. As mentioned in the literature review, in geometric correction studies, GCPs are very effective in obtaining better results. Checkpoint (CP) is the GCP that is not included in the process and is used to control how accurate the result of the process is. The following platforms were used as GCP and CP sources: 40 points from Google Earth (GE) as GCP and 20 points from General Directorate of Mapping (HGM) of Turkey as CP within this study.

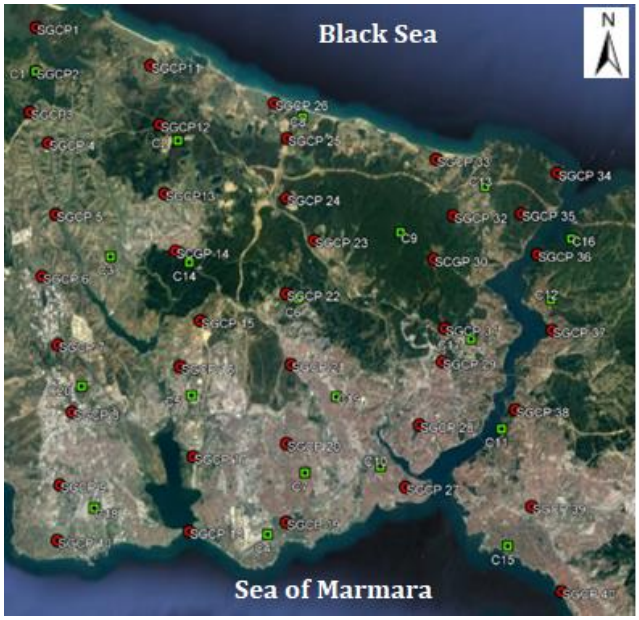

Figure 2. Distribution of GCPs (red) and CPs (green) in the study region

2.3. Digital Elevation Models

A Digital Elevation Model (DEM) represents the ground surface elevations with respect to any reference datum. DEM is a commonly used abstract model for the digital representation of topography. As DEM sources, we used Advanced Land Observing Satellite (ALOS), Advanced Spaceborne Thermal Emission and Reflection Radiometer Satellite (ASTER), and Shuttle Radar Topography Mission (SRTM) platforms in this study (2018).

The ALOS DEM has 30 meters spatial resolution. In the study of Alganci et al. [14], which evaluated the accuracy of DEMs for the same study region, the RMSE value of ALOS DEM was computed as 2.14 meters, and the accuracy value was calculated as 4.19 meters. ALOS DEM has the least RMSE value and is the most accurate among the other freely available DEMs. ASTER has 30 meters of spatial resolution, and it provides an RMSE value of 5.72 meters with an accuracy of 11.21 meters. SRTMDEM is the last DEM used in this study, which also has 30 meters spatial resolution. In the same study by Alganci et al., [14], the RMSE value of SRTM DEM was computed as 3.53 meters, and accuracy was calculated as 6.92 meters.

3. Methodology

In this study, we thoroughly examined both dependent and independent sensor models and then compared the results of different models. In addition, we also employed a physical model known as the Toutin Model. All processing, analysis and accuracy assessment procedures were performed with the PCI Geomatica software. A flowchart of the process chain is provided in Figure 3.

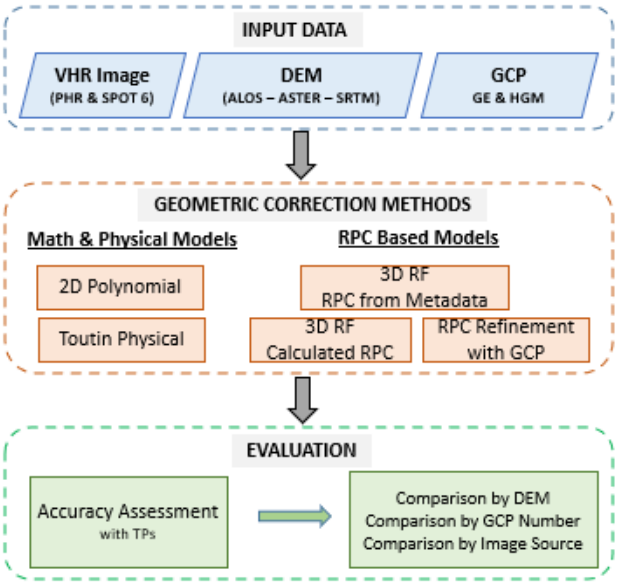

Figure 3. Methodological flowchart

3.1. 2D Polynomial Model

Polynomial models are used to transform between coordinate systems. The basic working principle of the 2-dimensional polynomial model is to establish a mathematical relationship between the pixel coordinates of the ground control points and the known ground coordinates. The degree of polynomial function may vary depending on the field conditions, the number of GCPs, and the targeted accuracy. Although a more accurate polynomial model is formed as the degree of polynomial increases, higher-order polynomials can create large distortions in parts of the image that do not have GCP [22]. In this study, 2nd order polynomial transformation is used.

Since surface topography variations are not considered in the 2-dimensional polynomial model, it is more appropriate to use it in flatlands where the height factor does not have a significant effect. The basic transformation function can be represented as Eq. 1 [13,23].

$$P_{2D}(XY) = \sum_{i=0}^{m}\sum_{j=0}^{n} a_{ij} X^i Y^j \qquad (1)$$

3.2 3D Rational Functional Model with Calculated RPCs

The Rational Function Model (RFM) is a mathematical model that correlates the pixels in the satellite image and their actual positions on the earth. Since the RFM uses height information of GCPs obtained from the DEM data used, it offers higher accuracy than polynomial models [24]. The x and y parameters are calculated by proportioning the two polynomial functions. The most significant advancement for RFM is working as a sensor-independent model by generating the RPC (Rational Polynomial Coefficient) from GCPs, which now include height information using DEM. The RFM structure is provided in Eq. 2 [13,23].

$$R_{3D}(XYZ) = \frac{\sum_{i=0}^{m}\sum_{j=0}^{n}\sum_{p=0}^{k} a_{ijk} X^i Y^j Z^k}{\sum_{i=0}^{m}\sum_{j=0}^{n}\sum_{p=0}^{k} a_{ijk} X^i Y^j Z^k} \qquad (2)$$

3.3. 3D Rational Functional Model with RPCs From Satellite

In addition to RPCs calculated from GCPs, RPCs provided by satellite companies to users within metadata can be used in the RFM model implementation [25]. These RPC files usually contain 20 numerator and denominator polynomial coefficients for the direct and inverse rational functional model. Although RPCs can be produced in different ways, they are mostly produced by the non-linear least square method to derive mathematical models that reflect the acquisition geometry.

3.4. RPC Refinement Model Using GCPs

After the RPC based geometric correction, the results could contain biases and random errors due to topography and sensor characteristics. To improve the results of the RPC model and eliminate the biases and random errors, a refinement function can be used together with GCPs [26]. The refinement functions are defined as:

$$Line_i^{(j)} = \Delta p^{(j)} + p^{(j)}(\Phi_k, \lambda_k, h_k) + \varepsilon_{Li} \qquad (3)$$

$$Sample_i^{(j)} = \Delta r^{(j)} + r^{(j)}(\Phi_k, \lambda_k, h_k) + \varepsilon_{Si} \qquad (4)$$

Image coordinates of GCPs are represented with $Line_i^{(j)}$ and $Sample_i^{(j)}$. The difference of the coordinates is calculated using the RPC based and reference coordinates and $\Delta p^{(j)}$ and $\Delta r^{(j)}$ are the functions of these differences. Coefficients obtained from the metadata file are used to generate the rational functions, $p^{(j)}(\Phi_k, \lambda_k, h_k)$ and $r^{(j)}(\Phi_k, \lambda_k, h_k)$.

The adjustment parameters are a_0, aS, aL, b_0, bL, bS, … terms in these equations.

Difference functions can be shown as:

$$\Delta p = a_0 + aS \,.\, Sample + aL \,.\, Line + aSL \,.\, Sample \,.\, Line + aL2 \,.\, Line^2 + aS2 \,.\, Sample^2 + \ldots \qquad (5)$$

$$\Delta r = b_0 + bS \,.\, Sample + bL \,.\, Line + bSL \,.\, Sample \,.\, Line + bL2 \,.\, Line^2 + bS2 \,.\, Sample^2 + \ldots \qquad (6)$$

3.5. Toutin's Model

The Toutin model is a physical model, in which the physical sensor parameters can be considered to generate collinearity equations that describe the relationship between 2D images and 3D objects. Toutin's model is one of these physical models to eliminate some errors caused by the physical parameters of the sensor. Even if the physical parameters are integrated, some distortions remain, such as inaccuracies in platform velocity and orientation, Earth curvature, integration time of the signal, and cartographic projection [27]. Image coordinates can be calculated by the equations below:

$$Pp + y(1 + \delta\gamma X) - \tau H - H_0 \Delta T^* = 0 \quad (7)$$

$$X + \theta H/\cos X + \alpha q(Q + \theta X - H/\cos X) - Q\Delta R = 0 \quad (8)$$

$$X = (x - ay)(1 + h/N_0) + by^2 + cxy \quad (9)$$

$$H = h - X^2/2N_0 \quad (10)$$

In the along-track and across-track directions, P and Q are the scale factors; correspondingly, p and q are the image coordinates, $\delta\gamma$, b, c and X are second-order variables, τ and θ are leveling angle functions in along-track and across-track directions, α is the field of view in real-time, x, y and h are ground coordinates, a is a function derived from a situation of non-perpendicularity in the axes, and finally N_0 is the distance of the normal to the ellipsoid.

3. Results

During the model testing, the use of various DEMs and GCP resources enabled us to investigate the effects of the DEM and GCP resources, and perform a comparative evaluation of the models. In addition, the models were applied using different numbers of GCPs, and the effect of the GCP number on the results was also examined. Except for the 2D Polynomial Model, which does not use a DEM as an input, 3 DEMs were integrated into each model. As the GCP resource, two datasets were used: Google Earth (GE) and the General Directorate of Mapping - Globe (HGM). In each GCP set, GCPs were selected homogeneously on the terrain. For accuracy assessment, 20 test points that were collected from the HGM Globe were used and kept constant for all models to ensure a fair comparison among different models.

4.1. Results of 2D Polynomial Model

The 2D polynomial models do not require elevation information. Thus, the effects of GCPs quantity and source of GCPs were tested by applying the model on PHR and SPOT images. To analyze the effects of GCP amount, we conducted geometric corrections with 20, 30, and 40 GCPs sets from each source (Table 1).

According to the RMSE results, the best results were obtained using 30 GCPs obtained from the HGM source for PHR and SPOT images. The RMSE values ranged between 9.2 to 10.5 meters for all GCP combinations from HGM, which were slightly better than the GCP combinations from GE. In all cases, total RMSE values are around 10m, and error values along X directions are higher than in Y direction in the 2D polynomial model

Table 1. RMSE table of the 2D polynomial model with different numbers of GCPs from GE and HGM. (Error values are in meters)

		GE		HGM	
		PHR	SPOT	PHR	SPOT
20 GCP	X	10.37	9.76	10.27	9.82
	Y	3.27	4.14	1.68	2.18
	Total	10.87	10.60	**10.40**	**10.06**
30 GCP	X	9.31	9.15	9.22	9.03
	Y	3.83	4.72	1.78	1.88
	Total	10.07	10.29	**9.39**	**9.22**
40 GCP	X	9.73	10.27	9.62	10.27
	Y	3.61	4.84	1.66	2.06
	Total	10.37	11.35	**9.76**	**10.47**

4.2. Results of 3D Rational Function Model with Calculated RPCs

In the 3D RFM model with calculated RPCs, the RPC coefficients were calculated with the use of GCPs but not RPC files provided with images. 3 DEMs were used to provide elevation information to GCPs and CPs. For this testing 40 GCPs - 20 coefficients, 30 GCPs-15 coefficients, and 20 GCPs - 10 coefficients setups were examined.

According to results for the SPOT image, the lowest RMSE values are obtained with ALOS DEM and HGM derived GCPs in all experiments. An increasing number of GCPs from 20 to 30 improved the results; whereas results are very similar to each other for 30 GCP and 40 GCP combinations (Table 2). Therefore, the usage of 30 GCPs would be a reasonable choice to minimize efforts. Integration of DEM and 3D RFM model provide similar error values along X and Y direction, which was not the case in 2D polynomials. Considering that GE is openly available and results of GE-based GCPs provided approximately 8m RMSE, GE might be a good alternative for those locations where other GCP sources are not available.

Table 2. RMSE table of RFM model of SPOT image with different DEMs and number of GCPs from GE and HGM. (Error values are in meters)

		SPOT - RFM - GE			SPOT - RFM - HGM		
		SRTM	ALOS	ASTER	SRTM	ALOS	ASTER
20 GCP	X	6.96	4.55	8.76	6.39	4.56	7.55
	Y	5.41	5.51	5.77	3.37	3.29	2.91
	Total	8.81	**7.15**	10.49	7.23	**5.62**	8.09
30 GCP	X	4.92	3.80	5.68	4.81	4.00	4.96
	Y	5.44	5.36	5.52	2.29	2.45	2.27
	Total	7.34	**6.57**	7.92	5.33	**4.69**	5.46
40 GCP	X	4.87	4.02	5.18	4.62	3.85	4.84
	Y	5.45	5.39	5.45	2.78	2.84	2.78
	Total	7.31	**6.72**	7.52	5.39	**4.78**	5.58

When the PHR results were examined in the tests of this model, it was observed that the accuracy was lower than the SPOT image, and the combination of HGM - 40

GCP - 20 RPC had large distortions in the model and increased RMSE values (Table 3). Less number of GCPs seems to be a better solution for the PHR case.

Table 3. RMSE table of RFM model of PHR image with different DEMs and number of GCPs from GE and HGM. (Error values are in meters)

		PHR - RFM - GE			PHR - RFM - HGM		
		SRTM	ALOS	ASTER	SRTM	ALOS	ASTER
20 GCP	X	2.20	2.12	2.97	4.47	5.49	4.35
	Y	7.70	8.30	7.53	3.95	5.72	3.92
	Total	**8.00**	8.57	8.09	5.96	7.93	**5.86**
30 GCP	X	3.16	3.18	4.11	5.75	5.72	6.64
	Y	6.87	7.32	7.54	7.08	8.98	7.89
	Total	**7.56**	7.98	8.59	**9.12**	10.65	10.31
40 GCP	X	5.41	3.51	11.04	19.24	7.89	22.85
	Y	5.93	6.38	8.56	9.83	11.79	23.02
	Total	8.02	**7.28**	13.97	21.61	**14.18**	32.43

4.3. Results of 3D Rational Functional Model with RPCs From Satellite

RFM model with original RPCs was applied to compare calculated RPCs and original RPCs results. 20 coefficients which were taken from SPOT and PHR imageries' RPC files were used and accuracy was tested via RMSE of 20 constant CPs. GCPs were not used in this model.

According to the results obtained by applying the 3D RFM model with the original RPC coefficients coming from the sensor, the DEM from the ALOS source gave more successful results in both images. The lowest RMSE in this model was obtained with the ALOS - PHR combination and is 2.38 meters (Table 3).

The RMSE values illustrate that RPC coefficients provided by Airbus are quite reliable and highly accurate ortho-rectified images could be generated by using RPCs without the need of GCPs.

Table 4. RMSE table of RFM model with original RPCs. (Error values are in meters)

	RFM with Original RPCs								
	ALOS			ASTER			SRTM		
(m)	X	Y	Total	X	Y	Total	X	Y	Total
PHR	1.60	1.77	**2.38**	2.17	1.78	**2.81**	1.71	1.74	**2.44**
SPOT	4.38	1.84	4.75	4.87	1.81	5.19	4.58	1.80	4.92

4.4. Results of RPC Refinement Model Using GCPs

The goal of the RPC refinement model was to evaluate how much the accuracy of the original RPCs from the satellite could be improved. For this purpose, 8 GCPs from 2 different sources were used for this improvement.

According to the application of the RPC Refinement model for SPOT image, 2nd degree was more successful when GE originated points were used, and 0^{th} degree when HGM originated points were used. The lowest RMSE in this image is obtained from the combination of HGM - ASTER with 4.06 meters (Table 5).

Table 5. RMSE table of RPC Refinement model of SPOT image with GCPs from Google Earth. with different DEMs and GCPs from GE and HGM. (Error values are in meters)

		SPOT - RPC REFINEMENT - GE			SPOT - RPC REFINEMENT - HGM		
		Adj Ord - 0	Adj Ord - 1	Adj Ord - 2	Adj Ord - 0	Adj Ord - 1	Adj Ord - 2
ALOS	X	3.62	3.63	3.62	3.67	3.78	3.84
	Y	5.01	5.07	4.33	1.90	2.06	2.08
	Total	6.18	6.24	5.64	4.13	4.30	4.36
ASTER	X	3.58	3.62	3.57	3.58	3.75	3.78
	Y	4.98	5.04	4.29	1.91	2.07	2.07
	Total	6.13	6.20	5.58	4.06	4.28	4.31
SRTM	X	4.07	4.09	4.14	4.11	4.14	4.23
	Y	5.02	5.08	4.33	1.85	1.99	2.00
	Total	6.46	6.52	5.99	4.50	4.60	4.67

Table 6. RMSE table of RPC Refinement model of PHR image with GCPs from Google Earth. with different DEMs and GCPs from GE and HGM. (Error values are in meters**)**

		PHR - RPC REFINEMENT - GE			PHR - RPC REFINEMENT - HGM		
		Adj Ord - 0	Adj Ord - 1	Adj Ord - 2	Adj Ord - 0	Adj Ord - 1	Adj Ord - 2
ALOS	X	1.60	1.71	1.69	1.80	1.80	1.80
	Y	2.02	2.03	2.15	1.31	1.44	1.47
	Total	2.58	2.65	2.73	2.23	2.30	2.32
ASTER	X	2.15	2.25	2.24	2.05	2.12	2.10
	Y	1.97	2.01	2.14	1.30	1.42	1.45
	Total	2.91	3.02	3.10	2.43	2.55	2.55
SRTM	X	1.77	1.88	1.89	1.59	1.59	1.63
	Y	1.98	2.00	2.13	1.34	1.45	1.47
	Total	2.66	2.75	2.85	2.08	2.15	2.20

The best results for the PHR image were observed with Adjustment Order - 0. Among all combinations, the lowest RMSE was obtained with the combination of SRTM DEM, and HGM based GCPs as 2.08 meters (Table 6).

4.5. Results of Toutin's Model

Toutin's Model was performed on two images using 8 GCPs from two different sources. While applying this model, three different DEMs were used to obtain elevations of GCPs. Thus, three different parameters were tested: terrain characteristics, effects of GCP sources and effects of DEM sources. It is also aimed to examine the differences between empirical and physical models in this step.

As a result of applying the Toutin Model, which is the only physical model in this study, the best results for the PHR image were obtained by using ALOS DEM. For the SPOT image, ASTER DEM provided slightly better results. One highlight here is that the PHR-ALOS and SPOT-ASTER combinations gave the highest accuracy in both GCP sources. The best result in this model was obtained at 3.21 meters with the combination of PHR - ALOS DEM and GE-based GCPs.

Table 7. RMSE table of Toutin's model with GCPs from GE and HGM. (Error values are in meters)

		TOUTIN - GE		TOUTIN - HGM	
		PHR	SPOT	PHR	SPOT
ALOS	X	1.76	3.27	1.94	3.88
	Y	2.69	3.86	2.92	2.14
	Total	**3.21**	5.06	**3.51**	4.43
ASTER	X	2.28	3.18	2.36	3.71
	Y	2.72	3.89	2.99	2.15
	Total	**3.55**	5.02	**3.80**	4.29
SRTM	X	2.11	3.74	2.07	4.20
	Y	2.71	3.91	2.91	2.12
	Total	**3.43**	5.41	**3.57**	4.71

4. Discussion

According to the accuracy assessment results, the best results were obtained with RFM modeling, which used RPC from the data provider for both PHR and SPOT images. The GCPs derived from the HGM source provided lower RMSE values when compared to GCPs from GE. The analysis with different numbers of GCPs provided that increasing the number from 20 to 30 provided improvement in accuracy; however, further increment to 40 GCPs did not help improvement, and even lowered the performance in some experiment setups. In terms of DEM data contribution, in most of the experiments, better results were obtained using ALOS DEM. The experiments on the PHR image provided lower RMSE values except for the RFM modeling with calculated RPCs, where a significant bias is observed in the Y direction. Toutin physical model and RFM modeling with RPCs from the data provider were found to be the most stable geometric correction methods considering various DEMs and GCP sources. Toutin model provided very close results for different DEMs for both GCP data sources. This showed the fidelity of the physical model even with different cases in which different accuracy DEMs and GCPs were used. It can be inferred that, Toutin model could be reliably applied to different regions by using open-source DEMs and GE GCPs. Moreover, in case of not having reliable RPC files from the data provider, Toutin physical model will be a good alternative for the geometric correction.

5. Conclusion

Extracting accurate and reliable locational information from satellite images require efficient geometric correction procedure. In this study, we comparatively evaluated five different geometric correction methods with various experimental designs including different GCP sources and numbers, multi-source DEMs over the Pleiades and SPOT 6 satellite images with different spatial resolutions. Lower RMSE values were obtained with the model that uses RPC from data providers for PHR and SPOT, followed by the RPC refinement method for PHR and the Toutin method for SPOT. GCPs from the HGM data source and the ALOS DEM combination produced better results in general. Finally, with the exception of one test, the PHR image has lower RMSE values and thus better locational accuracies. Toutin model is a good solution for geometrically correcting the satellite images without RPC files.

Acknowledgement

Authors acknowledge the support of ITU-CSCRS for providing Pleiades and Spot 6 satellite images.

Author contributions

Buğrahan Özcihan: Methodology, Analysis, Writing-Original draft preparation **Levent Doğukan Özlü:** Methodology, Analysis, Writing-Original draft preparation **Mümin İlker Karakap:** Methodology, Analysis, Writing-Original draft preparation **Halime Sürmeli:** Methodology, Analysis, Writing-Original draft preparation **Ugur Alganci:** Methodology, Visualization, Investigation, Writing-Reviewing and Editing **Elif Sertel:** Supervision, Methodology, Visualization, Writing-Reviewing and Editing

Conflicts of interest

The authors declare no conflicts of interest.

References

1. Bai, X., Zhang, H., & Zhou, J. (2014). VHR object detection based on structural feature extraction and query expansion. IEEE Transactions on Geoscience and Remote Sensing, 52, 6508–6520.
2. Joshi, N., Baumann, M., Ehammer, A., Fensholt, R., Grogan, K., Hostert, P., Jepsen, M.R., Kuemmerle, T., Meyfroidt, P., Mitchard, E.T.A., Reiche, J., Ryan, C.M., & Waske, B. (2016). A review of the application of

optical and radar remote sensing data fusion to land use mapping and monitoring, Remote Sensing, 8(1), 70.
3. Göksel, Ç. & Bozkaya Karip, G. (2017). İğneada Koruma Alanının Arazi Örtüsü/Arazi Kullanımının Zamana Bağlı Değişiminin Markov Zincirleri İle Modellenmesi. Geomatik, 2 (2), 94-105.
4. Durkut, Z., Algancı, U. & Sertel, E. (2020). Uydu Görüntüsü İşleme ve Sıkıştırma Süreçlerinin WEB Tabanlı Harita Servisi Yayın Performansına Etkilerinin Araştırılması. Geomatik, 5 (3), 186-192.
5. Zabcı, C. (2021). Çok bantlı Landsat 8-OLI ve Sentinel-2A MSI uydu görüntülerinin karşılaştırmalı jeoloji uygulaması: Örnek çalışma alanı olarak Doğu Anadolu Fayı boyunca Palu – Hazar Gölü bölgesi (Elazığ, Türkiye). Geomatik, 6 (3), 238-246.
6. Karagianni, A. (2022). Road extraction through digital processing and visual interpretation of satellite images. International Journal of Engineering and Geosciences, 7 (3), 264-271.
7. Guha, S. & Govil, H. (2022). Estimating the seasonal relationship between land surface temperature and normalized difference bareness index using Landsat data series. International Journal of Engineering and Geosciences, 7 (1), 9-16.
8. Paul, S. (2022). Change detection and future change prediction in Habra I and II block using remote sensing and GIS – A case study. International Journal of Engineering and Geosciences, 7 (2), 191-207.
9. Saroğlu, E. (2004). Farklı çözünürlükteki uydu görüntülerinin geometrik dönüşümü ve dönüşüm sonucunda elde edilen görüntülerin dış doğruluğunun araştırılması (Master of Science dissertation, Fen Bilimleri Enstitüsü).
10. Sertel, E., Kutoglu, S. H., & Kaya, S. (2007). Geometric correction accuracy of different satellite sensor images: Application of figure condition. International Journal of Remote Sensing, 28, 4685–4692.
11. Kartal, H., Alganci, U., & Sertel, E. (2018). Automated orthorectification of VHR satellite images by SIFT-based RPC refinement. ISPRS International Journal of Geo-Information, 7(6), 229.
12. Toutin, T. (2003). Geometric correction of remotely sensed images. In Remote Sensing of Forest Environments (pp. 143-180). Springer, Boston, MA.
13. Toutin, T. (2004). Geometric processing of remote sensing images: Models, algorithms and methods. International Journal of Remote Sensing, 25, 1893–1924.
14. Alganci, U., Besol, B., & Sertel, E. (2018). Accuracy assessment of different digital surface models. ISPRS International Journal of Geo-Information, 7(3), 114.
15. Zhang, Ying, Zhaohui Chi, Fengming Hui, Teng Li, Xuying Liu, Baogang Zhang, Xiao Cheng, and Zhuoqi Chen. (2021). Accuracy Evaluation on Geolocation of the Chinese First Polar Microsatellite (Ice Pathfinder) Imagery. Remote Sensing, 13(21), 4278.
16. Samadzadegan, F., Milanlak, A., & Majdabadi, M. (2006). Geometrical Correction of Satellite Images by Generic Models. In Proceedings of the ISPRS Commission VII Symposium 'Remote Sensing: From Pixels to Processes', Enschede, Netherlands, (pp. 1-5)
17. Ye, J., Lin, X., & Xu, T. (2017). Mathematical modeling and accuracy testing of worldview-2 level-1B stereo pairs without ground control points. Remote Sensing, 9(7), 737.
18. Son, J.-H., Yoon, W., Kim, T., & Rhee, S. (2021). Iterative Precision Geometric Correction for High-Resolution Satellite Images. Korean Journal of Remote Sensing, 37(3), 431–447.
19. Mezouar, O., Meskine, F., Boukerch, I. & Taleb N (2021). A Hybrid particle swarm optimization of the rational function model for satellite strip images ortho-rectification. International Journal of Remote Sensing, 42(21), 8056-8076.
20. Misra, I., Rohil, M. K., Moorthi, S. M. & Dhar, D. (2022). FIRM: Framework for Image Registration Using Multistage Feature Detection and Mode-Guided Motion Smoothness Keypoint Optimization. IEEE Transactions on Geoscience and Remote Sensing, 60, 1-12.
21. Wang, T., Li, X., Zhang, G., Lin, M., Deng, M., Cui, H., Jiang, B., Wang, Y., Zhu, Y., Wang, H. & Yuan, X. (2022). Large-Scale Orthorectification of GF-3 SAR Images Without Ground Control Points for China's Land Area. IEEE Transactions on Geoscience and Remote Sensing, 60, 1-17, 5221617
22. Shaker, A., Shi, W., & Barakat, H. (2005). Assessment of the rectification accuracy of IKONOS imagery based on two-dimensional models, International Journal of Remote Sensing, 26(4), 719-731
23. PCI Geomatics. (2012). Geomatica Help. PCI Geomatics: Markham, ON, Canada.
24. Tao, V., & Hu, Y. (2001). A Comprehensive Study of the Rational Function Model for Photogrammetric Processing. Photogrammetric Engineering & Remote Sensing, 67(12), 1347 – 1357.
25. Grodecki, J. (2001). Ikonos Stereo Feature Extraction-RPC Approach. Annual Conference of the ASPRS 2001, St. Louis, 23-27 April 2001
26. Hu, Y., Tao, V., Croitoru, A. (2004). Understanding the rational function model: Methods and applications. International Archives of Photogrammetry and Remote Sensing 20, 119–124.
27. Toutin, T. (1995). Generating DEM from stereo-images with a photogrammetric approach: examples with VIR and SAR data. EARSeL Advances in Remote Sensing, 4, 110–117.

International Journal of Engineering and Geosciences
https://dergipark.org.tr/en/pub/ijeg
e-ISSN 2548-0960

Genesis and spatio-temporal analysis of glacial lakes in the peri-glacial environment of Western Himalayas

Fareeha Siddique [*1], **Atta-ur Rahman** [1]

[1]*University of Peshawar, Department of Geography, Peshawar, Pakistan*

Keywords
Glacial Lake
Astore Drainage Basin
Normalized Difference Water Index
Normalized Difference Snow Index
Landsat

Research Article
DOI: 10.26833/ijeg.1097912

Received: 04.04.2022
Accepted: 14.05.2022
Published: 19.10.2022

Abstract

Glaciers are retreating in the highest mountainous regions of the world, like Himalayan region as a result of climate change and global warming. This leads to the formation of different types of glacial lakes. These lakes are not only the source of fresh water but it also causes disaster in the form of Glacial Lake Outburst Flood (GLOF). Astore Drainage Basin is located in north eastern mountainous region of Himalayas. This area is prone to GLOFs because of the increasing number of glacial lakes and the growth of existing lakes as a result of global warming. To provide a detailed information about the spatial and temporal information of glacial lakes detailed inventories has been developed for the study area using Landsat images for the year 1989, 1999, 2009 and 2019. Glacial lakes were mapped and identified by using Normalized Different Water Index, Normalized Difference Snow Index and high-resolution Google Earth images. It was found from the analysis that the number of the glacial lakes increased from 120 to 128 in a period of thirty years (i.e., from 1989 to 2019). During the study period two lakes disappeared whereas ten new lakes were formed. There were 21 lakes which show area expansion more than 100% representing high susceptibility for GLOF. The results also showed that smaller lakes expanded more rapidly in area than the larger lakes.

1. Introduction

Glaciers store a massive volume of water in the form of ice. Glaciers form naturally as a result of the interaction between relief and climate and are majorly formed from solid precipitation [1]. These are an important renewable source of fresh water and supply water for many purposes; drinking, irrigation, agriculture, industrial and hydropower development. Meltwater from glacier is not only the part of hydrological processes but also responsible for the global sea level rise [2]. About 1/6th of the world population is dependent directly on the water coming from these glaciers [3].

There are several glaciated mountainous places in the globe, but the Himalayan and Karakoram regions, after the Polar Region, are the most glaciated [4]. This region is known as the "Third Pole" because it contains the largest concentration of glaciers and snow after the Polar Regions [5], and it covers an area of 40,800 km^2 [4]. The Hindukush-Himalayan (HKH) area has around 54,252 glaciers with total ice reserves of 6,127 km^3. These glaciers and snow provide water to the region's major rivers [6]. This mountainous terrain is extremely vulnerable to global warming and climate change, and the stability of the glacier is determined by slope, aspect, elevation, and the geomorphology of the surrounding area [7].

Global warming patterns are causing glaciers to retreat [8-9]. As a result, several glacial lakes form in, around, and under the glacier [10-11]. According to previous research, glaciers with low flow velocity or those that are stationary and have a low surface slope angle are more vulnerable to lake formation [12]. Glacial lakes are the lakes “which form as a result of glacier retreat or which are primarily supplied by glacier meltwater” [13]. Glacial lakes are common in high mountain ranges across the world [14]; in the Rockies and Coastal Mountains of Alaska, of North America [15], in the Andes of South America [16], in the Alps and Caucasus of Europe [17-18] and in the Karakoram, Himalayas and Tien-Shan mountains of Asia [19-21].

* **Corresponding Author**

*(fareehasiddique47@gmail.com) ORCID ID 0000-0002-9773-008X
(atta-ur-rehman@uop.edu.pk) ORCID ID 0000-0002-5932-2288

Cite this article

Siddique, F., & Rahman, A. (2023). Genesis and spatio-temporal analysis of glacial lakes in the peri-glacial environment of Western Himalayas. International Journal of Engineering and Geosciences, 8(2), 154-164

Glacial lakes are considered as the indirect indicators of glacier changes, as most the lake formed and the existing lakes increases in size as a result of glacial melting [2]. These lakes provide fresh water and have drawn a significant number of people to the hilly areas for a variety of activities [20]. The majority of the lakes are unstable and located in remote, inaccessible places. Glacial Lake Outburst Flood (GLOF) is a catastrophic outpouring of water from these lakes that affects the living population and damages natural and man-made infrastructure downstream [22].

Glacial lakes are found in northern Pakistan's high mountain ranges. In the Hindu Kush Himalayas (HKH) area of the country, there are currently around 2,600 glacial lakes [23]. According to the inventory, developed by International Centre for Integrated Mountain Development (ICIMOD), 2,500 glacial lakes were identified in ten river basins of Pakistan's HKH region in 2005 [24]. Nonetheless, it was estimated to be 2,420 in 2010, with 52 of them being deemed potentially hazardous. Cirque type accounts for 25% of these lakes, while End Moraine Dammed accounts for 62% [25]. The Indus, Astore, and Gilgit River Basins form the bulk of these lakes. This study aims to conduct Spatio-temporal distribution of glacial lakes for the period of thirty years (from 1989 to 2019) in Astore Drainage Basin by using remotely sensed data through geospatial techniques. The findings of the proposed study will provide baseline information for future research.

2. Study area

The Astore Drainage Basin is situated in the Himalayan northwestern mountain ranges (Fig 1). The study area spans between 34º 46' 31" to 35º 38' 38" North latitude and 74º 24' 12" to 75º 14' 52" East longitude. The Astore Drainage Basin is bordered on the north by Gilgit district (Pakistan), on the south by Neelum valley (Pakistan), on the east by Skardu district (Pakistan), and on the west by Diamir (Pakistan). It covers a total area of 3,988.7 km^2. The basin's elevation varies between 1,237m and 8,105m above sea level. Astore, Rama, and Rattu are the three meteorological stations, while Doyian is the only hydrometric station. There are 372 glaciers in the study area, occupying a total area of 239.59 km^2. The Astore Sub-basin has the lowest ice reserves in the Upper Indus Basin (UIB), with just 16.88 km^3 of ice [22]. In the winter, this area gets heavy precipitation, and most of the peaks are snow-covered all year [26-27].

Topographically, the ground surface is uneven. The Astore Drainage Basin is flanked on all sides by mountains. The basin is wider at the bottom (South) and narrower at the top (North). The basin's mountains span from south to north, with abrupt elevation variations. The southern side has a higher elevation than the northern side.

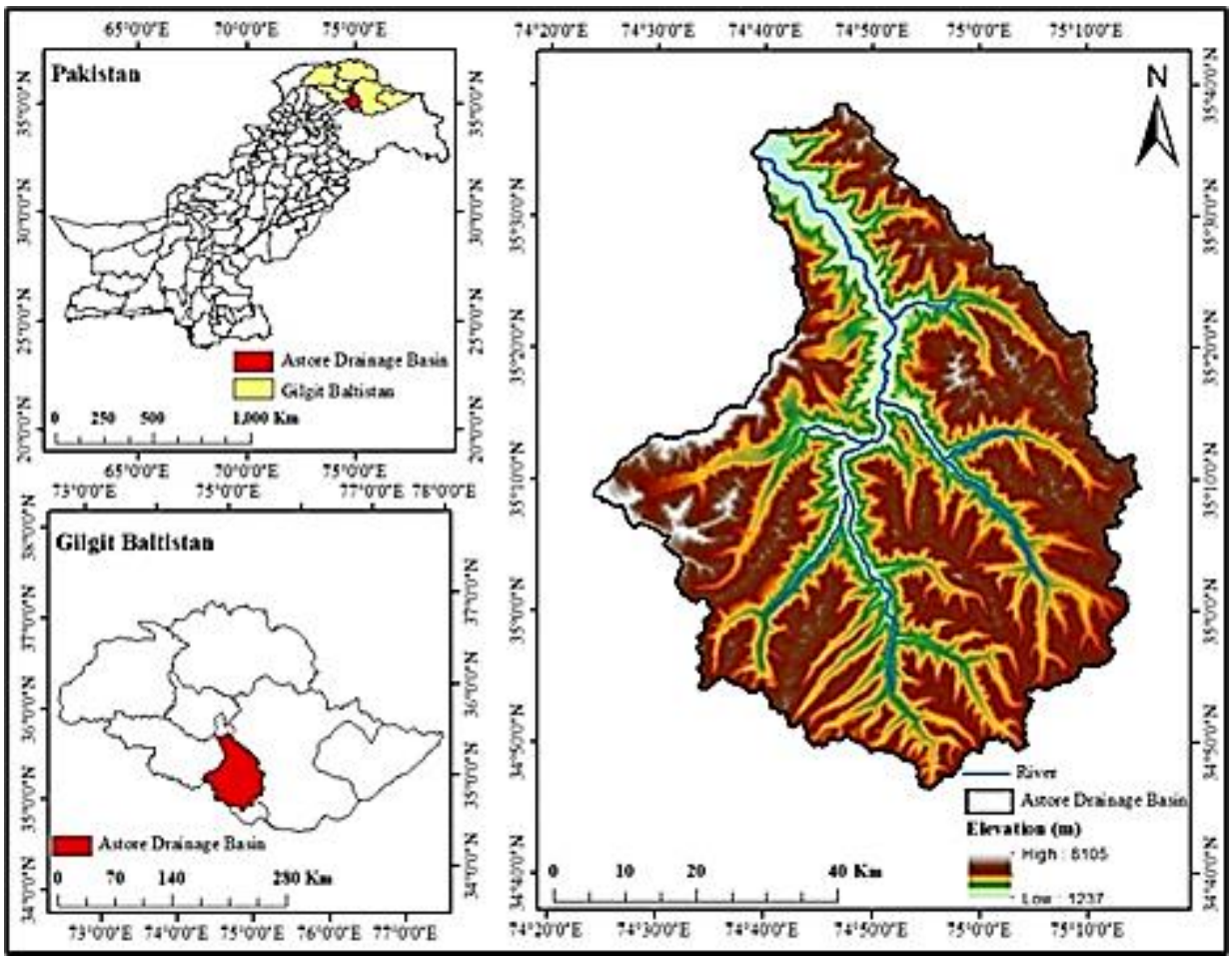

Figure 1. Location of Astore Drainage Basin, North Pakistan

3. Materials and methods

This section consists of the methods used for collection of data and mapping of the glacial lakes.

3.1. Collection of data and mapping of glacial lakes

Landsat satellite images with a spatial resolution of 30m and some with a resolution of 15m (panchromatic) were utilized in this work to create glacial lake inventories in the Astore Drainage Basin for the observation years 1989, 1999, 2009, and 2019. In ArcGIS, the Normalized Difference Water Index (NDWI) [28-30] and the Normalized Difference Snow Index (NDSI) were used to identify glacial lakes, as shown in Equations 1 and 2, respectively [31-32].

$$NDWI = \frac{GREEN - NIR}{GREEN + NIR} \quad (1)$$

$$NDSI = \frac{GREEN - SWIR}{GREEN + SWIR} \quad (2)$$

NDWI stands for Normalized Difference Water Index, and NDSI stands for Normalized Difference Snow Index, with GREEN representing the green band, NIR representing Near Infra-Red, and SWIR representing Short Wave Infra-Red. The NDWI scale runs from +1.00 to -1.00, with higher values representing water bodies and lower values representing non-water bodies. NDSI values also vary between +1.00 and -1.00, with all positive values indicating that snow is present.

High quality Google Earth pictures and the Hill Shading method were used to remove misclassified lakes and verifies lake location. The Google Earth images for various parts of the study area are available from 1984 to 2019. According to [22], glacial activity is responsible for the formation of all lakes over 3,500m. As a result, all glacial lakes over 3,500m were digitized and mapped in order to map the glacier lake. The lakes were designated from top to bottom of the basin for convenience, with identification numbers ranging from Astore-GL01 to Astore-GL130. Lakes that are not visible in the photos are not included in the inventories. All of these lakes were then classified based on the following characteristics:

i. ***Identity Number:*** To ensure uniformity, identity numbers ranging from Astore-GL01 to Astore-GL130 were allocated to each lake.
ii. ***Coordinates:*** The approximate center of the glacial lake was given World Geodetic System 1984 coordinates (Longitude and Latitude) by producing a point map.
iii. ***Area:*** The vector glacial lake layer was utilized to automatically compute the area of each lake using the raster calculator in ArcMap 10.5.
iv. ***Elevation:*** The elevation (in meters) above sea level for the lakes was obtained using the DEM.
v. ***Lake Type:*** Glacier lakes were categorized into two groups based on their hydrologic link to their mother glaciers: glacier-fed lakes and non-glacier-fed lakes.
vi. ***Volume and Depth:*** The volume and depth of each lake in this study were determined using the following formulae (Equations 3 & 4) devised by [31] to estimate the depth and volume of glacial lakes in the Swiss Alps:

$$V = 0.104A^{1.42} \quad (3)$$

$$D = 0.104A^{0.42} \quad (4)$$

Where V is the volume (m^3), D is the depth (m) and A represents area (m^2) of the lake.

Without comprehensive knowledge about an area's topography, lake water volume cannot be computed directly from remotely sensed data or any other data source [33]. It is important to note that the volume and depth obtained using the above methods are simply estimates because they are dependent on a number of other parameters.

Glacial lakes are divided into two kinds in current inventories. They are classified as glacier-fed lakes or non-glacier-fed lakes based on whether they are in direct touch with the parent glacier and get glacial meltwater or not [34]. To do this, the Shuttle Radar Topography Mission Digital Elevation Model (SRTM DEM) was employed in ArcGIS to outline the watershed for each lake. If glaciers lie within a lake's watershed, it signifies that the lake receives meltwater from the glacier, and so the lake is termed glacier-fed, and vice versa.

4. Results and Discussions

This section deals with the analysis, results and discussions. Section one explains glacial lake inventories for the year 1989, 1999, 2009 and 2019 whereas, section two elucidates Spatio-temporal distribution of glacial lakes.

4.1. Glacial Lake Inventories

4.1.1. Glacial Lake Inventory 1989

Based on Landsat imagery, there were 120 glacial lakes in the Astore Drainage Basin in 1989, covering a total area of 4.75 km^2. According to the classification, there were 54 glacier-fed lakes and 66 non-glacial-fed lakes with a total area of 2.227 km^2 and 2.523 km^2 respectively (Fig. 2). The lakes ranged in size from 0.0009 km^2 and 0.468 km^2. There were 31 lakes with an area of less than 0.01 km^2 and others with an area of more than 0.01 km^2. Only three lakes (two non-glacial-fed and one Glacial-fed) had an area greater than 0.02 km^2, and only one (Astore-GL108) had an area greater than 0.4 km^2.

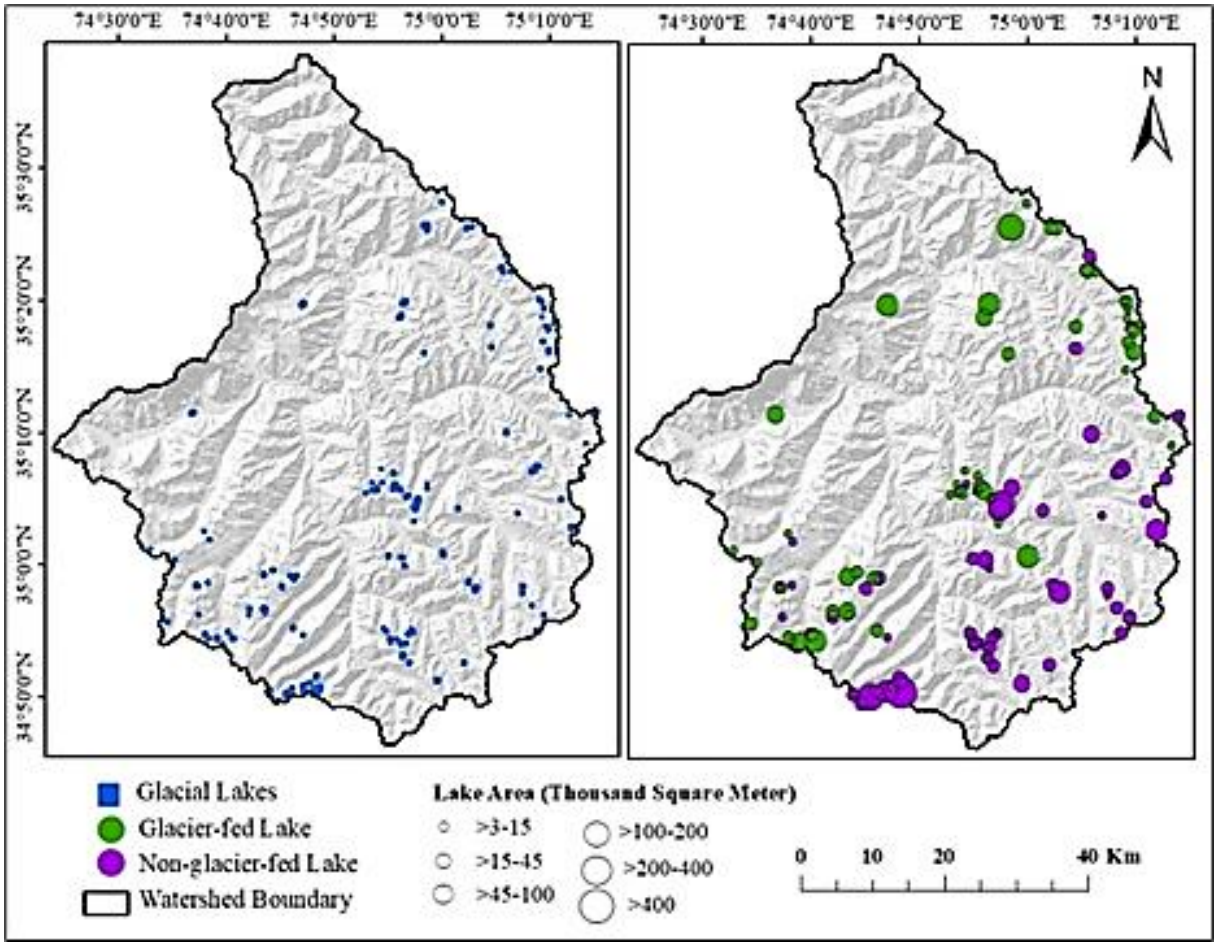

Figure 2. Astore Drainage Basin, 1989 (a) Distribution of glacial lakes (b) Lake types and area

4.1.2. Glacial Lake Inventory 1999

According to a 1999 inventory, the study area had 126 glacial lakes, with 59 Glacial-fed and 67 non-glacial-fed lakes (Fig 3). Glacial lakes occupied a total area of 5.457 km^2. Non-glacial-fed lakes occupied 58.18 percent (3.175 km^2) of the total glacial lakes area, while Glacial-fed lakes accounted for 41.82 percent (2.282 km^2). The lakes' surface area ranged from 0.0035 km^2 to 0.520 km^2 while their volume ranged from 1,545.55 m^3 to 223,821.3 m^3. There were 23 lakes with an area of less than 0.01 km^2 (18.25%). Just two lakes, both non-glacial-fed, had an area greater than 0.2 km^2. The only lake with a surface area greater than 0.5 km^2 was Astore-GL108. The lakes' elevations ranged from 3,501m to 4,949m above mean sea level (M.S.L), with an average of 4,354.95m. There were 41 lakes above 4,500m (M.S.L) with a maximum number of Glacial-fed lakes. The depth of the lakes varied from 3.20m to 26.17m.

4.1.3. Glacial Lake Inventory 2009

In 2009, remotely sensed data revealed 127 glacial lakes with a total area of 5.576 km^2 in Astore Drainage Basin. These include 67 non-glacial-fed lakes and 60 Glacial-fed lakes occupied an area of 3.298 km^2 and 2.278 km^2, respectively, accounting for 0.082 percent and 0.057 percent of the basin's total area (Fig 4). The lakes ranged in size from 0.0036 km^2 to 0.521 km^2, with volumes ranging from 1,548.9 m^3 to 224,208.2 m^3. Only 23 (18.11%) of the lakes were smaller than 0.01 km^2, covering a total area of 0.18 km^2. Three lakes (two non-glacial-fed and one Glacial-fed) had an area greater than 0.2 km^2, with only one (Astore-GL108) exceeding 0.5 km^2.

4.1.4. Glacial Lake Inventory 2019

There were 128 glacial lakes in the study area according to a 2019 inventory. These lakes occupied 5.861 km^2 of area, accounting for 0.147 percent of the Astore Drainage Basin's total area. There were 61 Glacier-fed lakes with the remaining lakes listed as non-glacial-fed (Fig 5). The lakes ranged in size from 0.0036 km^2 to 0.54 km^2. Only three lakes had an area greater than 0.02 km^2 and 19 (14.84 percent) had an area less than 0.01 km^2. Astore-GL108 was the basin's largest lake with a surface area of 0.5400 km^2. Non-glacial-fed lakes occupied 3.370 km^2 area which was 0.88 km^2 more than the area occupied by Glacial-fed lakes. The lakes' volumes ranged from 1,548.9 m^3 to 232,340.79 m^3. Glacial lakes were located at elevations ranging from 3,501m to 4,947m above mean sea level with an average altitude of 4,358.09m. Above 4,500m above M.S.L, there were 42 lakes, the majority of which belonged to the Glacial-fed group of glacial lakes. According to the 2019 inventory, the depth of the glacial lakes varied from 3.24m to 26.59m.

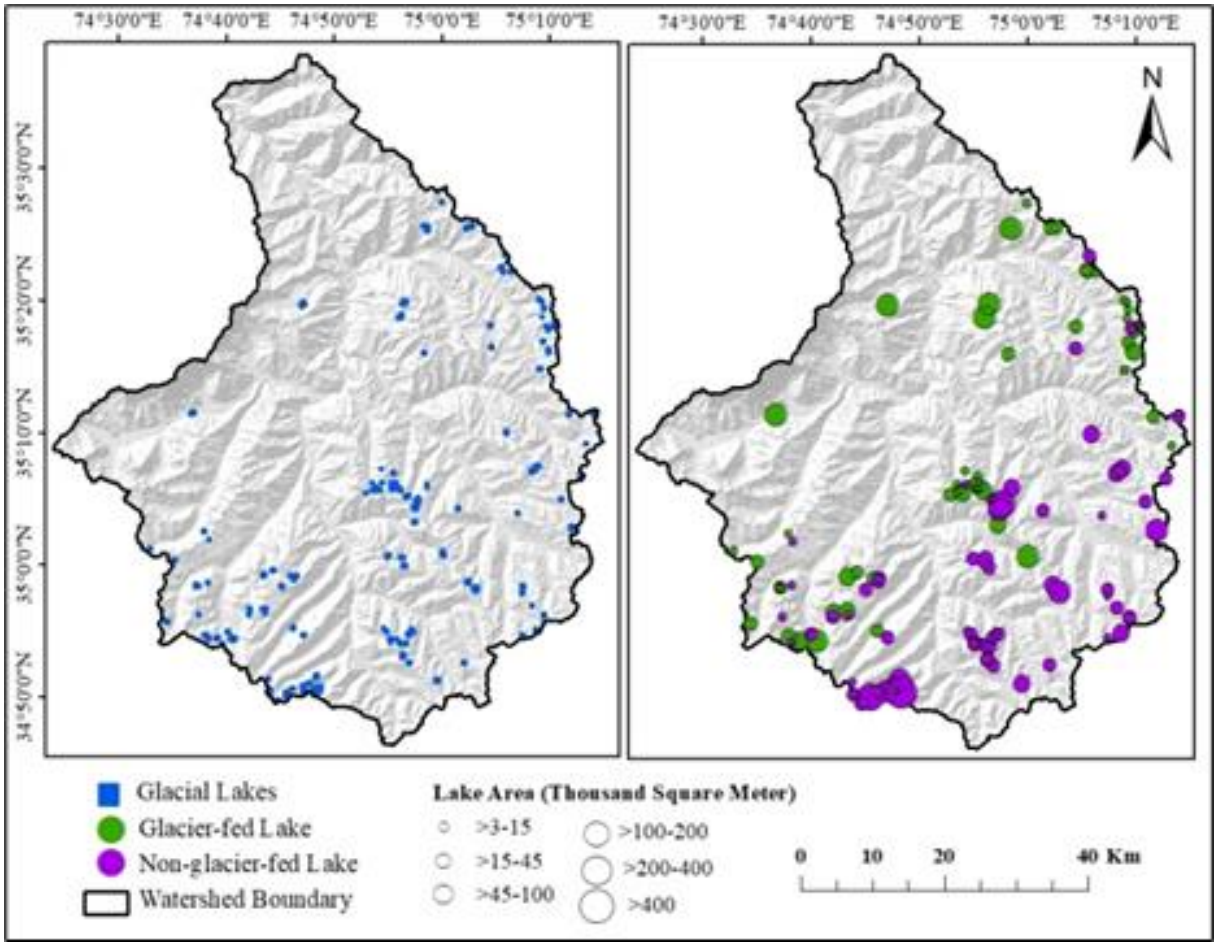

Figure 3. Astore Drainage Basin, 1999 (a) Distribution of glacial lakes (b) Lake types and area

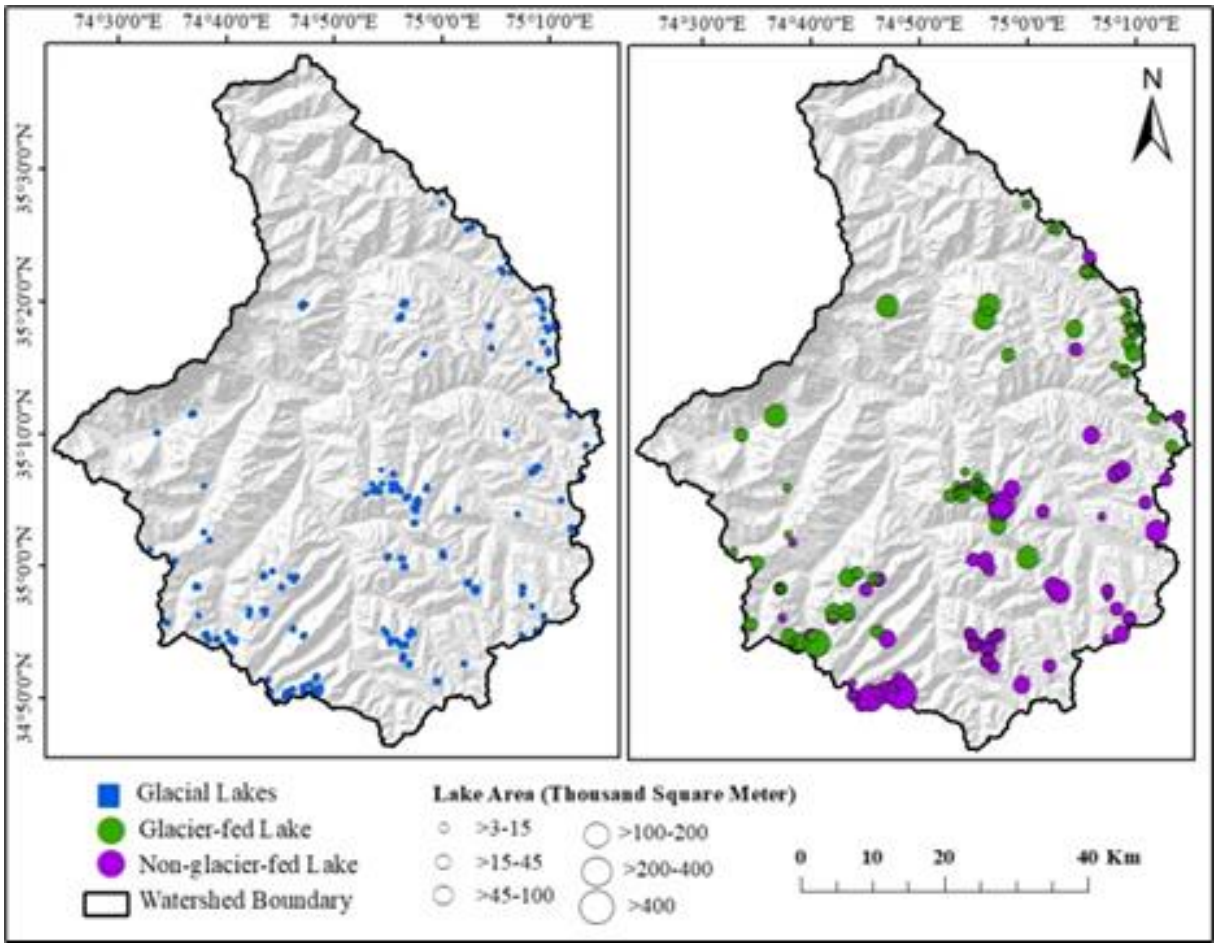

Figure 4. Astore Drainage Basin, 2009 (a) Distribution of glacial lakes (b) Lake types and area

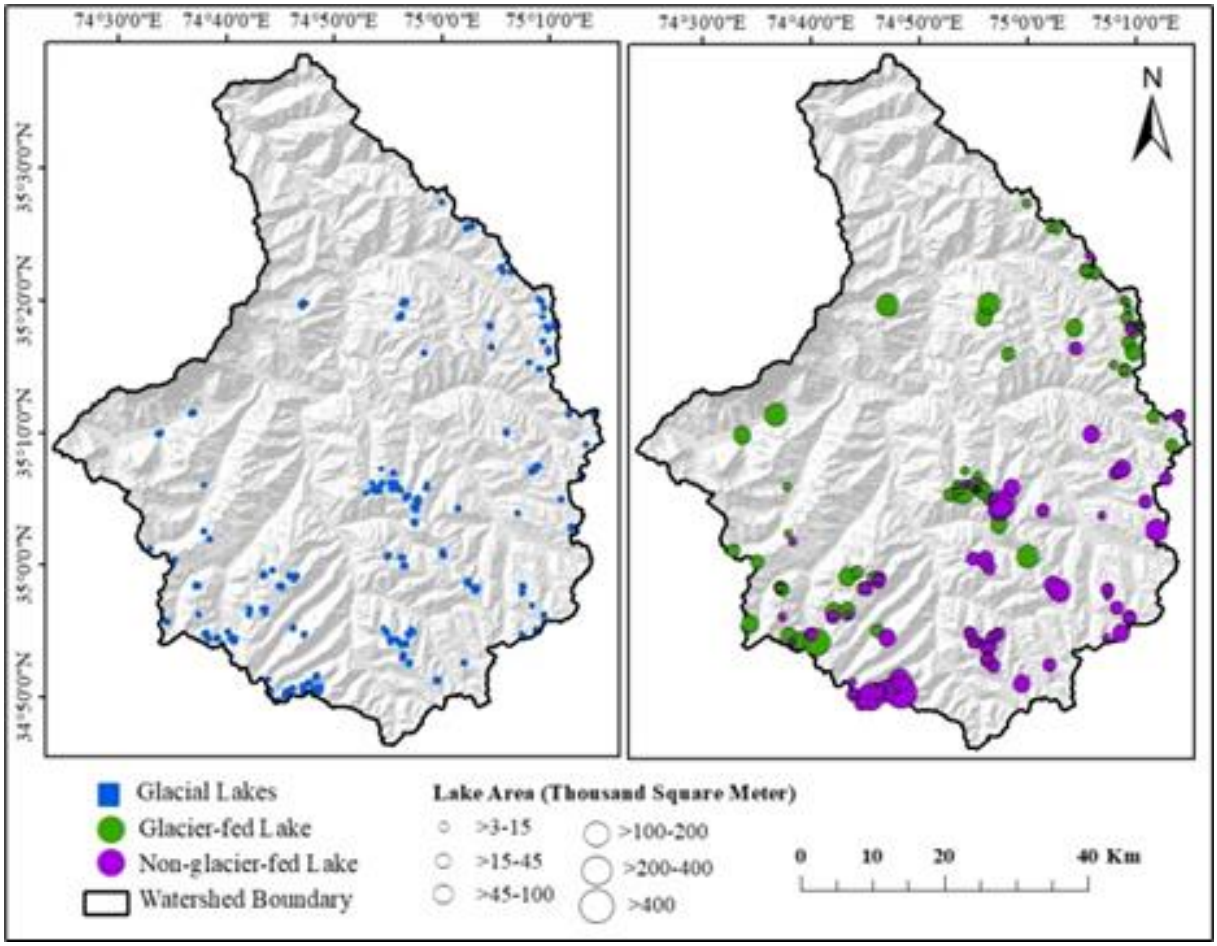

Figure 5. Astore Drainage Basin, 2019 (a) Distribution of glacial lakes (b) Lake types and area

4.2. Spatio-temporal Distribution of Glacial Lakes (1989-2019)

From 1989 to 2019, the evolution and development of glacial lakes in the Astore Drainage Basin was extremely complicated with the depletion of some lakes, the emergence of new ones, and the growth of existing glacial lakes. Between 1989 and 2019, the number and size of glacial lakes changed dramatically. The Astore Drainage Basin had 120 glacial lakes in 1989. In 1999, there were 126 lakes in the inventory. According to Landsat imagery, the number of glacial lakes increased from 127 in 2009 to 128 in 2019.

Over the investigated period, the volumetric and areal extents of the lakes also grew with the growing number. The lakes' total area grew from 4.75 km^2 to 5.86 km^2, and their approximate volume increased from 2,043,463.17 m^3 to 2,522,083.32 m^3. The specifics can be found in the Table 1.

Table 1. Areal and volumetric extents of the lakes

Year	Areal Extent (Km^2)			Volumetric Extent (m^3)		
	Glacial-fed Lakes	Non-glacial-fed Lakes	Total	Glacial-fed Lakes	Non-glacial-fed Lakes	Total
1989	1.93	2.82	4.75	830,241.01	1,213,222.16	2,043,463.17
1999	2.282	3.175	5.457	982,004.21	1,366,495.78	2,348,499.99
2009	2.278	3.298	5.576	980,046.56	1,419,182.01	2,399,228.57

From 2009 to 2019, the area of the glacial lakes expanded at a faster pace than the rest of the decades/years. Glacial-fed lakes have grown by 29.07 percent in the last 30 years from 1.93 km^2 in 1989 to 2.491 km^2 in 2019 which is considerably more than non-glacial-fed lakes which have grown by just 19.50 percent (from 2.82 km^2 in 1989 to 3.370 km^2 in 2019). Furthermore, the findings revealed that smaller lakes grew in size faster than larger lakes. The Himalayas have been warming at a rate of 0.15°C-0.6°C per decade over the last three decades [35], and as a result, the glaciers are melting over this mountainous area [2]. This retreat has resulted in the creation of new lakes as well as the expansion of the area and volume of present lakes. Glacial-fed lakes collect meltwater from the glaciers and increase in size because they are in contact with them. Non-glacial-fed lakes, on the other hand, have no glacier in their watershed and their area and volume are mostly dependent on precipitation or other sources. As the number of lakes grows and the glacier retreats, the results will lead to higher number of GLOFs. Non-glacial-fed lakes are mainly located in the basin's south-eastern side. Glacial-fed lakes, on the other hand, are located across the basin with the largest concentration in the

study area's northwestern corner. Furthermore, there are almost no glacial lakes in the basin's upper reaches.

According to the findings of all inventories, there is a strong correlation between number of glacial-fed lakes and the elevation, i.e., the greater the quantity of glacially fed lakes, the higher the elevation. The finding is not surprising since it is commonly assumed that non-glacier-fed lakes are found in ponds left by Quaternary glaciers, which are lower in height than present glacier termini where Glacier-fed lakes are located [34].

4.2.1. Disappearance of Lakes

According to this study, two lakes in the basin are vanished within the thirty-year span (1989-2019). Both the lakes faded after 1999 and are only showed in inventories of 1989 and 1999. The detail of the lakes is:

i. Astore-GL02; in 1989, this lake had an area of 0.288 km^2 but by 1999, it had shrunk to 0.1944 km^2. This lake was 4,646m above mean sea level and belonged to the Glacial-fed Lake group.
ii. Astore-GL92; this non-glacier-fed lake was located at an elevation of 4,467m above M.S.L and had an area of 0.0063 km^2 in 1989 and 0.0045 km^2 in 1999.

The glacial lakes may become extinct in one of the following ways [18]:

i. In a non-catastrophic manner
ii. Because of sedimentation (lakes being filled with sediments)
iii. As a result of the lake's water intake being limited
iv. Without any Lake Outburst Flood as a result of dam incision
v. In a devastating manner (GLOFs)

According to the findings, the area of both lakes reduced between 1989 and 1999. So, it is possible that after 1999, the aforementioned two lakes were perished in a non-catastrophic fashion, either as a result of losing their primary source of water, alluviation, or as result of one of the reasons mentioned above.

4.2.2. Formation of New Lakes

Between 1989 and 2019, the number and area of lakes in the Astore watershed increased dramatically. In all, 10 glacial lakes have appeared in the study area, marking a 6.67 percent rise in the entire number of lakes from 120 in 1989 (two of which vanished after 1999) to 128 in 2019 (Fig 6). Two of them are non-glacial while the others are Glacial-fed lakes. Non-glacial-fed lakes, as it is well known, are typically created in the ponds left by Quaternary glaciers. Two non-glacial-fed lakes (Astore-GL80, Astore-GL105) are shown to have formed after 1989 in this study. This may be due to one of the two possibilities:

i. These lakes may have existed in 1989 but were not apparent in satellite images due to various factors such as cloud cover, snow cover, and so on.
ii. The second explanation is, may be these lakes developed after 1989 as a result of rainwater runoff or significant amounts of snow melting.

The majority of the newly formed lakes are glacier-fed, indicating that the glaciers in the study region are constantly retreating. This supported numerous researchers' hypothesis that glaciers in the world's highest mountainous regions are melting, resulting in the creation of various forms of glacial lakes around, inside, or beneath the glacier [9-10]. Pakistan's average yearly temperature will rise by 4.3-4.9 Degrees Celsius by 2085, with the rise being greater in the north than in the south [36]. As a result, glacier retreat and lake formation will become more common in the future. 90% of the lakes appeared at altitudes greater than 4,000m above M.S.L. In research conducted in the Himalayas, Nie et al. [37] found similar findings. According to this report, because of rising temperatures, the greatest number of glacial lakes appeared at elevations greater than 4,000m between 1989 and 2019. In addition, the area of these newly developed lakes has varied over time Table 2.

Glacier retreat is related to the growth, progression, and extinction of lakes, which frequently modifies the vulnerability of glacial lakes with time [38-40]. The bulk of the lakes emerged after 1989, and glacial loss in the study region is estimated to have peaked between 1989 and 1999.

Table 2. Newly emerged lakes (1989-2019)

Name	Lake Type	Area (km^2)		
		1999	2009	2019
Astore-GL14	Glacial-fed	0.0063	0.0062	0.0063
Astore-GL17	Glacial-fed	0.0054	0.0054	0.0036
Astore-GL27	Glacial-fed	0.0072	0.0062	0.0107
Astore-GL28	Glacial-fed	_	0.0108	0.0108
Astore-GL35	Glacial-fed	_	0.0153	0.0567
Astore-GL54	Glacial-fed	0.0171	0.018	0.0242
Astore-GL63	Glacial-fed	_	0.0063	0.0063
Astore-GL80	Non-glacial-fed	0.009	0.0125	0.0125
Astore-GL86	Glacial-fed	_	_	0.018
Astore-GL105	Non-glacial-fed	0.0071	0.0098	0.0081

For a deeper understanding of the link between lake development and glacier ablation, more detailed knowledge about the glacier is needed. Despite all the uncertainties related with mapping of glacial lakes from satellite images, the appearance and development of lakes suggests that they are highly dynamic in nature, with a consistent growth pattern. The study area's fast fluctuation in the quantity and extent of glacial lakes can raise the danger of GLOFs.

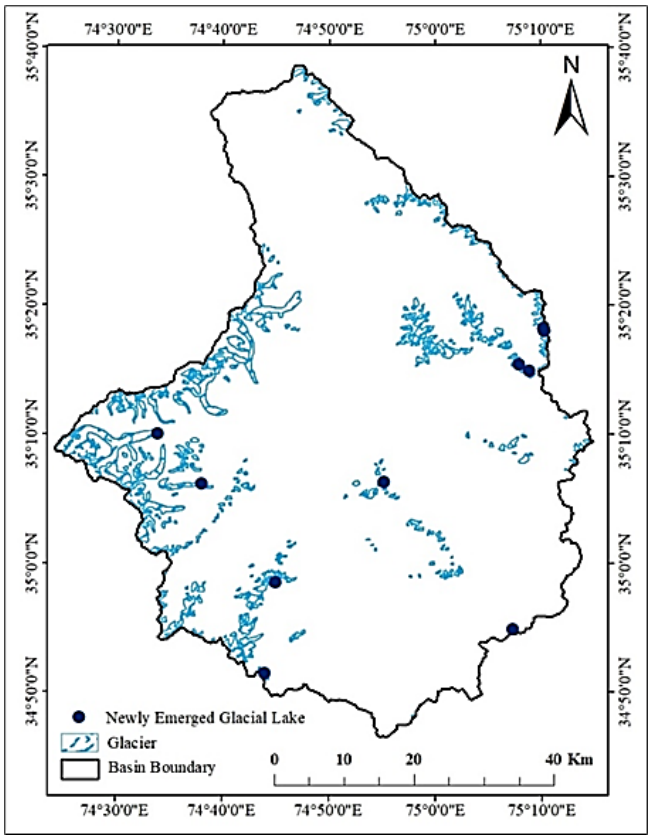

Figure 6. Newly emerged glacial lakes in Astore Drainage Basin (1989-2019)

4.2.3. Growth of The Existing Lakes

Over the study era, the area of the lakes fluctuates in Astore Drainage Basin. Some lakes have seen an increase in their area; some have seen a decline, while others remained unchanged.

The results indicate that 45 Glacial-fed and 47 non-glacial-fed lakes grew in size during the study period. This means that the glaciers in the region are rapidly melting. Twenty-two lakes have experienced negative growth in their area (16 non-glacial-fed and 6 Glacial-fed). According to Emmer et al. [35], the negative growth suggests that the production of these lakes is heading towards the non-glacial stage. Only four lakes, including one non-glacial-fed lake and three Glacial-fed lakes show no improvement. There are 21 lakes with an area expansion rate of more than 100% (7 non-glacial-fed and 14 Glacial-fed). Water spread boundaries of some lakes for different years are shown in Fig 7.

5. Conclusion

Glacial lakes are generated as glaciers recede. There are several forms of glacial lakes, and they pose serious dangers to downstream communities and properties. In all, 120, 126, 127, and 128 glacial lakes were discovered in the Astore Drainage Basin in the Himalaya's northwestern slopes in 1989, 1999, 2009, and 2019. During the research period, these glacial lakes encompass an area of 4.75, 5.457, 5.576, and 5.861 km^2. Lakes were divided into two types: glacially fed and non-glacially fed, and they were defined using quantitative and qualitative criteria. Glacial-fed lakes are more over 4,500m above mean sea level, than non-glacial-fed lakes which are present in lower elevation. The area growth rate of glacier-fed lakes that are in direct touch with the glacier's snout is greater than the area expansion rate of non-glacier-fed lakes that are not in direct contact with the parent glacier snout. During the research period, the quantity and size of lakes change. Between 1989 and 2019, two lakes vanished, while ten new lakes emerged. There were 21 lakes with an area expansion of more than 100%, indicating a strong vulnerability to GLOF.

In changing climate scenario, the list of glaciers in the study region is fluctuating. Therefore, the number of glaciers and Glacial Lakes are gradually increasing and pose serious threat to the downstream communities. Based on the mentioned facts, this study is a pioneering attempt in the region and it is very useful for decision makers, Disaster Risk Reduction experts and local communities in addressing and mitigating Glacial Lake Outburst floods.

Acknowledgement

This study is part of MPhil thesis of principal author and completed under the supervision of co-author. This research is not submitted to any other journal. All authors have declared that no conflicts of interests.

Author contributions

Fareeha Siddique: Conceptualization, Methodology, Software, Field study, Writing-Original draft preparation
Atta-ur-Rahman: Data curation, Software, Validation., Field study, Visualization, Investigation, Writing-Reviewing and Editing.

Conflicts of interest

The authors declare no conflicts of interest.

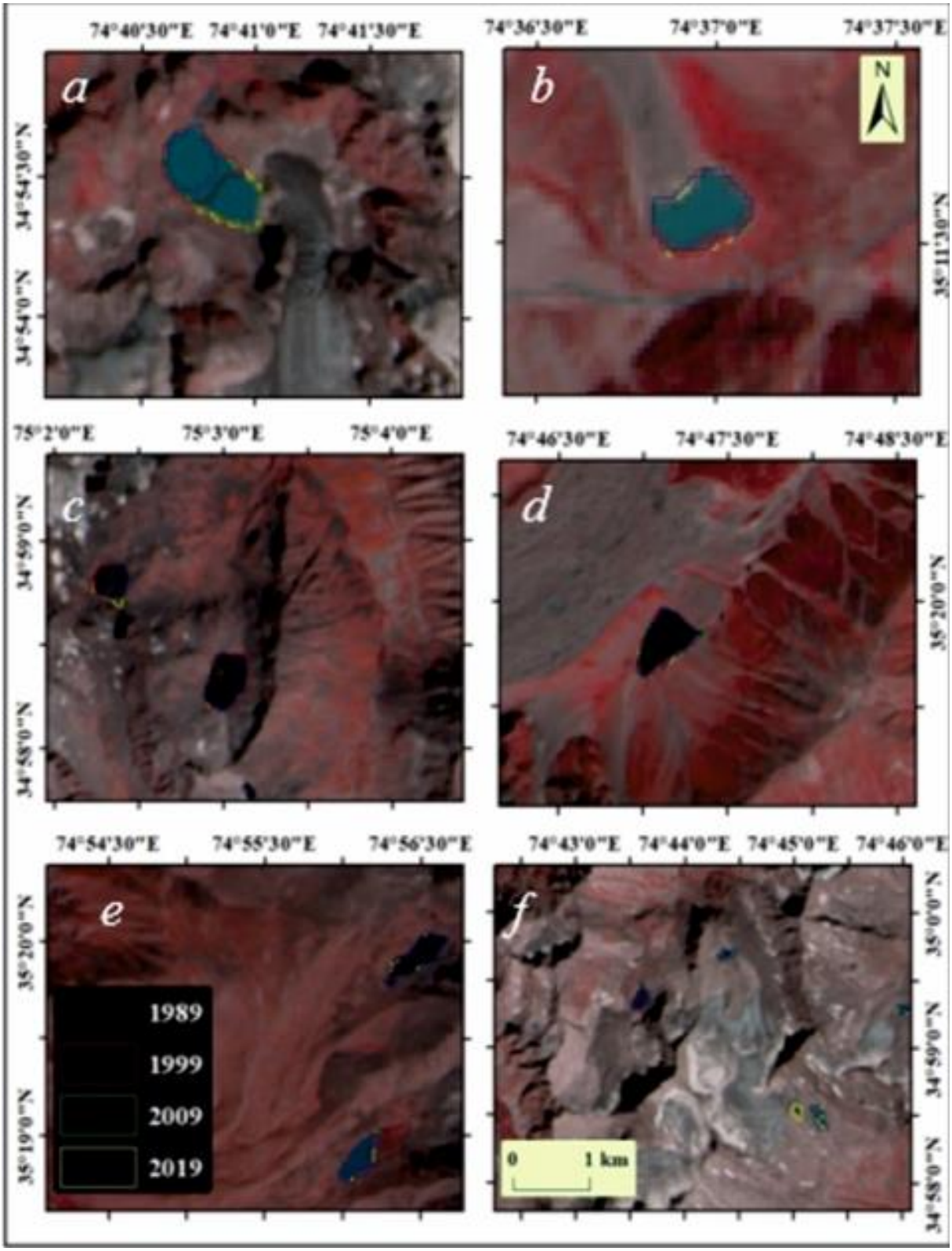

Figure 7. Satellite view of different lakes with water spread border (a). Astore-GL98, (b). Astore-GL34, (c). Astore-GL72 and Astore-GL73, (d). Astore-GL21, (e). Astore-GL19 and Astore-GL20, (f). Several tiny glacier-fed lakes

References

1. Jain, S. K., & Mir, R. A. (2019). Glacier and glacial lake classification for change detection studies using satellite data: a case study from Baspa basin, western Himalaya. Geocarto International, 34(4), 391-414.
2. Gardelle, J., Arnaud, Y., & Berthier, E. (2011). Contrasted evolution of glacial lakes along the Hindu Kush Himalaya Mountain range between 1990 and 2009. Global and Planetary Change, 75(1), 47-55.
3. Immerzeel, W. W. (2008). Spatial modeling of mountainous basins: an integrated analysis of the hydrological cycle, Climate Change and Agriculture.
4. Bolch, T., Kulkarni, A., Kääb, A., Huggel, C., Paul, F., Cogley, J., . . . Stoffel, M. (2012). The State and Fate of Himalayan Glaciers. Science, 336, 310-314.

5. Dyhrenfurth, G. O. (1955). The third Pole – The history of the High Himalaya (1st UK Edition). London: Ex Libris, Werner Laurie.
6. Bajracharya, S. R., Maharjan, S., Shrestha, F., Guo, W., Liu, S., Immerzeel, W. W., & Shrestha, B. (2015). The glaciers of the Hindu Kush Himalayas: current status and observed changes from the 1980s to 2010. International Journal of Water Resources Development, 31, 1-13.
7. Gilany, N., Iqbal, J., & Hussain, E. (2020). Geospatial Analysis and Simulation of Glacial Lake Outburst Flood Hazard in Hunza and Shyok Basins of Upper Indus Basin. The Cryosphere Discussions, 1-24.
8. Benn, D. I., Bolch, T., Hands, K., Gulley, J., Luckman, A., Nicholson, L. I., . . .Wiseman, S. (2012). Response of debris-covered glaciers in the Mount Everest region to recent warming, and implications for outburst flood hazards. Earth-Science Reviews, 114(1), 156-174.
9. Zemp, M., Frey, H., Gärtner-Roer, I., Nussbaumer, S. U., Hoelzle, M., Paul, F., . . . Vincent, C. (2015). Historically unprecedented global glacier decline in the early 21st century. Journal of Glaciology, 61(228), 745-762.
10. Campbell, J. G. (2005). Inventory of glaciers and glacial lake and the identification of potential glacial lake outburst floods (GLOFs) affected by global warming in the mountains of India, Pakistan and China/Tibet Autonomous Region. Final report submitted to APN, 2004-03 CMY Kathmandu Nepal: ICIMOD & APN, 39.
11. Linsbauer, A., Frey, H., Haeberli, W., Machguth, H., Azam, M. F., & Allen, S. (2015). Modelling glacier-bed overdeepenings and possible future lakes for the glaciers in the Himalaya—Karakoram region. Annals of Glaciology, 57(71), 119-130.
12. Frey, H., Huggel, C., Paul, F., & Haeberli, W. (2010). Automated detection of glacier lakes based on remote sensing in view of assessing associated hazard potential. Grazer Schriften der Geographie und Raumforschung, 45, 261-272.
13. Wang, X., Siegert, F., Zhou, A. G., & Franke, J. (2013). Glacier and glacial lake changes and their relationship in the context of climate change, Central Tibetan Plateau 1972–2010. Global and Planetary Change, 111, 246-257.
14. Fan, J., An, C., Zhang, X., Li, X., & Tan, J. (2019). Hazard assessment of glacial lake outburst floods in Southeast Tibet based on RS and GIS technologies. International Journal of Remote Sensing, 40, 1-25.
15. Clague, J. J., & Evans, S. G. (2000). A review of catastrophic drainage of moraine dammed lakes in British Columbia. Quaternary Science Reviews, 19(17), 1763-1783.
16. Carey, M. (2005). Living and dying with glaciers: people's historical vulnerability to avalanches and outburst floods in Peru. Global and Planetary Change, 47(2), 122-134.
17. Stokes, C. R., Popovnin, V., Aleynikov, A., Gurney, S. D., & Shahgedanova, M. (2007). Recent glacier retreat in the Caucasus Mountains, Russia, and associated increase in supraglacial debris cover and supra-/proglacial lake development. Annals of Glaciology, 46, 195-203.
18. Emmer, A., Merkl, S., & Mergili, M. (2015). Spatiotemporal patterns of high-mountain lakes and related hazards in western Austria. Geomorphology, 246, 602-616.
19. Fujita, K., Suzuki, R., Nuimura, T., & Sakai, A. (2008). Performance of ASTER and SRTM DEMs, and their potential for assessing glacial lakes in the Lunana region, Bhutan Himalaya. Journal of Glaciology, 54, 220-228.
20. Wang, X., Liu, Q., Liu, S., Wei, J., & Jiang, Z. (2016). Heterogeneity of glacial lake expansion and its contrasting signals with climate change in Tarim Basin, Central Asia. Environmental Earth Sciences, 75, 1-11.
21. Song, C., Sheng, Y., Wang, J., Ke, L., Madson, A., & Nie, Y. (2017). Heterogeneous glacial lake changes and links of lake expansions to the rapid thinning of adjacent glacier termini in the Himalayas. Geomorphology, 280, 30-38.
22. ICIMOD. (2011). Report on the Status of Glaciers in the Hindu Kush-Himalayan Region. Kathmandu, Nepal.
23. Rehman, G. (2015). GLOF Risk and Reduction Approaches in Pakistan. In A.-U. Rahman, A. N. Khan & R. Shaw (Eds.), Disaster Risk Reduction Approaches in Pakistan (pp. 217-237). Tokyo: Springer Japan.
24. ICIMOD. (2005). Report on inventory of the glacier and glacial lakes of HKH region. Kathmandu, Nepal.
25. ICIMOD. (2010). Report on formation of glacial lakes in the Hindu Kush Himalayas and GLOF risk assessment. Kathmandu, Nepal.
26. Archer, D. (2003). Contrasting hydrological regimes in the upper Indus Basin. Journal of Hydrology, 274(1), 198-210.
27. Ahmad, I., Ahmad, Z., Munir, S., Rehman, O. –u., Shah, S. R., & Shabbir, Y. (2018). Geo-spatial dynamics of snowcover and hydro-meteorological parameters of Astore basin, UIB, HKH Region, Pakistan. Arabian Journal of Geosciences, 11, 1-15.
28. Morsy, S., & Hadi, M. (2023). Impact of land use/land cover on land surface temperature and its relationship with spectral indices in Dakahlia Governorate, Egypt. *International Journal of Engineering and Geosciences*, *7*(3), 272-282.
29. Rahman, S. A., Islam, M. M., Salman, M. A., & Rafiq, M. R. (2022). Evaluating bank erosion and identifying possible anthropogenic causative factors of Kirtankhola River in Barishal, Bangladesh: an integrated GIS and Remote Sensing approaches. *International Journal of Engineering and Geosciences*, *7*(2), 179-190.
30. Khorrami, B., & Kamran, K. V. (2022). A fuzzy multi-criteria decision-making approach for the assessment of forest health applying hyper spectral imageries: A case study from Ramsar forest, North of Iran. *International Journal of Engineering and Geosciences*, *7*(3), 214-220.
31. Huggel, C., Kääb, A., Haeberli, W., Teysseire, P., & Paul, F. (2002). Remote sensing-based assessment of hazards from glacier lake outbursts: A case study in the Swiss Alps. Canadian Geotechnical Journal, 39, 316-330.

32. Choi, H., & Bindschadler, R. (2004). Cloud detection in Landsat imagery of ice sheets using shadow matching technique and automatic normalized difference snow index threshold value decision. Remote Sensing of Environment, 91(2), 237-242.
33. Wilson, R., Glasser, N. F., Reynolds, J. M., Harrison, S., Anacona, P. I., Schaefer, M., . . . Shannon, S. (2018). Glacial lakes of the Central and Patagonian Andes. Global and Planetary Change, 162, 275-291.
34. Wang, W., Xiang, Y., Gao, Y., Lu, A., & Yao, T. (2014). Rapid expansion of glacial lakes caused by climate and glacier retreat in the Central Himalayas. Hydrological Processes, 29(6), 859-874.
35. Shrestha, B. B., Nakagawa, H., Kawaike. K., Baba, Y., & Zhang, H. (2010). Glacial lake outburst due to Moraine Dam failure by seepage and overtopping with impact of climate change. Annuals of Disaster Prevention Research Institute 53(B), 569-582.
36. Akram, N., & Hamid, A. (2014). Climate change: A threat to the economic growth of Pakistan. Progress in Development Studies, 15, 1-14.
37. Nie, Y., Liu, Q., Sheng, Y., Liu, L., Liu, S., Zhang, Y., . . . Song, C. (2017). A regional-scale assessment of Himalayan glacial lake changes using satellite observations from 1990 to 2015. Remote Sensing of Environment, 189, 1-13.
38. Emmer, A., Vilímek, V., Klimeš, J., Mergili, M., & Cochachin, A. (2016). 882 lakes of the Cordillera Blanca: An inventory, classification, evolution and assessment of susceptibility to outburst floods. Catena, 147, 269-279.
39. Demir, V. & Ülke Keskin, A. (2022). Flood flow calculation and flood modeling in rivers that do not have enough flow measurement (Samsun, Mert River sample). Geomatik, 7 (2), 149-162. https://doi.org/10.29128/geomatik.918502
40. Yiğit, A. Y., Şenol, H. İ. & Kaya, Y. (2022). Using multi-temporal and multispectral satellite data for coastal change analysis in Marmara Lake. Geomatik, 7 (3), 253-260. https://doi.org/10.29128/geomatik.1017376

International Journal of Engineering and Geosciences
https://dergipark.org.tr/en/pub/ijeg
e-ISSN 2548-0960

The effect of DEM resolution on topographic wetness index calculation and visualization: An insight to the hidden danger unraveled in August, 2021 in Bozkurt

Arif Oguz Altunel[*1]

[1]*Kastamonu University, Faculty of Forestry, Forest Engineering, Türkiye*

Keywords
Global DEMs
Quad maps
DEM resolution
TWI
Flood

Research Article
DOI: 10.26833/ijeg.1110560

Received: 28.04.2022
Accepted: 24.07.2022
Published: 19.10.2022

Abstract

Topographic Wetness Index, also known as the compound topographic index, (TWI) is a topographic indicator that calculates the potential of where water is likely to accumulate during excessive precipitation cycles resulting from abrupt atmospheric anomalies. High index values represent serious potential of water accumulation due to low slope, and the opposite for high slope. As expected from the term, slope, Digital Elevation Model (DEM) datasets play an important role in the calculation of TWI. DEMs are produced utilizing tachometry, GPS benchmarking, UAV, aerial or satellite image capture and LIDAR capabilities. However, no matter how it is generated, a DEM is as good as the actual ground sampling algorithm, on which the final resolution is based. Using six different DEM resolutions coming from three global and one national source presented in three different setting coverages, upper feeder basin of Bozkurt sub-province, Kastamonu, was analyzed emphasizing the urbanized part of the sub-province, which was devastated during the August 11th, 2021 flood. Coarser resolution missed the overall precision while the finer resolution captured it nicely. On the flip side, finer resolution excessively fragmented the questioned area while the coarser resolution formed a unity coinciding with the destructed area recorded during the event.

1. Introduction

Habitation on the Turkish Black-sea coast dates back quite some time. Due to the morphological structuring of the topography, which the mountains run parallel to the coast line, many provinces and sub-provinces have settled on or near the coast line, which have provided easy access to sea, warmer climate year-round and nicer aesthetics to be around. However, this living preference had a catch from time to time. Each and every urbanized location on Black-sea coast has experienced floods and landslides varying in severity during their existence [1-2]. The reason for the devastations has resulted from the fact that the towns situated at and around sea-bound discharge paths of docile looking waterways, are swept out to sea causing immense property damage and death along with the surging water coming fully loaded down from the feeder basins, aka upper watersheds [3]. Alluvial fans between the feeder basins and the sea are where the surging water is dispersed losing its destructive energy during heavy rains before converging with the sea. When towns are situated on them, they are in danger to some degree because the feeder basins can only collect and convey a certain amount of water during such events [4]. However, when towns are situated right at the mouth of the feeder basins, where topography is still not tame enough for the hurdling downward water, the damage becomes proportionately high because man made infrastructures cannot withstand against that much force. One such sub-province, Bozkurt, of Kastamonu was hit by a record-breaking rain storm in August 11th, 2021 when the majority of the town was run down by the rushing waters coming from its feeder basin. Along with the neighboring two other sub-provinces, property damage and death toll were unprecedented.

In the scope of this study, a frequently used hydrology indices, topographic wetness index, which has been known as an indicator for determining the places inherently keeping water accumulation potential, through a raster surface [5-6], was evaluated. Reliably forecasting soil moisture patterns in landscapes was a serious challenge in the past so that many notable occurrences cost considerable property damage and death all across the Earth [7-10]. TWI was first developed

* **Corresponding Author**
*(aoaltunel@kastamonu.edu.tr) ORCID ID 0000-0003-2597-5587

Cite this article
Altunel, A. O. (2023). The effect of DEM resolution on topographic wetness index calculation and visualization: An insight to the hidden danger unraveled in August, 2021 in Bozkurt. International Journal of Engineering and Geosciences, 8(2), 165-172

by physically basing on a runoff model, TOPMODEL, which ran with the assumption that the hydraulic slope could be estimated by the topographic slope [11]. It has lately been accepted as a powerful measure in defining flood preparedness scenarios [12-13]. The index specializes in rainfall runoff predictions and spatial soil moisture and water accumulation simulations [14]. Six different DEM datasets, three from global sources and one displayed in three different visualization settings, from Turkish national quad map coverage of 2010, were used to delineate Bozkurt feeder basin to see how DEM resolution can differ and can help specify residential flood risk areas during heavy rain storms.

2. Materials and Methodology

2.1. Study area

Bozkurt is one of six Black Sea bound sub-provinces of Kastamonu. It has typical Black Sea topography and morphological characteristics (Figure 1) along with lush deciduous and coniferous forests managed by the Turkish forest service. Although considered as a coastal town, its residential part extends inland along its docile looking creek/stream, so that the neighboring sub-province Abana sits directly on the alluvial fan of Bozkurt's feeder basin. Sub-province's neighborhoods, recreation infrastructure and commercial districts are all situated immediately around the stream channel, which was overwhelmed by the deluge coming from the feeder basin on August 11th, 2021. Compared to the neighboring ones, it has a rather small feeder basin of 11851.5 ha whereas Catalzeytin had 31252 ha and Ayancik had 59081 ha. Considerable property damage and human loss also occurred in these mentioned sub-provinces, however what Bozkurt experienced was beyond comprehension. That's why it is singled out for analysis in this study.

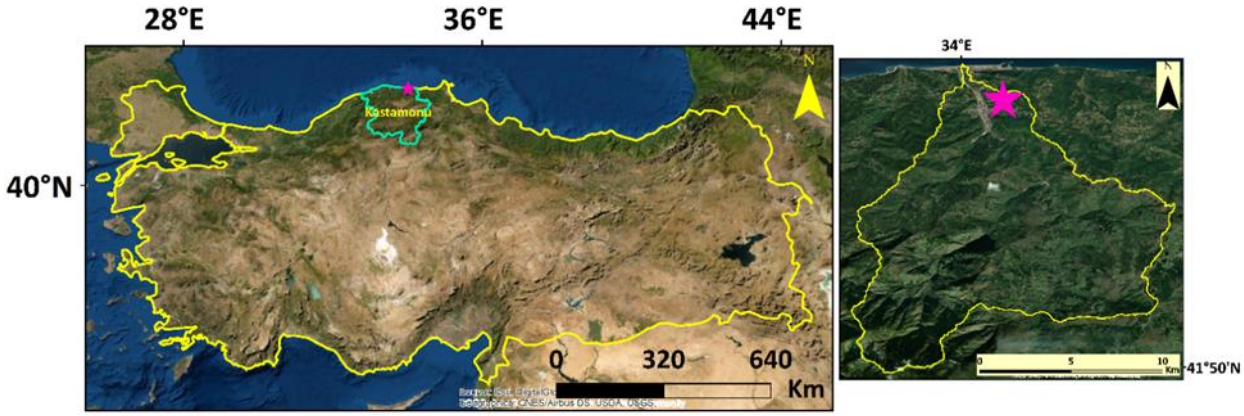

Figure 1. Location of Bozkurt sub-province and its feeder basin

2.2. Methodology

Three different-resolution global DEM datasets, ALOS PALSAR, 12.5 m [15], AW3D30, 30 m [16] and TanDEM-X, 90 m [17] were acquired from their respective geo-portals. ALOS PALSAR and TanDEM-X DEMs were respectively produced with the capabilities of L-band and X-band Synthetic Aperture Radar (SAR) interferometric techniques [18-19] whereas the initial and the successive releases of AW3D30 DEM have been produced with panchromatic optical sensor (PRISM) captured stereo image processing [20-21]. Many studies have surfaced questioning and validating their effectiveness and practicality in various fields of studies [22-26]. All three DEM datasets were positioned defining Universal Transverse Mercator projection over World Geodetic System, 1984 horizontal datum under Bozkurt feeder basin polygon. 34 m Geoid height [27] was deducted from ALOS-PALSAR DEM [28].

Besides, three more DEM datasets were produced from vectorized and 1:25000 scaled national quad maps [29]. First, four such maps were simultaneously tied together to form an initial Triangulated Irregular Network (TIN) surface. Then, a TIN to raster conversion was carried out accepting the default resolution(s), 104 m. Second, all maps were clipped by Bozkurt feeder basin polygon (Figure 2), the clipped parts were tied together and a second TIN surface was generated expecting a tighter GRID pattern. When the conversion was again applied, the result indeed produced a better resolution, 67 m. No resampling algorithm was applied in achieving these figures in either case.

National quad map(s) which have been produced via photogrammetric capabilities, solely relying on stereo air-photo capture, depict the stationary topography of a region in a medium scale. Accepted as a reasonable scale by many nations [30-31], they include contour lines following the natural formation of the terrain. Contour intervals widens in distance due to subtle elevation differences in flat areas whereas they come tightly together as topography becomes treacherous, accentuating the elevation in short distances [32]. This uneven, non-systematic elevation distribution within quad maps is the reason behind their DEM generation performance. Since TIN algorithm uses these contour lines to form a surface, it changes in precision when the area of interest shifts, even within the same map(s) as well as in the subsequently produced raster model(s). No one quad map depending surface model distinctness is the same as another. This is how two initial different raster models given above, were produced from the same number of national quad maps (Table 1). Additionally, a

resampled DEM derived from the same national quad map(s) was also produced while converting from TIN, specifying a 30 m cell size. A total of six DEM datasets with different resolutions were individually subjected to "Topographic Wetness Index" algorithm to see how DEM resolutions would differ, and which one would approximate the extend of the heavily damaged area devastated in Bozkurt sub-province in August 11th, 2021. All analyses were performed using ArcGIS 10.8.

Table 1. Specifications of the directly used and produced DEM datasets

DEM Source	Production type	Resolution (m)	Maker	Availability
ALOS_PALSAR	L-band SAR	12.5	JAXA	https://search.asf.alaska.edu/#/?dataset=ALOS
AW3D30	Stereo Image	23.18	JAXA	https://www.eorc.jaxa.jp/ALOS/en/aw3d30/data/index.htm
TanDEM-X	X-band SAR	80.7	DLR	https://download.geoservice.dlr.de/TDM90/
National Quad-cut	Aerial stereo photography	67	Turkish Mapping Command	upon institutional request
National Quad-whole		104		
Resampled nat. quad.		30		

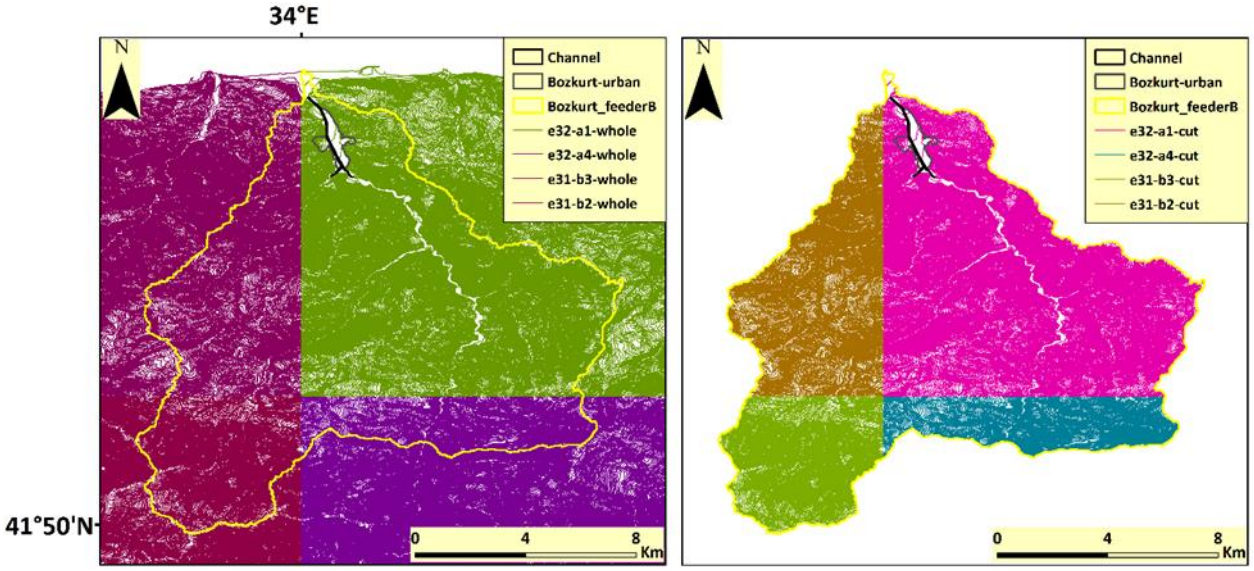

Figure 2. Start of surface generation scheme from vectorized quad maps as whole vs. cut

2.3. Topographic Wetness Index Algorithm and calculation progress on a raster

TWI is an algorithm which is frequently addressed in hydrology driven studies [33-34]. It can be applied on any DEM no matter what its resolution is because DEM resolution is the driving factor behind the successful generation of TWI. The practicality of knowing where water might accumulate at unexpected times, also translate to where water might be sought after in case of need because every water droplet accumulated during rain surely feeds the ground water in the long run. Figure 3 shows how TWI is calculated starting from the initial DEM input.

Through this algorithm, elevation embedded raster DEM cells are transformed into water accumulation risk bearing values ranging from less than 0 to 30 [13]. High index values would indicate high potential of water accumulation due to low slope and vice versa. To find a better TWI producing DEM performance, a hypothetical threshold value, which was applied to all six TWI results, was set. Thus, flood plain acreages were calculated, classifying the TWI results elaborating over this threshold value of more than or equal to "10". Total count of raster cells with TWI values of "10 ≤" was multiplied with the square of the respected raster cell size to achieve the acreages within flood plain (*-fld pln) designated blue polygon in Figure 4. TWI is a unique tool allowing users, decision makers and planners to identify areas which have the potential of getting adversely affected by water accumulation or flooding during excessive rainfall scenarios. Thus city planners can benefit from its visual mechanism in residential site selection and preventive vegetative or afforestation initiatives. Six different resolution DEMs, i.e., three obtained from open-access geo-portals and three manufactured from national quad map coverages, were used to produce TWIs for Bozkurt sub-province of Kastamonu.

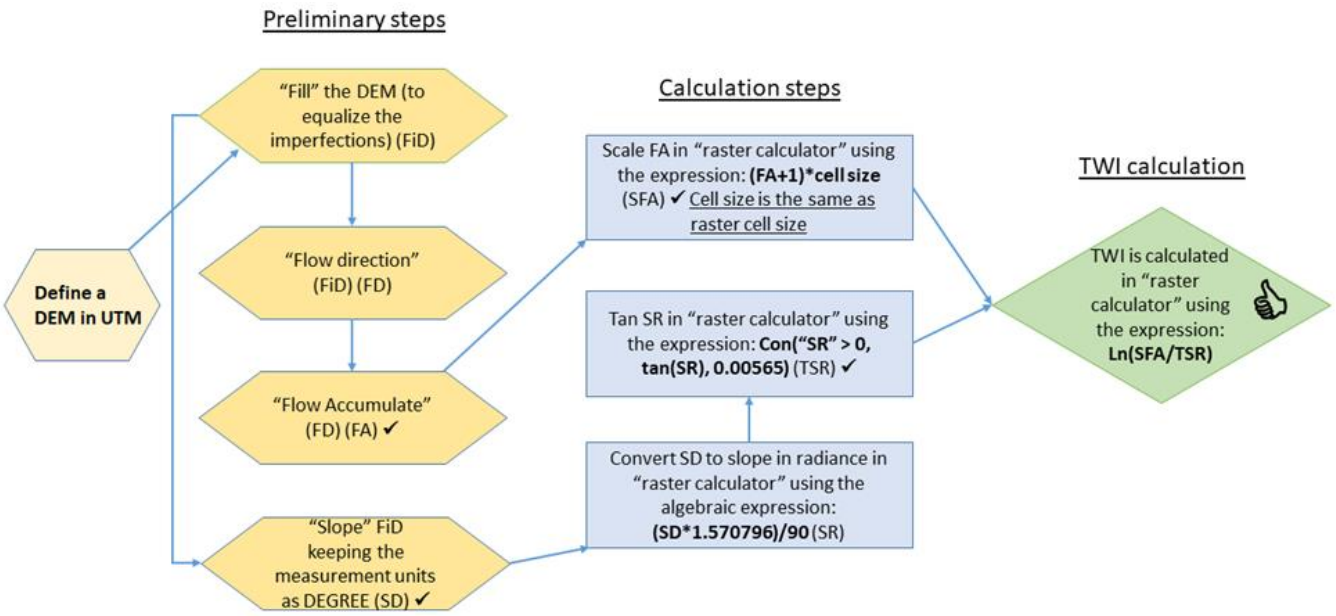

Figure 3. Sequence of turning a DEM into calculated TWI surface

3. Results and Discussion

DEM resolution is important for topographic visualization if intricate work is required. As of today, the highest precision is acquired through LIDAR [35-37] although there are other possibilities, i.e., UAV, air-borne or space-borne image capture derived site specific or large-scale DEM productions, varying in degree of accuracy [29, 38-39]. However, highest precision is not always the sought after or guaranteed requirement obtained from a DEM [40-41]. In an attempt to find suitable flood inundation maps for places where high resolution DEM datasets were not available, Saksena and Merwade [42] unearthed the fact that coarser resolution DEM datasets can provide reliable and improved maps. Quad map extracted inserts in Figure 4 appeared to display better areal distributions compared to much higher resolution ALSO-PALSAR and AW3D30 DEM derived fragmented looking ones. Jeon et al. [43] stated that channel slope became steeper as DEM resolution increased. Although this was a conclusion derived from a simulation, it might very well be one of the underlying factors in real-time feeder basin dynamics of Bozkurt sub-province (Figure 4) because given its small size, 11852 ha, the precipitation falling inside feeder basin swiftly descended into the city and wreak havoc especially on flood plain designated area (blue polygon). Hancock [44] mentioned that hillslope and hydrological details would be lost when larger than 10 m DEM resolutions are used. Similarly, this study also confirmed that topographical detail would be lost from the low resolution onward simply because minute slope differences are aggregated into larger surfaces as the DEM resolution is increased, however this situation obviously did not tarnish the fact that quad map derived inserts in Figure 4 produced comparably better inundation scenarios compared to Global DEM derived results [45].

Although the analyses were performed on the Bozkurt feeder basin's entirety, the emphasize was given to the residential part of the sub-province because the damage mostly concentrated in this part (Figure 4). As the DEM resolution increased, the practicality of the visualization started losing its appeal. ALOS-PALSAR DEM calculated TWI which comparatively provided the highest resolution in this study, indicated almost a no-development area right within the present-day Bozkurt residential extent concentrating around the channel apparent from the water indicating blue-patchy looking pixels in the respectable insert in Figure 4. Nevertheless, this high resolution captured so much detail that it lost the complete picture, thus the insert showed only partial risk as if the rest was secure to settle within the flood plain. The east and west wings of the area were not as heavily risky as the rest of the extent because those were the suburbs erected on steeper topography where no water accumulated during the flooding, whereas the rest was completely inundated as national quad derived DEM calculated TWIs also indicated nicely. AW3D30 and TanDEM-X DEM calculated TWIs produced similar results in visualization as well as in calculation despite the varying resolutions. However, their concentrations were mostly limited to established channel width. Dixon and Earls [46] stated that no matter how the GRID spacing was in a DEM, even if one is resampled to match another one with a specified GRID spacing, they all behave differently in hydrological studies. Bozkurt channel as experienced in many parts of the country, was in a so-called rehabilitated state, directing the water to a not-wide-enough waterway which was completely overwhelmed during the flood. Almost entire residential parts of the sub-province turned into a flood-plain, which was also apparent through the calculations done via national quad maps. Both of the quad map generated DEMs', 67 m and 104 m, visual appeal was better than the intentionally produced 30 m resampled DEM. Sorensen and Seibert [47] stated that calculated designated upstream area got smaller on average for high resolution DEMs with varying information content. Although resampled anticipating a better performance, the resulting high resolution did not necessarily produce as good of a performance as the coarser resolution ones.

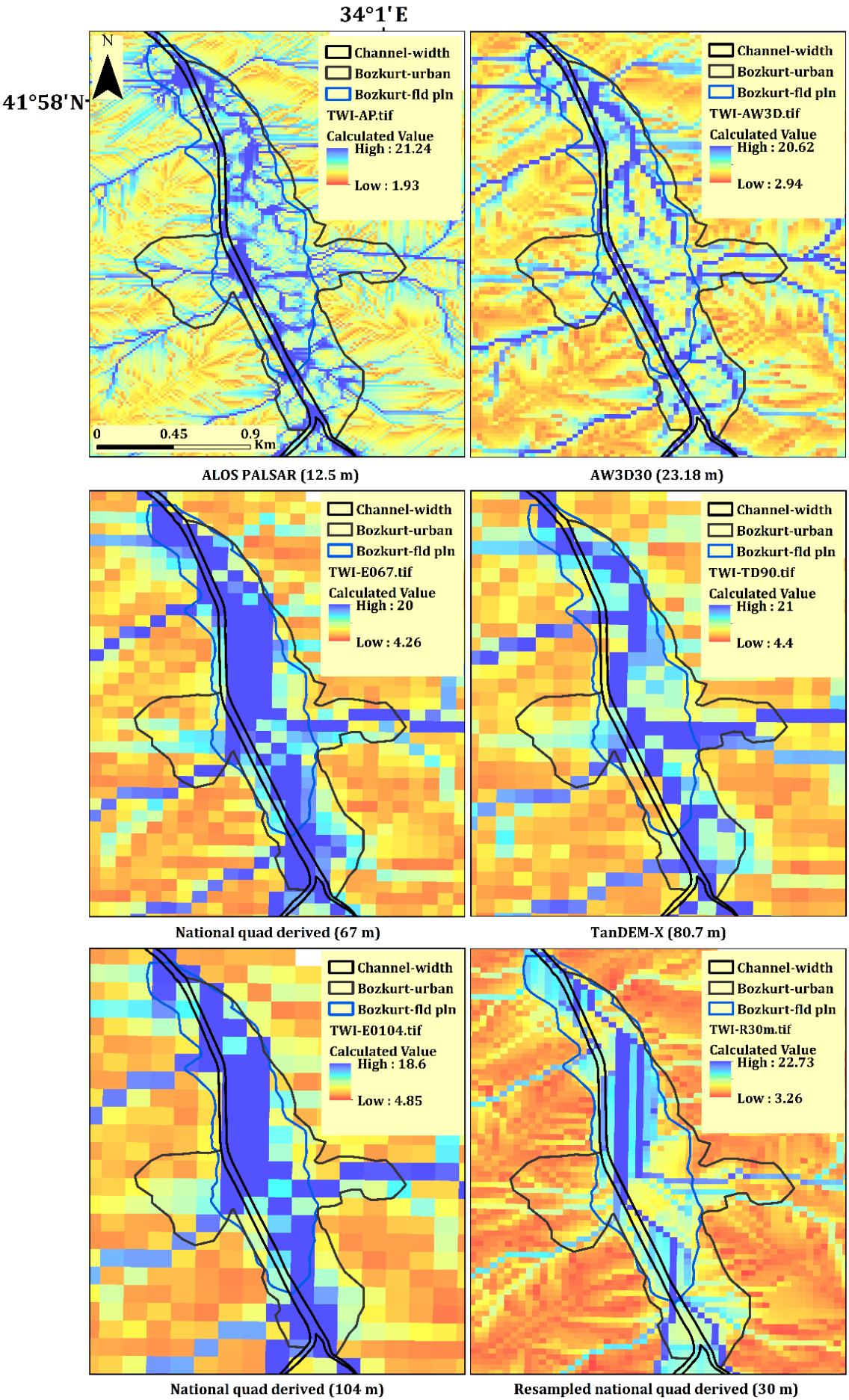

Figure 4. DEM resolution-based Bozkurt residential area inundation scenarios

Calculated TWI value-wise, all tested DEM datasets produced enough warning that a considerable part of the present-day Bozkurt sub-province residential extend will always be under flood risk unless a complete relocation of the people and infrastructure is undertaken. Besides, a comparison calculated to detect which of the tested DEMs generated approximate acreage to the heavily damaged part of the sub-province, indicated as flood plain, 60.7 ha, in Figure 4, produced the respective figures, ALOS PALSAR DEM, 13.5 ha; AW3D30 DEM, 17.2 ha; high resolution quad map derived DEM, 39.2 ha; TanDEM-X, 33.8 ha, low resolution quad map derived DEM, 46.7 ha and resampled national quad map derived DEM, 41.6 ha. Excessive detail captured with high resolution DEMs caused the results to produce rather less acreages compared to those captured with low resolution DEMs. Despite varying figures, it was obvious that quad map derived DEM variants, especially the ones generated without resampling algorithm, produced the overall best results in terms of the questioned objectives. Whether fragmented resulting from high DEM resolution, or aggregated due to low DEM resolution, TWI is a practical and valuable hydrological index for urban development strategies when new sites are planned for residential expansions or flood or landslide mitigation works.

4. Conclusion

Digital Elevation Models have become an indispensable part of the engineering works, today. Along with the technological advancements, GRID spacing is brought to unprecedented small sizes. Geoscience capabilities are also improved considerably. When one knows what to do using the data and the instrument, the results are invaluable on many matters. This simple example was applied to a feeder basin which produced record breaking flood to the town erected in lower elevations. Topographic Wetness Index algorithms calculated over different resolution DEMs showed that the threat was simply sleeping as if nothing would ever have happened. Threats must be taken seriously. Thanks to geoscience capabilities, nothing should be left unturned when lives and country's assets are at stake. Investments tied to the development phases of the cities and the well-being of the people choosing to live in them should not be taken lightly. Technology and know-how are available for the ones willing to accept and incorporate them in their planning. Thus, each and every attempt must be considered to make the living easier, more enjoyable and safer for everyone. Türkiye is not a third World country where capacity build-up is essential before the actual initiative, because financial capabilities, know-how, and trained personal are all present. More derivatives must be integrated into final decisions if they will have long term critical impacts on people's well-being. This way prosperity will thrive and ambitions will be achieved.

Acknowledgement

I thank JAXA and DLR for making the dissemination of such datasets freely accessible. I also thank Turkish General Directorate of Mapping for supplying the quad maps upon request.

Conflicts of interest

The authors declare no conflicts of interest.

References

1. Usul, N. & Turan, B. (2006). Flood forecasting and analysis within the Ulus Basin, Turkey, using geographic information systems. Natural Hazards, 39, 213-229.
2. Yuksek, O., Kankal, M. & Ucuncu, O. (2012). Assessment of big floods in the Eastern Black Sea Basin of Turkey. Environmental Monitoring and Assessment, 185, 797–814.
3. Anilan, T. & Yuksek, O. (2017). Perception of flood risk and mitigation: survey results from the Eastern Black Sea Basin, Turkey. Natural Hazards Review, 18(2), 05016006.
4. Lucà, F. & Robustelli, G. (2020). Comparison of logistic regression and neural network models in assessing geomorphic control on alluvial fan depositional processes (Calabria, southern Italy). Environmental Earth Sciences, 79, 39.
5. Hojati, M. & Mokarram, M. (2016). Determination of a topographic wetness index using high resolution digital elevation models. European Journal of Geography, 7(4), 41-52.
6. Altunel, A. O. (2018). Suitability of open-access elevation models for micro-scale watershed planning. Environmental Monitoring and Assessment, 190(9), 512.
7. Niebur, C. S., Arvidson, R. E., Guinness, E. A., & Galford, G. L. (2003). Lower Missouri River floodplain at arrow rock before and after the great floods of 1993. At the confluence: rivers, floods and water quality in the St. Louis Region, 115-134.
8. Kundzewicz, Z. W., Pińskwar, I., & Brakenridge, G. R. (2013). Large floods in Europe, 1985–2009. Hydrological Sciences Journal, 58(1), 1-7.
9. Milly, P. C. D., Wetherald, R. T., Dunne, K. A., & Delworth, T. L. (2002). Increasing risk of great floods in a changing climate. Nature, 415(6871), 514-517.
10. Dutta, D., & Herath, S. (2004). Trend of floods in Asia and flood risk management with integrated river basin approach. In Proceedings of the 2nd international conference of Asia-Pacific hydrology and water resources Association, Singapore, 1, 55-63.
11. Beven, K. J. & Kirkby, M. J. (1979). A physically based variable contributing area model of basin hydrology. Hydrological Science Bulletin, 24, 43-69.
12. Buchanan, B. P., Fleming, M., Schneider, R. L., Richards B. K., Archibald, J., Qiu, Z. & Walter, M. T. (2014). Evaluating topographic wetness indices across central New York agricultural landscapes. Hydrology and Earth System Sciences, 18, 3279-3299.
13. Ballerine, C. (2017). Topographic wetness index urban flooding awareness act action support, Will & DuPage Counties, Illinois. Illinois State Water Survey.

Available through https://www.ideals.illinois.edu/items/104004 last accessed on 07/07/2022.
14. Qin, C. Z., Zhu, A. X., Pei, T., Li, B. L., Scholten, T., Behrens, T., & Zhou, C. H. (2011). An approach to computing topographic wetness index based on maximum downslope gradient. *Precision agriculture*, *12*(1), 32-43.
15. ALOS-PALSAR. (2022). Alaska Satellite Facility (ASF) Data Search-Vertex. Available through https://search.asf.alaska.edu/#/?dataset=ALOS, last accessed on 21/04/2022.
16. AW3D30. (2022). ALOS Global Digital Surface Model "ALOS World 3D – 30m" (AW3D30). Available through https://www.eorc.jaxa.jp/ALOS/en/aw3d30/data/index.htm, last accessed on 21/04/2022.
17. TanDEM-X. (2022). TanDEM-X Digital Elevation Model (DEM)-Global 90m. Available through https://download.geoservice.dlr.de/TDM90/, last accessed on 21/04/2022.
18. Yan, S., Guo, H., Liu, G. & Ruan, Z. (2013). Mountain glacier displacement estimation using a DEM-assisted offset tracking method with ALOS/PALSAR data. Remote Sensing Letters, 4(5), 494-503.
19. Wessel, B., Huber, M., Wohlfart, C., Marschalk, U., Kosmann, D. & Roth, A. (2018). Accuracy assessment of the global TanDEM-X Digital Elevation Model with GPS data. ISPRS Journal of Photogrammetry and Remote Sensing, 139, 171-182.
20. Santillan, J. R., Makinano-Santillan, M. & Makinano, R. M. (2016). Vertical accuracy assessment of ALOS World 3D-30M Digital Elevation Model over northeastern Mindanao, Philippines. In 2016 IEEE International Geoscience and Remote Sensing Symposium (IGARSS) (pp. 5374-5377).
21. Caglar, B., Becek, K., Mekik, C. & Ozendi, M. (2018). On the vertical accuracy of the ALOS world 3D-30m digital elevation model. Remote Sensing Letters, 9(6), 607-615.
22. De Oliveira A. F. C. & De FáTima R. D. (2012). Effectiveness of SRTM and ALOS-PALSAR data for identifying morphostructural lineaments in northeastern Brazil. International Journal of Remote Sensing, 33(4), 1058-1077.
23. Senkal, E., Kaplan, G., & Avdan, U. (2021). Accuracy assessment of digital surface models from unmanned aerial vehicles' imagery on archaeological sites. International Journal of Engineering and Geosciences, 6(2), 81-89.
24. Ghosh, S. & Kundu, S. (2022). Morphometric Characterization and Erosion Assessment of Gullies in the Lateritic Badlands of Eastern India using ALOS AW3D30 DEM and Topographic Indices. *Geocarto International*, 1-34 https://doi.org/10.1080/10106049.2022.2032390
25. Pandey, P., Manickam, S., Bhattacharya, A., Ramanathan, A. L., Singh, G. & Venkataraman, G. (2017). Qualitative and quantitative assessment of TanDEM-X DEM over western Himalayan glaciated terrain. Geocarto International, 32(4), 442-454.
26. Akar, A. (2017). Evaluation of accuracy of dems obtained from uav-point clouds for different topographical areas. International Journal of Engineering and Geosciences, 2(3), 110-117.
27. Kilicoglu, A., Direnc, A., Yildiz, H., Bolme, M., Aktug, B., Simav, M. & Lenk, O. (2011). Regional gravimetric quasi-geoid model and transformation surface to national height system for Turkey (THG-09). Studia geophysica et geodaetica, 55(4), 557-578.
28. ALOS-PALSAR. (2022). ALOS PALSAR – Radiometric Terrain Correction. Available through https://asf.alaska.edu/data-sets/derived-data-sets/alos-palsar-rtc/alos-palsar-radiometric-terrain-correction/, last accessed on 25/04/2022.
29. Yilmaz, A. & Erdogan, M. (2018). Designing high resolution countrywide DEM for Turkey. International Journal of Engineering and Geosciences, 3(3), 98-107.
30. Pike, R. J., & Wilson, S. E. (1971). Elevation-relief ratio, hypsometric integral, and geomorphic area-altitude analysis. Geological Society of America Bulletin, 82(4), 1079-1084.
31. Lecordix, F., Gallic, J. L., Gondol, L., & Braun, A. (2007, August). Development of a new generalization flowline for topographic maps. In *10th ICA workshop on Generalisation and Multiple Representation* (pp. 2-3).
32. Oka, S., Garg, A. & Varghese, K. (2012). Vectorization of contour lines from scanned topographic map. Automation in Construction, 22, 192-2020.
33. Pourali, S. H., Arrowsmith, C., Chrisman, N., Matkan, A. A. & Mitchell, D. (2016). Topography wetness index application in flood-risk-based land use planning. Applied Spatial Analysis and Policy, 9(1), 39-54.
34. Aksoy, H., Kirca, V. S. O., Burgan, H. I. & Kellecioglu, D. (2016). Hydrological and hydraulic models for determination of flood-prone and flood inundation areas. Proceedings of the International Association of Hydrological Sciences, 373, 137-141.
35. Werbrouck, I., Antrop, M., Van Eetvelde, V., Stal, C., De Maeyer, P., Bats, M., ... & Zwertvaegher, A. (2011). Digital Elevation Model generation for historical landscape analysis based on LiDAR data, a case study in Flanders (Belgium). Expert Systems with Applications, 38(7), 8178-8185.
36. Bühler, Y., Marty, M. & Ginzler, C. (2012). High resolution DEM generation in high-alpine terrain using airborne remote sensing techniques. Transactions in GIS, 16(5), 635-647.
37. Tepeköylü, S. (2016). Mobil Lidar Uygulamaları, Veri İşleme Yazılımları ve Modelleri. Geomatik, 1(1), 1-7.
38. San, B. T. & Suzen, M. L. (2005). Digital elevation model (DEM) generation and accuracy assessment from ASTER stereo data. International Journal of Remote Sensing, 26(22), 5013-5027.
39. Uysal, M., Toprak, A. S. & Polat, N. (2015). DEM generation with UAV Photogrammetry and accuracy analysis in Sahitler hill. Measurement, 73, 539-543.
40. Li, J. & Wong, D. W. (2010). Effects of DEM sources on hydrologic applications. Computers, Environment and Urban Systems, 34(3), 251-261.
41. Walker, J. P. & Willgoose, G. R. (1999). On the effect of digital elevation model accuracy on hydrology and geomorphology. Water Resources Research, 35(7), 2259-2268.

42. Saksena, S., & Merwade, V. (2015). Incorporating the effect of DEM resolution and accuracy for improved flood inundation mapping. Journal of Hydrology, 530, 180-194.
43. Jeon, J. H., Ham, J. H., Chun, G. Y. & Kim, S. J. (2002). Effects of DEM Resolution on Hydrological Simulation in, BASINS-BSPF Modeling. *Magazine of the Korean Society of Agricultural Engineers, 44(7),* 25-35.
44. Hancock, G. R. (2005). The use of digital elevation models in the identification and characterization of catchments over different grid scales. Hydrological Processes: An International Journal, 19(9), 1727-1749.
45. Mohanty, M. P., Nithya, S., Nair, A. S., Indu, J., Ghosh, S., Bhatt, C. M., ... & Karmakar, S. (2020). Sensitivity of various topographic data in flood management: Implications on inundation mapping over large data-scarce regions. Journal of Hydrology, 590, 125523.
46. Dixon, B & Earls, J. (2009). Resample or Not?! Effects of resolution of DEMs in watershed modeling. *Hydrological Processes: An International Journal*, 23(12), 1714-1724.
47. Sorensen, R. & Seibert, J. (2007). Effects of DEM resolution on the calculation of topographical indices: TWI and its components. Journal of Hydrology, 347(1-2), 79-89.

International Journal of Engineering and Geosciences
https://dergipark.org.tr/en/pub/ijeg
e-ISSN 2548-0960

Seasonal analysis and mapping of air pollution (PM10 and SO_2) during Covid-19 lockdown in Kocaeli (Türkiye)

Burak Kotan [*1], **Arzu Erener** [2]

[1]*Kocaeli University, Graduate School of Natural and Applied Sciences, Department of Geodesy and Geoinformation Engineering, Türkiye*
[2]*Kocaeli University, Faculty of Engineering, Department of Geomatics Engineering, Türkiye*

Keywords
Air Pollution
Covid-19
IDW
Pollution Map
Temporal Change

Research Article
DOI: 10.26833/ijeg.1111699

Received: 30.04.2022
Accepted: 13.08.2022
Published: 19.10.2022

Abstract

The Covid-19 epidemic has adversely affected the world in terms of health, education, economic, tourism, social and psychological. During to the epidemic, different measures were taken to prevent the epidemic, such as travel bans, curfews, stopping in production. These measures have reduced and improved air pollution. Within the scope of this study, the change in air pollution in Kocaeli between 2019 and 2021 was examined monthly. PM10 and SO2 maps were created with inverse distance weighted (IDW) technique using geographic information systems technology (GIS). The year 2020, when Covid-19 measures were taken, was compared with 2019 and 2021. Change maps were created by taking the difference between 2020-2019 and 2021-2020 with GIS technology. As a result of the research, it was determined that the level of air pollution decreased in 2020. On the contrary, in 2021, an increase in air pollution levels was observed. In the study, a decrease was observed in PM10 concentration during the Covid-19 lockdowns, however a decrease was not observed for SO_2.

1. Introduction

In the last days of December 2019, it was reported that the novel coronavirus (2019-nCoV, or COVID-19) epidemic first broke out in Wuhan and has been spreading in whole China and the world. It was declared a pandemic by the WHO for the disease spread rapidly and turned into a global epidemic [1]. First, measures were taken by governments, such as personal hygiene, restrictions on human mobility, and social isolation. Within this scope, restrictions were imposed on public gatherings (entertainment, religious, political, business, sports, education), public transportation, some production facilities, and international and local travel around the world [2].

As Covid-19 cases started to be identified in Turkey's border neighboring countries (Iran, Iraq, Greece, Bulgaria), measures have started to be increased in Turkey. General information about the disease and the pandemic was published, and the public was informed with videos and posters. Hospitals that provide certain conditions in the country were defined as pandemic hospitals. The first coronavirus case in Turkey was detected on 10 March 2020 and the public was informed on 11 March. Since this date, restrictions include suspending education, bans on travel, stopping activities in places where people spend time together, switching flexible shift systems, banning risk group people from going out, and the lockdown has been taken. With the spread of the disease, restrictions continued [3-4].

Social isolation measures taken to prevent the spread of the virus did not only provide its progress but also affects the environment positively [2]. The isolation measures taken due to the Covid-19 epidemic adversely affected the country's economies and human activities. On the contrary, it has had a positive effect on the improvement of air quality thanks to reduced human activities and reduced pollutant emissions [5]. It is said that there are significant changes in air pollution within the scope of the measures taken due to the Covid-19 epidemic [6].

Urbanization with industrialization causes the population and the number of vehicles to increase in the world. One of these environmental problems is air pollution [7-8]. The primary pollutants in the atmosphere list as follows: particulate matter (PM), sulfur dioxide (SO_2), carbon monoxide (CO), carbon dioxide (CO_2), ozone (O_3), nitrogen dioxide (NO_2), nitrogen oxides (NO_X). WHO considers that using PM_{10} and SO_2 to measure air quality is enough [9]. World

* **Corresponding Author**
*(bkotan19@gmail.com) ORCID ID 0000-0003-2105-7498
(arzu.erener@kocaeli.edu.tr) ORCID ID 0000-0002-9168-4254

Cite this article
Kotan, B., & Erener, A. (2023). Seasonal analysis and mapping of air pollution (PM10 and SO_2) during Covid-19 lockdown in Kocaeli (Türkiye). International Journal of Engineering and Geosciences, 8(2), 173-187

Health Organization list premature deaths, lung cancer deaths, acute respiratory infections, strokes, and chronic obstructive pulmonary disease as the deaths caused by air pollution [10].

It is aimed to examine the effect of the restrictions taken during the Covid-19 period on air pollution by examining the change in air pollution in Kocaeli, one of the important industrial cities of Turkey in this study.

1.1. Covid-19 and Air Pollution

Measures such as reducing human activities and reducing pollutant emissions taken to control the pandemic are important in terms of improving air quality. Studies within the scope of this purpose were examined in the literature. Sahrei et al. [11] determined that there was a 90% diminished in the use of public transport during the Covid-19 quarantine period. They confirmed reductions in air pollutants at the same time. Vega et al. [12] conducted research in Mexico City, London, and Delhi 2021. They confirm that Covid-19 restrictions reduced traffic in the urban area and improved air quality. Gouda et al. [1] study for the city of Bangalore, confirmed reductions in air pollutant concentrations during the Covid-19 quarantine period compared to the previous year. In their study conducted in many parts of India in 2022, Marwah and Agrawala confirm that air pollutants reduce according to 2019 data [2]. In another study conducted in India, it was concluded that $PM_{2,5}$, $PM_{10,}$ and NO_2 decreased within the scope of Covid-19 measures. It was concluded that the air quality has improved significantly in the city of Delhi [6]. They observed the effect of air pollution. They examined the quarantine period that they divided into 6 parts in Iraq. In this study, they found that the air quality improved as a result of the reduction in human activities in Iraq [5]. Yang et al. [13] conducted research within the scope of Covid-19. They ascertained a decrease in $PM_{2,5}$, PM_{10}, $NO_{2,}$ and CO levels as a result of studies carried out in different parts of the world. They found that no improvement could be detected in SO_2 and O_3 levels. They examined $PM_{2.5}$ changes during Covid-19. As a result of the study, it was determined that the highest decrease was in America, Asia, and Africa. The highest decrease was found in Bogotá, Colombia with 57% [14]. Özel et al. [15] studied in the Çernezköy organized industrial zone in 2021. The temporal variation of the air quality index was examined in the study. It was observed that the air quality index was at a good level compared to previous years at the time of the restrictions due to the pandemic. Collivignarelli et al. studied air quality during the Covid-19 quarantine period in Milan. They detected a decrease in the concentration of most pollutants such as PM_{10}, $PM_{2,5}$, and CO. But they did not see a decrease in SO_2 [16]. Kumari and Toshniwal researched Beijing, Bengaluru, Delhi, Las Vegas, Lima, London, Madrid, Moscow, Mumbai, Rome, Sao Paulo, and Wuhan in 2020. They found that $PM_{2.5}$, $PM_{10,}$ and NO_2 parameters decreased during the Covid-19 lockdowns. They did not find a regular change in SO_2 and O_3 parameters [17]. Lian et al. [18] in their study in Wuhan, found that the air quality index decreased significantly. Adams [19] researched it in Ontario, Canada in 2020. Adams [19] studied air pollution during the Covid-19 state of emergency. As a result of the study, Adams [19] observed that NO_2 and NO parameters decreased.

2. Method

2.1. Study area

Kocaeli city is located in Marmara Region. Figure 1 shows the location of Kocaeli city. It is the 10th most populous city in Turkey and the 2nd city in terms of population density. According to 2021 TUIK data, it has a population of 2.033.441 people according to the data of 2021 and an area of 3397 km^2 [20].

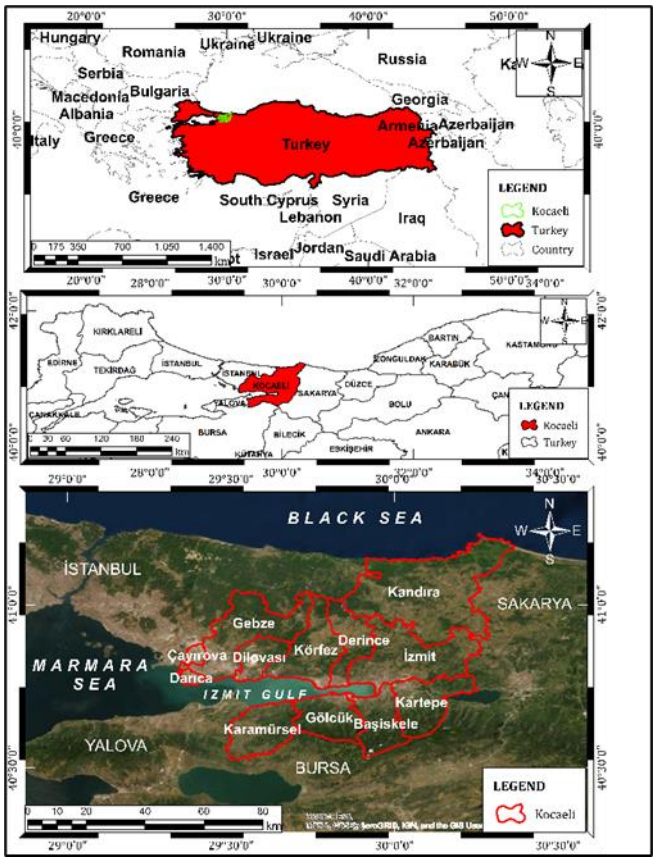

Figure 1. Kocaeli location map

It is among the important industrial cities of Turkey. There are sectors such as the automotive industry, iron-steel, chemistry, and plastics in the city. It is at a crossroads between the Asian and European continents. It has a busy sea route with the Körfez Port, which is a natural port. Kocaeli has research-development and innovation centers and ranks 2nd in Türkiye.

2.2. Data set

Data used in the study were obtained from the National Air Quality Monitoring Network. PM_{10} and SO_2 concentration data, which are pollution parameters, were provided daily for the years 2019-2021 [21]. The monthly averages of the pollution parameters were calculated from 10 stations (Figure 2).

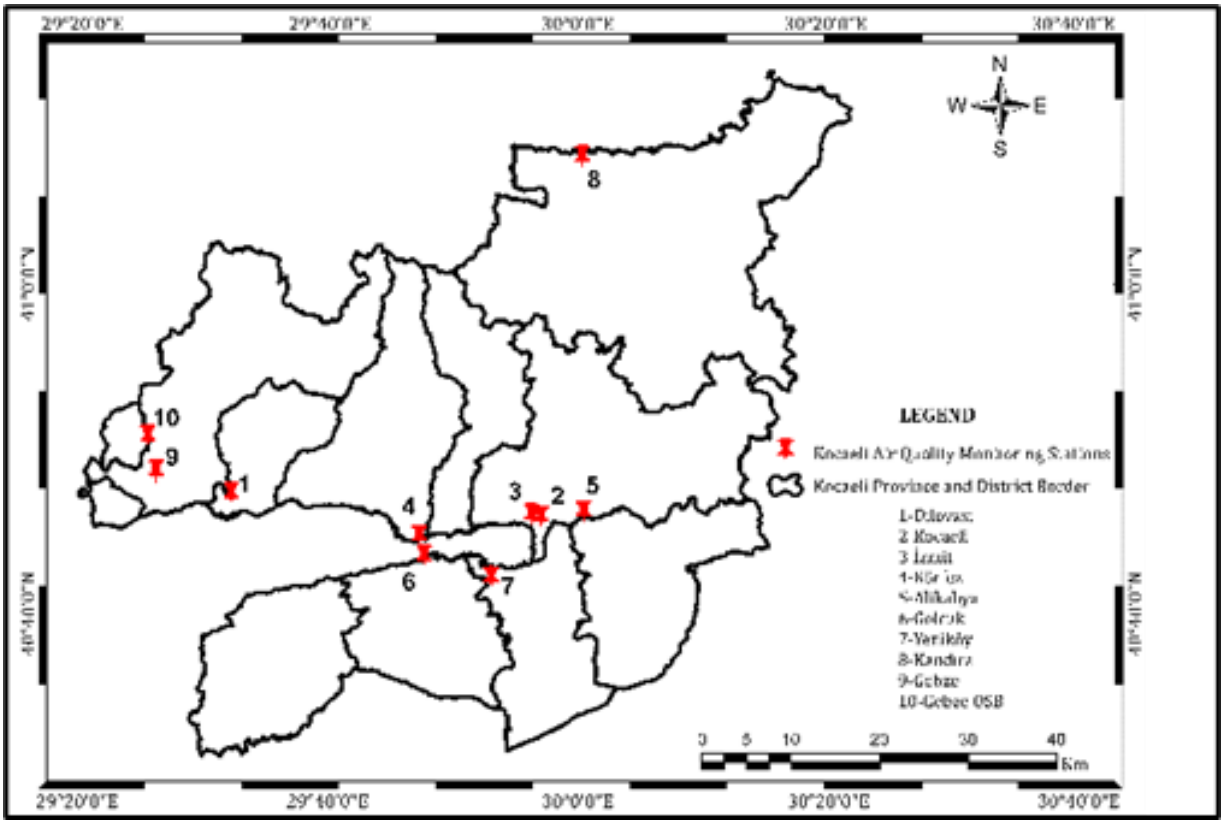

Figure 2. Kocaeli air quality monitoring stations

The monthly average PM_{10} and SO_2 concentration data between 2019 and 2021 are shown in Table 1.

Table 1. Monthly average concentration values

Months	Polluting	2019	2020	2021
January	PM_{10}	40.03	35.48	45.65
	SO_2	8.64	9.66	11.72
February	PM_{10}	45.73	36.23	51.89
	SO_2	8.60	11.21	12.30
March	PM_{10}	47.53	41.36	42.36
	SO_2	9.67	11.09	15.46
April	PM_{10}	41.84	31.73	43.19
	SO_2	6.61	10.65	14.09
May	PM_{10}	41.25	29.71	38.92
	SO_2	9.08	10.02	11.74
June	PM_{10}	33.77	28.64	35.10
	SO_2	5.04	6.18	11.79
July	PM_{10}	26.90	25.60	34.21
	SO_2	4.29	4.50	6.29
August	PM_{10}	27.47	27.71	36.05
	SO_2	4.11	7.88	6.34
September	PM_{10}	30.05	37.28	29.15
	SO_2	5.32	7.73	7.26
October	PM_{10}	38.49	52.61	34.14
	SO_2	6.81	11.52	10.42
November	PM_{10}	50.28	43.24	59.94
	SO_2	10.89	7.64	16.34
December	PM_{10}	43.96	45.88	37.48
	SO_2	10.81	11.62	14.11

2.3. Inverse Distance Weighted (IDW)

Inverse distance weighted (IDW) is one of the interpolation methods. This method aims to generate data by interpolation using sample points. This technique is based on over-weighting the nearby sampling points on the surface to be interpolated. The weight decreases as the sample point get farther away. It performs surface interpolation by taking the weighted average of the sample points with this method [22-23].

The IDW method is said to be more suitable for interpolating air pollution parameters. Jumaah et al. [24] studied the estimation of the air quality index. The IDW technique was used for the interpolation of the parameters for this study. Vorapracha et al. [25] studied interpolation methods. In the study, they produced values for PM_{10} by interpolation. They found that the best interpolation result was IDW [25].

Geographic information systems (GIS) are important for decision-makers to better interpret and visualize events and data [26-30]. It is also said that GIS is an important technology for air pollution [31-33] and natural disaster studies [34-36].

3. Results

3.1. Mapping of Air Pollution

Air pollution was mapped using the data of the measuring stations for Kocaeli province. Pollution was mapped using the IDW technique within ArcGIS 10.6.1. software.

Monthly maps of air pollution (PM_{10} and SO_2) between 2019 and 2021 were created and it was aimed to compare the months in terms of air pollution.

PM_{10} concentration maps for December, January, and February are shown in Figure 3.

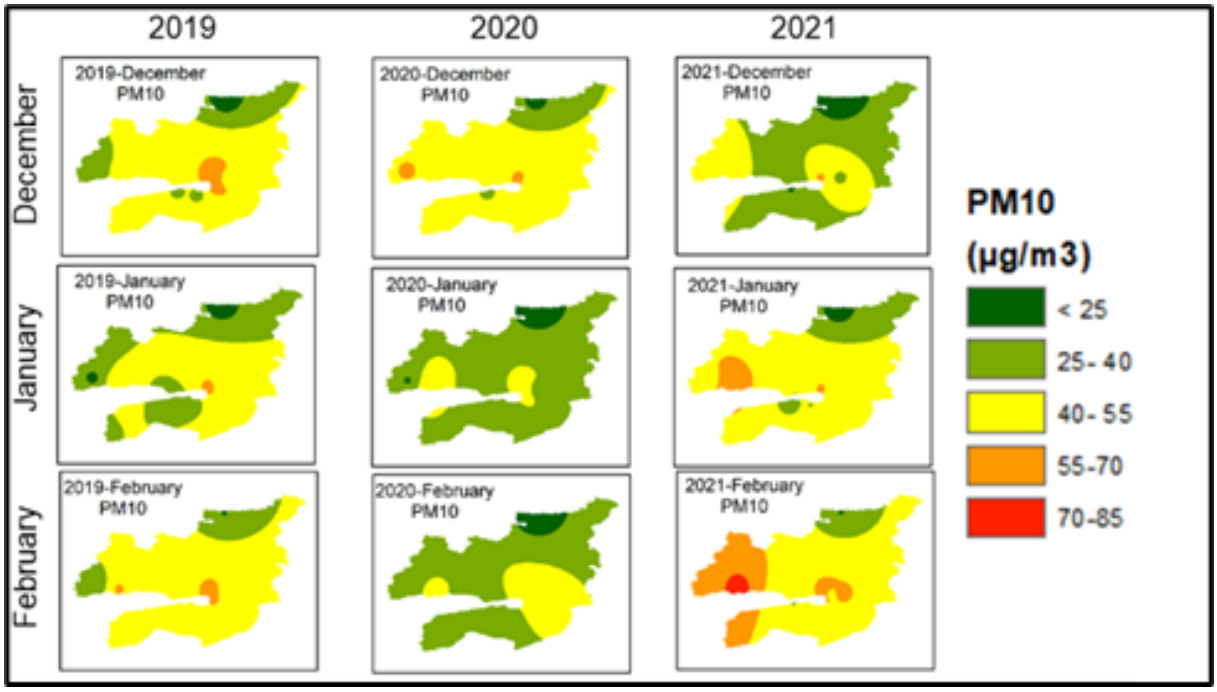

Figure 3. PM_{10} concentrations for winter

Winter term PM_{10} maps demonstrate a decrease in PM_{10} concentration in December 2021 compared to December 2019 and 2020. A decrease in PM_{10} concentration was observed in January and February 2020 compared 2019. On the contrary, PM_{10} concentration increased in January and February 2021 in the whole city and especially in the western part of Kocaeli. In addition, there is a lot of industrial density in this area. Therefore, it is a factor in the rise in pollutant concentrations. This can be considered as an indication that the covid measures are held more tightly in 2020 than in 2021. SO_2 concentration maps for December, January, and February are presented in Figure 4.

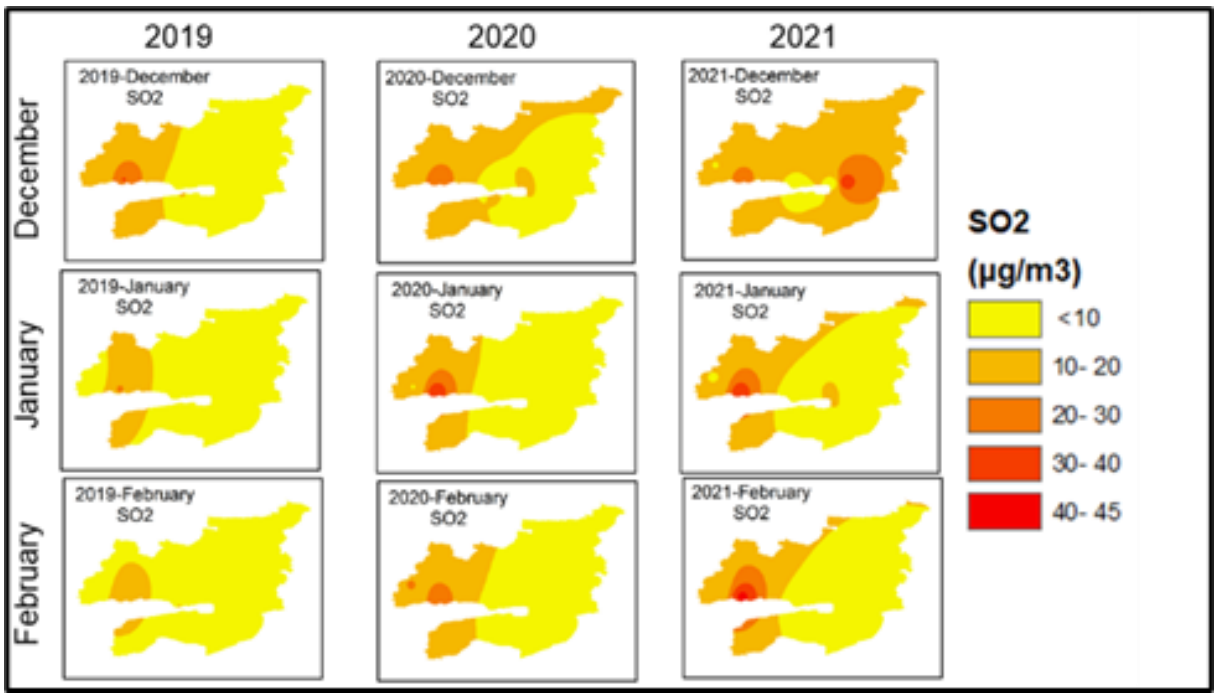

Figure 4. SO_2 concentrations for winter

The winter term SO_2 parameter concentration increased continuously from 2019 to 2021 in December, January, and February in western part of Kocaeli. In December 2021, it is observed that the SO_2 parameter values increased especially in the İzmit Kocaeli Bay end region. In addition, it can be said that this value has increased in an industrialized region Dilovası, in January and February of 2020 and 2021.

PM_{10} concentration maps for March, April and May are shown in Figure 5.

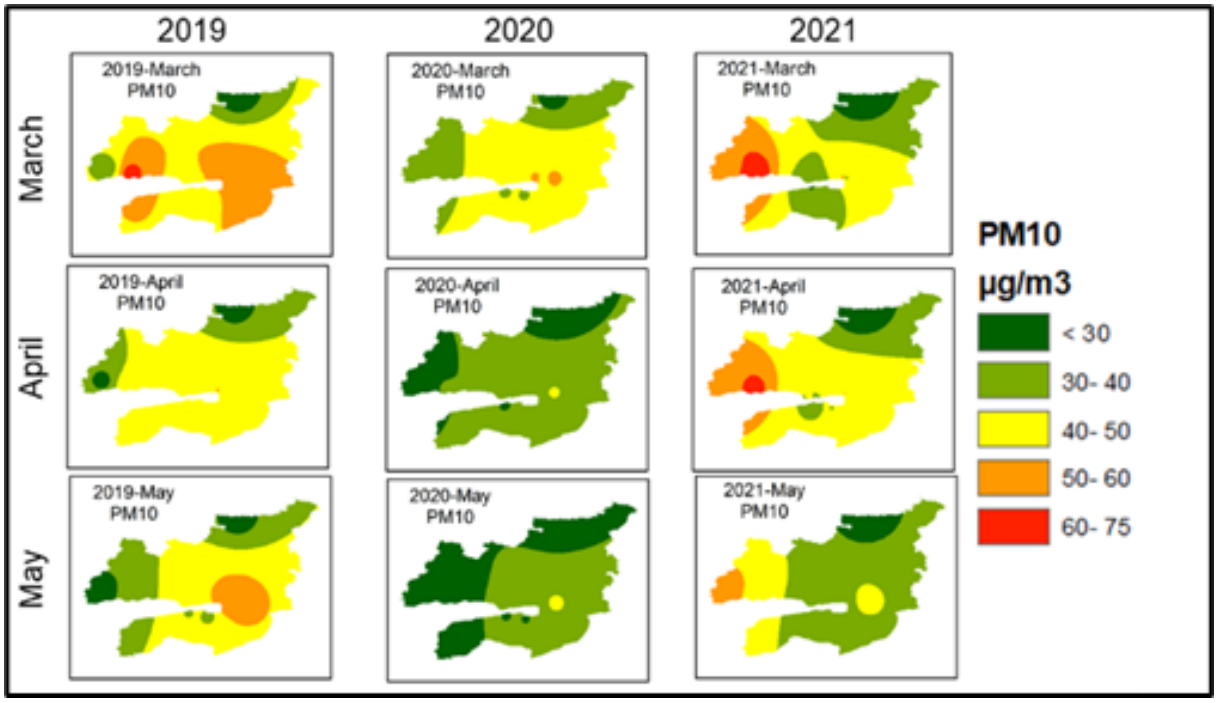

Figure 5. PM_{10} concentrations for spring

A notable reduction in PM_{10} concentration was observed in the spring season of 2020 compared to 2019. On the other hand, the PM_{10} concentration increased in 2021. March, April, and May of 2020 are the months with the most Covid-19 restrictions occurred. Under this case: It can be said that the reason for the PM_{10} decreases in 2020 might be Covid-19 restrictions.

SO_2 concentration maps for March, April, and May are shown in Figure 6.

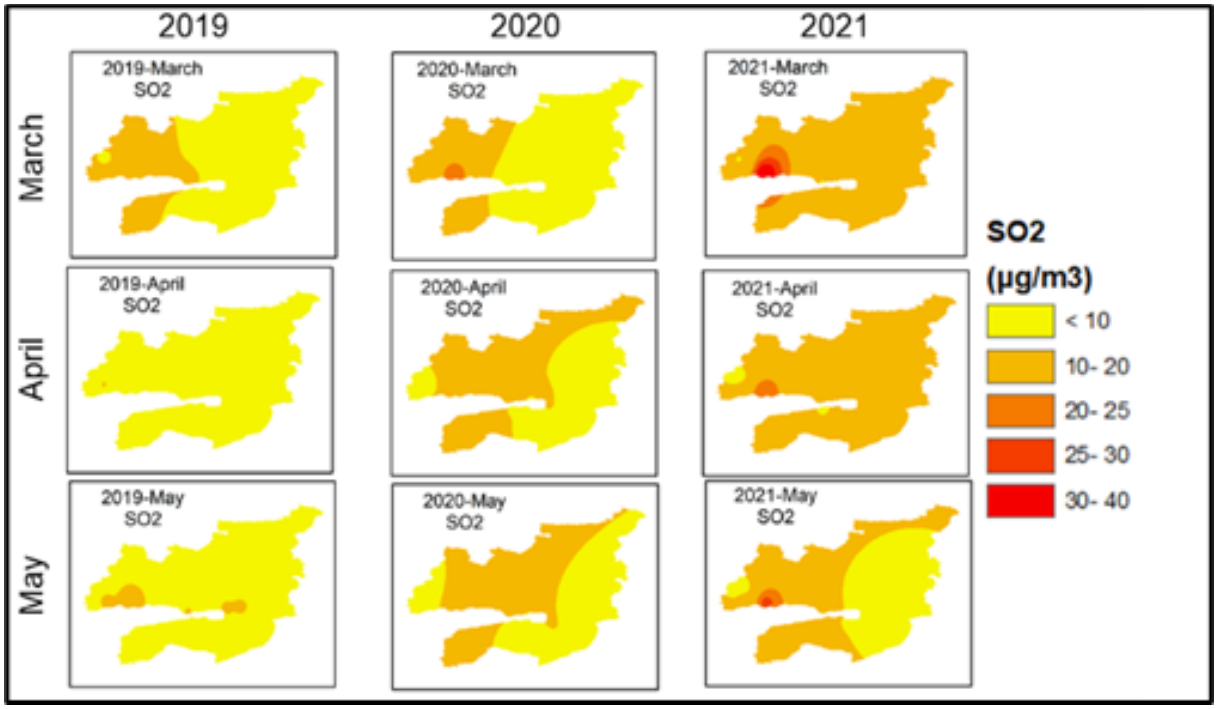

Figure 6. SO_2 concentrations for spring

The SO_2 parameter in the spring term increased continuously from 2019 to 2021. March is the month where the most SO_2 spread in the whole city especially in Dilovası.

PM_{10} concentration maps for June, July, and August are presented in Figure 7.

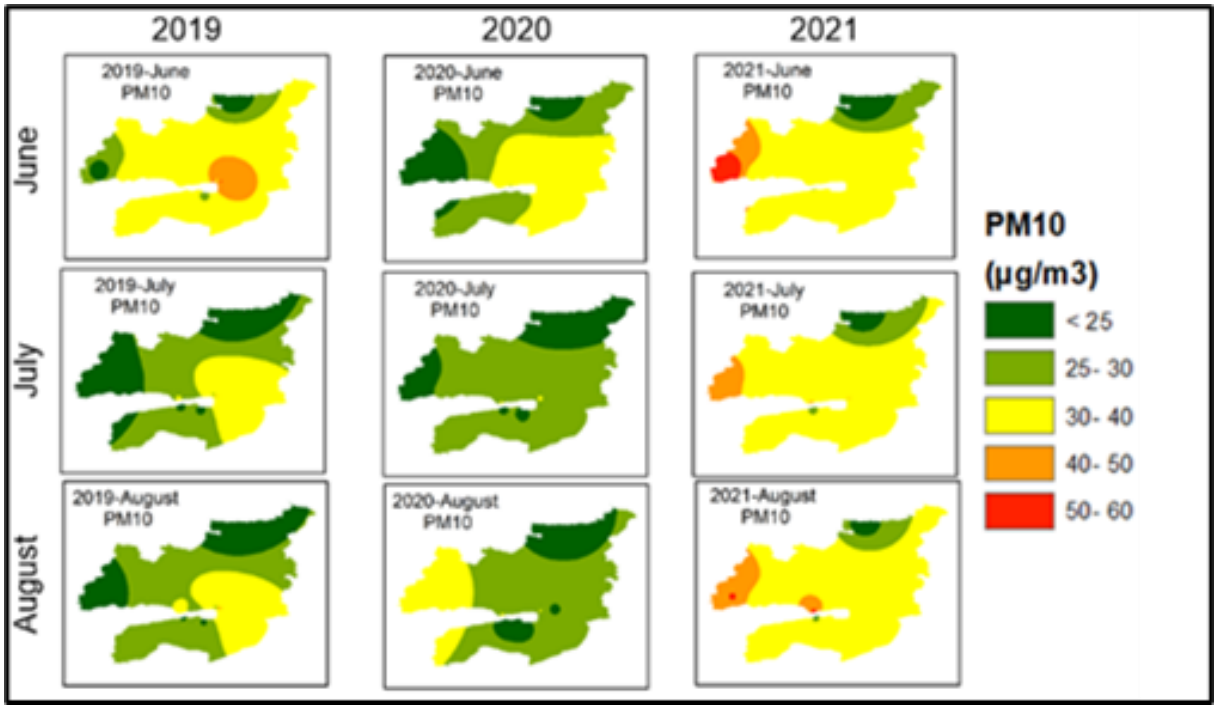

Figure 7. PM_{10} concentrations for summer

A significant decline in PM_{10} concentration in June, July 2020 compared to 2019 was observed in the whole city. There was no change in August 2019 compared to July 2019. Also, PM_{10} concentration increased in summer term in 2021 compared to 2020.

SO_2 concentration maps for June, July, and August are shown in Figure 8.

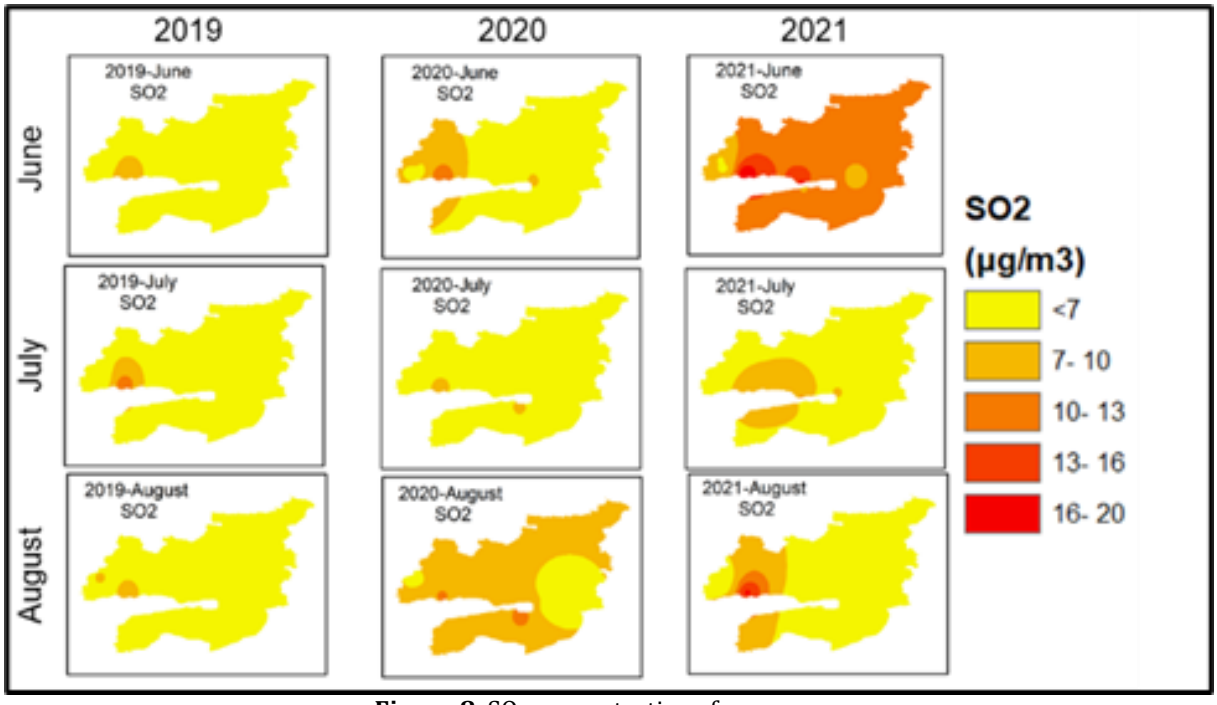

Figure 8. SO_2 concentrations for summer

The SO_2 parameter increased continuously from 2019 to 2021 in summer term, except for August. June 2021 was the month where highest SO_2 concentration was observed in the whole city. This might be due to reducing the covid restrictions in the beginning period of summer.

PM_{10} concentration maps for September, October, and November are shown in Figure 9.

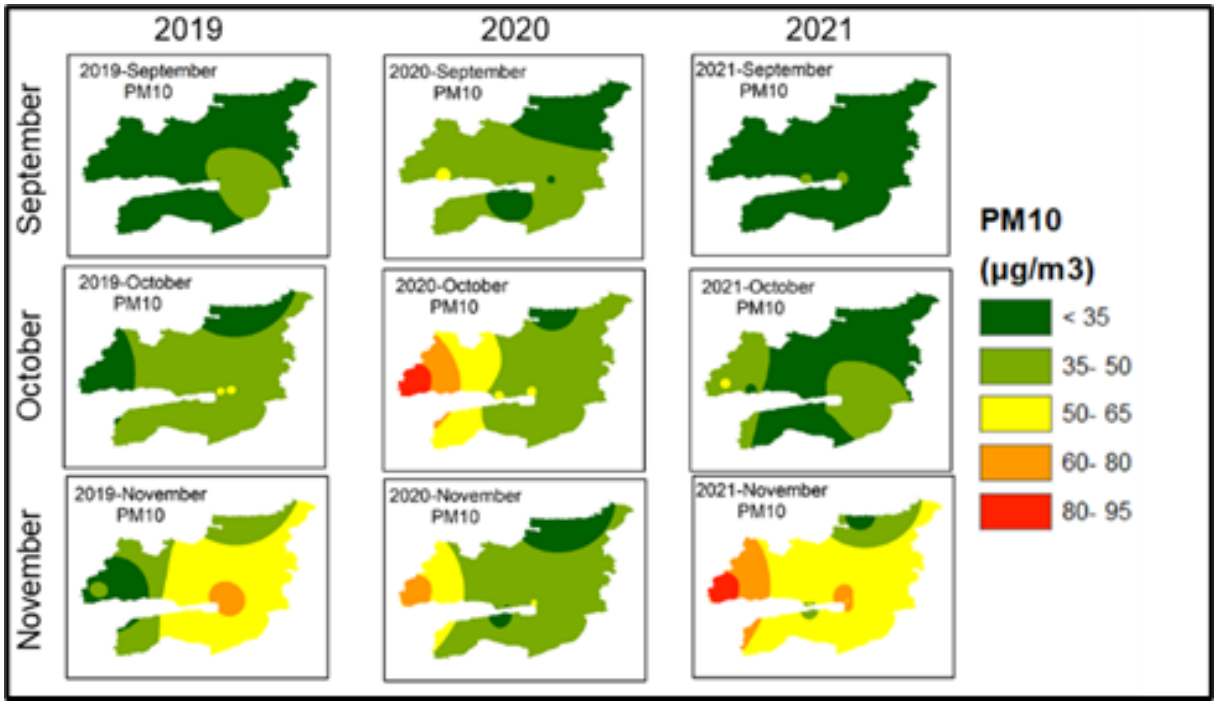

Figure 9. PM_{10} concentrations for autumn

The autumn term PM_{10} concentration for 2019, 2020, and 2021 was observed. An increase was identified in September and October 2020 compared to 2019 however, a decrease in PM_{10} concentration was founded in November 2020 compared to 2019. September 2021 is the month with the lowest PM_{10} spread throughout the city. September 2021, on the other hand, is the month with the lowest PM_{10} Emission throughout the city, however, in November, this value showed a gradual increase in the Gulf and its environs.

SO_2 concentration maps for September, October, and November are shown in Figure 10.

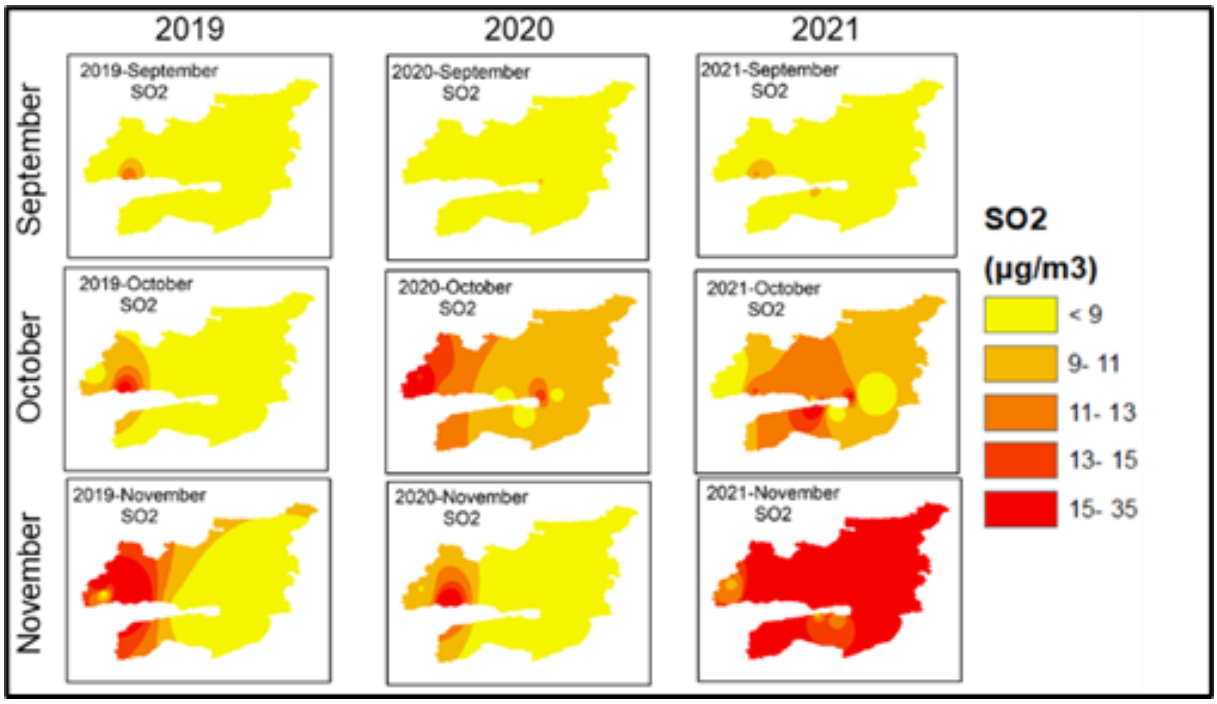

Figure 10. SO_2 concentrations for autumn

SO_2 concentration spread over Kocaeli was observed for 2019, 2020, and 2021 for the autumn term. An increase in SO_2 concentration in October 2020 and 2021 was observed compared to October 2019. A decrease in November 2020 compared to November 2019 was also identified in the eastern parts of the city. SO_2 concentrations reach highest values in the entire city surroundings in November 2021.

Temporal change maps will be more effective in visualizing concentration differences between months. These maps provide spatially the locations of decreases and increases of concentration.

3.2. Temporal Change Maps

The increase and decrease of PM_{10} and SO_2 concentration parameters obtained as a result of the study by months are show in Table 2 and Table 3 as percentages. The year 2020 has been compared with the data of 2019. Likewise, the year 2021 is compared with the data of 2020.

The maximum decrease in PM_{10} parameter in 2020 compared to 2019 was 27.97% in May. The maximum increase in PM_{10} parameter in 2020 compared to 2019 was obtained in October with 36.68%. The maximum decrease in PM_{10} parameter in 2021 compared to 2020 was seen in October with 35.11%. The maximum increase in PM_{10} parameter in 2021 compared to 2020 was seen in February with 43.23%.

In general, while decreases were observed in 2020 compared to 2019 for the PM_{10} parameter, there was an increase in the amount of concentration in 2021 compared to 2020.

The maximum decrease in SO_2 parameter in 2020 compared to 2019 was 29.85% in November. The maximum increase in SO_2 parameter in 2020 compared to 2019 was seen in August with 91.76%. The maximum decrease in SO_2 parameter in 2021 compared to 2020 was seen in August with 19.56%. The maximum increase in SO_2 parameter in 2021 compared to 2020 was seen in November with 114.03%. It was observed that there was a general upward trend for SO_2.

Overlay analysis was used for temporal change maps. As a result, raster maps were subtracted from each other, and change maps were obtained. The map of 2019 was subtracted from the 2020 map. Likewise, the map of 2020 was subtracted from the 2021 map. At the end of the proses, 2 new change maps were obtained. The negative values on the maps show the areas where the concentration value decreased compared to the previous year, while the positive values show the areas where the concentration value increased compared to the previous year. The temporal chance Figures also includes the PM10 or SO_2 concentration for the whole months.

The temporal change maps for PM_{10} concentration between 2019-2020 and 2020-2021 for December, January, and February are shown in Figure 11.

Figure 11 presents the concentration of change by years and the trend of change for each month of the years. When the spatial change maps are examined, it is observed that the decrease from December to February from 2019 to 2020 spread gradually to the city. In February, it is observed that the PM_{10} value has decreased all around the city. On the other hand, when the difference in the concentration distributions of 2020 and 2021 is analyzed spatially, a decrease was observed in the whole city in November, but this difference turned into an increase in January and February. Graphically, PM_{10} 2019 and 2020 tend to decrease from January to August. In this period, 2020 values are lower than 2019. After August, the values of 2020 and 2019 have returned to an increasing trend and 2020 shows this increasing trend more rapidly. Similarly, the PM_{10} value observed between months in 2020 and 2021 shows a downward trend until September, and the values for 2020 are lower than 2021. It has returned to an increasing trend since August 2020 and September 2021. After these months, the values turned to a rapidly increasing trend and decreased in December.

The temporal change maps and change trends over months for SO_2 concentration between 2019-2020 and 2020-2021 for December, January and February are shown in Figure 12.

Figure 12 presents the decreasing concentration mostly on the eastern part of the city in January (2020-2019). However, the SO_2 concentration tends to increase on winter term of 2021-2020 terms. The increasing trend also may be observer from the graphics of SO_2 between 2021-2020.

The temporal change maps and change trends over months for PM_{10} concentration between 2019-2020 and 2020-2021 for Marc, April, and May is shown in Figure 13.

Table 2. PM_{10} concentration difference

	PM_{10} (%)	
Month	2020-2019	2021-2020
January	-11.38	28.69
February	-20.78	**43.23**
March	-12.97	2.43
April	-24.16	36.14
May	**-27.97**	30.97
June	-15.19	22.53
July	-4.86	33.64
August	0.89	30.07
September	24.07	-21.80
October	**36.68**	**-35.11**
November	-14.01	38.63
December	4.36	-18.32

Table 3. SO_2 concentration difference

	SO_2 (%)	
Month	2020-2019	2021-2020
January	11.87	21.25
February	30.32	9.76
March	14.75	39.36
April	61.08	32.29
May	10.31	17.13
June	22.68	90.73
July	4.86	39.97
August	**91.76**	**-19.56**
September	45.30	-6.05
October	69.12	-9.57
November	**-29.85**	**114.03**
December	7.54	21.39

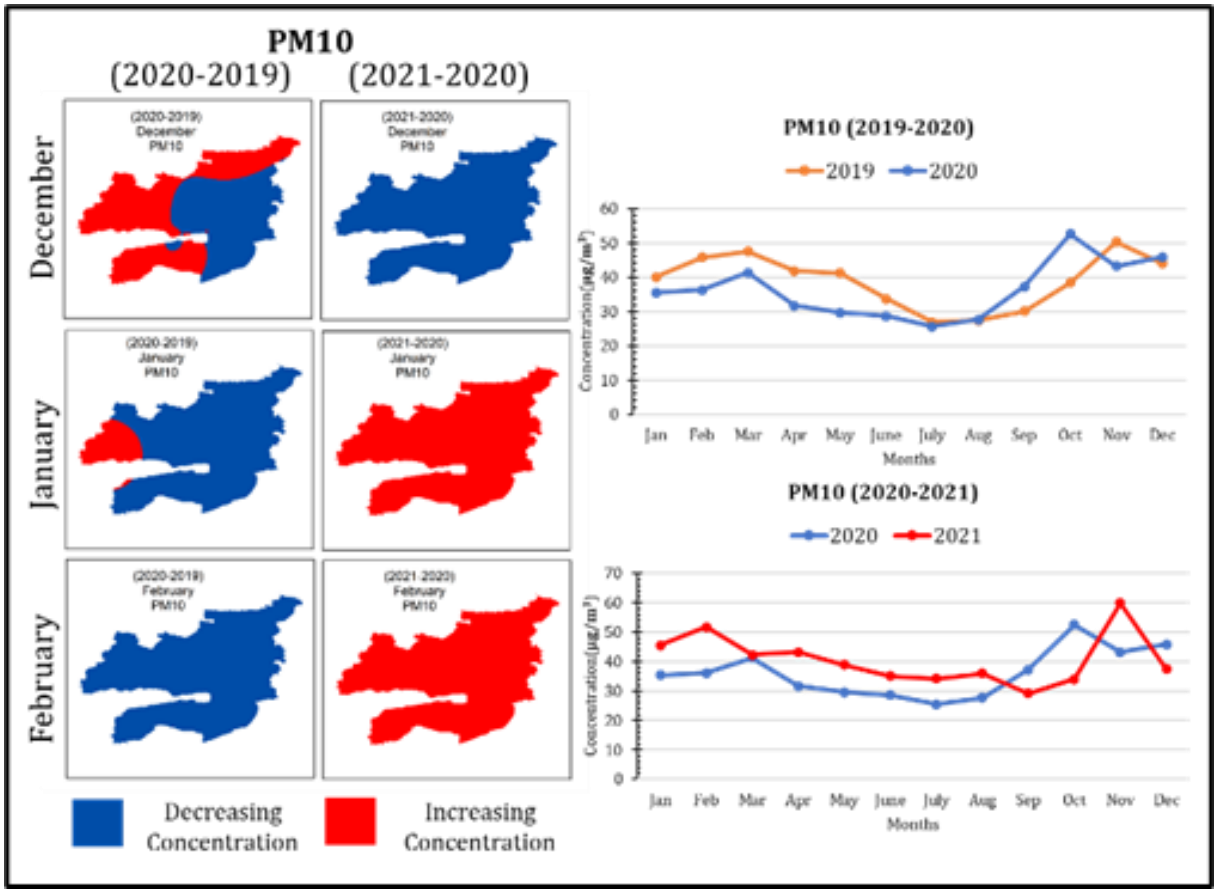

Figure 11. PM_{10} winter concentration temporal change map and trend over months

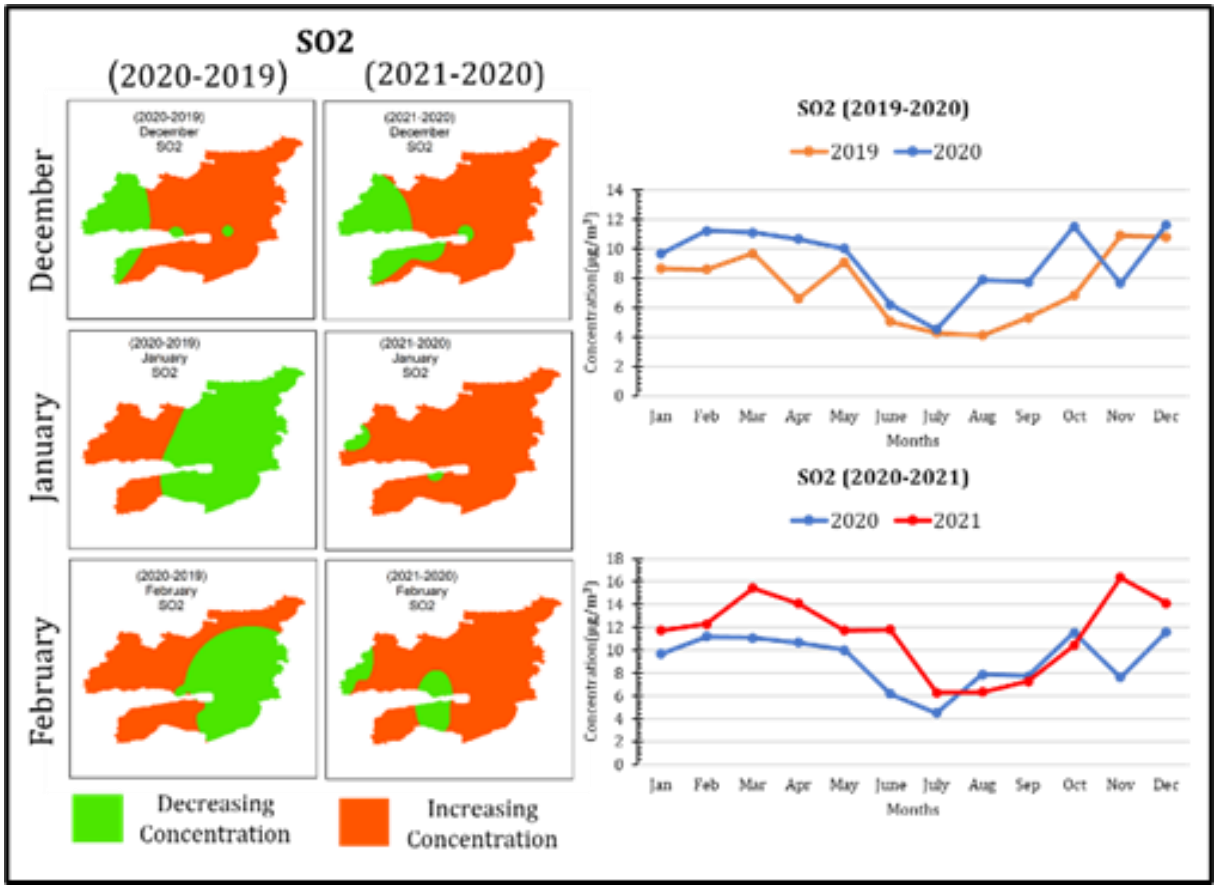

Figure 12. SO_2 Concentration winter temporal change map and trend over months

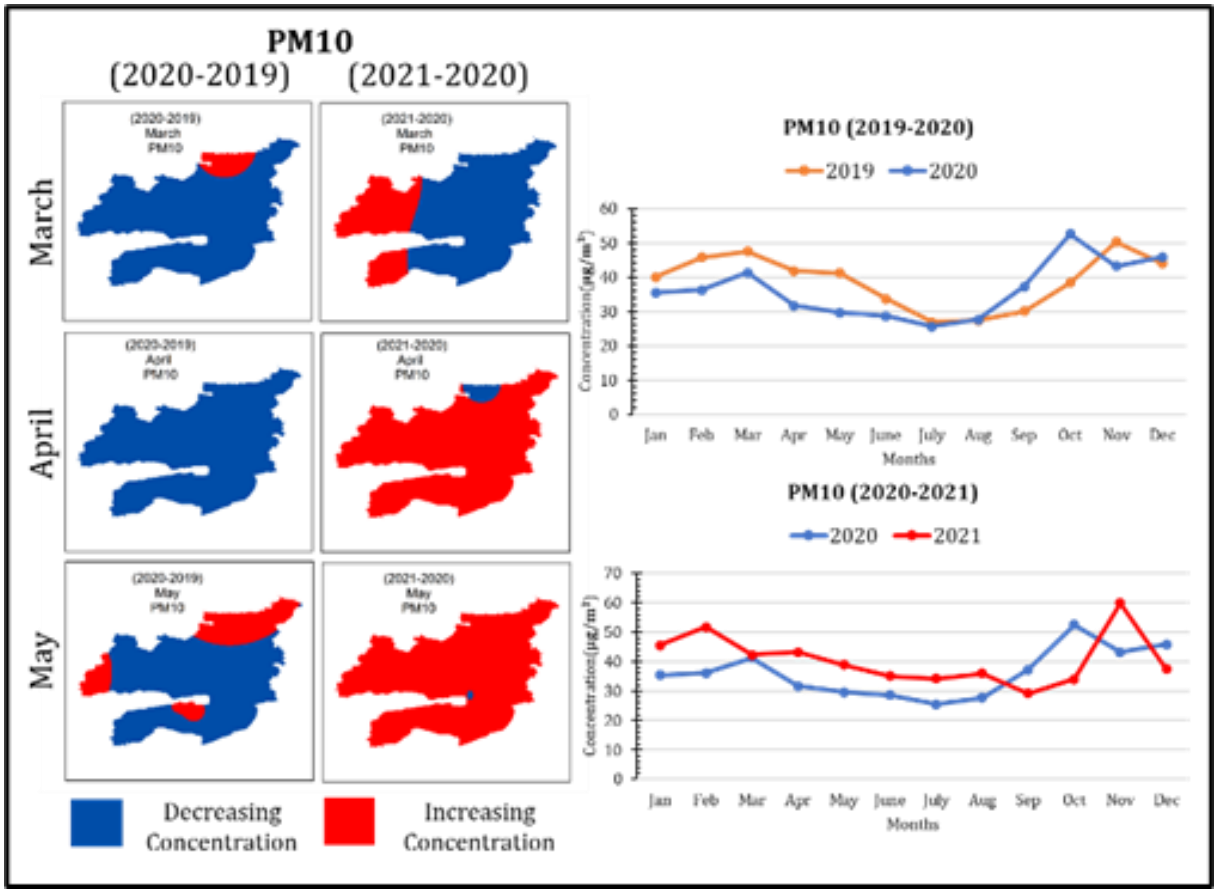

Figure 13. PM_{10} spring concentration temporal change map and trend over months

The spring term indicates a decrease of PM_{10} all over the city especially in April between 2020-2019. Similarly, in March and May it tend to decrease in the city center and regions around the gulf. The difference map 2020-2021 indicates that the PM_{10} tend to increase all over the city in April and May. However, in March, it represents a decrease of PM_{10} especially on eastern part of the city. The Graphics indicates a decreasing trend for all years in spring term. The spring term 2019 and 2021 have a higher concentration of PM_{10} values compared to 2020.

The temporal change maps and change trends over months for SO_2 concentration between 2019-2020 and 2020-2021 for March, April, and May are shown in Figure 14.

The spring term indicates an increase of SO_2 all over the city between 2020-2019 and 2021-2020 change maps. In March (2020-2019) and May (2021-2020) it tends to decrease in the city center and regions around the gulf. The Graphics indicates higher concentrations of SO_2 in 2021 compared to other years.

The temporal change maps and change trends over months for PM_{10} concentration between 2019-2020 and 2020-2021 for June, July, and August is shown in Figure 15.

Figure 15 presents the concentration of change for the summer term by years and the trend of change for each month of the 2019, 2020 and 2021 years. The spatial change maps are examined, it is observed that the PM10 concentration tend to decrease for 2020-2019 change maps, on the contrary it tends to increase on 2021-2020 change maps. It was observed that the PM10 concentrations in the summer period did not show much change in the graphics compared to the other seasons and were stable.

The temporal change maps and change trends over months for SO_2 concentration between 2019-2020 and 2020-2021 for June, July, and August is shown in Figure 16.

The summer term indicates an increase of SO_2 all over the city between 2020-2019 and 2021-2020 change maps except August 2021-2020. In August (2021-2020) it is observed that it is worth falling in almost the entire city. The increase trend of summer term can also be observed from the graphics for all years.

The temporal change maps and change trends over months for PM_{10} concentration between 2019-2020 and 2020-2021 for September, October, and November is shown in Figure 17.

The autumn term indicates an increase of PM_{10} all over the city except eastern regions of gulf especially in September and October between 2020-2019. On the contrary, it tends to decrease in all over the city between 2021-2020 change maps on these months. The difference map of November 2020-2019 indicates that the PM_{10} tend to decrease especially on eastern parts of the region, however it increased all over the city at 2021-2020 on November. The Graphics indicates a sudden trend of increase for all years on autumn term. 2020 have a higher concentration of PM_{10} values compared to 2019 and 2021 for autumn term.

The temporal change maps and change trends over months for SO_2 concentration between 2019-2020 and 2020-2021 for September, October and November is show in Figure 18.

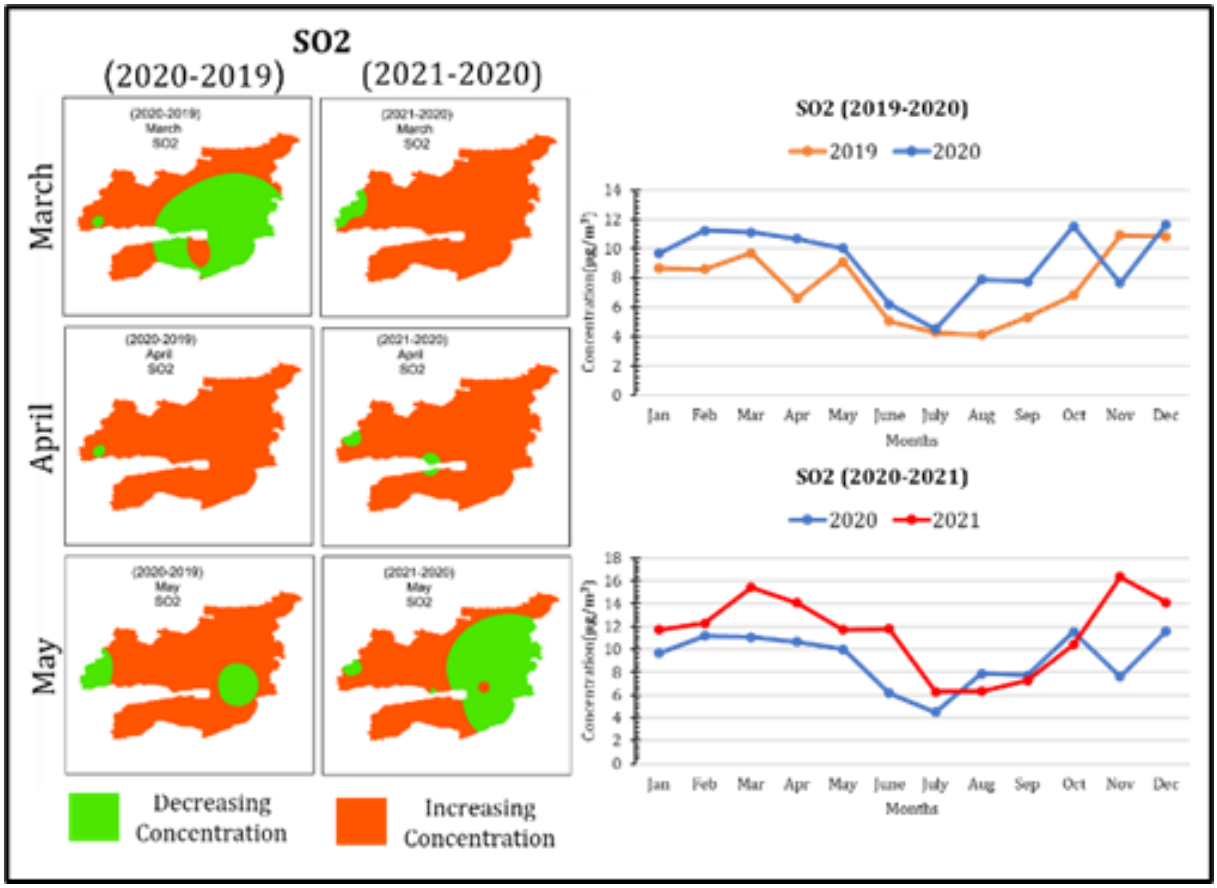

Figure 14. SO_2 Concentration spring temporal change map and trend over months

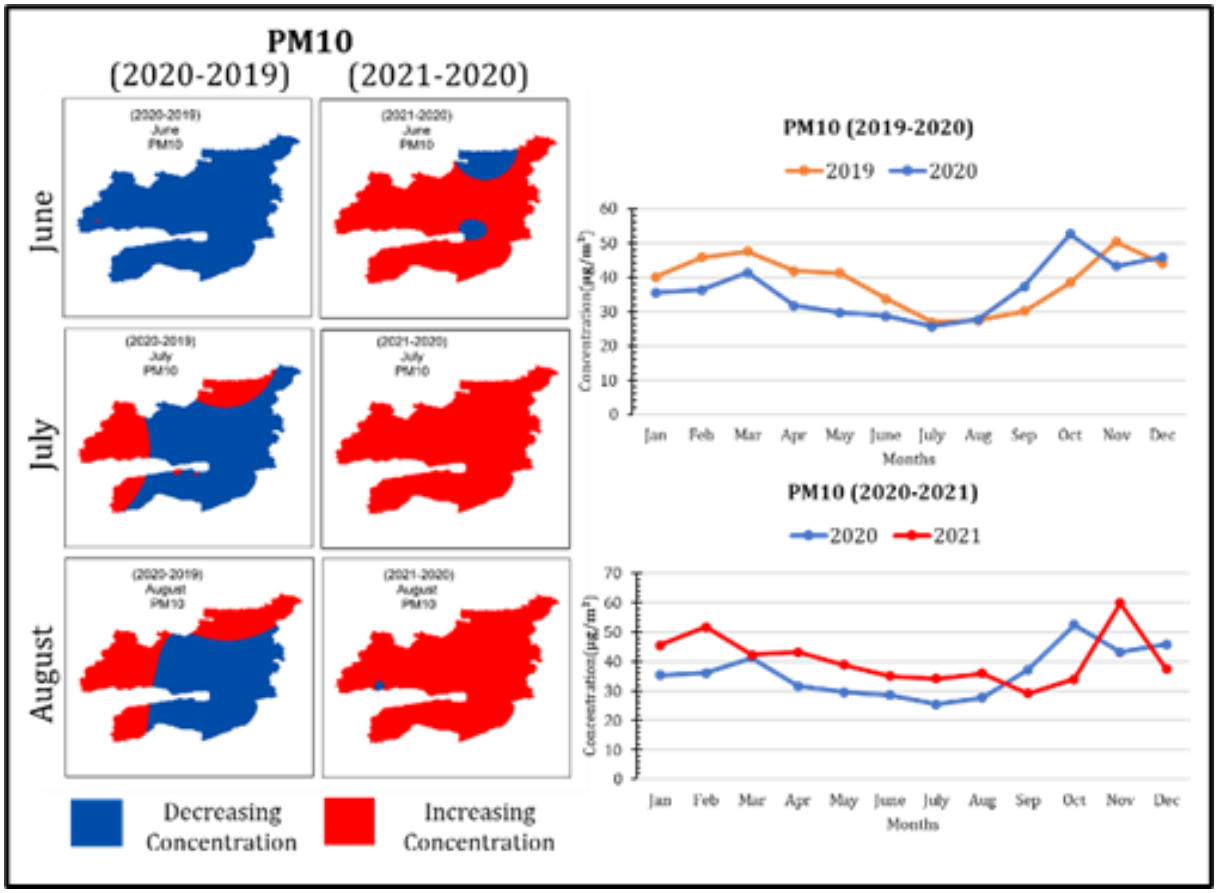

Figure 15. PM_{10} Concentration summer temporal change map and trend over months

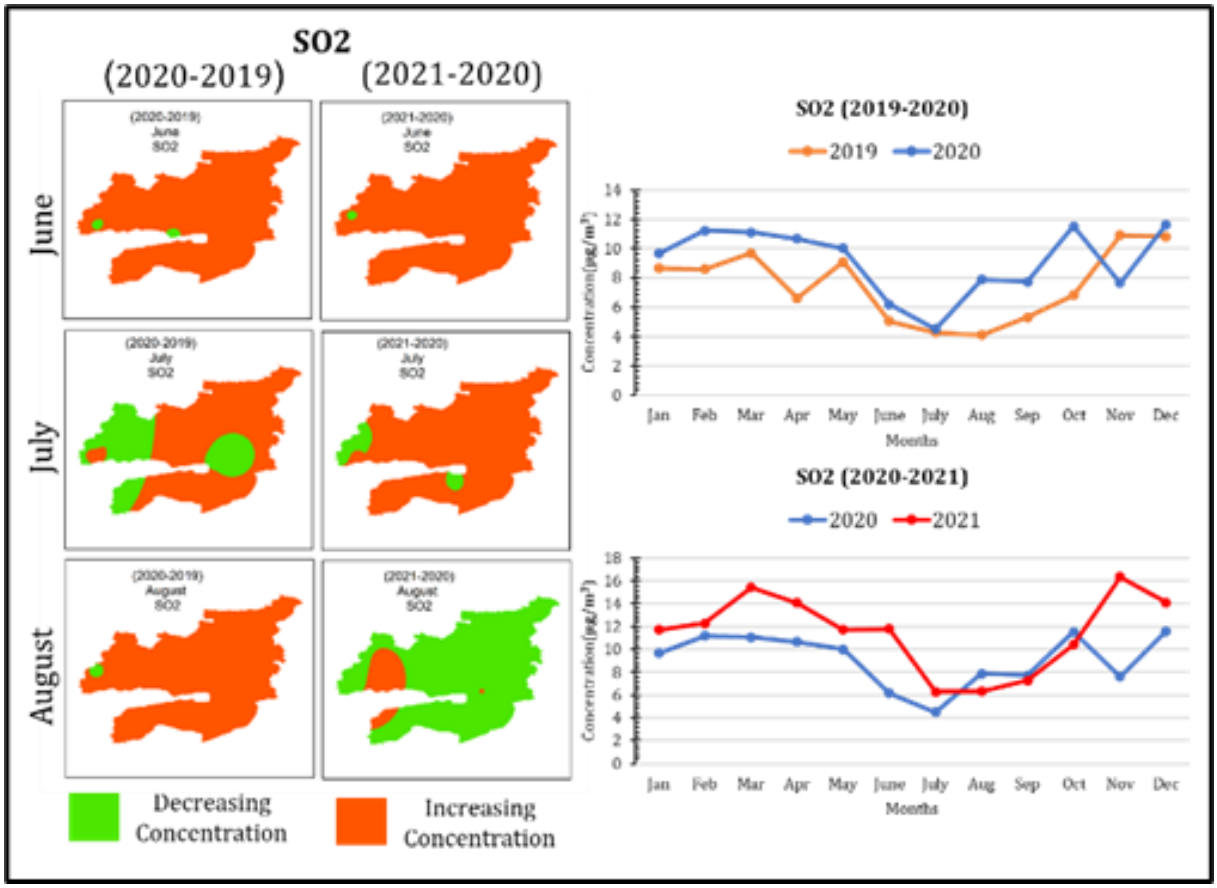

Figure 16. SO_2 Concentration summer temporal change map

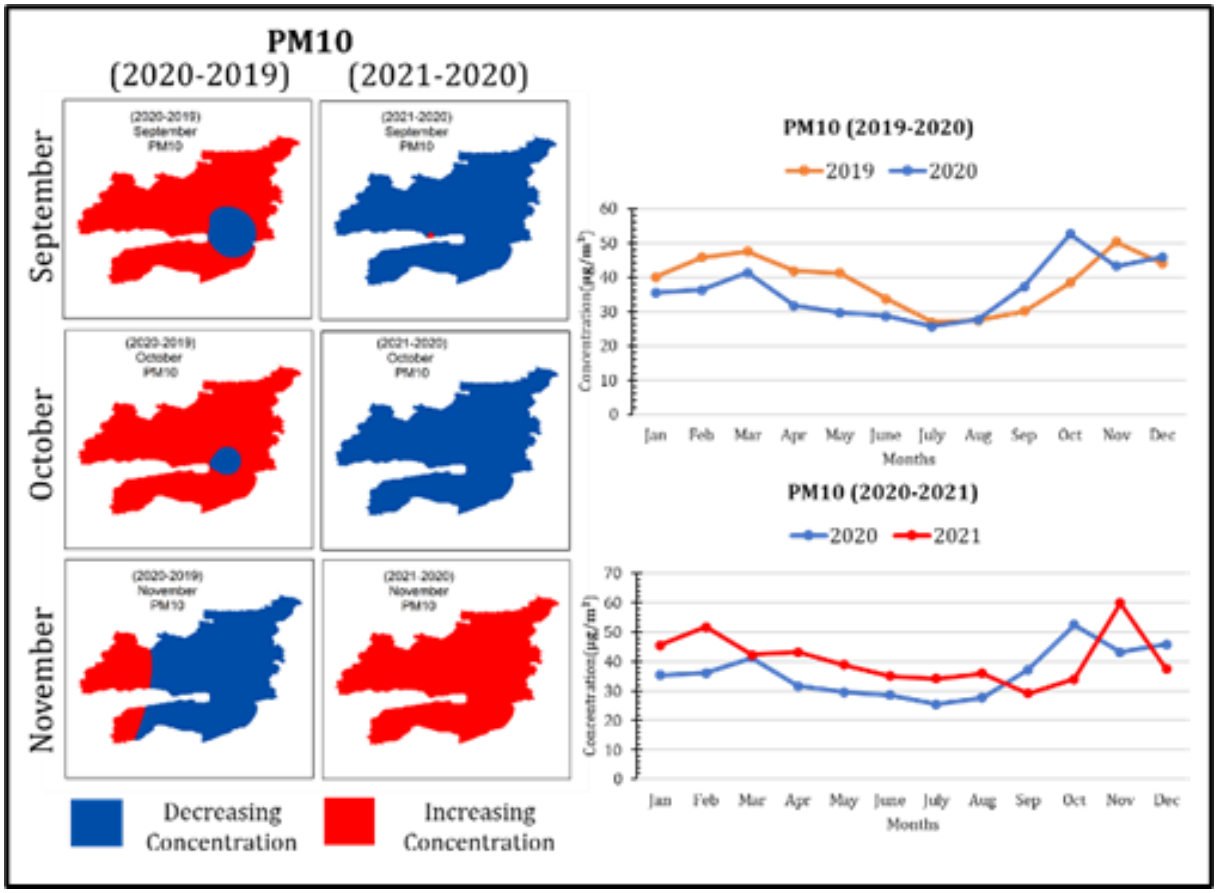

Figure 17. PM_{10} Concentration autumn temporal change map

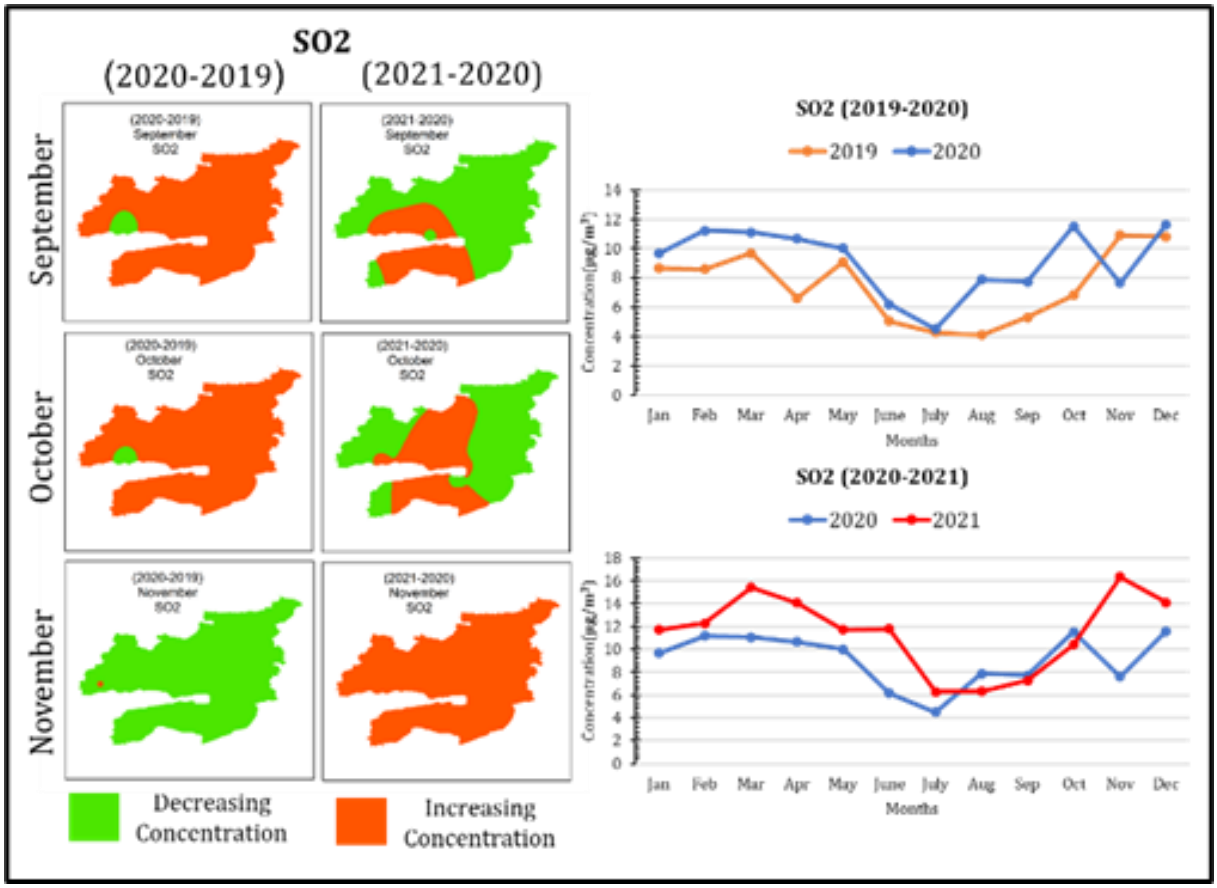

Figure 18. SO_2 Concentration autumn temporal change map

The autumn term indicates an increase of SO_2 all over the city between 2020-2019 change maps except November. In November (2020-2019) it is observed that it is worth falling in almost the entire city. 2021-2020 change maps for September and October indicate an increase of SO_2 mostly on the mid parts of the city. And it indicates an increasing concentration in November all over the city. The increase trend of autumn term can also be observed from the graphics for all years.

4. Discussion

The results of the study showed that the PM_{10} concentration, which is one of the air pollution parameters, decreased during the Covid-19 lockdown. As a result of this study, it is seen that the lockdown, restrictions on population mobility, curfews the pandemic have a positive effect on air pollution. Considering the results of the study, it was observed that the PM_{10} parameter showed serious decreases especially in March, April and May of 2020, when the measures were taken. In addition, no decrease in SO_2 concentration was detected during the Covid-19 lockdowns. These results support other studies as well. In these studies researchers conducted studies that proved that air pollution decreased and the amount of PM_{10} concentration decreased during the Covid-19 lockdowns [1,2,5,6,11,12,14,15,18,19]. In addition, [13,16,17] reported that air pollution decreased during the Covid-19 lockdowns, while PM_{10} concentration decreased, but they did not observe a decrease in SO_2 concentration.

The study reveals pollution maps in 2021. From this point of view, it is seen that Kocaeli air pollution has increased gradually compared to 2019 and 2020. Local governments should work to prevent air pollution.

The usability of GIS technology is also effective in terms of assessing the situation of air pollution, mapping it and interpreting it by visualizing it.

In terms of developing and improving this study, due to the uneven distribution of the current stations, it is believed that high-quality data will be collected by expanding the number of stations in a limited number and adding stations that appropriately reflect the research region. In recent years, satellite data and remote sensing technology have made it possible to continuously collect data on air pollution. These studies, which are based on data from the stations, may be contrasted with data on air pollution obtained through the use of satellite data and the study's findings. In addition, the study can be improved by making comparisons with different interpolation methods in future studies. By working on modeling of air pollution, it can be facilitated to control pollution with estimation of air pollution for the future.

5. Conclusion

In this study, it was aimed to examine the temporal change of air pollution during the Covid-19 lockdown period of Kocaeli province. In this context, pollution maps and temporal change maps were produced using

GIS technology. Data were obtained from 10 stations in the study area. Outliers in the data were eliminated. Pollution maps were created using the IDW technique from monthly data. Temporal change maps were created by overlay analyses. In this context, maps are important in terms of visualization of pollution and easy interpretation by decision makers. It is important in terms of evaluating air pollution and providing information about the progress of pollution.

The study's findings indicate that May of 2020 had the greatest decline in the PM10 concentration when compared to 2019 at 27.97%. The PM10 measure showed the greatest rise in 2021 compared to 2020 in February, at 43.23%. The SO2 concentration decreased by a high of 29.85% November 2020 compared to November 2019. The highest rise in the SO2 concentration in 2021 over 2020 was detected in November to be 114.03%. When the PM10 concentration is examined seasonally, it can be seen that the spring of 2020 sees a significant decline in comparison to other seasons. At the same time, increases in PM10 concentrations are noticeable when spring season values from 2021 were examined. One of the elements contributing to the declines in PM10 concentration is the fact that the lockdowns during this time were significantly more stringent because of the pandemic in the spring of 2020.

Covid-19 pandemic restrictions seen to improve air quality. These and other studies lockdown are show that a solution to can be produced as an emergency action plan when air pollution gives a red alarm.

Author contributions

Burak Kotan*:* Conceptualization, Methodology, Software, Data curation, Writing-Original Draft Preparation, Validation. Visualization
Arzu Erener: Visualization, Investigation, Writing-Reviewing and Editing.

Conflicts of interest

The authors declare no conflicts of interest.

References

1. Gouda, K C, Singh P, P N, Benke M, Kumari R, Agnihotri G, Hungund K M, Chandrika M, Kantha Rao B, Ramesh V, & Himesh S. (2021). Assessment of air pollution status during COVID-19 lockdown (March–May 2020) over Bangalore City in India. Environmental Monitoring and Assessment, 193(395).
2. Marwah M, & Agrawala P K. (2022). COVID-19 Lockdown and Environmental Pollution: An Indian Multi-State Investigation. Environmental Monitoring and Assessment, 194(49).
3. Erdem, İ. (2020) Koronavirüse (Covid-19) Karşı Türkiye'nin Karantina ve Tedbir Politikaları. Turkish Studies, 15(4), 377-388.
4. Başeğmez, M., & Aydın, C. C. (2022). Türkiye'de COVID-19 sürecinde alınan önlemler çerçevesinde okul bahçe ve sınıflarının CBS ile değerlendirilmesi. *Geomatik*, *7*(3), 209-219.
5. Hashim, B. M., Al-Naseri, S. K., Maliki, A. A., Sa'adi, Z., Malik, A., & Yaseen, Z. M. (2021). On the investigation of COVID-19 lockdown influence on air pollution concentration: regional investigation over eighteen provinces in Iraq. Environmental Science and Pollution Research, 28(36), 50344-50362.
6. Singh, V., Singh, S., Biswal, A., Kesarkar, A. P., Mor, S., & Ravindra, K. (2020). Diurnal and temporal changes in air pollution during COVID-19 strict lockdown over different regions of India. Environmental Pollution, 266(3)
7. Su, Y., Sha, Y., Zhai, G., Zong, S., & Jia, J. (2019). Comparison of Air Pollution in Shanghai and Lanzhou Based on Wavelet *Transform. Environmental Science and Pollution Research*, 26(17), 16825-16834
8. Aydınoğlu, A. Ç., Bovkır, R., & Bulut, M. Akıllı şehirlerde büyük coğrafi veri yönetimi ve analizi: hava kalitesi örneği. *Geomatik*, *7*(3), 174-186.
9. Yılmaz, A. (2017). İklim Parametrelerinin Hava Kirliliği Parametreleri Üzerine Etkisi: Bolu İli Örneği. Journal of Current Researches on Social Sciences, 7(2), 413-436.
10. Ahamed Ibrahim, S. N., Sri Shalini, S., Ramachandran, A., & Palanivelu, K. (2022). Spatio-Temporal Variation and Sensitivity Analysis of Aerosol Particulate Matter During the COVID-19 Phase-Wise Lockdowns in Indian Cities. Journal of Atmospheric Chemistry.
11. Sahrei, M. A., Kuşkapan, E., & Çodur, M. Y. (2021). Public Transit Usage and Air Quality Index During The COVID-19 Lockdown. Journal of Environmental Management, 286.
12. Vega, E., Namdeo, A., Bramwell, L., Miquelajauregui, Y., Resendiz-Martinez, C. G., Jaimes-Palomera, M., Luna-Falfan, F., Terrazas-Ahumada, A., Maji, K. J., Entwistle, J., Enríquez, J. C. N., Mejia, J. M., Portas, A., Hayes, L., & McNally, R. (2021). Changes in Air Quality in Mexico City, London and Delhi in Response to Various Stages and Levels of Lockdowns and Easing of Restrictions During COVID-19 Pandemic. Environmental Pollution, 285.
13. Yang, M., Chen, L., Msigwa, K., Daniel Tang, K. H., Yap, P. S. (2022). Implications of COVID-19 On Global Environmental Pollution and Carbon Emissions with Strategies for Sustainability in the COVID-19 ERA. Science of The Total Environment, 809.
14. Rodríguez-Urrego, D., & Rodríguez-Urrego, L. (2020). Air Quality During the COVID-19: PM2.5 Analysis in the 50 Most Polluted Capital Cities in the World. Environmental Pollution, 266.
15. Özel, H., Cihan, P., Özcan, H. K., Aydın, S., & Hanedan, A. (2021). Hava Kirletici Parametrelerin Hava Kalitesi İndeksine Uzun Zamanlı Etkilerinin İncelenmesi: Çernezköy Organize Sanayi Bölgesi Örneği. Kırklareli University Journal of Engineering and Science, 7(1), 94-106.
16. Collivignarelli, M. S., Abbà, A., Bertanza, G., Pedrazzani, R., Ricciardi, P., & Carnevale Miino, M. (2020). Lockdown for Covid-2019 in Milan: What are the Effects on Air Quality? Science of The Total Environment, 732.

17. Kumari, P., & Toshniwal, D. (2020). Impact of Lockdown on Air Quality Over Major Cities Across the Globe During COVID-19 Pandemic. Urban Climate, 34.
18. Lian, X., Huang, J., Huang, R., Liu, C., Wang, L., & Zhang, T. (2020). Impact of City Lockdown on the Air Quality of COVID-19-hit of Wuhan City. Science of The Total Environment, 742.
19. Adams, M. D. (2020). Air pollution in Ontario, Canada during the COVID-19 State of Emergency. Science of The Total Environment, 742.
20. https://data.tuik.gov.tr/Bulten/Index?p=Adrese-Dayali-Nufus-Kayit-Sistemi-Sonuclari-2021-45500
21. http://sim.csb.gov.tr/STN/STN_Report/StationData DownloadNew
22. Toros, H., Bağış, S., & Gemici, Z. (2018). Ankara'da Hava Kirliliği Mekansal Dağılımının Modellenmesi. Ulusal Çevre Bilimleri Araştırma Dergisi, 1(1), 20-53.
23. İlker, A., Terzi, Ö., & Şener, E. (2019). Yağışın Alansal Dağılımının Haritalandırılmasında Enterpolasyon Yöntemlerinin Karşılaştırılması: Akdeniz Bölgesi Örneği. Teknik Dergi, 30(3), 9213-9219
24. Jumaah, H. J., Ameen, M. H., Kalantar, B., Rizeei, H. M., & Jumaah, S. J. (2019). Air quality index prediction using IDW geostatistical technique and OLS-based GIS technique in Kuala Lumpur, Malaysia. Geomatics, Natural Hazards and Risk, 10(1), 2185-2199.
25. Vorapracha, P., Phonprasert, P., Khanaruksombat, S., & Pijarn, N. (2015). A Comparison of Spatial Interpolation Methods for Predicting Concentrations of Particle Pollution (PM10). International Journal of Chemical, Environmental & Biological Sciences, 3(4), 302–306.
26. Civelekler, E., & Pekkan, E. The application of GIS in visualization of geotechnical data (SPT-Soil Properties): a case study in Eskisehir-Tepebaşı, Turkey. *International Journal of Engineering and Geosciences*, *7*(3), 302-313.
27. İşcan, F., & Güler, E. (2021). Developing a mobile GIS application related to the collection of land data in soil mapping studies. *International Journal of Engineering and Geosciences*, *6*(1), 27-39.
28. Uyan, M. (2019). Comparison Of Different Interpolation Techniques in Determining of Agricultural Soil Index on Land Consolidation Projects. *International Journal of Engineering and Geosciences*, *4*(1), 28-35.
29. Arca, D., & Çıtıroğlu, H. K. (2022). Güneş enerjisi santral (GES) yapım yerlerinin CBS dayalı çok kriterli karar analizi ile belirlenmesi: Karabük örneği. *Geomatik*, *7*(1), 17-25.
30. Alkayış, M. H., Karslıoğlu, A., & Onur, M. İ. (2022). Muğla ili Menteşe yöresi orman yangını risk potansiyeli haritasının coğrafi bilgi sistemleri ile belirlenmesi. *Geomatik*, *7*(1), 10-16.
31. Murayama, Y., & Thapa, R. B. (2011). Spatial Analysis and Modeling in Geographical Transformation Process. Springer, ISBN:978-94-007-0671-2.
32. Tian, B. (2016). GIS Technology Applications in Environmental and Earth Sciences. Boca Raton, ISBN:978-13-153-6697-5.
33. Erener, A., Sarp, G., & Yıldırım, Ö. (2018). Seasonal Air Pollution Investigation and Relation Analysis of Air Pollution Parameters to Meteorological Data (Kocaeli/Turkey). Proceedings of the 1st Springer Conference of the Arabian Journal of Geosciences, Tunisia.
34. Şentürk, E. & Erener, A. (2017). Determination of temporary shelter areas in natural disasters by GIS: a case study, Gölcük/Turkey. International Journal of Engineering and Geosciences, 2 (3), 84-90. https://doi.org/10.26833/ijeg.317314
35. Rahman, S. A., Islam, M. M., Salman, M. A. & Rafiq, M. R. (2022). Evaluating bank erosion and identifying possible anthropogenic causative factors of Kirtankhola River in Barishal, Bangladesh: an integrated GIS and Remote Sensing approaches. International Journal of Engineering and Geosciences, 7 (2), 179-190. https://doi.org/ 10.26833/ijeg.947493
36. Keleş, M. D. & Aydın, C. C. (2020). Mobil Lidar Verisi ile Kent Ölçeğinde Cadde Bazlı Envanter Çalışması ve Coğrafi Sistemleri Entegrasyonu-Ankara Örneği. Geomatik, 5 (3), 193-200. https://doi.org/ 10.29128/geomatik.643569

International Journal of Engineering and Geosciences
https://dergipark.org.tr/en/pub/ijeg
e-ISSN 2548-0960

Assessment of the solar energy potential of rooftops using LiDAR datasets and GIS based approach

Vancho Adjiski [*1], **Gordana Kaplan** [2], **Stojance Mijalkovski** [1]

[1]*Goce Delcev University, Faculty of natural and technical sciences, Macedonia*
[2]*Eskisehir Technical University, Institute of Earth and Space Sciences, Türkiye*

Keywords
LiDAR
GIS
Solar irradiation
Photovoltaic (PV) potential
Rooftop

Research Article
DOI: 10.26833/ijeg.1112274

Received: 03.05.2022
Accepted: 22.09.2022
Published: 19.10.2022

Abstract

The importance of solar energy as a global energy source is expected to grow. Solar power's future looks bright, especially with an aged and deteriorating energy grid and rising fossil fuel prices. More precise methods for assessment of solar capacity are needed as more homes and companies investigate the possibility of small-scale photovoltaic (PV) solar installations. In this study, a spatial solar energy PV potential assessment method based on the combination of LiDAR (Light Detection and Ranging) datasets and GIS (Geographic Information System) is proposed. The proposed methodology is applied to an area in the capital city of Skopje in N. Macedonia, from where the results of the possible annual energy output of PV systems for the selected rooftops were presented. The results of the study were presented in a map showing rooftops that are most suitable for installing PV systems. From this map, three random roofs were selected to perform manual estimates of the number of panels that could fit on them and the potential energy output of the solar PV systems. This study provides crucial results for financial and urban planning, policy formulation for future energy projects and also allows to analyze different mechanisms to promote PV installations on publicly available rooftops.

1. Introduction

Solar energy is the most abundant and cleanest renewable energy source. Because of its availability and long-term viability, solar energy is recognized as one of the most important renewable energy sources in the world [1-2]. The relevance of solar energy as a global energy source is expected to grow. Electricity from photovoltaic (PV) systems are expected to become increasingly essential in this scenario as performance improves, production costs decrease, and the cost of electricity from other sources rises [3]. Solar energy is also seen as a democratic energy source, with anyone able to explore and utilize it.

Unlike commercial sources such as fuel and coal, using renewable energies such as solar does not contribute to today's ever-increasing environmental challenge [4]. More countries are turning to use solar power to meet their energy needs, harnessing this high-potential energy source through PV systems, which converts sunlight into electricity [5].

According to the United Nations (UN), half of the world's population now lives in cities, which will rise to 60 % by the year 2050 [6]. As a result, developing urban plans that secure their long-term expansion should be a more significant problem. All countries' energy policies should prioritize promoting the transition to a new energy model based on efficient use of electricity and renewable energy sources [7]. The European Union (EU) has recommended a reform of the energy system to adapt to this situation. According to Directive 2009/28/EC, the EU shall achieve a minimum 25 % renewable energy share after 2025 [8].

Sustainable development refers to meeting current needs without jeopardizing future generations' ability to meet their own. There is an endeavor to reconcile environmental, economic, and social concerns within sustainable community development.

While this study focuses on the feasibility of solar PV systems as a means of reaching environmental targets for greenhouse gas reduction, there are additional social and economic considerations when examining the viability of

* **Corresponding Author**

*(vanco.adziski@ugd.edu.mk) ORCID ID 0000-0001-6401-6835
(kaplangorde@gmail.com) ORCID ID 0000-0001-7522-9924
(stojance.mijalkovski@ugd.edu.mk) ORCID ID 0000-0003-3352-2158

Cite this article

Adjiski, V., Kaplan, G. & Mijalkovski, S. (2023). Assessment of the solar energy potential of rooftops using LiDAR datasets and GIS based approach. International Journal of Engineering and Geosciences, 8(2), 188-199

solar energy. For numerous reasons, the study is limited to the solar energy potential of rooftops. Solar conversion technologies such as solar heating and solar PV are often implemented on building roofs [9-12]. Furthermore, the usage of these technologies on rooftops implies that they are being used on the existing area and do not require space that forgoes other opportunities [13].

For this reason, having a methodology that can estimate the sun irradiation of specific locations is critical. These roof potential measurements can help solar planners, installers, and property owners to save money and speed up the evaluation process for rooftops and "green" structures [14].

Active airborne remote sensing is increasingly being utilized to acquire high-resolution data that can be used to create urban models with various detail levels. A remote sensing technique based on LiDAR (Light Detection and Ranging) can be used for developing high-resolution 3D Digital Terrain Model (DTM) and Digital Surface Model (DSM) for the simulation of incoming solar radiation hitting the rooftops [15-18]. Furthermore, information about ambient temperature and attributes of the chosen solar systems must be included to produce the best results for PV potential estimations.

The main data used in this study was the 1 m spatial resolution LiDAR point cloud obtained from the Agency for Real Estate Cadastre of N. Macedonia [19] as well as data for the Typical Meteorological Year (TMY) from the European Union Joint Research Centre [20]. The LiDAR data is from an area in the capital city Skopje (Fig. 1). The processed LiDAR data was used to identify roof planes within the selected area and determine their suitability by measuring their area, slope, aspect, and other characteristics like shade. In order to predict the possible annual energy output of each roof within the selected area, this was paired with the irradiation data. The development of this kind of model, which combines the ability of GIS to correlate alphanumeric data with spatial data, has become a crucial tool for comprehending the territory and, as a result, has contributed to the development of true "smart cities".

This research aims to create a methodology based on publicly available data that will enable for large-scale assessments of roof spaces and the maximum capacity of solar PV panels that can be put throughout entire cities and neighborhoods.

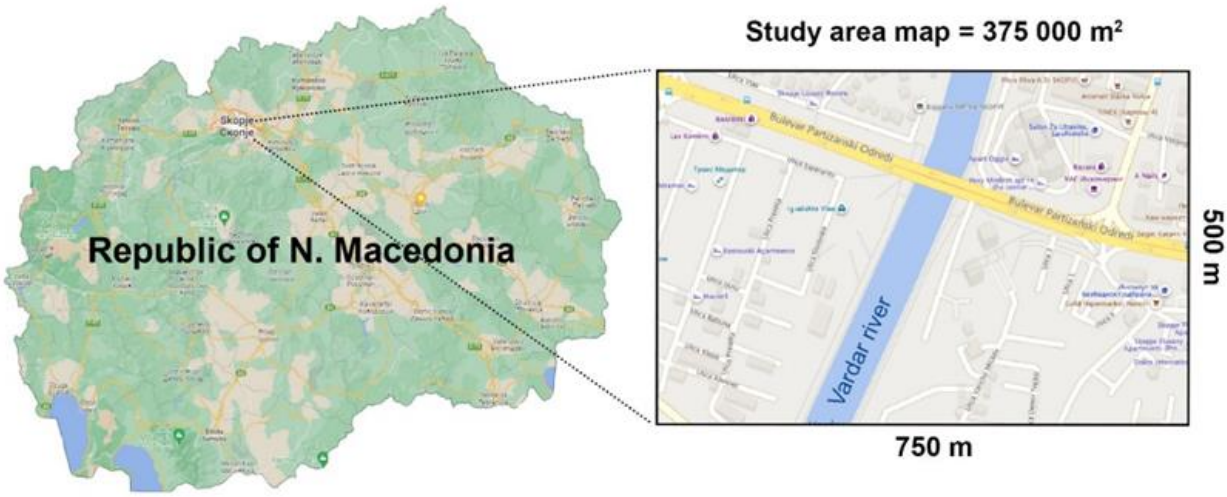

Figure 1. The study area in city of Skopje, used for the analyses

2. Method

2.1. Tools and data

The free and open-source GIS software QGIS was used for most of the core analysis in this study [21-24]. To generate the urban 3D model and to calculate the solar potential, the following open-source plugins within QGIS were employed:

- LAStools: LiDAR data-processing tool for seamless processing of large amounts of points that represent the selected urban objects [25].
- The Urban Multi-scale Environmental Predictor (UMEP): a group of tools that can be used for various applications related to outdoor thermal comfort, urban energy consumption, climate change mitigation, etc. The following services from this open-source plugin were utilized [26]:
  - UMEP MetPreprocessor: this tool is used to convert the required temporal meteorological data into the UMEP format. The following variables are usually required as a minimum input: air temperature, relative humidity, barometric pressure, wind speed, incoming shortwave radiation and rainfall (if available), other variables can be supplied as well.
  - UMEP Wall Height and Aspect: this tool is used to calculate the orientations and heights of the facades of buildings from a DSM. Wall aspect is given in degrees where north facing wall pixel has a zero value. The output of this plugin is used in other UMEP plugins such as Solar Energy on Building Envelopes.
- The SEBE (Solar Energy on Building Envelopes) plugin (inside UMEP): this tool calculates pixel-wise

potential solar energy using ground and building DSM. SEBE is also able to estimate irradiance on building walls.
- UMEP Daily Shadow Pattern: this tool calculates the pixel-wise shadow analysis using ground and building DSM.

The Agency for Real Estate Cadastre has started conducting LiDAR scanning of the territory of N. Macedonia. The activities are implemented within the project entitles "LiDAR survey of the entire territory of Republic of Macedonia for creating precise DEM and other quantitative and qualitative analyses of the Earth surface" [19]. The project activities include the LiDAR scanning of part of the Republic of North Macedonia territory. Most important input data which form the backbone of the methodology are described as follows:

- LiDAR point cloud data from the selected area (file from The Agency for Real Estate Cadastre N. Macedonia).
- Digital Surface Model (DSM): topographic digital file with elevation data of the urban environment, including the elevations of urban elements and represents the earth's surface, including all objects on it such as buildings, vegetation or roads.
- Digital Terrain Model (DTM): digital file with elevation data of the ground (bare Earth), on which the urban environment is based.
- Weather Data: Detailed climate file of the study area. This file is in the form of Typical Meteorological Year (TMY), a collation of selected weather data for a specific location, listing hourly values of solar radiation and meteorological elements for a one-year period. This detailed climate file was obtained from the EU JRC using their online TMY tool. The data used in this study is an average from the years 2006 - 2015 and contains the air temperature, air pressure, wind speed, wind direction, humidity, global horizontal irradiance, direct normal irradiance and diffuse horizontal irradiance [27].

Fig. 2 depicts the workflow process using these tools and data for analyzing the solar PV energy potential based on an urban 3D model.

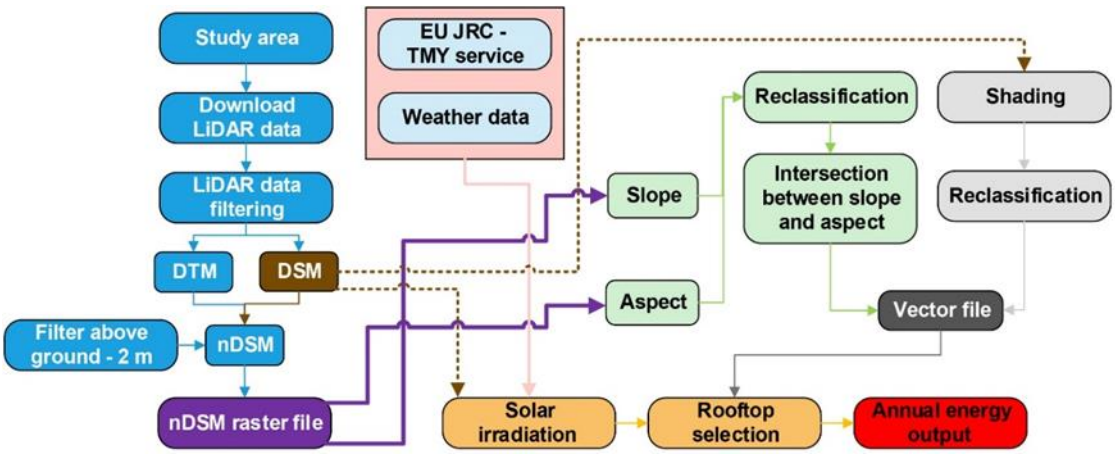

Figure 2. Proposed methodology for solar energy potential assessment

The methodology begins with the definition of the research area. The relevant LiDAR files (point cloud, DSM and/or DTM - depending on availability) are downloaded once the study area has been defined (download LiDAR data from The Agency for Real Estate Cadastre N. Macedonia). The LiDAR files must cover the entire research region. Prior to use, the LiDAR data (point cloud) must be filtered using LASTools (LiDAR data filtering) (Fig. 3a). A raster files containing only ground and building points is required due to this operation. This raster files represent greyscale images where the color of each pixel represents the elevation above sea level in meters. Two different forms of LiDAR images were generated in this process, a Digital Surface Model (DSM) (Fig. 3b) and a Digital Terrain Model (DTM) (Fig. 3c). A DTM contains only data for the bare ground, whereas a DSM contains elevation data for buildings, trees, and other surface structures. Both data sets have a spatial resolution of 1 m, implying that each pixel represents a 1 m^2 area.

A meteorological file is the final piece of data needed to do the solar analysis. The EU JRC provided this information via their online TMY service [27]. A TMY is a whole year's worth of meteorological data for a certain place on an hour by hour basis, including irradiance data. It is made up of averaging over several years to get the typical weather at any given period. The data used in this study is an average of air temperature, humidity, wind speed, wind direction, air pressure, global horizontal irradiance, direct normal irradiance, and diffuse horizontal irradiance for the years 2006 to 2015. This file must be formatted in a specified manner. First, from the EU JRC a Comma-Separated Values (CSV) file is downloaded. Second, in the UMEP MetPreprocessor tool, a matching between EU JRC weather data and UMEP meteorological parameters needs to be defined and performed. Finally, from the MetPreprocessor tool the UMEP meteorological file is obtained, which is then used in the SEBE tool.

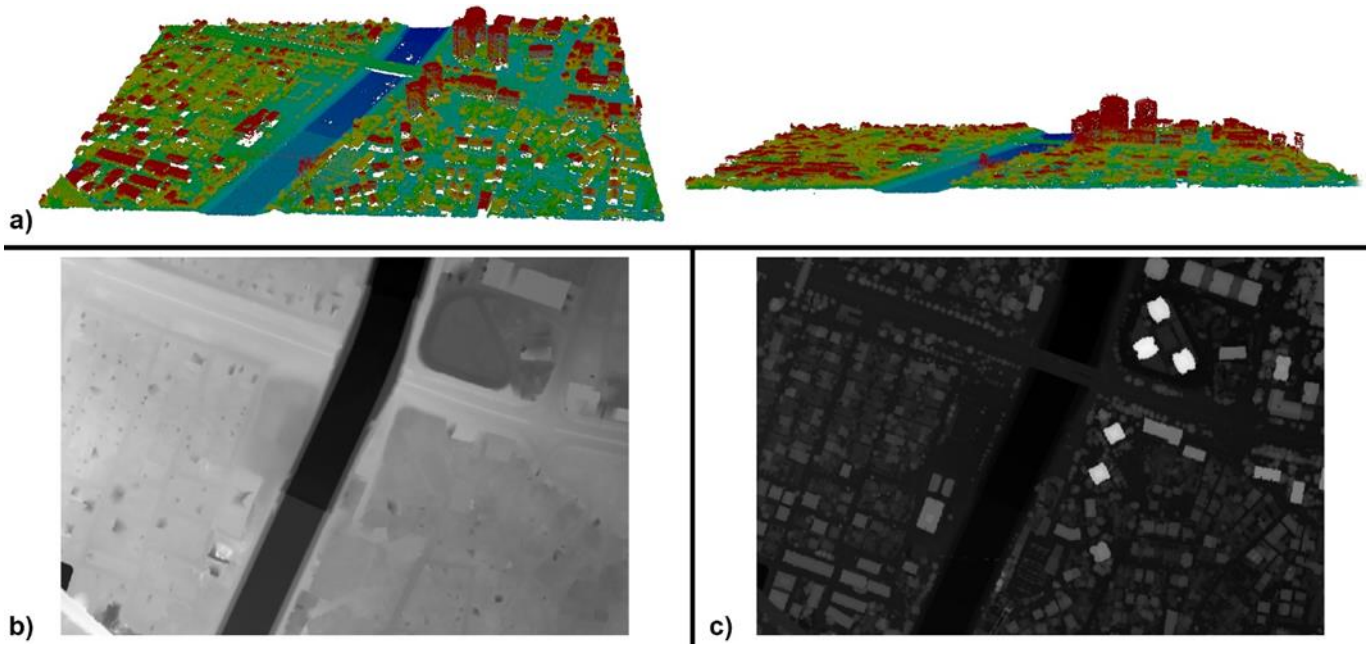

Figure 3. a) LiDAR 3D point cloud from the study area b) Digital Terrain Model (DTM) generated from the LiDAR 3D point cloud c) Digital Surface Model (DSM) generated from the LiDAR 3D point cloud

The next step of the proposed methodology in this study is to identify the potentially suitable roofs upon which a PV system could be installed.

The initial stage in this process was to generate a difference layer by subtracting the LiDAR DSM elevation values from the DTM elevation values. This results in a nDSM, or normalized DSM, which gives the elevation of surface features in meters above ground level rather than above sea level. This makes processing the roofs easier because a minimum height limit of 2 m (above the ground) can be set to filter out some of the ground characteristics. Fig. 4 shows the nDSM raster file with 2 m above the ground height limit filter.

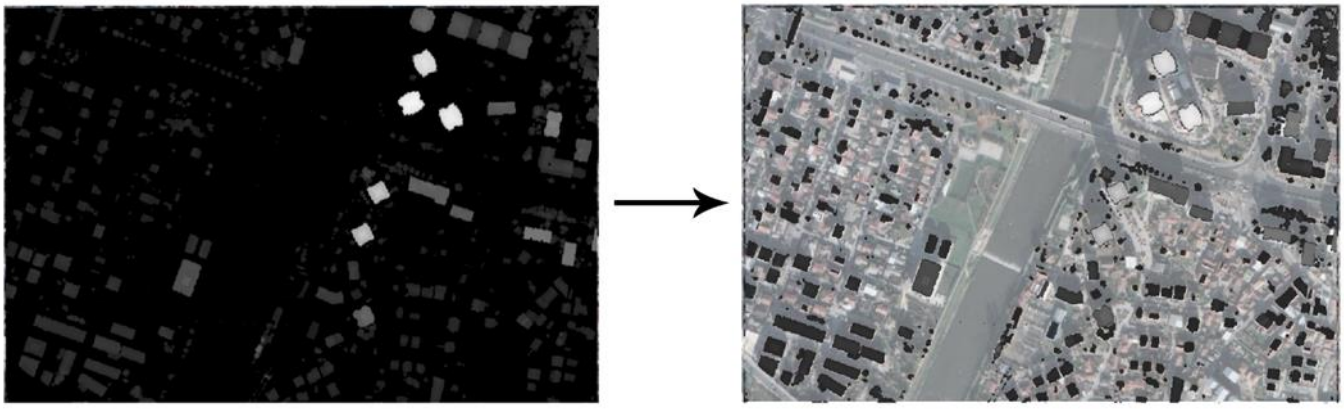

Figure 4. The nDSM raster file is shown on the left (subtract DTM from DSM). The right image, which is overlaid on aerial image from the study area, is obtained by applying a 2 m height filter.

The next step in this methodology is using LiDAR data in QGIS to analyze the slope and aspect of every roof in the study area. Using the built-in QGIS capabilities the height filtered nDSM was then used to construct an aspect raster and a slope raster, assigning each pixel an angle. The created aspect raster file represents an angular direction where black represents 0° (North) then each degree is assigned by shades of grey until looping around to white representing 360°. Each pixel has an angle assigned to it for the created slope raster file, with black representing 0° (flat) and white representing 90° (vertical). From these raster files, roof planes can be distinguished because they usually face a common direction and slope across the whole surface of the roof plane. Fig. 5a shows aspect raster file with the shades of grey represents a different angle, starting with black for North, through grey, and wrapping around to white. Fig. 5b shows slope raster file that represents a different angle, with the shades of grey starting with black for flat slopes and white for vertical slopes.

In order to identify the roof planes, the aspect raster was reclassified to 4 classes and the slope raster was reclassified to 3 classes in order to reduce the whole range of values. The classes are value ranges that the pixels in the raster's are assumed to have similar values. This permits regions with similar aspects and slopes to be grouped together. Fig. 6a and Fig. 6b depict this aspect and slope reclassification process.

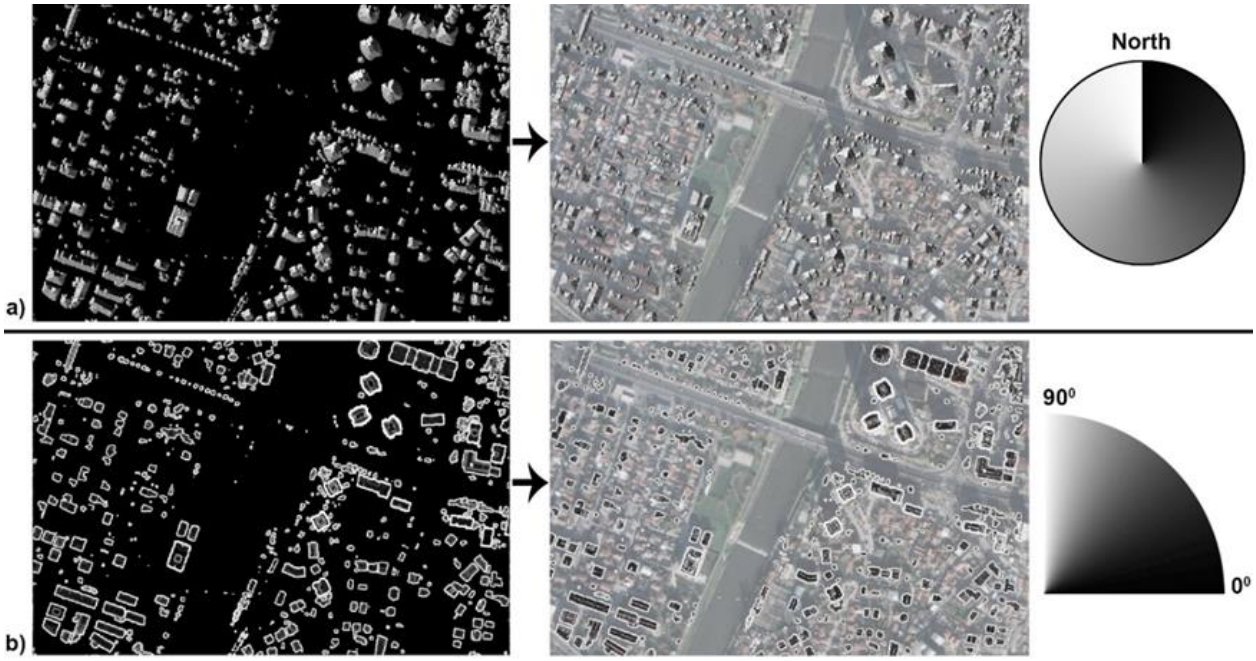

Figure 5. a) Aspect raster file created from the nDSM with shades of grey as color representation, starting with black for North, through grey, and wrapping around to white. b) Slope raster file created from the nDSM with shades of grey as color representation, starting with black for flat slopes, white for vertical slopes and grey in-between.

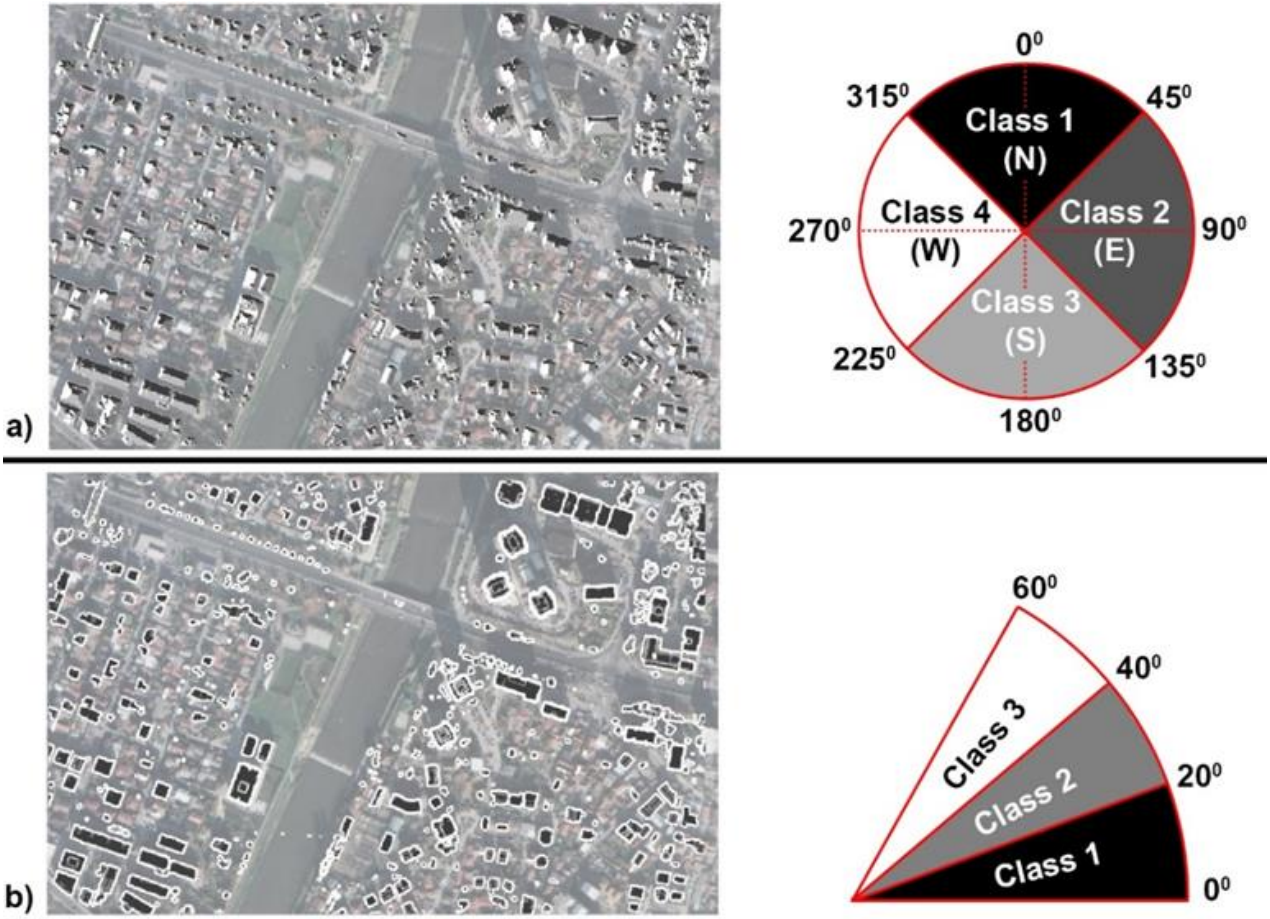

Figure 6. a) Aspect raster with 4 classes (N, E, S, W) by which each pixel was reclassified b) Slope raster with 3 classes by which each pixel was reclassified

Points with slopes greater than 60° were deleted because they were unsuitable for PV installation. Following reclassification, the aspect and slope raster's were filtered to eliminate noise using the Sieve tool in QGIS.

The QGIS Polygonise tool was then used to transform the aspect and slope raster's into vector polygons. This tool builds a polygon to represent the area of pixels by grouping together neighboring pixels with the same value. This format is significantly more useful because

the polygons may be saved as an ESRI Shapefile, which allows for the storage of the shape and position of each polygon as well as any additional attributes like aspect and slope that can be preserved as part of the database file.

Because roof planes share a common aspect and slope across their surface, the intersection of the aspect and slope polygons may be used to identify them. This intersection produces a new collection of shapes with a single aspect value and a single slope value representing roof planes. Fig. 7 shows the result of the intersection between the aspect and slope polygons.

Gathering information on each polygon shown in Fig. 7 such as accurate values for their aspect, slope, area, and location was the final stage in determining the roof planes. The latitude and longitude of each point were kept as an attribute of each shape in the database file, and QGIS was used to compute the center of each polygon. The Zonal Statistics tool in QGIS was used to determine the mean value for the aspect and slope of each roof plane, which allows for statistical computations involving a raster with a vector overlay layer. Circular statistics were used for the aspect data to get an accurate mean since the data is in circular form (0^0-360^0). QGIS was used to determine the planimetric area of each polygon and the true area, which was computed by correcting the planimetric area using the mean slope of each polygon to account for the roof planes' top down projection.

Shading can be a critical component in determining a solar PV system's output, therefore it must be taken into account. The shading analysis was conducted using the LiDAR DSM data from Fig. 3c since it allows for the consideration of shade from buildings as well as other tall objects such as trees and the landscape in general.

The DSM was used into the UMEP Daily Shadow Pattern tool in QGIS, which generates a raster image of the shadow pattern at any given moment, with 0 representing shaded areas and 1 representing bright areas.

The plugin was used to create a shadow pattern for every hour between dawn and sunset for 4 different days. The solstices and equinoxes were chosen as the 4 days to account for the whole range of the Sun's locations throughout the year. Specifically, the days were 20th March 2021, 21st June 2021, 23rd September 2021 and 22nd December 2021.

The generated hourly shadow raster's for each of the selected days were combined to create a continuous raster with values ranging from 0 to 1, where 0 means that is shaded and 1 is lit throughout the whole day. Fig. 8(a-d) depicts these daily shadow raster's.

Because summer days are more significant for energy generation than winter days, the allowed shade was determined differently for each day of the season to reflect the relative value of each day. A shade level of 50 % was found suitable for the days in March and September. A shade level of 40 % was found suitable for the day in June, and a shading level of 60 % was found suitable for the day in December. This suggests that pixels with a value of less than 0.5 for March and September, less than 0.4 for June, and less than 0.6 for December, could be regarded unacceptable for the daily shadow raster's shown in Fig. 8(a-d).

By reclassifying unsuitable pixels to a value of 0 and suitable pixels to a value of 1, these criteria were used to construct daily binary shadow raster's (Fig. 9a). Finally, the generated four binary raster (shown in Fig. 9a) were multiplied to form a single binary raster. This means that in order for a pixel to have a value of 1, it must have a value of 1 in each of the four raster's. Fig. 9b depicts the final shading raster, which can be used to determine whether the roof planes are suitable or not.

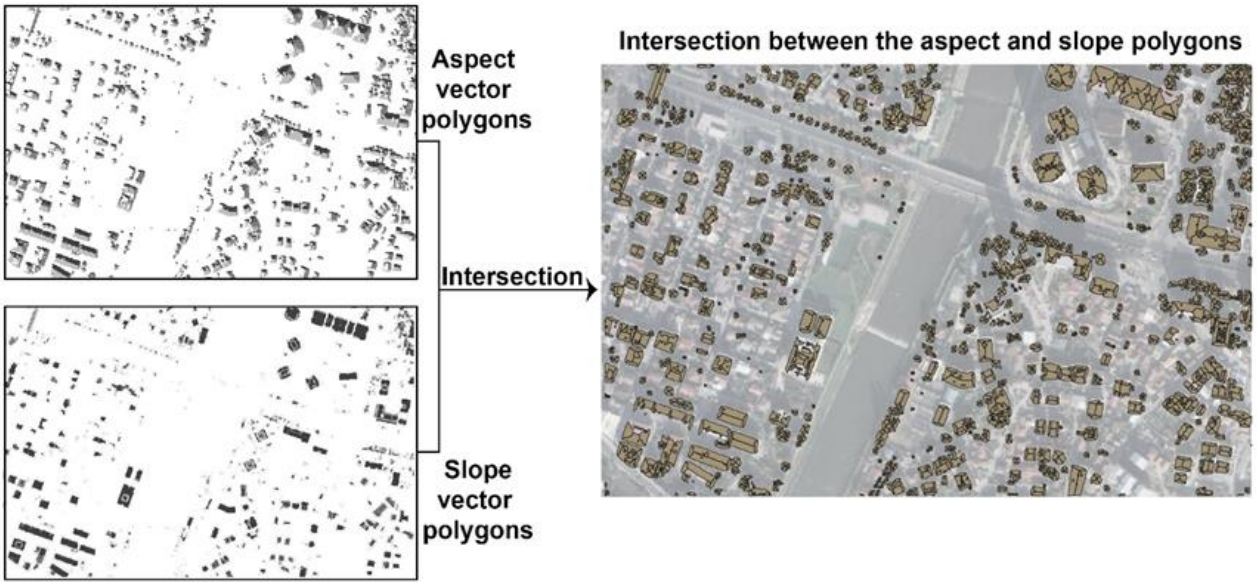

Figure 7. The intersection between the aspect and slope polygons representing roof planes with some additional surrounding artefacts

Figure 8. a) March shadow raster b) June shadow raster c) September shadow raster d) December shadow raster

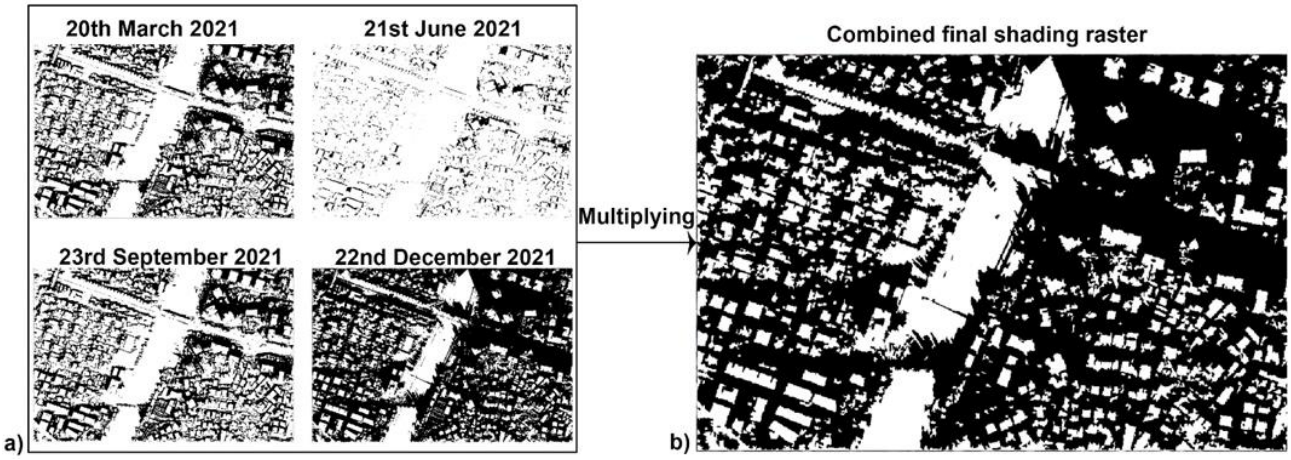

Figure 9. a) Binary shadow raster's where black pixel takes a value of 0 (unsuitable) and white pixels take a value of 1 (suitable) b) Combined final shading raster depicting the area locations which are suitable (white pixels) and unsuitable (black pixels) throughout the entire year

3. Results and Discussion

The first factor for a roof plane to be consider suitable was that it exceeded the minimum suitable area. In their study, Melius et al [28] characterized three approaches to assessing roof suitability: constant-value methods, manual selection, and GIS-based approaches. Most previous estimates of PV technical potential have relied on constant-value methods, which assume that a certain percentage of building rooftops can be used as PV areas, and these percentages are then applied to the total building stock to estimate the area available for PV systems [29-31]. Manual selection is based on visual clues such as aerial photography and Google Earth to determine the suitability of individual buildings for PV installations [32-33]. Methods based on GIS provide more precision than methods based on constant-value and can handle much larger data sets than methods based on manual selection [28]. In this paper, we used GIS-based method to provide a detailed analysis of the area available for PV system installations. A literature review was conducted and it was concluded that the minimum system size is a six-panel array which is equivalent to an area of around 10 m^2 [16,18,23]. Also, another factor must be considered: the buffer of minimum 0.5 m around the installed panels. As a result, considering the area of the panels and the buffer space between them a minimum roof area of 16 m^2 was chosen.

The potentially acceptable polygons were then filtered based on their slope and aspect. Following the reviewed literature, any polygon with a mean slope greater than 60° was ruled out as being too steep for a PV system to be installed [23].

The acceptable aspect range for pitched roofs was ENE through WNW or 67.5° to 292.5°, any roof outside this range was excluded. Fig. 10 shows a sample of the filtered, suitable roof planes represented by red polygons.

Figure 10. Identified red polygons that represent roof planes suitable for a solar PV system

The SEBE tools in UMEP was used to build a solar irradiation raster file, which was utilized to estimate the energy output of each roof [34]. This tool used the elevation data from the DSM and the weather and irradiance data from the TMY to generate the solar irradiation raster shown in Fig. 11. The output raster's units are in kWh, and because each pixel represents 1 m^2, the output is numerically equivalent to the average energy over an area of 1 m^2, expressed in kWh/m^2.

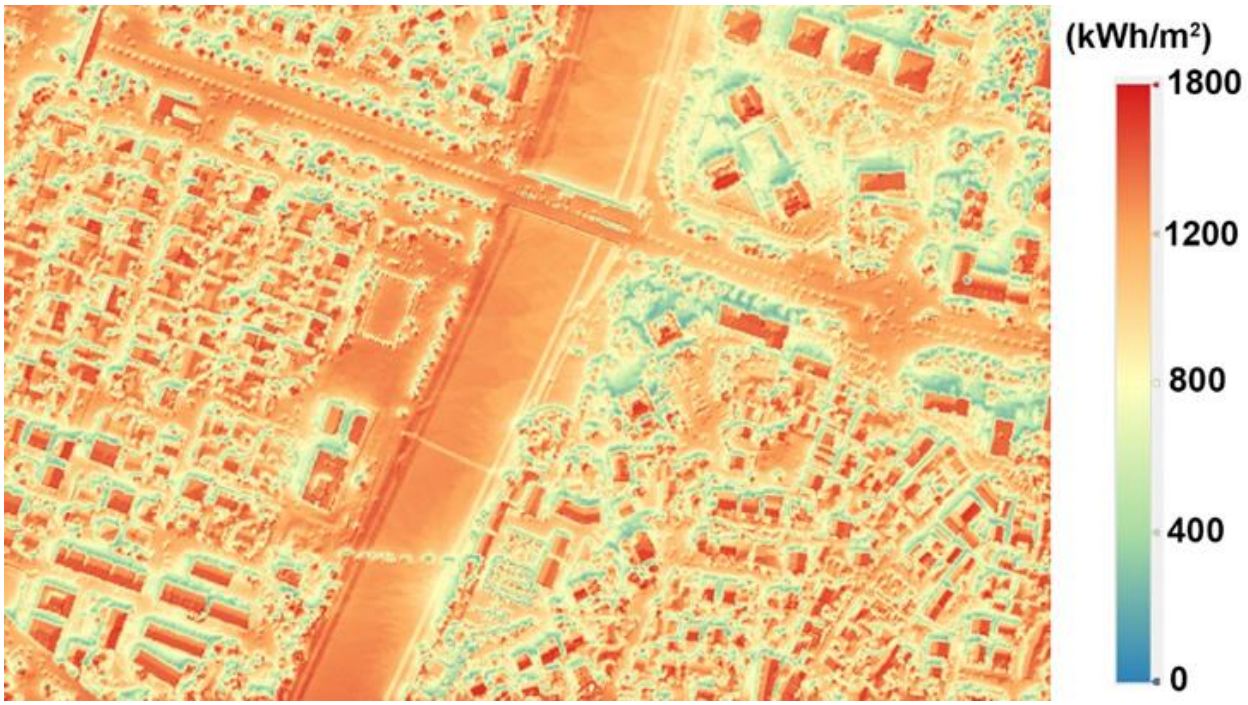

Figure 11. Annual solar irradiation raster from the study area

In order to make an assessment of the energy output of a rooftop solar PV system, the number of panels that could fit on each rooftop had to be estimated. This is a very difficult and time-consuming task to be performed manually for large-scale areas. Future work will include an extension of the research to deal with this process. The idea behind this step will be to develop an algorithm that can find the maximum number of rectangles that can fit inside any given shape.

In order to present the methodology, three random roofs were selected to have manual estimates of the number of panels that could fit on them (Fig. 12). For each of the selected roofs, a rectangular grid with the appropriate dimensions was generated to represent a solar array and the number of panels was then counted that could fit inside the roof polygon.

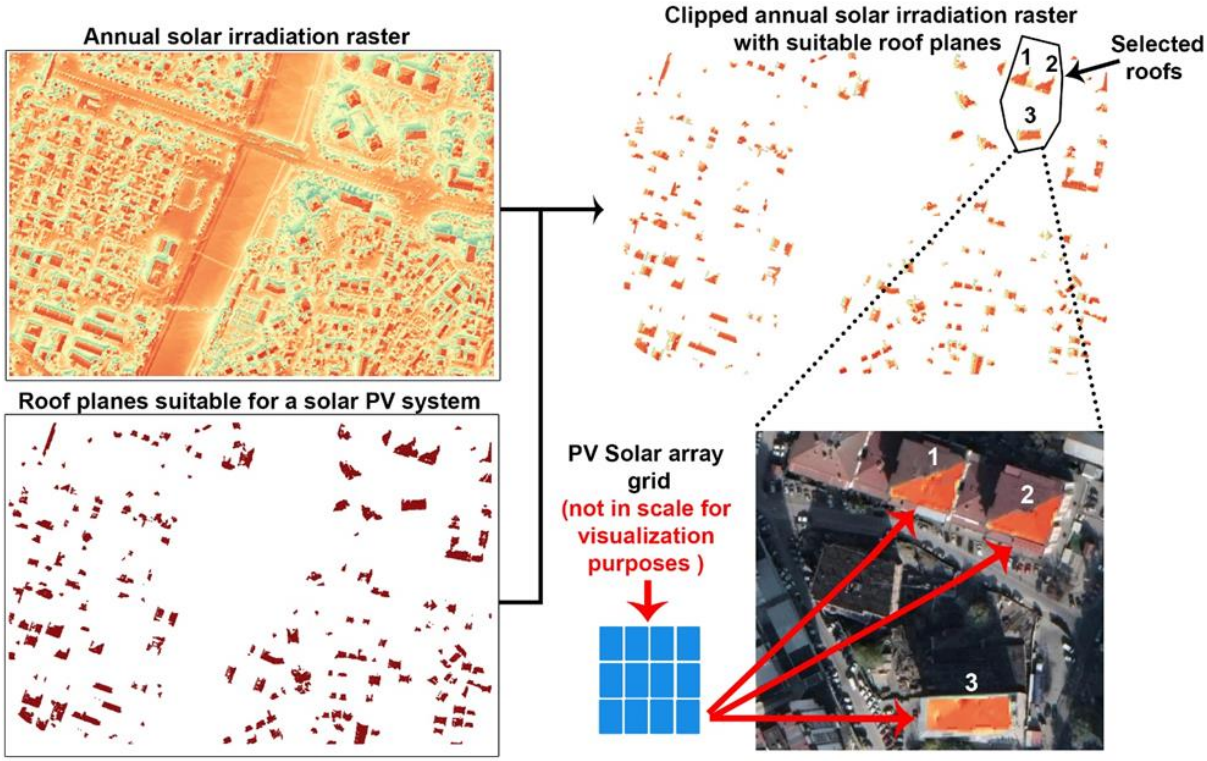

Figure 12. Manual panel number estimation for the selected roofs

The efficiency of the solar PV panels was the last variable to be determined in order to estimate the annual energy output for the selected roof.

The online EU PVGIS tool was used to calculate the average percentage loss for the selected location [27]. With a typical system loss of 14 %, the tool was used to determine the overall percentage loss for a 310 Wp (watt peak) yield crystalline silicon solar PV panel. The EU PVGIS online tool estimate an average overall loss of 22.9 % for the selected location in this study.

Now that the annual irradiation, number of panels, panel area, yield, and overall loss were estimated for each of the selected roofs, the annual energy production could be determined using the following term [35]:

$$E = A * N * r * H * PR \quad (1)$$

where:

E - annual energy output (kWh);

A - area of the solar panel (m^2);

N - number of panels for a given roof

r - solar panel yield or efficiency given by the ratio: electrical power (in kWp) of one solar panel divided by the area of one panel (%) (in this case this value is 0.18 %);

H - Annual mean irradiation for a given roof (kWh/m^2);

PR - Performance ratio, coefficient for losses (%) (this value is 0.77- takes into account the 22.9 % energy loss).

Equation (1) was applied to each of the selected rooftops to calculate the potential energy output if a solar PV system with the previously defined electrical characteristics were to be installed. The results are shown in Table 1.

Table 1. Potential energy output of a solar PV system for the selected rooftops in the study area

Roof ID	Roof area (m^2)	Number of panels	Area of one panel (m^2)	Area of the PV solar array grid (m^2)	Irradiation (kWh/m^2)	Energy output (kWh)
1	227	78	1.65	128.7	1416	25258
2	241	82	1.65	135.3	1434	26891
3	497	154	1.65	254.1	1372	50502

The results from Table 1 show the high potential energy output of a solar PV system for the selected rooftops. The calculated total annual energy output from the selected roofs was 102.6 MWh from 314 panels installed on 965 m^2 roof area. The results are promising and emphasize the fact there is good potential for residential solar PV energy production in N.Macedonia that have annual mean solar irradiation of 1450 kWh/m^2.

The results of the study are significant as remote sensing data and methods offer new techniques in many fields [36], and especially the use of Lidar data is getting more and more popular in the recent years [37-42].

4. Conclusion

Solar energy is one of the most promising ways for cities to shift to lower-carbon energy sources, so identifying potentially suitable roof spaces is vital for PV system deployment modeling.

Small area from the capital city Skopje in N. Macedonia was chosen as the study area. The analysis relied heavily on 1 m resolution aerial LiDAR point cloud for the selected area from the Agency for Real Estate Cadastre of N. Macedonia as well as data for the TMY for the selected area from the EU JRC.

The LiDAR data was used to locate roof planes in the study area and determine their suitability by measuring their area, slope, aspect, and other characteristics like shade. This was paired with the irradiation data. In order to predict the potential PV annual energy output, three randomly selected roofs were chosen from the study area.

Furthermore, the applicability of this assessment method can be used as a guide for solar energy utilization development plans in urban areas that can be extended to all appropriate infrastructure facilities.

The presented methodology in this study with the use of remote sensing, such as LiDAR, and GIS applications, has proven to be tools with extremely promising results. This type of research is expected to be extremely valuable for city energy planning because it allows for the assessment of PV solar energy potential of rooftops, which might account for a considerable portion of total building energy demand in cities.

The proposed method is repeatable, systematic, and based on high-resolution open-data sources and non-commercial software. The generated results offer high precision because are considering the 3D geometry of the buildings.

Acknowledgement

The authors would like to thank the Agency for Real Estate Cadastre of N. Macedonia for providing the LiDAR dataset.

Author contributions

Vancho Adjiski: Conceptualization, Methodology, Software, Writing-Original draft preparation, Visualization. **Gordana Kaplan:** Review, Writing-Review, Software-Verification. **Stojance Mijalkovski:** Checking draft and Editing.

Conflicts of interest

The authors declare no conflicts of interest.

References

1. Freitas, S., Catita, C., Redweik, P., & Brito, M.C. (2015). Modelling solar potential in the urban environment: state-of-the-art review. Renewable and Sustainable Energy Reviews, 41, 915-931.
2. Suri, M., Huld, T. A., Dunlop, E. D., & Ossenbrink, H. A. (2007). Potential of solar electricity generation in the European Union member states and candidate countries. Solar Energy, 81(10), 1295-1305. http://dx.doi.org/10.1016/j.solener.2006.12.007
3. Nwaigwe, K.N., Mutabilwa, P., & Dintwa, E. (2019). An overview of solar power (PV systems) integration into electricity grids. Materials Science for Energy Technologies, 2(3), 629-633. https://doi.org/10.1016/j.mset.2019.07.002.
4. Kåberger, T. (2018). Progress of renewable electricity replacing fossil fuels. Global Energy Interconnection, 1(1) 48-52. https://doi.org/10.14171/j.2096-5117.gei.2018.01.006.
5. Koo, C., Hong, T., Park, H.S., & Yun, G. (2014). Framework for the analysis of the potential of the rooftop photovoltaic system to achieve the net-zero energy solar buildings. Progress in photovoltaics: research and applications, 22(4), 462-478. https://doi.org/10.1002/pip.2448
6. United Nations, Department of Economic and Social Affairs, Population Division. (2014). World Urbanization Prospects: The 2014 Revision, Highlights, 32 p.
7. Lu, Y., Khan, Z.A., Alvarez-Alvarado, M.S., Zhang, Y., Huang, Z., & Imran, M. A. (2020). Critical Review of Sustainable Energy Policies for the Promotion of Renewable Energy Sources. Sustainability, 12(12), 1-30. https://doi.org/10.3390/su12125078
8. Directive 2009/28/EC of the European Parliament and of the Council of 23 April 2009 on the promotion of the use of energy from renewable sources and amending and subsequently repealing Directives 2001/77/EC and 2003/30/EC. Official Journal of the European Union L140. pp. 16–62.
9. Hong, T., Lee, M., Koo, C., Jeong, K., & Kim, J. (2017). Development of a method for estimating the rooftop solar photovoltaic (PV) potential by analyzing the available rooftop area using Hillshade analysis. Applied Energy, 194, 320-332. https://doi.org/10.1016/j.apenergy.2016.07.001
10. Bergamasco, L., & Asinari, P. (2011). Scalable methodology for the photovoltaic solar energy potential assessment based on available roof surface area: further improvements by ortho-image analysis and application to Turin (Italy). Solar Energy, 85(11), 2741-2756. https://doi.org/10.1016/j.solener.2011.08.010

11. Kodysh, J.B., Omitaomu, O.A., Bhaduri, B.L., & Neish, B.S. (2013). Methodology for estimating solar potential on multiple building rooftops for photovoltaic systems. Sustainable Cities and Society, 8, 31-41. https://doi.org/10.1016/j.scs.2013.01.002
12. Li, Y., Ding, D., Liu, C., & Wang, C. (2016). A pixel-based approach to estimation of solar energy potential on building roofs. Energy and Buildings, 129, 563-573. https://doi.org/10.1016/j.enbuild.2016.08.025
13. Adeleke, A.K., & Smit, J.L. (2016). Intergration of LiDAR data with aerial imagery for estimating rooftop solar photovoltaic potentials in city of Cape Town. ISPRS - International Archives of the Photogrammetry, Remote Sensing and Spatial Information Sciences, 41, 617-624.
14. Byrne, J., Taminiau, J., Kurdgelashvili, L., & Kim, K.N. (2015). A review of the solar city concept and methods to assess rooftop solar electric potential, with an illustrative application to the city of Seoul. Renewable and Sustainable Energy Reviews, Volume 41, 830-844. https://doi.org/10.1016/j.rser.2014.08.023.
15. Lukač, N., Žlaus, D., Seme, S., Žalik, B., & Štumberger, G. (2013). Rating of roofs' surfaces regarding their solar potential and suitability for PV systems, based on LiDAR data. Applied Energy, 102, 803-812. https://doi.org/10.1016/j.apenergy.2012.08.042
16. Jacques, D.A., Gooding, J., Giesekam, J.J., Tomlin, A.S., & Crook, R. (2014). Methodology for the assessment of PV capacity over a city region using low-resolution LiDAR data and application to the City of Leeds (UK). Applied Energy, 124, 28-34. https://doi.org/10.1016/j.apenergy.2014.02.076
17. Suomalainen, K., Wang, V., & Sharp, B. (2017). Rooftop solar potential based on LiDAR data: bottom-up assessment at neighbourhood level. Renewable Energy, 111, 463-475. https://doi.org/10.1016/j.renene.2017.04.025
18. Prieto, I., Izkara, J.L., & Usobiaga, E. (2019). The Application of LiDAR Data for the Solar Potential Analysis Based on Urban 3D Model. Remote Sensing, 11(20), 2348-2358. https://doi.org/10.3390/rs11202348
19. https://www.katastar.gov.mk/
20. European Union Joint Research Centre, "Typical Meteorological Year" (2017). [Online]. Available: https://re.jrc.ec.europa.eu/tmy.html (Date of access: 15 03 2022).
21. Latif, Z. A., Zak,i N. A. M., & Salleh, S. A. (2012). GIS-based estimation of rooftop solar photovoltaic potential using LiDAR. 2012 IEEE 8th International Colloquium on Signal Processing and its Applications, 2012, 388-392. https://doi.org/10.1109/CSPA.2012.6194755.
22. Suri, M., & Hofierka, J. (2004). A new GIS-based solar radiation model and its application to photovoltaic assessments. Transactions in GIS, 8(2), 175-190. https://doi.org/10.1111/j.1467-9671.2004.00174.x
23. Margolis, R., Gagnon, P., Melius, J., Phillips, C., & Elmore, R. (2017). Using GIS-based methods and LiDAR data to estimate rooftop solar technical potential in US cities. Environmental Research Letters, 12(7), 1-10. https://doi.org/10.1088/1748-9326/aa7225
24. Palmer, D., Koumpli, E., Cole, I., Gottschalg, R., & Bettts, T. (2018). A GIS-Based Method for Identification of Wide Area Rooftop Suitability for Minimum Size PV Systems Using LiDAR Data and Photogrammetry. Energies, 11(12), 1-22. https://doi.org/10.3390/en11123506
25. Rapidlasso GmbH LAStools. Available online: https://rapidlasso.com/lastools/ (Date of access: 15 03 2022).
26. Lindberg, F., Grimmond, C., Gabey, A., Jarvi, L., Kent, C., Krave, N., Sun, T., Wallenberg, N., & Ward, H. (2019). Urban Multi-scale Environmental Predictor (UMEP) Manual. University of Reading UK, University of Gothenburg Sweden, SIMS China, [Online] Available: https://umep-docs.readthedocs.io. (Date of access: 15 03 2022).
27. European Union Joint Reasearch Centre, Photovoltaic Geographical Reference System. (2017). [Online]. Available:https://re.jrc.ec.europa.eu/pvg_tools/en/tools.html (Date of access: 15 03 2022).
28. Melius, J., Margolis, R., & Ong, S. (2013). Estimating Rooftop Suitability for PV: A Review of Methods, Patents, and Validation Techniques. Golden (CO): National Renewable Energy Laboratory; 2013 December. Report No.: NREL/TP-6A20-60593.
29. Chaudhari, M., Frantzis, L., & Hoff, T.E. (2004). PV Grid Connected Market Potential Under a Cost Breakthrough Scenario. EF-Final-September 2004-117373 (Chicago: Navigant Consulting).
30. Frantzis, L., Graham, S., & Paidipati, J. (2007). California Rooftop Photovoltaic (PV) Resource Assessment and Growth Potential by County. CEC-500–2007-048 (Chicago: Navigant Consulting).
31. Paidipati, J., Frantzis, L., Sawyer, H., & Kurrasch, A. (2008). Rooftop Photovoltaics Market Penetration Scenarios. NREL/SR- 581–42306 (Golden, CO: National Renewable Energy Laboratory). https://doi.org/10.2172/924645
32. Ordonez, J., Jadraque, E., Alegre, J., & Martinez, G. (2010). Analysis of the photovoltaic solar energy capacity of residential rooftops in Andalusia (Spain). Renewable and Sustainable Energy Reviews,14, 2122-2130. https://doi.org/10.1016/j.rser.2010.01.001
33. Zhang, X., Walker, R., Salisbury, M., Hromiko, R., & Schreiber, J. (2009). Creating a Solar City: Determining the Potential of Solar Rooftop Systems in the City of Newark. Newark, DE: University of Delaware, Center for Energy and Environmental Policy.
34. Lindberg, F., Jonsson, P., Honjo, T., & Wästberg, D. (2015). Solar energy on building envelopes – 3D modelling in a 2D environment. Solar Energy, 115, 369-378. https://doi.org/10.1016/j.solener.2015.03.001.
35. Boyd, A. (2019). Mapping Solar PV Potential in Ambleside. Centre for Global Eco-Innovation, Joint report between CAfS and Lancaster University, 1-32.
36. Senkal, E., Kaplan, G., & Avdan, U. (2021). Accuracy assessment of digital surface models from unmanned aerial vehicles' imagery on archaeological sites.

International Journal of Engineering and Geosciences, 6(2), 81-89.
37. Diaz, B. S., Mata-Zayas, E. E., Gama-Campillo, L. M., Rincon-Ramirez, J. A., Vidal-Garcia, F., Rullan-Silva, C. D., & Sanchez-Gutierrez, F. (2022) LiDAR modeling to determine the height of shade canopy tree in cocoa agrosystems as available habitat for wildlife. International Journal of Engineering and Geosciences, 7(3), 283-293.
38. Özdemir, S., Akbulut, Z., Karsli, F., & Acar, H. (2021). Automatic extraction of trees by using multiple return properties of the lidar point cloud. International Journal of Engineering and Geosciences, 6(1), 20-26.
39. Sevgen, S. C. (2019). Airborne lidar data classification in complex urban area using random forest: a case study of Bergama, Turkey. International Journal of Engineering and Geosciences, 4(1), 45-51.
40. Özendi, M. (2022). Kültür varlıklarının yersel lazer tarama yöntemi ile dijital dokümantasyonu: Zonguldak Uzun Mehmet Anıtı örneği. Geomatik, 7 (2), 139-148. https://doi.org/10.29128/geomatik.917528
41. Yakar, İ., Çelik, M. Ö., Hamal, S. N. G. & Bilgi, S. (2021). Kültürel Mirasın Dokümantasyonu Çalışmalarında Farklı Yazılımların Karşılaştırılması: Dikilitaş (Theodosius Obeliski) Örneği. Geomatik, 6 (3), 217-226. https://doi.org/10.29128/geomatik.761475
42. Keleş, M. D. & Aydın, C. C. (2020). Mobil Lidar Verisi ile Kent Ölçeğinde Cadde Bazlı Envanter Çalışması ve Coğrafi Sistemleri Entegrasyonu-Ankara Örneği. Geomatik, 5 (3), 193-200. https://doi.org/10.29128/geomatik.643569

International Journal of Engineering and Geosciences
https://dergipark.org.tr/en/pub/ijeg
e-ISSN 2548-0960

Modeling of annual maximum flows with geographic data components and artificial neural networks

Esra Aslı Çubukçu*[1], Vahdettin Demir [1], Mehmet Faik Sevimli [1]

[1]*KTO Karatay University, Faculty of Engineering and Natural Sciences, Civil Engineering Department, Türkiye*

Keywords
Modeling
Flood
Artificial Neural Networks
Annual Maximum Flow
Geographical Information Systems

Research Article
DOI: 10.26833/ijeg.1125412

Received: 04.06.2022
Accepted: 07.10.2022
Published: 19.10.2022

Abstract

The flow rate at which the instantaneous maximum flow is recorded throughout the year is called the Annual Maximum Flow (AMF). These flow rates often cause disasters such as floods. Snow melts and extreme precipitation associated with temperature fluctuations are the two most important factors that occurred flooding. The deluge that follows kills people and destroys property in communities and agricultural lands. As a result, it's critical to predict the flow that causes flooding and take appropriate precautions to limit the damage. The prediction of the probability of a flood event in advance is very important for the safety of life and property of large masses and agricultural lands. Early warning systems, disaster management plans and minimizing these losses are among the important goals of the country's administration. This study was used in five Current Observation Stations (COS) located in Yeşilırmak Basin in Turkey. By using 8 input data including geographical location, altitude and area information of these stations, AMF data were tried to be estimated for each COS. A total of 240 input data was used in the study. The data period covers the years 1964-2012. Unfortunately, AMF values cannot be monitored for all 5 stations used after 2012. Therefore, the data period was stopped in 2012. In this study, Multilayer Artificial Neural Networks (MANN), Generalized Artificial Neural Networks (GANN), Radial Based Artificial Neural Networks (RBANN) and Multiple Linear Regulation (MLR) methods were used. Input data sets were made into 4 packets and these packages were used respectively in both training and testing stages. In these packages, the AMF data measured for the 5 stations mentioned above between 1965 and 2012 were divided into 4 and used by creating 25% (test) and 75% (training) packages. Root Means Square Error (RMSE), Mean Absolute Error (MAE) and correlation coefficient (R) were used as the comparison criteria. The results are as follow; MANN (RMSE = 119.118, MAE = 93.213, R = 0.808), and RBANN (RMSE = 111.559, MAE = 81.114, R = 0.900). These results show that AMF can be predicted with artificial intelligence techniques and can be used as an alternative method.

1. Introduction

A flood is defined as a rapid increase in the amount of water in a river or stream bed due to more than-normal rainfall or sudden snowmelt. Floods have the power to greatly damage living creatures and land around the beds according to their flow rates. The most dangerous floods are the sudden rise of the water in the side branches as a result of the sudden temperature change in the heavily sloping and impermeable soil areas and the basins with heavy snowfall after heavy rainfall. While changes occur in the water cycle of the atmosphere as a result of global warming and climate change, an increase is observed in the occurrence of heavy precipitation events and meteorological natural disasters. Warming climatic conditions increase the risks of drought and flood at different times and places [1]. Another reason is the precipitation regime of the basin. While the rate of floods seen in rivers between 1967-1987 among all hydrometeorological disasters was 33%; Between 1998 and 2008, this rate decreased to 14%. The increase in the number of dams established in the region in recent years, stream improvement works, and migrations from villages to cities have led to a decrease in floods originating from rivers in this way. However, despite this, according to Directorate General For State

* **Corresponding Author**

*(cubukcuasli@gmail.com) ORCID ID 0000-0003-4159-205X
(vahdettin.demir@karatay.edu.tr) ORCID ID 0000-0002-6590-5658
(mehmet.faik.sevimli@karatay.edu.tr) ORCID ID 0000-0002-4676-8782

Cite this article

Çubukçu, E. A., Demir, V., & Sevimli, M. F. (2023). Modeling of annual maximum flows with geographic data components and artificial neural networks. International Journal of Engineering and Geosciences, 8(2), 200-211

Hydraulic Works data, 1209 flood events occurred between 1975 and 2015, 720 deaths occurred as a result of these floods 893.933 hectares of agricultural land were flooded [2].

According to the data of the Turkish State Meteorological Service (TSMS), 109 of the 2372 floods that occurred between 1940 and 2010 occurred in the provinces where the stations selected in the study are located. It has been observed that this rate covers approximately 9.317% of all floods that occur [3]. It is very important in terms of the measures to be taken and the infrastructure systems to be established in order to remove the resulting flood from the settlements and agricultural lands with the least damage. At this point, predicting the flood helps us to minimize the unexpected loss of life and property. Predicting a possible future flood has always been a difficult issue as it depends on precipitation and snowmelt parameters due to sudden weather changes. While hydrological forecasting and flood response is a very important issue, current atmospheric forecasts often do not provide a sufficient level of accuracy for climate forecasts or hydrological forecasts [1]. This study aims to estimate this difficulty with Artificial Neural Networks (ANN) or regression methods based on the closed box model, apart from known functions, and to complete the missing data.

ANNs are computer systems that perform the learning function, which is the most basic feature of the human brain. They perform the learning process with the help of examples [4]. The learning and generalization ability of ANN presents this method as an ideal tool for solving complex problems [5].

Hundreds of studies have been carried out since the introduction of ANNs, the studies started in the first half of the 20th century and continued at a rapid pace until today. The first artificial neural network model was developed in 1943 by Doctor Warren McCulloch and mathematician Walter Pitts. McCulloch and Pitts modeled a simple neural network with electrical circuits, inspired by the human brain's ability to calculate and learn through experience. The 1970s became a turning point for ANNs, and many problems that were not previously considered possible to be solved began to be solved in this period [6]. Dibike et al. in their work in 2001, started to apply rainfall-runoff modeling, which can be used to obtain data on river systems design, operation and river flow, with closed box methods. When the results were compared, it was observed that ANN methods gave successful results [7]. Dawson and Wilby made precipitation-flow modeling and flood forecasting using ANN architecture in 2001. They demonstrated that the model and results could be improved [8]. In their 2002 study, Lim and Lye examined the flood records of the river basin in Sarawak, Malaysia, using an index-flood forecasting model based on the L-moment method. The results presented here are useful for engineering applications in Sarawak. It can also be used in other areas, provided that generally flood records are available. It can also be applied to unaffected basins in or near a defined homogeneous region in Sarawak [9]. Dahamsheh in 2008, In his study modeled the future monthly precipitation with Markov chain-added conditional ANNs by using the precipitation data of the previous days and months of Amman, Baqura and Safawi stations selected from different regions of Jordan. As a result, it has been seen that ANN and MLR models and models strengthened with synthetic series are insufficient, and by combining them with Markov chain, ANN and MLR models have achieved success in drought-precipitation forecasts. He concluded that the conditional ANN and conditional MLR models can be used in future studies of precipitation and drought or to complete missing data [10]. Hu et al., in their research in 2009, conducted studies to investigate new measures to improve the generalization performance of the precipitation flow model based on ANN and to evaluate the applicability of new measures. They chose the basin areas in China as the study area and applied them in 7 basins. As a result of this study, they recommended combining previous hydrological knowledge with a neural network learning algorithm instead of using neural networks as a closed-box model for rain conversion, providing consistent improvements in all seven watersheds. Second, changing the training target function offers variable results, despite improved model performance for high and low flows. Finally, work should continue to impose additional sensitivity constraints to reduce network sensitivity to input errors, improve neural network model performance, and especially generalization features. It was observed that the improved models performed better than the BP, and the 3 proposed models improved performance [11]. Ren et al. in their study in 2010, combined fuzzy logic and ANN methods with a hydrological model and modeled real-time flood forecasting for a basin in Liaoning province of China. By looking at the results, they showed that the classified models were more accurate than the others [12]. Ahmad et al., in their study in 2015, performed frequency analysis using the hydrological characteristics of 18 different regions of 5 different rivers in Pakistan. When looking at the results, Generalized Pareto, Generalized Logistics, and GEV were accepted as the best three distributions out of 10 probability distributions, L Moments method was found to be the most appropriate estimation method. For flood frequency analysis, they are in close agreement with observed flows, while also estimating different return times associated with given flood magnitudes [13]. Haktanır et al. in 2016 investigated regional frequency analyses with annual maximum rainfall data and L-moments method [14]. In the study conducted by Akkaya and Doğan in 2016, 2-dimensional flood modeling of Meriç and Tunca Rivers passing through Edirne city center was made and flood maps were created. With the analysis of the results obtained from the flood maps, a drainage channel that can discharge the flood flows exceeding the maximum flow rate that the Meriç River main bed can carry was designed and the downstream conditions of the channel were evaluated [15]. Çıtakoğlu et al. in 2017, performed regional frequency analysis using the L-Moments method using the AMF data of 52 current observation stations in the Black Sea. The application covers the five major basins. It has been revealed that the study area is not a homogeneous region as a whole. Considering the physiographic and hydrological characteristics of the basins and according to the H_1 criterion the study area is

divided into 11 different homogeneous regions. According to Z_{DIST} conformity test results, there were 11 sub-regions. In five of them, the Generalized Normal distribution was determined as the most appropriate probability distribution. Generalized The Extreme Values, Pearson Type 3, and Generalized Logistic distributions are the most common in three, two, and one subregion, respectively. As a result of the index-flood frequency analyzes made with these distributions, the study Regional AMF with grid method in recurrence periods between 2 years and 1000 years for the area created maps [16]. Aghayev took a sample of the flood damage assessment, using 2010 flood data downstream of the Kura River. Using ArcGIS 10.2.1 software, maps of flooded areas and possible infrastructures in flooded areas were created. The study showed that combining multiple spatial data can significantly aid in flood damage estimates [17]. Oyebode and Stretch gave information about the advantages and disadvantages of ANN in hydrological modeling. They revealed that ANN is an important structure for obtaining good predictions in hydrological models [18]. Ovcharuk et al., used materials from 54 water measuring stations (WGS) to characterize the maximum flow during rain and melt-rain floods in rivers in the Crimean Mountains. A modified reduction structure of a calculation formula was used to evaluate the maximum flow of flash floods of different origin for rivers in mountainous Crimea. The main parameters of the proposed model are summarized as dependencies on the mean height of the basins and generalized in the form of a map. It is also possible to use the second variant of the proposed method, taking into account that the underlying surface factor is introduced. A comparison of the calculated maximum flow values shows good convergence with both the initial information and the largest values in the observation period [19]. Taylan et al. [20] developed hybrid wavelet-artificial intelligence models used in meteorological drought forecasting. Wavelet transform (W), adaptive neural-based fuzzy inference system (ANFIS), support vector machine (SVM) and ANN were used to develop drought forecasting models of Çanakkale province. Hezarani and colleagues created drought prediction models using ANN in 2021. ANN and SPI combination meteorological predicted drought with high accuracy. However, the combination of ANN and SDI isn't good for predicting hydrological drought [21]. Demir and Keskin, who did not have enough flow measurement in their studies, modeled the flood repetition rates of the Mert River in Samsun by using unit hydrograph methods and the flood propagation created by the flood hydrographs with certain recurrences in the study area. While applying the methods, precipitation data from 3 meteorological stations covering the basin, representing the Mert River basin, were used. They compared using various statistical distributions. The optimal distribution was determined by the Kolmogorov-Smirnov fitness test. Obtained flood flow rates were modeled with the FLO-2D program. Flood spreading areas and water heights were examined in different recurrences, and suggestions were made for the bridges on the river and the areas where there is construction [22].

Based on the surveyed literature in the Scopus database, it is worth mentioning that over 48 research articles were observed on the domain of maximum flow forecasting using ANN models. Figure 1 reports the VOSviewer algorithm on the interconnection between the keywords. It can be observed from this figure, this topic has major importance on water resources engineering domain addition, the connection of the "ANN and maximum flow forecast" keywords revealed the implication of those two words for the majority of the displayed keywords.

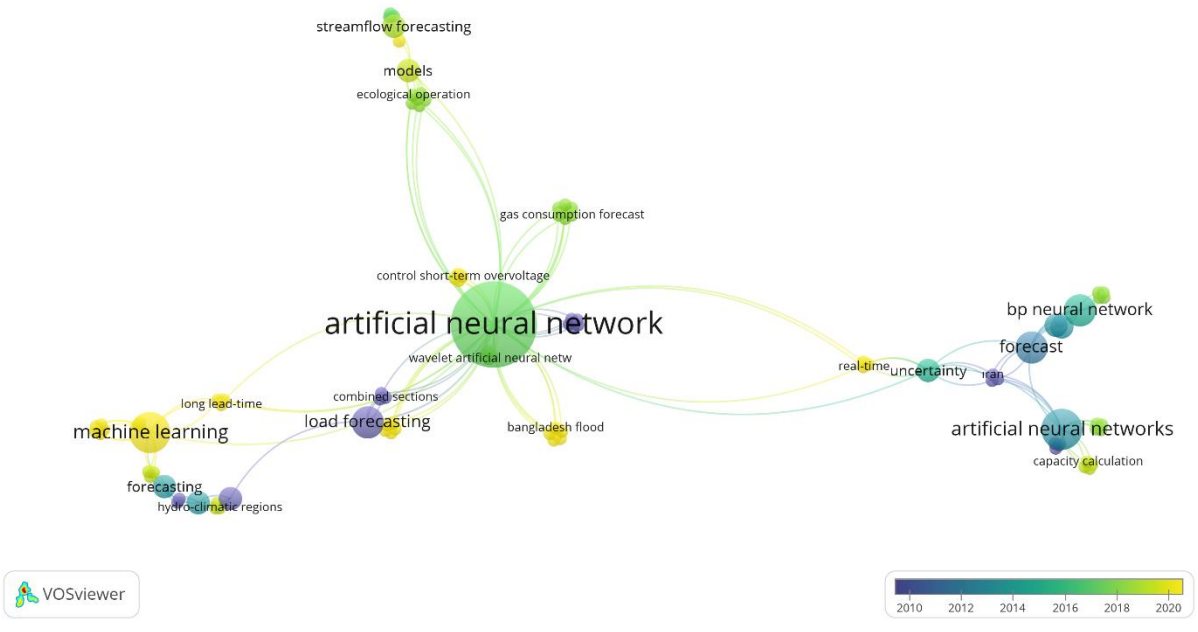

Figure 1. Relationship of ANN and maximum flow forecast keywords on Scopus database

Estimating the flood flow rate is the first stage of flood modeling studies. With this modeling, we can present the flood visually. We need data continuity for predictive modeling with ANN. The floods experienced may damage the Current Observation Stations (COS) and disrupt the data continuity. In the study, we tried to estimate the AMF data of 5 COS (1402, 1412, 1413, 1414, 1418) located in the Yeşilırmak Basin of the Black Sea Region in Turkey with their geographical components. The biggest reason for choosing this area is the flood events experienced in the past years and the continuity we can provide in the data. In this study, using the data sets created with AMF data and geographic information between 1964 and 2012, all data sets were subjected to training and testing stages, respectively. There is a problem of data deficiency in stations caused by natural disasters in the past. This study aims to complete missing data while testing past packages.

2. Method

2.1. Material

AMFs are flows recorded by COSs that show the largest instantaneously recorded flow rate in a water year, often resulting in flooding. Descriptive statistical information on the parameters examined in the study is given in Table 1.

Looking at the statistical information of the AMF data, it is seen that the maximum value is 1252 m^3/sec and the minimum value is 5.010 m^3/sec. This shows that the differences between the data can be very large and the AMF is too variable. While the average of the data is 259.571 m^3/sec, the standard deviation of the data is 246.695. The skewness coefficient is 1.542. Because this number is more than 1, the data is skewed to the right.

Right skewness makes modeling difficult, while the margin of error in modeling the result is expected to be high. Since the North (Degrees) parameter is at the same latitude for each station, its maximum value, minimum value and average are equal.

The workstations and flow networks in Figure 2 were created in the Geographical Information Systems (GIS) environment [23]. River networks and basin boundaries can be determined via ArcGIS and Basin toolbox, which are GIS software. GIS is used to solve many water engineering problems and to prepare base data such as digital elevation model data [17, 22, 24-31].

The study area is in the Yeşilırmak Basin no. 14 and the flow observation stations on the Yeşilırmak River and Çorum Çat River are shown on the map with their numbers. When the elevation map of the basin is examined, it is understood that the elevation increases from west to east [23]. Maximum current data from 1964 to 2012 were used for COS coded 1402, 1412, 1413, 1414, and 1418 as study data, but since there was no data for all stations in 1968, estimates were made by excluding the data for 1968. Since the data after 2012 were the stations that were closed or damaged by the flood, there was data discontinuity, analysis could not be made after this year because it could not be provided by all stations.

According to the information in Table 1 and Table 2, since the parameter expressed as North (Degrees) is located at 40° latitude for all COS, no correlation was found with this variable and this parameter was not used by subtracting it for all stations.

Table 1. Descriptive statistical information of the studied parameters

Variable	Unit	Number of data	Max Value	Min Value	Average	Standard deviation	Skewness coefficient
Area	(Km^2)	240	33904.00	1608.00	13251.44	12566.14	0.66
East (Degree)	°	240	37.00	35.00	36.00	0.63	0.00
East (Minutes)	'	240	30.00	6.00	15.00	10.35	0.47
East (Seconds)	''	240	45.00	3.00	27.80	19.49	-0.40
North (Degree)	°	240	40.00	40.00	40.00	0.00	0.00
North (Minute)	'	240	46.00	18.00	32.20	10.94	0.15
North (Seconds)	''	240	42.00	3.00	21.40	16.61	0.22
Height	m	240	820.00	190.00	470.20	217.09	0.32
Year	1964-2012	240	2012.00	1964.00	1988.41	14.01	-0.02
AMF	m^3/s	240	1252.00	5.01	259.57	246.69	1.54

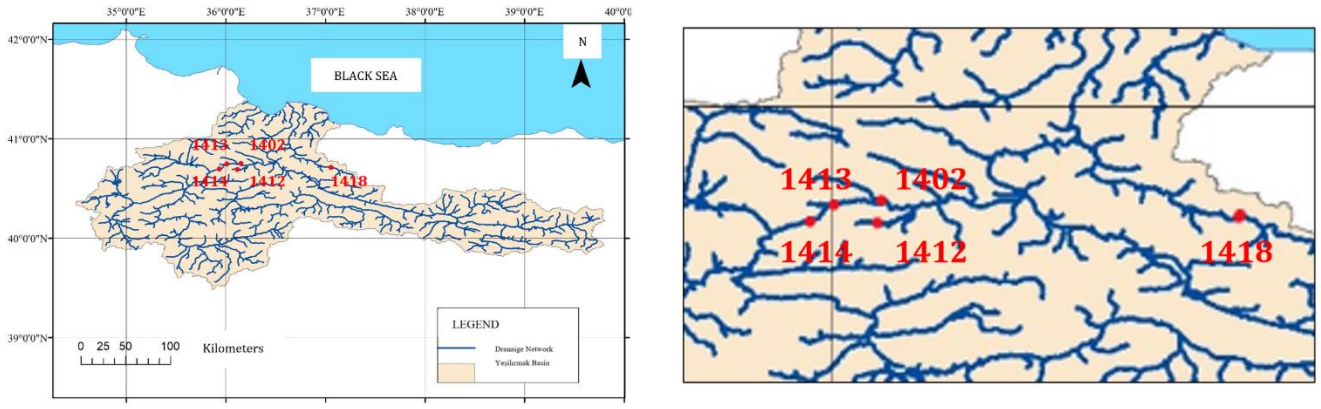

Figure 2. Yeşilırmak Basin drainage network [23]

Table 2. Summary information about the stations used in the study (*The year 1968 was not used)

Code	Province	Station Name	Latitude	Longitude	Height	Data Period
1402	Tokat	Kale	40° 46' N	36° 30' E	190 m	1964-2012*
1412	Çorum	Şeyhoğlu	40° 27' N	35° 25' E	530 m	1964-2012*
1413	Amasya	Durucasu	40° 44' N	36° 30' E	301 m	1964-2012*
1414	Tokat	Sütlüce	40° 26' N	36° 7' E	510 m	1964-2012*
1418	Tokat	Gömeleönü	40° 18' N	37° 7' E	820 m	1964-2012*

2.2. Method

ANN can be defined as machine systems that perform the learning function, which is the most basic feature of the human brain. ANNs perform learning processes with the help of examples. ANNs can be defined as the transfer of the learning mechanism in the human brain to the machine by experience. This learning mechanism, unlike what is known, brings the computational feature to the computer by using the ability to adapt to the environment, to adapt, to work according to past experiences or incomplete information in times of uncertainty.

In ANNs, various pre-processes are applied to the inputs and outputs of the network cells, and the training process of the data that is included in the ANN cycle and trained can become more efficient. This pre-process is called "Normalization". The training process of ANN data can take a very long time when applied without normalization. There are many data normalization methods in the literature. Min-Max normalization is used in this study. For the application of the ANN model, all data were first normalized between 0.2 - 0.8 using Eq. 1 [32].

$$X' = 0.6 * \frac{X_1 - X_{min}}{X_{max} - X_{min}} + 0.2 \quad (1)$$

X' = Normalized data
X_1 = Input value
X_{min} = Minimum data
X_{max} = Maximum data

2.2.1. *Multi-Layered Artificial Neural Networks*

Multi-layer Artificial Neural Networks (MANN) consist of an input layer, one or more hidden (intermediate) layers, and an output layer where information is input. MANN has transitions between layers called forward and backward propagation. In the forward propagation phase, the output and error values of the network are calculated. In the back-propagation phase, the inter-layer link weight values are updated to minimize the calculated error value [33]. The MANN model uses the backpropagation learning algorithm, which is the generalization of the least squares algorithm in linear perception. The input layer contains neurons that receive these inputs. Therefore, the number of neurons in the input layer must be the same as the number of input values in the data set. The neurons in the input layer pass the input values directly to the hidden layer. Each neuron in the hidden layer calculates the total value by adding the threshold value to the weighted input values and processes them with an activation function and passes them to the next layer or directly to the output layer. Weights between layers are usually randomly selected at the beginning. The error value is calculated by comparing the output values of the network with the expected output values. Figure 3 shows the structure of the MANN. The multi-layer sensor model consists of an input (X_1, X_2, X_3,....., X_D), a hidden, and an output layer (Y). Each layer may also have one or more processing elements [34].

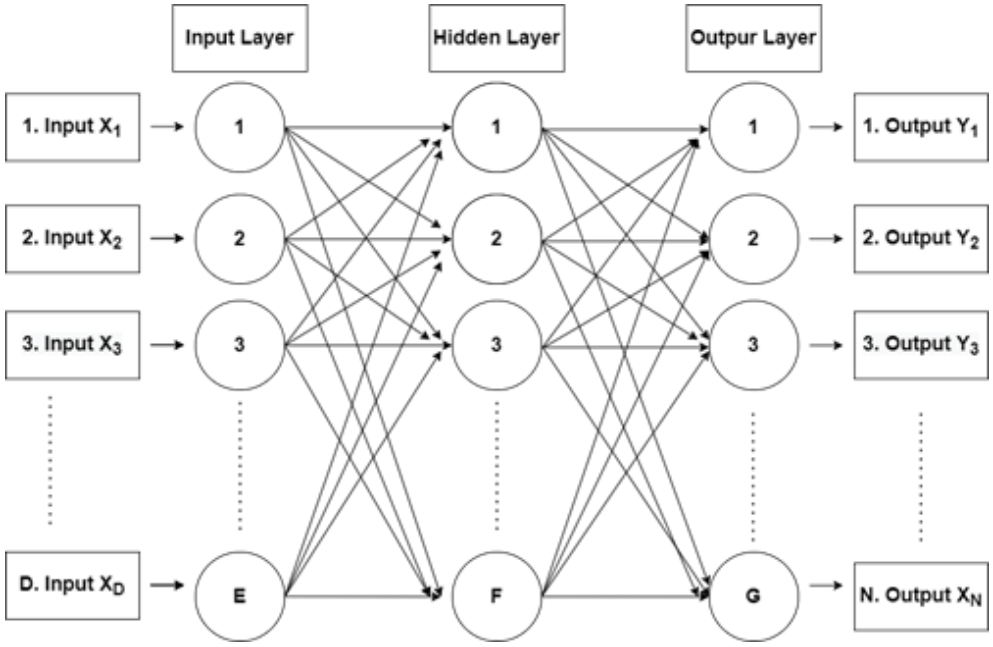

Figure 3. Structure of MANN

In Figure 2, each cell in the hidden and output layers takes the NET-weighted total outputs from the previous layer as input. NET values are found in Eq. 2.

$$NET_{xb} = \sum_{a=1}^{D} A_{ab} Ç_{xa} + \theta_b \quad (2)$$

θ_b is the bias constant (bias), A_{ab} is the set of weights between the input and hidden layers, D is the size of the input vector, $Ç_{xa}$ is the output set of the input layer for the x sample. Each cell from the second layer, the hidden layer, and the third layer, output layer, passes the NET value through a non-linear sorting function. As a result, the output f(NET) is produced in Eq. 3.

$$f(NET) = \frac{1}{1+e^{-NET}} \quad (3)$$

The total error "H_t" for sample "t" is calculated as in Eq. 4 during the training phase, depending on the difference of squares between the estimated and actual outputs.

$$H_t = \sum_{c=1}^{N} (G_{tc} + T_{tc})^2 \quad (4)$$

"G_{tc}" is the actual output value for the "c" sample, "T_{tc}" is the estimated output value for the c sample, "N" is the number of iterations. Depending on the total error, each connection weight, "A_{ab}", is renewed with the help of the equation in Eq. 5.

$$A_{ab}^{new} = A_{ab}^{old} - \left[J^T J + \mu I \right]^{-1} J^T H_t \quad (5)$$

"J" is a parameter that affects the Jacobian matrix, "J^T" is the transpose of the Jacobian matrix, "I" is the unit matrix, and "μ" is a parameter that affects the convergence rate.

In Matlab
net=train
Y1(output) = sim;

Net value obtained by running the code Y1(output) = sim; The training and testing process using the code is modeled in MANN.

2.2.2. Radial-Based Artificial Neural Networks

Radial-Based ANN (RBANN) concept was introduced into the literature in 1988 by Broomhead and Lowe [35]. ANN model and Radial-based functions have been developed by considering the effect-response states of neuron cells in human nervous system. It is possible to see the education of RBANN models as a curve fitting approach in multidimensional space [36, 37]. Thus, the educational performance of the RBANN sample turns into a problem of finding the closest result to the data in the output vector space and thus an interpolation problem [38]. RBANN structure generally consists of input layer, hidden layer and output layer similar to ANN structure. However, unlike other ANNs, the data is subjected to radial based activation functions and a nonlinear cluster analysis when passing from the input layer to the hidden layer. The structure between the hidden layer and the output layer functions as in other ANN types and the actual training takes place in this layer. In the RBANN model we used, the problem was solved with purelin function [39].

In Matlab
net=newrb
Y1(output) = sim;

Net value obtained by running the code Y1(output) = sim; The training and testing process using the code is modeled in RBANN.

2.2.3. Generalized Regression Neural Network

The generalized regression neural network proposed by Specht does not require an iterative training procedure like the back propagation method [40]. Unlike the feedback ANN models, it can perform all calculations in a single pass. It can produce results faster than others. However, in standard GRNN, where no preprocessor algorithm is used, the number of neurons in the pattern layer is equal to the amount of data in the training set. Therefore, in problems with large training data, the network structure becomes larger at the same rate as the training data set, and the number of operations increases.

GRNN is a 4-layer, feed-forward ANN model with input layer, pattern layer, collection layer and output layer. Unlike it does not require iterative. Each layer in its structure consists of different numbers of neurons [41].

net = newgrnn
Y1 (output) = sim;

Net value obtained by running the code Y1(output) = sim; The training and testing process using the code is modeled in GRNN.

2.2.4. Multi-Layered Regression

According to the equation "y" dependent, "x" is an independent variable, "ε" can be expressed as an error [42]. Equations where variable number increases. Linear regression between two variables can express with Eq. 6.

$$y = a + bx + \varepsilon \quad (6)$$

Linear regression biger then two variables can express with equation.

$$y = a + b_1 x_1 + b_2 x_2 + b_3 x_3 + \ldots\ldots b_n x_n + \varepsilon \quad (7)$$

These equations are called multiple linear regression equations.

3. Results

In the correlation relationship obtained by using the data of the stations selected within the Yeşilırmak basin no 14 selected as the study area; The correlation coefficient between AMF and Area was found to be 0.803, making it Minute (D) 0.677, Second (K) -0.616, Second (D) 0.603, Z (m) 0.384, Minute (K) 0.151, Degree (D) It follows with 0.147 and finally the year parameter with a correlation coefficient of 0.113 (Table 3).

Between 1964 and 2012, it was divided into packages equally and the packages it represented are given in Table 4.

Table 3. Correlation of input parameters

	Area (km^2)	Minutes'(N)	Z(m)	Second''(E)	Degree°(N)	Minute'(E)	Degree°(E)	Second''(N)	Year	AMF
Area (km^2)	1.00									
Minutes'(N)	-0.05	1.00								
Z(m)	0.45	-0.55	1.00							
Second''(E)	0.59	0.65	-0.07	1.00						
Degree°(N)	***	***	***	***	1.00					
Minute'(E)	0.94	-0.26	0.37	0.44	***	1.00				
Degree°(E)	0.08	0.69	-0.50	0.80	***	0.04	1.00			
Second''(N)	-0.89	0.42	-0.46	-0.21	***	-0.96	0.22	1.00		
Year	0.01	0.00	0.01	0.02	***	0.01	0.02	-0.00	1.00	
AMF	**0.80**	**0.15**	**0.38**	**0.60**	***	**0.67**	**0.14**	**-0.61**	**-0.11**	**1.00**

***5. Column (Degree (N)) values will not be used, since all of our stations are located at 40° latitude, no relationship could be established.

Table 4. Data packets used

Data Package	Years
A_1	2012-2001
A_2	2000-1989
A_3	1988-1977
A_4	1976-1964

Correlation coefficients were analyzed according to both sign and order of magnitude in the first place and the results were compared. Since there were very small differences in the results, the study was continued by ordering them from the largest to the smallest regardless of the sign according to the coefficient relationship, and the input order of the parameters was determined. While the correlation coefficients were found, since the Degree (N) parameter was located at 40° latitude for all stations and their data, no relationship could be established with this parameter and Degree (N) data was not used in the analysis.

The distribution of the test packages and the analysis names named according to each case are given in Table 4. The A_1 package represents the years 2012- 2001, the A_2 package represents the years 2000- 1989, the A_3 package represents the years 1988 - 1977, the A_4 package represents the years 1976 - 1964.

Table 5. Data packages used in analysis

Analysis	Training Package	Test Package
M_1	A_2+ A_3+ A_4	A_1
M_2	A_1+ A_3+ A_4	A_2
M_3	A_1+ A_2+ A_4	A_3
M_4	A_1+ A_2+ A_3	A_4

The grouping of data packages as training and test packages is given in Table 5. As seen in the Table 5, in M_1 analysis, A_1 package is used in testing, A_2+ A_3+ A_4 package is used in education. In M_2 analysis, A_2 package is used in testing, A_1+ A_3+ A_4 package is used in education. In M_3 analysis, A_3 package is used in testing, A_1+ A_2+ A_4 package is used in education. In M_4 analysis, A_4 package is used in testing, A_1+ A_2+ A_3 packages are used in training.

RMSE, MAE and R were used as comparison criteria. According to these criteria, the methods giving the best results were determined and the results were tabulated.

$$RMSE = \sqrt{\frac{1}{N}\sum_{i=1}^{N}(Z_e - Z_o)^2} \quad (8)$$

$$MAE = \frac{1}{N}\sum_{i=1}^{N}\left|Z_e - Z_o\right| \quad (9)$$

$$R = \left(\frac{N*\left(\sum Z_o * Z_e\right)-\left(\sum Z_o\right)*\left(\sum Z_e\right)}{\sqrt{\left(N*\sum Z_o^2\right)-\left(\sum Z_e\right)^2 * \left(N*\sum Z_e^2\right)-\left(\sum Z_e\right)^2}}\right) \quad (10)$$

In the Equations 8-10, "Z_e" and "Z_o" show the estimated and observed AMF values and "N" represents the number of data [43]. M_1 analysis test results are shown in Table 6.

When the test results are examined, in Table 6 the MANN gives the lowest error and the highest accuracy rate in the averages of all inputs. M_2 analysis test results are shown in Table 7.

In Table 7, the averages give close results according to the methods. Individually, RBANN (8 Entries) gave the best results. M_3 analysis test results are shown in Table 8.

In Table 8, the averages give close results according to the methods. RBANN (1 Input) gave the best results locally. M_4 analysis test results are shown in Table 9.

In Table 9, the averages give close results according to the methods. RBANN (2 Inputs) gave the best results individually.

Since AMF data could not be obtained at all stations for the year 1968, entries were made in the data sets used in the analysis, excluding that year. In Table 10, the study of completing the missing data of 1968 was carried out. The estimated flow rates for each station according to the methods are as in the table. However, since we do not have data for that year, there is no situation that we can control [44].

In Table 10, MLR method makes higher estimations for all stations compared to other methods. It is observed that the MANN and GRNN methods give very close results as in the results of other packages.

Table 6. M_1 Analysis Comparison of test data

Test	Method	Input Data (M_1 analysis)								
		(i)	(ii)	(iii)	(iv)	(v)	(vi)	(vii)	(viii)	Average
RMSE	MANN	167.98	167.35	167.35	167.35	167.35	167.35	167.35	119.11	161.40
	RBANN	167.35	163.16	163.67	158.92	167.79	167.35	167.35	140.25	161.98
	GRNN	170.56	167.66	167.57	167.36	167.36	167.35	167.35	161.31	167.06
	MLR	182.56	180.60	164.27	167.23	167.35	167.35	167.35	158.53	169.40
Average		172.11	169.69	165.71	165.21	167.46	167.35	167.35	144.80	164.96
MAE	MANN	120.79	118.73	118.73	118.73	118.73	118.73	118.73	93.21	115.79
	RBANN	118.73	120.30	117.93	111.05	119.73	118.73	118.73	108.64	116.73
	GRNN	126.14	120.03	119.77	118.81	118.80	118.73	118.73	120.15	120.14
	MLR	144.62	146.54	114.11	118.40	118.73	118.73	118.73	108.50	123.54
Average		127.57	126.40	117.63	116.75	119.00	118.73	118.73	107.62	119.05
R	MANN	0.77	0.77	0.77	0.77	0.77	0.77	0.77	0.80	0.78
	RBANN	0.77	0.78	0.78	0.77	0.77	0.77	0.77	0.63	0.76
	GRNN	0.75	0.77	0.77	0.77	0.77	0.77	0.77	0.79	0.77
	MLR	0.71	0.70	0.78	0.77	0.77	0.77	0.77	0.77	0.76
Average		0.75	0.75	0.78	0.77	0.77	0.77	0.77	0.75	0.77

Table 7. M_2 Analysis Comparison of test data

Test	Method	Input Data (M_2 analysis)								
		(i)	(ii)	(iii)	(iv)	(v)	(vi)	(vii)	(viii)	Average
RMSE	MANN	131.20	164.07	130.48	130.48	130.48	130.48	130.48	170.29	139.74
	RBANN	130.48	130.48	130.48	130.48	133.41	130.28	169.72	123.33	134.83
	GRNN	130.48	130.48	130.48	130.48	130.48	130.48	130.48	174.20	135.94
	MLR	147.73	146.86	129.86	130.47	130.48	130.48	130.48	129.83	134.52
Average		134.97	142.97	130.32	130.48	131.21	130.43	140.29	149.41	136.26
MAE	MANN	85.03	111.66	81.44	81.44	81.44	81.44	81.44	124.25	91.02
	RBANN	81.44	81.44	81.44	81.44	91.15	82.61	134.36	78.38	89.03
	GRNN	81.44	81.44	81.44	81.44	81.44	81.44	81.44	116.36	85.80
	MLR	101.83	103.26	80.57	81.37	81.44	81.44	81.44	80.96	86.54
Average		87.43	94.45	81.22	81.42	83.87	81.73	94.67	99.99	88.10
R	MANN	0.85	0.78	0.85	0.85	0.85	0.85	0.85	0.82	0.84
	RBANN	0.85	0.85	0.85	0.85	0.84	0.85	0.73	0.87	0.83
	GRNN	0.85	0.85	0.85	0.85	0.85	0.85	0.85	0.77	0.84
	MLR	0.81	0.80	0.85	0.85	0.85	0.85	0.85	0.85	0.84
Average		0.84	0.8	0.85	0.85	0.84	0.85	0.82	0.83	0.84

Table 8. M_3 Analysis Comparison of test data

Test	Method	Input Data (M_3 analysis)								
		(i)	(ii)	(iii)	(iv)	(v)	(vi)	(vii)	(viii)	Average
RMSE	MANN	157.16	157.16	157.16	157.16	157.16	157.16	157.16	133.83	154.25
	RBANN	156.76	156.10	156.22	157.16	157.09	162.57	194.34	168.39	163.58
	GRNN	157.16	157.16	157.16	157.16	157.16	157.16	157.16	131.45	153.95
	MLR	172.97	171.99	157.54	157.10	157.16	157.16	157.16	150.69	160.22
Average		161.02	160.60	157.02	157.15	157.15	158.52	166.46	146.09	158.00
MAE	MANN	94.76	94.76	94.76	94.76	94.76	94.76	94.76	90.31	94.21
	RBANN	95.49	93.05	93.43	94.76	94.62	115.80	139.45	109.61	104.53
	GRNN	94.76	94.76	94.76	94.76	94.76	94.76	94.76	85.03	93.55
	MLR	117.92	112.79	95.54	94.71	94.76	94.76	94.76	89.35	99.32
Average		100.74	98.84	94.63	94.75	94.73	100.02	105.94	93.58	97.90
R	MANN	0.90	0.90	0.90	0.90	0.90	0.90	0.90	0.89	0.90
	RBANN	0.91	0.90	0.90	0.90	0.90	0.89	0.81	0.86	0.87
	GRNN	0.90	0.90	0.90	0.90	0.90	0.90	0.90	0.88	0.90
	MLR	0.88	0.87	0.90	0.90	0.90	0.90	0.90	0.90	0.89
Average		0.90	0.89	0.90	0.90	0.90	0.87	0.88	0.89	0.89

Table 9. M_4 Analysis Comparison of test data

Test	Method	Input Data (M_4 analysis)								
		(i)	(ii)	(iii)	(iv)	(v)	(vi)	(vii)	(viii)	Average
RMSE	MANN	113.92	113.92	113.92	113.92	113.92	113.92	113.92	462.57	157.50
	RBANN	112.86	111.55	112.05	113.51	112.53	112.26	113.92	163.24	118.99
	GRNN	113.92	113.92	113.92	113.92	113.92	113.92	113.92	129.81	115.90
	MLR	131.54	131.84	114.17	113.81	113.92	113.92	113.92	158.06	123.90
Average		118.06	117.81	113.52	113.79	113.57	113.50	113.92	228.42	129.07
MAE	MANN	79.70	79.70	79.70	79.70	79.70	79.70	79.70	371.90	116.22
	RBANN	80.16	81.11	78.97	82.84	80.10	80.76	79.70	133.71	87.17
	GRNN	79.70	79.70	79.70	79.70	79.70	79.70	79.70	98.56	82.06
	MLR	97.14	95.16	80.12	79.78	79.70	79.70	79.70	138.36	91.21
Average		84.17	83.92	79.62	80.51	79.80	79.96	79.70	185.63	94.17
R	MANN	0.89	0.89	0.89	0.89	0.89	0.89	0.89	0.69	0.86
	RBANN	0.89	0.90	0.89	0.89	0.89	0.89	0.89	0.84	0.89
	GRNN	0.89	0.89	0.89	0.89	0.89	0.89	0.89	0.89	0.89
	MLR	0.86	0.85	0.89	0.89	0.89	0.89	0.89	0.89	0.88
Average		0.88	0.88	0.89	0.89	0.89	0.89	0.89	0.83	0.88

Table 10. Estimates of 1968 AMF data

Method	Station No	Station Name	Input number	Estimated Flow Rates (m^3/s)
MANN	1402	Kale	7	619.47
	1412	Şeyhoğlu		51.42
	1413	Durucasu		326.57
	1414	Sütlüce		109.79
	1418	Gömeleönü		182.58
RBANN	1402	Kale	2	636.50
	1412	Şeyhoğlu		105.20
	1413	Durucasu		283.47
	1414	Sütlüce		109.31
	1418	Gömeleönü		155.34
GRNN	1402	Kale	7	619.47
	1412	Şeyhoğlu		51.42
	1413	Durucasu		326.57
	1414	Sütlüce		109.79
	1418	Gömeleönü		182.58
MLR	1402	Kale	8	746.45
	1412	Şeyhoğlu		178.40
	1413	Durucasu		453.55
	1414	Sütlüce		236.77
	1418	Gömeleönü		309.56

4. Discussion

A flood is defined as a rapid and uncontrolled increase in the amount of water in a river or stream bed as a result of more than normal rainfall or sudden snowmelt. Floods have the power to greatly damage the living creatures and lands around the beds according to their flow rates. The sudden rise of water in the side branches in sloping and impermeable soil areas caused by snow melts after heavy rain or sudden warming in snowy areas causes the most dangerous floods. Estimating the flood flow rate is the first stage of flood modeling studies. We need data continuity for predictive modeling with ANN. Experienced floods can damage COS and disrupt data continuity. In our study, the AMF data of 5 COSs (1402, 1412, 1413, 1414, 1418) located in the Yeşilırmak Basin 14 in the Black Sea Region were tried to be estimated with their geographical components.

5. Conclusion

In this study; using 8 input data including geographical location (north and east; degree, minute, second), altitude and area information of 5 COS (1402, 1412, 1413, 1414, 1418) located in the Yeşilırmak Basin numbered 14, each an attempt was made to estimate the AMF data for a COS. The data period covers the years 1964-2012. 48 years of data are grouped as 75% training and 25% test packages. Analyzes were made 4 times, with 1 package being tested each time. The study aims aims to complete the missing data by modeling the deficiencies of data losses due to natural disasters. MANN, GRNN, RBANN and MLR methods were used to estimate AMF.

When the results are examined;

- For M_1 analysis, the best result was MANN (8 input) (RMSE=119.118, MAE= 93.213, R=0.808),
- For M_2 analysis, the best result is RBANN (8 input) (RMSE= 123.334, MAE= 78.381, R=0.870),
- For M_3 analysis, the smallest error rates were observed as GRNN (8 input) (RMSE= 131.457, MAE= 85.033, R= 0.889), while the largest R coefficient for RBANN (1 input) (RMSE= 156.763, MAE= 95.499, R= 0.910),
- For M_4 analysis, it was observed that the best results were obtained with RBANN (2 input) (RMSE=111.559, MAE= 81.114, R=0.900).

• There are years when COS's cannot save data for various reasons. It is observed that missing data occurs in years when data cannot be recorded in this way. It has been observed that the test results give sufficient accuracy to make predictions instead of missing data.

• Errors according to the input parameters used (Table 1); While the area decreased using minute(E), second(N), second(E) entries, it increased in year, degree(E) and minute(N) parameters. It was observed that there were small differences in the results when the correlation coefficients were ordered from largest to smallest sign. Therefore, in this study, the correlation coefficients were ordered by size, and the data were entered in the order of magnitude of the correlation coefficients while performing the analysis, regardless of the sign.

• Considering the results of the analysis, it was observed that although the MLR method was better than MANN, it could not provide a better estimation than RBANN and GRNN. Therefore, it was concluded that RBANN and GRNN models are an alternative solution to MLR. Therefore, it has been observed that RBANN provides a valid accuracy rate and can be used in anerage flood modeling.

• The reason why the accuracy rate in the A_1 package is low compared to other packages; It can be said as the global warming experienced in recent years and the variation of seasons and precipitation amounts accordingly.

• High estimations from the data observed as a result of the modeling are important in terms of taking precautions. AMF flow often causes flooding at its peaks. Considering this situation, the estimation of a flow rate higher than observed is beneficial in terms of minimizing the damage caused by flooding by taking precautions.

The limitations of this study are the estimation of AMFs and the completion of missing station data using 3 different ANNs. Modeling was carried out in 4 different test packages. In future studies, the authors aim to use more up-to-date data and more stations. In addition, the authors plan to make predictions using spatial and temporal inputs by trying different methods.

Acknowledgement

The author thanks KTO Karatay University for support and thanks the anonymous reviewers for their contributions.

Author contributions

Esra Aslı Çubukçu: Methodology, Application, Writing Original draft preparation, **Vahdettin Demir:** Conceptualization, Methodology, Reviewing and Editing. **Mehmet Faik Sevimli:** Last Editing.

Conflicts of interest

The authors declare no conflicts of interest.

References

1. Tonkaz T., Çetin M., Kızıloğlu F., & Fayrap A. (2010). Mixed Eastern Black Sea Water Basin Annual Probabılıty Analysıs of Instant Maxımum Currents. II. National Flood Symposium, 315-321.
2. Republic of Turkey Ministry of Agriculture And Forestry General Directorate of Water Management Flood Management (2017). Ministry of Forestry and Water Affairs, Ankara.
3. URL1: "Natural disasters, floods" access address: https://www.riob.org/fr/file/272232/download?token=PysGjbkb accessed 6 October 2022.
4. Öztemel E. (2012). Artificial Neural Networks, Istanbul.
5. Aydoğan B., Ayay B., & Çevik, E. (2011). Ann Current Profile Forecasting in Straits With an Example:Bosphorus. 7th Coastal Engineering Symposium, 403-409.
6. URL2: "Artificial Neural Networks" access address:https://www.kimnezamanicatetti.com/yapay-sinir-agi/, accessed May 1, 2019.
7. Dibike Y. B., & Solomatine, D. P. (2001). River Flow Forecasting Using Artificial Neural Networks. *Physics and Chemistry of the Earth, Part B: Hydrology, Oceans and Atmosphere (B), 26*(1), 1-7.
8. Dawson, C. W. & Wilby, R. L. (2001). Hydrological Modelling Using Artificial Neural Networks. *Prog. Phys. Geogr., 25*(1), 80–108. https://doi.org/10.1177/030913330102500104.
9. Lim, Y. H., & Lye, L. M. (2003). Regional flood estimation for ungauged basins in Sarawak , Malaysia Regional flood estimation for ungauged basins in Sarawak. *Malaysia, Hydrological Sciences Journal, 48*(1), 79–94.
10. Dahamsheh, A. (2008). *Forecasting Monthly Precipitation For Arid Regions Using Conditional Artificial Neural Networks Combined With Markov Chain*. (Ph.D. Thesis, ITU Institute of Science and Technology, Turkey).
11. Hu, T. S., Lam, K. C. & Ng, S. T. A. (2009). Modified Neural Network for Improving River Flow Prediction/Un Réseau de Neurones Modifié pour Améliorer la Prévision de L'Écoulement Fluvial. *Hydrological Sciences Journal, 50*(2), 298–318.
12. Ren, M., Wang, B., Liang, Q. & Fu, G. (2010). Classified Real-Time Flood Forecasting By Coupling Fuzzy Clustering and Neural Network. *International Journal of Sediment Research 25*(2), 134-148.
13. Ahmad, I., Fawad, M. & Mahmood, I. (2015). At-Site Flood Frequency Analysis of Annual Maximum Stream Flows in Pakistan Using Robust Estimation Methods. *Polish Journal of Environmental Studies, 24*(6), 2345–2353.
14. Haktanir, T., Citakoglu, H. & Seckin, N. (2016). Regional frequency analyses of successive-duration annual maximum rainfalls by L-moments method. *Hydrological Sciences Journal,* 61(4), 647–668. https://doi.org/10.1080/02626667.2014.966722.
15. Akkaya, U. & Doğan, E. (2016). Generation of 2D Flood İnundation Maps of Meriç and Tunca Rivers

Passing Through Edirne City Center. *Geofizika 33*(1), 15-34, https://doi.org/10.15233/gfz.2016.33.7
16. Çıtakoğlu, H., Demir, V. & Haktanir, T. (2017). Regional Frequency Analysis Of Annual Flood Peaks Of Natural Streams Discharging To The Black Sea By The L-Moments Method. *Omer Halisdemir Univercity Journal of Engineering Science, 6*(2), 571–580.
17. Aghayev, A. (2018). Determining of Different Inundated Land Use in Salyan Plain During 2010 the Kura River Flood Through Gis and Remote Sensing Tools. *Journal of Engineering and Geosciences, 3*(3) 80–86. https://doi.org/10.26833/ijeg.412348.
18. Oyebode, D. & Stretch, O. (2019). Neural Network Modeling Of Hydrologicalsystems: A Review Of İmplementation Techniques. Natural Resource Modeling. 32(1), 1–14. https://doi.org/10.1002/nrm.12189
19. Ovcharuk, V., Gopchenko, E., Todorova, O., & Myrza, K. (2020). Calculating the Characteristics of Flash FLoods on Small Rivers in the Mountainous Crimea, *Geofizika 37*(1), 27-43. https://doi.org/10.15233/gfz.2020.37.3, July.
20. Taylan, E. D., Terzi, Ö. & Baykal, T. (2021). Hybrid Wavelet–Artificial İntelligence Models İn Meteorological Drought Estimation. *J. Earth Syst. Sci., 130*(38), 2021, https://doi.org/10.1007/s12040-020-01488-9.
21. Boustani Hezarani, A., Zeybekoğlu, U. & Ülke Keskin, A. (2021). Hydrological And Meteorological Drought Forecasting For The Yesilirmak River Basin, Turkey. *Sürdürülebilir Mühendislik Uygulamaları ve Teknol. Gelişmeler Derg., 4*(2), 121–135. 2021, https://doi.org/10.51764/smutgd.993792
22. Demir, V. & Ülke Keskin, A. (2022). Flood flow calculation and flood modeling in rivers that do not have enough flow measurement (Samsun, Mert River sample). *Geomatik, 7*(2), pp. 149–162, https://doi.org/10.29128/geomatik.918502
23. Çay, F. (2018). *Determination of Morphological Characteristics Of Basins in Turkey with The Help of GIS.* (Master Thesis, KTO Karatay University Institute of Science and Technology, Turkey).
24. Akgül, M. A. (2018). Sentetik Açıklıklı Radar verilerinin Taşkın Çalışmalarında Kullanılması: Berdan Ovası Taşkını. Geomatik , 3 (2) , 154-162 . https://doi.org/10.29128/geomatik.378123
25. Oğuz, E., Oğuz, K. & Öztürk, K. (2022). Düzce bölgesi taşkın duyarlılık alanlarının belirlenmesi . *Geomatik*, 7(3) , 220-234 . https://doi.org/10.29128/geomatik.972343
26. Tona, A. U. , Demir, V. , Kuşak, L. & Yakar, M. (2022). Su Kaynakları Mühendisliğinde CBS'nin Kullanımı. T*ürkiye Coğrafi Bilgi Sistemleri Dergisi*, 4 (1), 23-33. https://doi.org/10.56130/tucbis.993807
27. Yılmaz, O. S. (2023). Frekans oranı yöntemiyle coğrafi bilgi sistemi ortamında heyelan duyarlılık haritasının üretilmesi: Manisa, Demirci, Tekeler Köyü örneği. *Geomatik*, 8(1), 42-54. https://doi.org/10.29128/geomatik.1108735
28. Yılmaz, A. & Erdoğan, M. (2018). Designing high resolution countrywide DEM for Turkey . International Journal of Engineering and Geosciences, 3(3), 98-107. https://doi.org/ 10.26833/ijeg.384822
29. Al Kalbani, K. & Rahman, A. A. (2022). 3D city model for monitoring flash flood risks in Salalah, Oman. International Journal of Engineering and Geosciences, 7(1), 17-23. https://doi.org/ 10.26833/ijeg.857971
30. Yağmur, N. , Tanık, A. , Tuzcu, A. , Musaoğlu, N. , Erten, E. & Bilgilioglu, B. (2020). Opportunities provided by remote sensing data for watershed management: example of Konya Closed Basin . International Journal of Engineering and Geosciences, 5(3), 120-129. https://doi.org/10.26833/ijeg.638669
31. Yakar, M. (2009). Digital elevation model generation by robotic total station instrument. *Experimental Techniques*, *33*(2), 52-59
32. Yavuz S. & Deveci M. (2012). The Effect of Statistical Normalization Techniques on The Performance of Artificial Neural Network. *Erciyes University Journal of the Faculty of Economics and Administrative Sciences,* 167–187.
33. Arı, A., & Berberler, M. E. (2017). Prediction and Classification with Artificial Neural Networks Interface Design for Solving Problems. *Acta Infologica, 1*(2): 55–73.
34. Çubukçu, E. A., Sancıoğlu S., Demir, V. & Sevimli, M. F. (2019). Sea Water Level Estimation Using Six Different Artificial Neural Networks Training Algorithm, International Civil Engineering Architecture Conference, 716-725.
35. Broomhead, D. D. & Lowe, S. (1988). Multivariable Functional Interpolation and Adaptive Networks. *Complex Syst., 2*, 321–355.
36. Partal, T., Kahya, E. & Cığızoğlu, K. (2008). Prediction of Precipitation Data with Artificial Neural Networks and Wavelet Transformation Methods. *ITU Journal of Engineering, 7*(3), 73–85.
37. Poggio, T. & Girosi, F. (1990). Regularization Algorithms for Learning That Are Equivalent to Multilayer Networks. *Science, 247*(4945), 978–982.
38. Okkan, U. & Dalkılıç, H. Y. (2012). Monthly Runoff Model for Kemer Dam with Radial Based Artificial Neural Networks. *IMO Technical Journal,* 5957–5966.
39. Demir, V., Çubukçu, E. A. & Sevimli, M. F. (2019). Long-Term Month Temperature Forecast With Inverse Distances Weighted, Kriging And Artificial Neural Networks. CISET-2nd Cilicia International Symposium On Engineering And Technology, 10-13.
40. Sürel, A., (2006). *The Use of Generalized Regression Neural Network in Water Resources Engineering.* (Master Thesis, ITU Institute of Science and Technology, Turkey).
41. Oral, M., Kartal, S. & Özyıldırım, M. (2017). A Cluster Based Approach to Reduce Pattern Layer Size for Generalized Regression Neural Network. *Pamukkale University Journal of Engineering Sciences, 24*(5), 857–863.
42. Okkan, U. & Mollamahmutoglu, A. (2010). Daily Runoff Modelling of Yiğitler Stream by Using Artificial Neural Networks and Regression Analysis.

Dumlupınar University Journal of Science Institute, 23: 33–48.

43. Çubukçu, E. A. (2019). *Modelıng Of Annual Maxımum Flows Wıth Geographıc Data Components And Artıfıcıal Neural Networks.* (Master Thesis, KTO Karatay University Institute of Science and Technology, Turkey).
44. Zhang, Q. Yuan, Q. Zeng, C. Li, X. &Wei, Y. (2018). Missing Data Reconstruction In Remote Sensing Image With A Unified Spatial-Temporal-Spectral Deep Convolutional Neural Network. *IEEE Trans. Geosci. Remote Sens., 56*(8), 4274–4288.